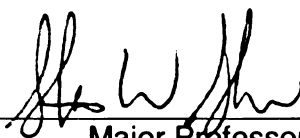This is to certify that the
dissertation entitled

MODEL REDUCTION OF NONLINEAR STRUCTURAL
SYSTEMS USING NONLINEAR NORMAL MODES AND
COMPONENT MODE SYNTHESIS

presented by

Polarit Apiwattanalunggarn

has been accepted towards fulfillment
of the requirements for the

__Ph.D.__   degree in   __Mechanical Engineering__

_____
Major Professor's Signature

_____8/21/03_____
Date

MSU is an Affirmative Action/Equal Opportunity Institution

PLACE IN RETURN BOX to remove this checkout from your record.
TO AVOID FINES return on or before date due.
MAY BE RECALLED with earlier due date if requested.

DATE DUE	DATE DUE	DATE DUE

MODEL REDUCTION OF NONLINEAR STRUCTURAL SYSTEMS USING NONLINEAR NORMAL MODES AND COMPONENT MODE SYNTHESIS

By

Polarit Apiwattanalunggarn

A DISSERTATION

Submitted to
Michigan State University
in partial fulfillment of the requirements
for the degree of

DOCTOR OF PHILOSOPHY

Department of Mechanical Engineering

2003

ABSTRACT

MODEL REDUCTION OF NONLINEAR STRUCTURAL SYSTEMS USING NONLINEAR NORMAL MODES AND COMPONENT MODE SYNTHESIS

By

Polarit Apiwattanalunggarn

This work addresses the general problem of model size reduction for describing the nonlinear vibration of structural elements and systems. The aim is to provide computational tools that allow one to accurately capture nonlinear dynamic behavior using a minimal number of degrees of freedom. In typical applications the finite element (FE) method is used to generate structural dynamic models, and model size reduction is carried out using linear modal analysis with truncation. However, in some cases one must retain many modes in order to accurately capture essential nonlinear coupling between the linear modes. In this work we utilize nonlinear normal modes (NNMs) defined in terms of invariant manifolds for the purposes of model size reduction, since it directly addresses modal coupling. This approach, which makes use of master and slave modes, along with the concept of dynamic invariance, allows one to generate accurate reduced order models (ROM) with only a few DOF, while capturing the effects of all modeled linear modes without directly simulating them. There are three main contributions of the present effort:

(1) Two new numerical approaches for solving the invariant manifold equations are introduced. Both approaches employ master modal displacement and velocity coordinates and are based on weighted-residual techniques. When compared with previous methods that utilize amplitude and phase variables, the new methods are found to be superior in terms of computational time but inferior in terms of accuracy.

(2) A specific application is considered: the finite amplitude vibrations of a rotating beam, which is a crude model for a rotorcraft blade. This system is known to possess essential nonlinear coupling between axial and transverse displacements, thereby leading to slow modal convergence. The proposed method systematically captures this coupling and provides an accurate single degree of freedom ROM. These results demonstrate the utility of NNM-based ROM, since they combine the versatility of the finite element method with the accurate NNM model reduction technique.

(3) A model reduction technique suitable for structures that can be partitioned into substructures is developed. This allows one to build ROMs using NNMs at the substructure level and to assemble these using a component mode synthesis (CMS) technique. It is found that the proposed nonlinear CMS technique generally provides an accurate model only when the couplings between substructures are weak.

To my father and mother

ACKNOWLEDGMENTS

TABLE OF CONTENTS

LIST OF TABLES

LIST OF FIGURES

CHAPTER 1

Introduction

1.1   Motivation

Modern engineers are sometimes required to accurately model the motions of complex structural systems, i.e., rotorcraft, turbo machines (turbines), vehicles, aircraft, bridges, off-shore platforms, robotic arms, etc., so that they can function properly and safely under certain operating conditions. Nowadays such structural systems are designed to be lighter, have more complex geometry, and operate at high speeds in order to enhance performance. These conditions can cause structural systems to experience responses in the nonlinear regime. To mathematically describe such motions, one must formulate nonlinear models, either discrete or continuous in nature. If they are continuous, in practice engineers typcially discretize them by using either direct modal discretization (Rayleigh-Ritz method) or the finite element (FE) method. The FE method is typically prefered in practice since it is a versatile tool for modeling very complex structures. However, it has a disadvantage in that it often requires a very large number of degrees of freedom (DOF) to accurately model the structure ([4]). The dynamic analysis (e.g., determination of natural frequencies, simulations, etc.) of nonlinear structures is typically more easily performed in modal coordinates than in physical coordinates, since it requires a smaller number of DOF. However, many modal coordinates are still needed for some nonlinear structures, typically those with some type of essential coupling between the linear modes. Therefore, this can result in considerable computational effort when ones try to analyze their dynamics ([5]).

The main objective of this research is to develop a class of techniques for generating accurate reduced order models for nonlinear structural systems. Our starting point is generally a nonlinear model, from either modal or FE analysis, whose dynamics are expressed by equations of motion expressed in terms of the linear modal coordinates. First, this work demonstrates a general framework on how to obtain nonlinear reduced order models (ROMs) using nonlinear normal modes (NNMs) that are defined in terms of invariant manifolds. Next, a methodology for obtaining nonlinear ROMs from FE based descriptions of structural elements is demonstrated through an example, the nonlinear rotating beam, which is a crude model for a helicopter rotor blade. Lastly, this work demonstrates how one can synthesize nonlinear ROMs using NNMs of relatively simple substructures that are assembled to form a complex structural system.

In this first chapter we offer brief overviews and literature surveys of the main themes considered in the thesis, specifically: nonlinear normal modes, rotating beams, and component mode synthesis. These are considered sequentially, and are followed by a description of the outline of the remainder of the thesis.

1.2   Nonlinear Normal Modes

Linear modal analysis is a fundamental tool used in linear vibration theory. It allows one to decompose a general motion into a linear combination of the fundamental motions (modal motions) that take place on the eigenspaces in the system phase space; this is the essence of superposition. These modal responses are invariant, since, if one starts with a purely modal response, the system stays in that mode for all time. Similarly, if the system is started with energy in a subset of modes, only those modes will be active during the ensuing response. For general responses, the individual modal responses remain uncoupled from one another during the motion.

Of course, these facts do not generally hold for nonlinear systems. Certainly superposition does not extend to nonlinear systems. But, the concept of fundamental invariant responses does carry over, even if one cannot construct general responses by combining them, whether in a linear or nonlinear manner. Rosenberg and Atkinson ([6] and [7]) provided the pioneering ideas which tried to extend the idea of fundamental motions to nonlinear systems. Rosenberg and coworkers carried out several studies along these lines ([6], [8], [7], [9], [10], [11]) and summarized these results in a classical review paper [12], in which Rosenberg offered a break-through definition of nonlinear normal modes (NNMs). In that work, the NNMs of conservative systems with n degrees of freedom were defined as vibration in unison, i.e., vibrations such that all degrees of freedom reach their extrema at the same time and pass through zero at the same time. By this definition, one can express all generalized displacements as functions of a chosen generalized displacement. When these systems possess certain types of symmetries, the constraint relations are linear in the configurations space (just as they always are in the linear case) and are referred to as "similar" NNMs. For more general, but still conservative, systems the constraint relations are nonlinear and the nonlinear modes are called "non-similar" NNMs, which can be depicted by curved lines in the configuration space. This definition was picked up and used by subsequent researchers who used it to construct NNMs and study their stability and bifurcations that occur due to changes in system parameters and system energy levels. These were typically conservative systems with two degrees of freedom (DOF) system ([13], [14], [15]). This definition, together with the conservation of energy, were employed by Vakakis to construct non-similar NNMs of a two DOF-conservative system in [16]. It was also used to study the steady state motions of two DOF systems subjected to periodic forcing; see [17] for similar NNMs and [18] for nonsimilar NNMs. Vakakis also discovered that the important phenomenon of mode localization can occur for NNMs, even for perfectly tuned subsystems [16]. This is in contrast to linear systems, wherein localized modes exist only when the subsystems are slightly mistuned. A good account of NNMs, their stability and bifurcations in unforced nonlinear systems, their existence in forced nonlinear systems, and their application to engineering systems is given in the monograph by Vakakis [19].

The NNM concept has been generalized to a wide class of systems, which includes discrete systems with dissipation and gyroscopic terms, as well as quite general continuous systems by Shaw and Pierre in ([20] and [21]). Therein, a definition of NNMs is given in terms of invariant manifolds, which are a natural way to define and construct fundamental motions of nonlinear systems. The procedures used to obtain the NNMs by this approach are closely related to center manifold theory, which is used for bifurcation analysis ([22]), and inertial manifold theory, which is used to study the long time behavior of dissipative partial differential equations (PDEs) ([23], [24]). Using this definition, the nonlinear system equations are restricted to a two-dimensional invariant manifold that describes the NNM of interest. The behavior on the NNM manifold is governed by a single second order differential equation of motion, which corresponds to the equation of motion for a nonlinear single mode reduced order model. In Shaw and Pierre ([20], [21]) approximate solutions of the invariant manifold equation were obtained by asymptotic expansions using polynomials expressed in terms of a generalized position-velocity pair of state variables.

King and Vakakis ([25]) developed an energy-based NNM approach based on [21] to investigate NNMs of one dimensional, conservative, continuous systems. Nayfeh and Nayfeh ([26]) computed NNMs of continuous systems based on a complex amplitude/phase formulation and the method of multiple scales. Nayfeh ([27]) compared the various methods for constructing NNMs of continuous systems as developed by Shaw and Pierre, King and Vakakis, Nayfeh and Nayfeh, and a new approach that employed normal form theory. They concluded that all expansion methods yielded the same results, but claimed that the method of multiple scales with complex variables was the simplest to implement.

All of these approaches are in some manner equivalent, but differ in terms of formulation, solution, and range of applicability. However, the invariant manifold definition is the most general, since it covers the widest range of systems and responses. It can also be generalized to the case of multiple modes, as required for the case of internal resonances, or if one requires a model that is valid over a wide frequency range. By defining the NNMs in terms

of two-dimensional invariant manifolds, the individual NNMs can be constructed, but they can not interact with each other once a motion is initiated on any one of them. Therefore, a motion involving multiple modes cannot be captured by this definition. In addition, the concept of mode superposition cannot be applied to construct non-linear multi-mode models using individual NNMs, since the essential interaction between the NNMs will be missing. Boivin *et al.* ([28]) generalized the individual NNM concept by defining a motion involving M NNMs as a motion that takes place on a $2M$-dimensional invariant manifold in the system's phase space. By this definition, the non-linear ODEs are restricted to the M-NNMs invariant manifold of interest. The behavior on the manifold is governed by M second order, coupled equations of motion (a nonlinear M-degree-of-freedom system). Boivin *et al.* also described how to detect the case of internal resonances from the multi-mode invariant manifold formulation [29]. NNMs were also constructed for discrete systems with internal resonances, based on the complex formulation, by Nayfeh *et al.* [30]. King *et al.* ([31]) also extended the energy-based NNM approach to cover the case of internal resonances. These latter two studies were for the case of $M = 2$ NNMs.

Slater ([32]) developed a numerical method for determining individual NNMs based on numerical searching techniques for periodic solutions of conservative non-linear systems. Using this approach, individual solutions are found, but the entire family of motions on the NNM manifold cannot be obtained, therefore one cannot develop ROMs using this approach. A similar shooting technique has been used in this work and by previous resarchers in the author's research group ([3], [33], [34], [35] and [36]). In this thesis it is employed for comparing ROMs with simulations of the original system, which has the full number of DOF.

Other works, related to the use of invariant manifolds for the generation of ROMs, include the use of Karhunen-Loeve (K-L) decomposition to develop accurate low-order models, by using data obtained from transient simulations of large-scale systems. See [37], [38], [39], and [40], for example.

In references [20], [21], [28], [41], and [29], the NNM invariant manifolds were approximated by a polynomial expansion (asymptotic series) of position-velocity pairs of chosen (master) modes, which provides a solution that is locally valid. The approximate invariant manifolds obtained by such an asymptotic series will diverge from the actual invariant manifold in some amplitude regime. Typically, the domain of validity of the approximation is not known a priori. Hence, the reduced equations of motion will generate inaccurate time responses when the amplitudes of the modes are "too large". Pesheck et al. ([33]) improved the approximation of the invariant manifolds by expressing the invariant manifolds as an expansion of basis functions defined over a specified domain and numerically solving the invariant manifold equations. The expansion of basis functions is introduced into the PDEs governing the NNM invariant manifold, and, using a Galerkin projection, the nonlinear equations for the expansion coefficients were obtained and then solved numerically. By this approach, the domain of approximation can be selected by the user, and the error of approximation can be minimized over the chosen domain by selection of the number and type of basis functions. Since the computational cost associated with the Galerkin projection can be quite expensive, the collocation method has recently been adopted in [35] to minimize computational efforts associated with this method. In this approach, instead of projecting each manifold governing equation onto each basis function, each manifold governing equation is projected onto a set of Dirac delta functions in the master coordinates, thereby providing a solution that minimizes an error that is measured in a point-wise manner.

Research on the construction and use of NNMs continues; here we outline recent work by others in the MSU/UM NNM research group, in particular by Mr. Dongying Jiang, a Ph.D. student at UM. Jiang et al. ([36]) have applied the work of Pesheck et al. ([33]) to construct NNMs of piecewise linear systems, and are working on systems with friction elements. They have also extended the work of Pesheck et al. ([33]) to numerically construct multi-NNM models which can capture internal resonances among participating modes, and are valid over a large range of amplitudes ([42]). They have also numerically constructed NNMs of nonlinear systems under periodic excitation ([43]). In this case the manifolds are

time-periodic in nature, and responses on them represent the steady-state responses of the full system. Current work is aimed at distilling ROMs from detailed FE models for rotor blades.

A detailed summary of the invariant manifold approach to NNMs, and the computational issues associated with its solution, are presented in Chapter 2 of this thesis.

1.3   Beam (Blade) Dynamics

The dynamic analyses of helicopter blades, turbopropeller blades, wind-turbine blades and robotic arms has provided motivation for investigations of the vibration of rotating beams. To predict the dynamic characteristics of rotating flexible structures, the kinematics must be carefully modeled, which leads to nonlinear coupling effects between degrees of freedom (DOF) in different directions. These coupling effects can cause slow modal convergence, thereby often requiring large system models for accurate dynamic representation. Simulation of such large-scale models is a time consuming process, which slows parametric studies and design cycles.

Much work has been done using finite elements (FE) to model the nonlinear, large amplitude vibrations of rotating beams, including [44], [45], [46], [47], [48], and [49]. These models are typically complex in nature due to their geometry, degrees of freedom (flap, lead-lag, axial, and torsion), and nonlinear coupling effects. Furthermore, because of the nature of the finite element approach, many elements are required in order to obtain an accurate model. A common approach is to use linearization of the finite element model about the nonlinear static equilibrium position and solve the eigenvalue problem of the resulting linearized model to obtain the linear natural frequencies of the system ([44] and [49]). Bauchau and Hong ([45]) also utilized finite elements in time to obtain nonlinear responses and stability results of the rotating beam undergoing large deflections. However, the computational time

associated with obtaining the equilibrium solution was expensive, because all of the spatial degrees of freedom are coupled at all time steps. Perturbation modes ([50] and [51]) were applied to the finite element model of a helicopter rotor blade in order to obtain a reduced order model ([46]). Bauchau and Bottasso ([52]) applied the perturbation modes to the space-time finite element model of a beam subjected to a sinusoidal load in order to obtain a reduced order model. Crespo da Silva ([53]) utilized a truncated set of eigenfunctions or eigenvectors obtained from the linearized system of PDEs or the linearized finite element model about the nonlinear static equilibrium position in order to obtain a reduced order model of a beam in planar motion. Crespo da Silva ([54]) also extended his work to handle multi-beam structures in planar motion.

In most nonlinear structures, there is no simple expansion of basis vectors which decouples the DOF (i.e., modes) in the frequency range of interest from those outside that range. For the rotating-beam problem, this is evident in the nonlinear coupling between transverse and axial motions. Therefore, some (potentially important) nonlinear effects may be ignored in the truncation process, unless one is careful. Generally, many linear modes must be retained in the nonlinear model in order to minimize these effects. NNMs is a natural approach for handling this issue.

Over the past decade, systematic procedures have been developed to obtain ROMs via NNMs that are based on invariant manifolds in the state space of nonlinear systems, as described above. These procedures initially used asymptotic series to approximate the geometry of the invariant manifold and have been used to study the nonlinear rotating Euler-Bernoulli Beam ([3]). More recent work has employed a numerically-based Galerkin approach to obtain the geometry of the NNM invariant manifolds out to large amplitudes ([33]). These procedures can be applied to more general nonlinearities over wider amplitude ranges, and have been recently applied to study the vibrations of a rotating Euler-Bernoulli beam ([34]). These approaches have provided accurate models for the fundamental nonlinear flapping mode, by systematically capturing the essential dynamic coupling that exists between the linear modes of the system. Chapter 3 of this

thesis considers this problem in detail, by investigating the NNMs of a rotating beam that is modeled using a nonlinear finite element formulation.

1.4   Substructure Synthesis

Many complex structures are composed of several relatively simple substructures that are assembled together. This occurs in trusses, bladed disk assemblies in turbine rotors, aerospace and ground vehicles, and other applications. In such cases it is convenient to develop a dynamic model for the overall structure by taking advantage of the dynamic properties of the substructures. Methods for doing this for linear structural models are well developed and have been used extensively, especially in the aerospace industry ([55], [56], [57], [58], etc.). These techniques construct ROMs of the overall structure by making use of modal-based ROM descriptions of the substructures and combining these using a technique known as Component Mode Synthesis (CMS). In this section we offer an overview of CMS for linear systems and describe the two main CMS approaches, fixed- and free- interface CMS. A thorough review of substructuring and CMS can be found in [59].

1.4.1   Component Mode Synthesis

CMS was developed to synthesize models that are described in terms of substructures, and to take advantage of model size reduction carried out at the substructure level ([60], [61], [62]). In CMS, the dynamics of each substructure is described by a set of dynamic (normal) modes and a set of static (constraint or residual attachment) modes that are used to describe the interfaces between the substructures. A set of component normal modes is selected from each substructure and are chosen and truncated in such a way that the modes lie in the frequency range of interest. A set of static (so-called constraint) modes is a key component for the low frequency response of the structure ([63]) and are used to couple the substructures together. There are two general types of CMS methods; they are

known as the fixed-interface and the free-interface approaches, as briefly described below.

1.4.1.1 Fixed-Interface Linear CMS

The fixed-interface CMS technique, developed by [62], is widely used, since the procedures are straightforward. Moreover, it produces very accurate models with very few component modes ([64]). The dynamics of each substructure is described by its modal description, which is composed of substructure normal modes (component modes) and constraint modes. The component normal modes are the normal modes of the substructure derived for the case when the interface coordinates between the substructures are held fixed. A constraint mode (static mode) of the substructure is the deflection obtained by imposing a unit displacement on one of the interface coordinates and holding the remaining interface coordinates fixed. To obtain all of the constraint modes, the process is applied in turn to each of the interface coordinates. By applying displacement and force compatibility conditions at the interface coordinates, one can obtain the reduced synthesized system, which is described by the component normal-mode coordinates and the generalized constrained coordinates. This approach is known as the Craig-Bampton method.

1.4.1.2 Free-Interface Linear CMS

Free-interface CMS methods are more attractive than fixed-interface CMS methods when the component modes are obtained from modal testing or when an experimental verification of the component modes is required ([65]). The free-interface CMS technique developed by Craig and Chang ([66], [67] and [63]) is the most accurate among the free-interface CMS techniques. It is a modified version of Rubin's method [68] and MacNeal's method [69]. It is superior to the CMS of Craig-Bampton in terms of accuracy, but is more difficult to implement ([64]).

In this synthesis technique, the dynamics of each substructure is described by a set of substructure component normal modes and residual attachment modes. The component normal modes are the normal modes of the substructures for the case when the interface coordinates between the substructures are free. The residual attachment modes of the substructure are a special type of static modes that are used to couple the substructures together, and they also account (at least partially) for the static deflections of the truncated normal modes of the substructures ([66], [67] and [63]). By applying the displacement and force compatibility conditions at the interface coordinates, and neglecting the inertial effects associated with the generalized residual attachment coordinates, one can obtain the reduced synthesized system. It is described in terms of only the component normal mode coordinates since, in this approach, the residual attachment modes can be condensed out of the equations of motion ([66], [67] and [63]). This approach is known as the Craig-Chang method.

Chapter 4 of this dissertation describes a CMS methodology developed for nonlinear systems, wherein the substructure ROMs are developed using NNMs, and these are assembled using a newly developed technique that is a extension of the fixed-interface CMS method.

1.5   Dissertation Organization

The Dissertation is organized as follows.

In Chapter 2, the formulation and solution of NNM invariant manifold equations are described. Both previous and original work is described. Asymptotic series expansions and weighted-residual type methods, i.e., Galerkin and collocation, are the methods employed to solve for the manifolds. In this chapter, two new methods, similar to those described in [33], are developed and implemented to solve for the single-mode manifold solutions. They

are both formulated in terms of modal position and velocity. The first alternative is to solve for the manifold solution using globally defined basis functions using the Galerkin method. The second is to obtain the manifold solution over several small patches using locally defined basis functions, and solving these smaller problems using a collocation method. A rough comparison of the relative computational efforts of these approaches is provided. Also, a two-DOF nonlinear spring-mass system and a FE model of a rotating beam are used for demonstrating these approaches and comparing their accuracies, by direct time simulations of the corresponding ROMs and the original system models (with full DOF).

In Chapter 3, the generation of nonlinear ROMs from FE based descriptions is demonstrated through the application to a nonlinear rotating beam, which is a highly idealized model for a helicopter rotor blade. First, the nonlinear FE model of a rotating beam is generated and converted into a truncated (but still large-scale) modal form that is convenient for the NNM analysis. The invariant manifold equations are formulated, and a numerical collocation method is used to obtain the solution of the NNM invariant manifold for the fundamental flapping mode of the beam. This invariant manifold is used to construct a nonlinear single DOF ROM, which is subsequently used for a simulation study. Note that the results of Chapter 3 have been recently published [35].

In Chapter 4, the development of NNMs, as needed for the individual substructures is first reviewed. The associated invariant manifold equations, parameterized by modal position and velocity, are formulated, and the numerical collocation method is reviewed, since it allows one to obtain the solution of the NNM invariant manifold. Then, the procedures for the fixed-interface nonlinear CMS are described. A five-DOF spring-mass system and a forty-one-DOF spring-mass system are used to demonstrate the effectiveness of the method, via direct time-simulation comparisons of different ROMs.

Chapter 5 offers a summary of the contributions of this research to the field of nonlinear structural dynamics, along with a discussion of potential areas for further work in this area.

CHAPTER 2

Comparison of Methods for Constructing Invariant Manifolds for Nonlinear Normal Modes

2.1 Introduction

In linear vibration theory one can decompose a general free vibration response as a linear combination of the fundamental motions (modal motions) that take place on the eigenspaces of the system. These motions are invariant, that is, if one initiates a purely modal response, the system remains in that mode for all time. The works of Rosenberg and Atkinson ([6] and [7]) were the pioneering works which extended the idea of fundamental motions to nonlinear systems. In those works, nonlinear spring-mass systems with two degrees of freedom (DOF) were studied. Due to special symmetries possessed by the systems, they were able to construct linear modal-constraint relations, the attendant nonlinear natural frequencies, and the stability of each nonlinear mode in terms of its amplitude. Rosenberg summarized his works ([6], [8], [7], [9], [10], [11]) on normal mode vibrations of nonlinear systems in [12], in which a fundamental definition of nonlinear normal modes (NNMs) for multi-DOF systems was given. In that work the concepts of similar and non-similar modes were introduced. Caughey *et al.* ([14]) studied similar normal modes and their bifurcations in terms of system parameters for two-DOF nonlinear conservative system,

based on Atkinson's work ([7]). Rand *et al.* ([15]) studied the general class of two-DOF nonlinear conservative systems. In that study, they were able to determine the number and stability of periodic motions of which the non-similar modes were special cases and also studied the bifurcation of the periodic motions in terms of system parameters. Vakakis ([16]) studied the non-similar modes of two-DOF nonlinear conservative systems, where the construction of the non-similar modes exploited the conservation of energy.

Shaw and Pierre ([70] and [20]) generalized the definition of NNMs by using concepts from invariant manifold theory, which encompassed a wide class of quite general nonlinear systems. The technique was constructive and allowed for traveling wave (that is, complex) and damped NNMs. Boivin and co-workers *et al.* ([28], [29], [71]) extended the construction of the single-mode NNM manifold developed by Shaw and Pierre to the multi-mode case, which allowed for the dynamic interactions among a subset of nonlinear modes of interest. A summary of these works by Shaw, Pierre, and coworkers ([72], [73], [41], [28], [29], and [71]) can be found in [74]. In these papers, the solution of the invariant manifold equatiosn were sought in terms of locally valid asymptotic power series expansions.

Pesheck *et al.* ([33]) developed a numerical method for solving the invariant manifold equations, such that the solution, while not analytically available, was valid over a relatively large amplitude range. An added feature of this approach is that the nonlinear terms are not limited to being smooth functions, which allows for extensions to more general classes of problems ([36]). Even though the Galerkin method gives accurate solutions, the computational cost of acquiring solutions is quite expensive, especially when one attempts to generate multi-mode models ([75]). This motivated the application of the collocation method, which significantly reduces computational costs, but does not sacrifice much in the way of accuracy ([76], [77], and [78]). This method has been applied in [35] to study the dynamics of a finite-element model of a rotating beam. In the forthcoming work of Jiang *et al.* ([42]), the Galerkin method developed by Pesheck *et al.* ([33]) has been generalized to construct accurate multi-mode manifolds that are able to capture internal resonances, and this method is applied to a model of a rotating beam.

In this chapter, we develop two alternative methods for the numerical solution of the single-mode invariant manifold equations, and offer a comparison of the various methods that have been used in this and previous studies. The new methods are Galerkin-based, in the same spirit of that developed in [33], except that the equations are formulated in terms of modal position and velocity, instead of modal amplitude and phase. The first new method uses global basis functions and obtains the unknown coefficients for the manifold solution using the Galerkin method; this method is described in section 2.3.2.2. The second new method uses a local patchwork of basis functions, and the unknown coefficients for the manifold solution are obtained using the collocation method; this method is described in section 2.3.2.4. In terms of computational time, both new methods have advantages over the approaches used in [33] and [35]; this is summarized in section 2.3.3.

This chapter is outlined as follows. The formulations for the NNM invariant manifolds are first introduced. The power series expansions methods and the weighted-residual type methods, i.e., Galerkin and collocation methods, are described in detail, for both amplitude-phase and displacement-velocity formulations. The computational effort associated with each approach is then discussed, and the accuracy of each approach is considered through direct comparisons in general terms and for calculations carried out for two example problems. Some conclusions are drawn at the end of the chapter.

2.2   Formulations of NNM Invariant Manifold

We begin with a general discrete representation of the vibrations of a nonlinear structural system obtained either by a finite element model followed by linear modal expansion, or by a Rayleigh-Ritz approach. We assume that the system at linear order is undamped. (This assumption greatly simplifies the problem, but can be relaxed, in principle.) In this case, the equations of motion for a Q-DOF system are uncoupled at linear order and can

be expressed in the form:

$$I\,\ddot{\boldsymbol{\eta}} + \Lambda\,\boldsymbol{\eta} = \boldsymbol{f}(\boldsymbol{\eta}, \dot{\boldsymbol{\eta}}) \tag{2.1}$$

where I is the identity matrix, Λ the diagonal matrix of squared linear natural frequencies, $\boldsymbol{f}(\boldsymbol{\eta}, \dot{\boldsymbol{\eta}})$ a vector of nonlinear forces, $\boldsymbol{\eta}$ the modal position vector, and $\dot{\boldsymbol{\eta}}$ the modal velocity vector. The component form of equation (2.1) is given by

$$\ddot{\eta}_i + \omega_i^2\,\eta_i \quad = \quad f_i(\eta_j, \dot{\eta}_j) \tag{2.2}$$

$$\text{for} \quad i, j = 1, 2, 3, ..., Q$$

where ω_i is the linear natural frequency of mode i and Q is the number of retained linear modes.

2.2.1 Invariant Manifold Equations in Terms of Modal Position and Velocity

The fundamental concepts for nonlinear normal modes of discrete, conservative, nonlinear systems were laid out by Rosenberg ([12]). Shaw and Pierre ([70], [20], [21]) used the theory of invariant manifolds for dynamical systems to generalize the concept of a nonlinear normal mode to a wide class of systems, including continuous systems and systems with dissipation and gyroscopic terms. Boivin *et al.* ([28], [29], [71]) extended the single-nonlinear-mode construction developed by Shaw and Pierre to the multi-mode

case, which is able to capture the dynamic interactions among a set of nonlinear modes of interest. A summary on the initial series of works by Shaw, Pierre, and coworkers ([72], [73], [41], [28], [29], and [71]) can be found in [74]. Below we provide a short account of the geometric definition of NNM invariant manifolds and methods of constructing single- and multi-mode versions of NNM models.

2.2.1.1 Singe-Mode Manifold Formulation

For present purposes one can consider an invariant manifold to be a low dimensional surface living in the system state space, such that motions initiated on the surface will remain on it for all time. This concept is the key to obtaining a reduced order NNM model, that is, a lower-dimensional dynamical system, specifically by restricting the equations of motion to this surface. In an N-degree-of-freedom, undamped, nongyroscopic, linear vibratory system, individual modal motions are synchronous responses that take place on a two-dimensional plane (linear eigenspace) in the $2N$-dimensional system state space. In this case the response of the system is a time-harmonic standing wave in which all degrees of freedom reach their extrema and pass through zero simultaneously. Such motions are governed by two first-order linear differential equations or, equivalently, by one second-order linear differential equation, which in this case is a simple undamped oscillator. For linear systems with gyroscopic and/or general dissipative terms this concept is also applicable, however the motions taking place on the invariant planes are generally nonsynchronous, and represent traveling wave responses of the system. This concept can be extended to nonlinear systems as well, however, the motions generally take place on non-planar surfaces, and the motions are governed by two first-order nonlinear differential equations, or by one second-order nonlinear differential equation. For smooth nonlinear systems, the manifolds are curved surfaces that are tangent to the manifolds (eigenplanes) of the linearized systems.

In [74], a definition for NNMs based on invariant manifolds was offered, as follows:

A normal mode for a nonlinear system is a motion that takes place on a two-

dimensional invariant manifold in the system's phase space. This manifold passes through the stable equilibrium point of interest and, at that point, is tangent to a two-dimensional eigenspace of the system linearized about that equilibrium. On this manifold, the system dynamics are governed by an equation of motion involving a pair of state variables; that is, it behaves like a single-degree-of-freedom system.

Based on the above definition, the construction of the nonlinear-mode manifold is straight-forward. In order to search for a particular individual NNM, it is assumed that the NNM manifold is parameterized by a single modal position-velocity pair corresponding to the mode of interest, referred to as the master mode. This is accomplished by using the fact that for a NNM response all of the remaining modal positions and velocities are slaved (constrained) to this master mode. For the kth nonlinear mode, we take $u_k = \eta_k$, and $v_k = \dot{\eta}_k$ as the master states. The remaining slave states are expressed as

$$\eta_i = X_i(u_k, v_k) = X_i(\eta_k, \dot{\eta}_k) \qquad (2.3)$$

$$\dot{\eta}_i = Y_i(u_k, v_k) = Y_i(\eta_k, \dot{\eta}_k) \qquad (2.4)$$

$$\text{for} \quad i = 1, 2, 3, ..., Q, \ i \neq k.$$

Equations (2.3) and (2.4) constitute a set of constraint equations that are to be determined. The constraint functions in equations (2.3) and (2.4) are obtained by an invariant manifold procedure that generates equations that can be solved for the unknown constraint relations. The process begins by taking a time derivative of the constraint equations, yielding

$$\dot{\eta_i} \quad = \quad \frac{\partial X_i}{\partial u_k} \dot{u}_k + \frac{\partial X_i}{\partial v_k} \dot{v}_k \tag{2.5}$$

$$\ddot{\eta_i} \quad = \quad \frac{\partial Y_i}{\partial u_k} \dot{u}_k + \frac{\partial Y_i}{\partial v_k} \dot{v}_k \tag{2.6}$$

for $\quad i = 1, 2, 3, ..., Q, \; i \neq k.$

The time dependence in these equations is eliminated by using the following relations: $\dot{u}_k = v_k$, $\dot{v}_k = \ddot{\eta}_k = -\omega_k^2 \, \eta_k + f_k(\eta_j, \dot{\eta}_j)$, and $\ddot{\eta}_i = -\omega_i^2 \, \eta_i + f_i(\eta_j, \dot{\eta}_j)$. Then, the constraints (equations (2.3) and (2.4)) are substituted in the resulting expression everywhere in place of the slave state variables, resulting in a set of partial differential equations for the functions $(X_i(u_k, v_k), Y_i(u_k, v_k))$. This set of $2Q$ - 2, time-independent, partial differential equations govern the geometry of the kth manifold, and are given by

$$Y_i \quad = \quad \frac{\partial X_i}{\partial u_k} v_k + \frac{\partial X_i}{\partial v_k} \left(-\omega_k^2 \, u_k \right.$$
$$\left. + f_k(X_j, Y_j, u_k, v_k) \right) \tag{2.7}$$

$$-\omega_i^2 \, X_i + f_i(X_j, Y_j, u_k, v_k) \quad = \quad \frac{\partial Y_i}{\partial u_k} v_k + \frac{\partial Y_i}{\partial v_k} \left(-\omega_k^2 \, u_k \right.$$
$$\left. + f_k(X_j, Y_j, u_k, v_k) \right) \tag{2.8}$$

for $\quad i, j = 1, 2, 3, ..., Q, \; i, j \neq k.$

These equations are not solvable in closed form (except in very special cases) and methods for obtaining approximate solutions for X_i and Y_i are described in detail in this chapter.

2.2.1.2 Multi-Mode Manifold Formulation

Single-mode motions are not general motions, since they take place on two dimensional manifolds in the system state space. In structural dynamics, we are also interested in more general motions in which more than a single mode participates. For linear systems, multi-mode motions take place in the space spanned by a set of two-dimensional planes that are the linear eigenspaces of the modes of interest. Furthermore, using superposition, multi-mode motions of linear systems can be obtained through a linear combination of responses of the individual modes of interest. For nonlinear systems, multi-mode motions cannot be obtained through the superposition of individual NNM responses, since the coupling between the NNMs cannot be accounted for in this manner. However, the idea of a nonlinear single-mode manifold can be generalized by defining a nonlinear multi-mode manifold to be a multi- dimensional surface that is tangent to the multi-dimensional linear eigenspace of the corresponding linear modes of interest.

Based on these ideas, in [74] the following definition of a nonlinear-multi mode was offered:

> *A nonlinear M-mode invariant motion of a system is a response that takes place on a 2M-dimensional invariant manifold in the system's phase space; the manifold passes through the stable equilibrium point of interest, and at that point it is tangent to a 2M-dimensional eigenspace of the system linearized about that equilibrium (representing M linear modes). On this manifold, the system dynamics are governed by M pairs of state variables; that is, it behaves like an M-degree-of-freedom system.*

The procedure for constructing the multi-mode manifold is similar to the procedure given in section 2.2.1.1, except that the manifolds are now parameterized by $2M$ variables. Note that the single-mode manifold is a special case of the multi-mode manifold with $M = 1$. Specifically, we take $u_k = \eta_k$, and $v_k = \dot{\eta}_k$, for $k \in S_M$, where S_M is a set of indices that describes the modes of interest (master modes). For example, if one is interested in

constructing a model that captures the interactions between the second, third and fifth nonlinear modes, then $S_M = \{2, 3, 5\}$. The sets $\{u_k\}$ and $\{v_k\}$, $k \in S_M$, are denoted by $\boldsymbol{u_M}$ and $\boldsymbol{v_M}$ respectively. The remaining slave states are expressed as

$$\eta_i = X_i(\boldsymbol{u_M}, \boldsymbol{v_M}) \tag{2.9}$$

$$\dot{\eta}_i = Y_i(\boldsymbol{u_M}, \boldsymbol{v_M}) \tag{2.10}$$

for $\quad i = 1, 2, 3, ..., Q, \ i \notin S_M.$

The procedure described in section 2.2.1.1 is again applied here by taking a time derivative of the constraint equations, eliminating the time dependence by using the default relations, the equations of motion of the master modes, and the equations of motion of the slave modes, and substituting the constraints every where in place of the slave state variables, yielding the following set of $2Q - 2M$ partial differential equations for the constraint functions:

$$Y_i = \sum_{k \in S_M} \left[\frac{\partial X_i}{\partial u_k} v_k + \frac{\partial X_i}{\partial v_k} \left(-\omega_k^2 \, u_k \right. \right.$$
$$\left. \left. + f_k(X_j, Y_j, u_k, v_k)) \right] \tag{2.11}$$

$$-\omega_i^2 \, X_i + f_i(X_j, Y_j, u_k, v_k) = \sum_{k \in S_M} \left[\frac{\partial Y_i}{\partial u_k} v_k + \frac{\partial Y_i}{\partial v_k} \left(-\omega_k^2 \, u_k \right. \right.$$
$$\left. \left. + f_k(X_j, Y_j, u_k, v_k)) \right] \tag{2.12}$$

for $\quad i, j = 1, 2, 3, ..., Q, \ i, j \notin S_M.$

As in section 2.2.1.1, closed-form solutions do not generally exist. The method for

obtaining approximate solutions for X_i and Y_i in terms of power series expansions is reviewed in section 2.3.1.2.

2.2.2 Invariant Manifold Equations in Terms of Modal Amplitude and Phase

Pesheck *et al.* ([33]) developed an alternative form of the single-mode invariant manifold equations that are expressed in terms of modal amplitude and phase. The procedure was similar to the formulation in modal position and velocity, and yields results that are, of course, equivalent. Recently Jiang *et al.* ([42]) have extended this formulation to the multi-mode case. These formulations are described in the following sections.

2.2.2.1 Singe-Mode Manifold Formulation

The coordinate transformations used here are typical of those used in the method of averaging ([79]), and are similar to those used in the method of variation of parameters, since they employ a time-varying amplitude and phase. They relate the master modal displacement and velocity (η_k, $\dot{\eta}_k$) to the master modal amplitude and phase (a_k, ϕ_k) via the following invertible transformation:

$$\eta_k = a_k \cos(\phi_k) \tag{2.13}$$

$$\dot{\eta}_k = -a_k \omega_k \sin(\phi_k). \tag{2.14}$$

Hence, the constraints for the slave modes, equations (2.3) and (2.4), can be expressed in term of a_k and ϕ_k as

$$\eta_i \quad = \quad P_i(a_k, \phi_k) \quad = \quad X_i(\eta_k(a_k, \phi_k), \dot{\eta}_k(a_k, \phi_k)) \qquad (2.15)$$

$$\dot{\eta}_i \quad = \quad Q_i(a_k, \phi_k) \quad = \quad Y_i(\eta_k(a_k, \phi_k), \dot{\eta}_k(a_k, \phi_k)) \qquad (2.16)$$

for $\quad i = 1, 2, 3, ..., Q, \ i \neq k.$

Using equations (2.13) and (2.14), the equation of motion governing the master mode can be expressed as two coupled 1st order ODEs in a_k and ϕ_k, as follows,

$$\dot{a}_k \quad = \quad \frac{-f_k(P_j, Q_j, a_k, \phi_k) \ \sin(\phi_k)}{\omega_k}, \qquad (2.17)$$

$$\dot{\phi}_k \quad = \quad \omega_k - \frac{f_k(P_j, Q_j, a_k, \phi_k) \ \cos(\phi_k)}{a_k \ \omega_k}, \qquad (2.18)$$

for $\quad j = 1, 2, 3, ..., Q, \ j \neq k.$

In order to determine the slave constraints, the procedure is identical to that for the (u_k, v_k) formulation, adapted to these coordinates. Using steps similar to those in equations (2.5) and (2.6), we obtain

$$\dot{\eta}_i \quad = \quad \frac{\partial P_i}{\partial a_k} \dot{a}_k + \frac{\partial P_i}{\partial \phi_k} \dot{\phi}_k \qquad (2.19)$$

$$\ddot{\eta}_i \quad = \quad \frac{\partial Q_i}{\partial a_k} \dot{a}_k + \frac{\partial Q_i}{\partial \phi_k} \dot{\phi}_k \qquad (2.20)$$

for $\quad i = 1, 2, 3, ..., Q, \ i \neq k.$

The time dependence in these equations is eliminated by using equations (2.17), (2.18), and $\ddot{\eta}_i = -\omega_i^2 \, \eta_i + f_i(\eta_j, \dot{\eta}_j)$. Then, the constraints (equations (2.15) and (2.16)) are substituted in the resulting expression everywhere in place of the slave state variables, resulting in a set of partial differential equations for the functions $(P_i(a_k, \phi_k), Q_i(a_k, \phi_k))$. This set of $2Q$ - 2, time-independent, partial differential equations govern the geometry of the kth manifold, and are given by

$$
\begin{aligned}
Q_i \;=\; & \frac{\partial P_i}{\partial a_k}\Big(\frac{-f_k(P_j, Q_j, a_k, \phi_k)\;\sin(\phi_k)}{\omega_k}\Big) \\
& + \frac{\partial P_i}{\partial \phi_k}\Big(\omega_k - \frac{f_k(P_j, Q_j, a_k, \phi_k)\;\cos(\phi_k)}{a_k\,\omega_k}\Big) \quad (2.21) \\
-\omega_i^2\,P_i + f_i(P_j, Q_j, a_k, \phi_k) \;=\; & \frac{\partial Q_i}{\partial a_k}\Big(\frac{-f_k(P_j, Q_j, a_k, \phi_k)\;\sin(\phi_k)}{\omega_k}\Big) \\
& + \frac{\partial Q_i}{\partial \phi_k}\Big(\omega_k - \frac{f_k(P_j, Q_j, a_k, \phi_k)\;\cos(\phi_k)}{a_k\,\omega_k}\Big) \quad (2.22)
\end{aligned}
$$

for $\quad i, j = 1, 2, 3, ..., Q, \; i, j \neq k.$

These equations are more complicated than the invariant-manifold governing equations represented in modal position and velocity, and have potential singularities at zero modal amplitude. However, as mentioned in [33], the constraint equations of the slave state variables are periodic in ϕ_k with period 2π, and therefore a Fourier basis can be used for shape functions in the ϕ_k direction. The methods for obtaining approximate solutions for P_i and Q_i are described in section 4.2.2.

2.2.2.2 Multi-Mode Manifold Formulation

The multi-mode manifold formulation in terms of modal amplitudes and phase angles can

be developed in the same manner as was done for the case of modal displacements and velocities. To avoid redundancy, only the important steps are given here. The transformations relating the master modal position and velocity $(\eta_k, \dot{\eta}_k)$ to the master modal amplitude and phase (a_k, ϕ_k) are given in equations (2.13) and (2.14); these are employed with $k \in S_M$, where S_M has the same definition as before. The sets $\{a_k\}$ and $\{\phi_k\}$ are denoted by a_M and ϕ_M respectively. The remaining slaved states are expressed as

$$\eta_i \quad = \quad P_i(a_M, \phi_M) \tag{2.23}$$

$$\dot{\eta}_i \quad = \quad Q_i(a_M, \phi_M) \tag{2.24}$$

$$\text{for} \quad i = 1, 2, 3, ..., Q, \; i \notin S_M.$$

Equations (2.17) and (2.18) are still valid with $j \notin S_M$. Next, we take a time derivative of the constraint equations, eliminate the time dependence by using the first-order equations of motion for the master and slave modes, and substitute the constraints every where in place of the slave state variables. This yields the following $2Q - 2M$ equations for the multi-mode invariant manifolds:

$$Q_i$$

$$= \sum_{k \in S_M} \left[\frac{\partial P_i}{\partial a_k} \left(\frac{-f_k(P_j, Q_j, a_k, \phi_k) \ \sin(\phi_k)}{\omega_k} \right) \right.$$

$$\left. + \frac{\partial P_i}{\partial \phi_k} \left(\omega_k - \frac{f_k(P_j, Q_j, a_k, \phi_k) \ \cos(\phi_k)}{a_k \ \omega_k} \right) \right] \qquad (2.25)$$

$$-\omega_i^2 \ P_i + f_i(P_j, Q_j, a_k, \phi_k)$$

$$= \sum_{k \in S_M} \left[\frac{\partial Q_i}{\partial a_k} \left(\frac{-f_k(P_j, Q_j, a_k, \phi_k) \ \sin(\phi_k)}{\omega_k} \right) \right.$$

$$\left. + \frac{\partial Q_i}{\partial \phi_k} \left(\omega_k - \frac{f_k(P_j, Q_j, a_k, \phi_k) \ \cos(\phi_k)}{a_k \ \omega_k} \right) \right] \qquad (2.26)$$

$$\text{for} \quad i, j = 1, 2, 3, ..., Q, \ i, j \notin S_M.$$

As before, closed-form solutions do not generally exist. A method for obtaining accurate approximate solutions for the P_i and Q_i is described and implemented on example systems in [42].

2.3   Solution of the Invariant Manifold Equations

In general, solutions of the invariant-manifold equations cannot be determined in closed form, since such a solution represents a family of solutions to the original equations of motion. However, in some special cases involving symmetries, closed-form solutions, which typically represent flat manifolds, can be determined ([14]). More generally, though, the manifolds are not flat, and other approaches are required (such as those described in sections 2.3.1 and 2.3.2). In the early works by Shaw and Pierre ([70], [20], [21]), approximate solutions for the NNM manifolds of smooth systems were obtained in the form of asymptotic

series expansions. Shaw, Pierre, and co-workers ([72], [73], [41], [28], [29], and [71]) used this approach to solve a variety of problems, as did others, notably [26], [27], [30], [18], [16], and [19]. However, the asymptotic series approximation of the manifold is only locally valid; therefore, if one tries to simulate a NNM model at large amplitudes, the time response of the NNM model will deviate from the time response of the original model. The primary difference is in the frequency of oscillation, which results in a phase drift.

As mentioned in section 2.1, the work by Pesheck *et al.* ([33]) employs a Galerkin method to solve the invariant manifold equations, which allows one to obtain accurate approximate individual NNM manifolds up to large amplitude ranges. This approach is also not limited to smooth systems, so that the nonlinear terms can be more general functions. However, the computational cost of acquiring such solutions can be quite expensive. Therefore, efficient means of computing coefficients in the Galerkin expansions were sought and, in particular, the collocation method has been found to provide accurate solutions with much greater computational efficiency.

The series expansion method is reviewed briefly in section 2.3.1, for both individual and multi-mode NNM models. The Galerkin and collocation methods for individual NNM models are reviewed in section 2.3.2. However, the Galerkin method used to solve multi-mode NNM manifolds, developed by Jiang *et al.* ([42]) is not reviewed here. Interested readers are referred to [42].

2.3.1 Solution by Asymptotic Series Expansion

A good summary of the series expansion method for individual and multi-mode NNM manifolds was given in [74]. A brief version of the method is given here. To use the series expansion method, the nonlinear terms in equation (2.2) are assumed to be second and third degree polynomials in the modal displacements. This assumption can be generalized

such that velocity-dependent and mixed nonlinear terms are included, but the solutions will be more complicated ([20]). Therefore, the form of the forces f_i in equation (2.2) is given by

$$f_i = -\sum_{p=1}^{Q}\sum_{q=p}^{Q} \alpha_{ipq}\, \eta_p\, \eta_q - \sum_{p=1}^{Q}\sum_{q=p}^{Q}\sum_{r=q}^{Q} \beta_{ipqr}\, \eta_p\, \eta_q\, \eta_r. \qquad (2.27)$$

2.3.1.1 Solutions for Individual NNM Manifolds

To construct the single-mode manifold, approximate local solutions of X_i and Y_i can be found using a power series expansions in terms of u_k and v_k as

$$\begin{aligned}
X_i &= a^k_{1,i}u_k + a^k_{2,i}v_k + a^k_{3,i}u_k^2 + a^k_{4,i}u_k v_k \\
&\quad + a^k_{5,i}v_k^2 + a^k_{6,i}u_k^3 + a^k_{7,i}u_k^2 v_k + a^k_{8,i}u_k v_k^2 + a^k_{9,i}v_k^3 + \ldots \qquad (2.28) \\
Y_i &= b^k_{1,i}u_k + b^k_{2,i}v_k + b^k_{3,i}u_k^2 + b^k_{4,i}u_k v_k \\
&\quad + b^k_{5,i}v_k^2 + b^k_{6,i}u_k^3 + b^k_{7,i}u_k^2 v_k + b^k_{8,i}u_k v_k^2 + b^k_{9,i}v_k^3 + \ldots \qquad (2.29)
\end{aligned}$$

The a's and b's are the unknown coefficients to be determined, and there are $9 \times (2Q - 2)$ of them. These coefficients can be determined by substituting equations (2.28) and (2.29) into equations (2.7) and (2.8) and collecting like powers in u_k and v_k. This yields a set of linear equations for the unknown coefficients, which can be solved successively. The first-order (linear) coefficients are solved for first, and they are all found to be zero. This is because equation (2.2) is given in terms of the linear modal coordinates, and therefore the linear parts are already uncoupled, and must remain so since the linear model satisfies invariance for its modes. Next, the $3 \times (2Q - 2)$ second-order coefficients are obtained, and they are required in the solution of the $4 \times (2Q - 2)$ third-order coefficients (as is typical in expansion solutions). General formulas for the a's and b's can be found in [74].

Once all of the expansion coefficients are obtained, the X's and Y's, which describe the slaved modes, are known functions of the master states (u_k, v_k). For $i = k$, these known functions are used to express f_k in equation (2.2) in terms of only u_k and v_k, rendering a single-DOF oscillator as the reduced-order-model for the kth NNM.

The coefficients of the polynomials in the expansions become singular when there exists low order resonances between modes. For the quadratic and cubic terms, 1:1, 2:1, and/or 3:1 resonances ([79]) between the linear natural frequencies of the master and slave modes will give rise to these singularities. In these cases there exists nonlinear coupling such that energy is exchanged among the resonant modes, and therefore these modes cannot be dynamically separated from one another, as is required for the construction of an individual NNM model. We should note that in this case the response of an individual NNM is not stable, and any perturbation will cause the response to leave the neighborhood of the NNM manifold, as the energy flows from that mode to others (and in most cases, back to that mode again at a later time). In these situations, the multi-mode formulation described in section 2.2.1.2 is required, with the necessary inclusion of the resonant modes. The series solution of these multi-mode manifolds is described in the next section.

2.3.1.2   Solution of Multi-NNM Manifolds

Here there are M pairs of master displacements and velocities. The assumed forms of the slave constraints X_i and Y_i in terms of u_k and v_k are given by

$$
\begin{aligned}
X_i(\boldsymbol{u}_M, \boldsymbol{v}_M) &= \sum_{k \in S_M} (a_{1,i}^k u_k + a_{2,i}^k v_k) + \sum_{k \in S_M} \sum_{l \in S_M} (a_{3,i}^{k,l} u_k u_l + a_{4,i}^{k,l} u_k v_l + a_{5,i}^{k,l} v_k v_l) \\
&\quad + \sum_{k \in S_M} \sum_{l \in S_M} \sum_{q \in S_M} (a_{6,i}^{k,l,q} u_k u_l u_q + a_{7,i}^{k,l,q} u_k u_l v_q + a_{8,i}^{k,l,q} u_k v_l v_q \\
&\quad + a_{9,i}^{k,l,q} v_k v_l v_q) + \ldots
\end{aligned}
\tag{2.30}
$$

$$
\begin{aligned}
Y_i(\boldsymbol{u}_M, \boldsymbol{v}_M) &= \sum_{k \in S_M} (b_{1,i}^k u_k + b_{2,i}^k v_k) + \sum_{k \in S_M} \sum_{l \in S_M} (b_{3,i}^{k,l} u_k u_l + b_{4,i}^{k,l} u_k v_l + b_{5,i}^{k,l} v_k v_l) \\
&\quad + \sum_{k \in S_M} \sum_{l \in S_M} \sum_{q \in S_M} (b_{6,i}^{k,l,q} u_k u_l u_q + b_{7,i}^{k,l,q} u_k u_l v_q + b_{8,i}^{k,l,q} u_k v_l v_q \\
&\quad + b_{9,i}^{k,l,q} v_k v_l v_q) + \ldots
\end{aligned}
\tag{2.31}
$$

The a's and b's are the unknown coefficients to be determined, of which there are $(2M + 3M^2 + 4M^3) \times (2Q - 2M)$. These coefficients can be determined by substituting equations (2.30) and (2.31) into equations (2.7) and (2.8) and collecting like powers in the master displacements and velocities. This yields a set of $(2M + 3M^2 + 4M^3) \times (2Q - 2M)$ linear equations for the $(2M + 3M^2 + 4M^3) \times (2Q - 2M)$ unknown coefficients, which can be solved at successive orders. Since the multi-mode invariant-manifold equations are formulated in terms of the linear modal coordinates, the linear terms in the above expansions are again zero. The formulas for the remaining a's and b's can be found in [74].

The coefficients a's and b's in equations (2.28) and (2.29) of the individual NNM manifold formulation become singular when $\omega_i = \omega_k$ and/or $\omega_i = 2\omega_k$ and/or $\omega_i = 3\omega_k$. This is a flag indicating that there exists 1:1, 2:1, and/or 3:1 internal resonance(s) among slave modes $i \neq k$ and master mode k ([79]). In this case there exists energy exchange among the resonant modes and the motions necessarily take place on higher-dimensional (dimension greater than two) manifolds. Once all of the participating modes in the internal resonance are included in the set S_M, the singularities in the coefficients a's and b's will be removed (at least up to polynomial degree 3) in u_k and v_k. Then we obtain the multi-mode invariant manifold that captures the internal resonance, and allows energy exchange among the

master modes.

Similarly, there are possibilities that the coefficient a's and b's in equations (2.30) and (2.31) of the multi-mode manifold formulation become singular when $\omega_i = \omega_k$ and/or $\omega_i = 2\omega_k$ and/or $\omega_i = 3\omega_k$ and/or $\omega_i = |\omega_k \pm \omega_l|$ and/or $\omega_i = |2\omega_k \pm \omega_l|$ and/or $\omega_i = |\omega_k \pm \omega_l \pm \omega_m|$. This is another flag indicating that there exists 1:1, 2:1, and/or 3:1 internal resonances among a slave mode $i \notin S_M$ and a master mode $k, l, m \in S_M$. The singularities in the coefficients a's and b's can be removed at least up to polynomial degree 3 (third order) in u_k and v_k by redefining the new set S_M such that it includes those extra modes.

Once all of the expansion coefficients are obtained, the X's and Y's, which describe the slaved modes, are known functions of the master states (u_k, v_k), where $k \in S_M$. For $i = k$, these known functions are used to express f_k in equation (2.2) in terms of only the u_k and v_k, rendering a M-DOF oscillator, which is the reduced-order-model that includes the desired NNMs.

2.3.2 Solution by Galerkin and Collocation Methods

The Galerkin and Collocation methods are techniques that employ a variational formulation to solve for discrete approximate solutions of continuous problems. Both methods belong to the general class of techniques known as weighted-residual methods. A good account of the theoretical aspects of these methods, and examples of how to apply them to engineering systems, can be found in [77]. Many useful guidelines and rules of thumb on how to use the methods effectively can be found in [78]. A brief summary of the methods is given here.

Consider the operator equation of the form

$$A(u(x)) = f(x) \qquad (2.32)$$

in an open domain Ω with appropriate homogeneous boundary conditions, where $x \in \Omega$ is the independent variable, A is an operator, $u(x)$ is the dependent variable to be determined such that it satisfies the operator equation and the boundary conditions, and $f(x)$ is a known function that represents a driving term. In the weighted-residual method, $u(x)$ is approximated by $u_N(x)$ in the expanded form

$$u(x) \approx u_N(x) = \sum_{i=1}^{N} c_i \; \phi_i(x) \qquad (2.33)$$

where $\{\phi_i(x)\}$ are elements of a complete set of basis functions that are differentiable up to the order of differential operator A and satisfy all homogeneous boundary conditions, and the c_i are constants to be determined. Substituting equation (2.33) in (2.32), we obtain the residual, R_N

$$R_N(x, c_i) \equiv A(u_N(x)) - f(x), \qquad (2.34)$$

which is generally not zero, since $u_N(x)$ is an approximation of $u(x)$. Note that $u_N(x)$ lies in a finite-dimensional space since $u_N(x)$ is represented by a finite linear combination of elements of the basis. However, $u(x)$ lies in infinite-dimensional space, since to represent $u(x)$ all elements of the basis are generally required.

If $\{\psi_i(x)\}$ is a complete set of basis functions (possibly different from $\{\phi_i(x)\}$) in the space

that $A(u(x))$ and $f(x)$ live in, then by projecting $R_N(x, c_i)$ onto $\psi_k(x)$ using the usual $L_2(\Omega)$ inner product, and equating the resulting terms to zero, we obtain

$$< R_N(x, c_i), \psi_k(x) > \quad = \quad \int_\Omega R_N(x, c_i)\, \psi_k(x)\, dx \quad = \quad 0 \qquad (2.35)$$

$$\text{for} \quad k = 1, 2, 3, ..., N.$$

If the set $\{\psi_i(x)\}$ is an orthonormal basis, $r_k = < R_N(x, c_i), \psi_k(x) >$ is the representation of $R_N(x, c_i)$ in that basis. We then have N algebraic equations with N unknowns, the $\{c_i\}$. Solving for the $\{c_i\}$ that satisfy equation (2.35) would make $R_N(x, c_i)$ small over Ω. In the limit $N \rightarrow \infty$, $R_N(x, c_i)$ must go to zero. This method is called the weighted-residual method.

If one chooses different basis functions for expansion and projection, $\psi_k \neq \phi_k$, the approach is known as the Petrov-Galerkin method. If one chooses the same basis functions $\psi_k = \phi_k$, it is known as the Bubnov-Galerkin method, or, more commonly in the West, the Galerkin method.

If one chooses $\psi_k = \delta(x - x_k)$, where $\delta(x)$ is the *Dirac delta function* and x_k are N selected points (called collocation points), this becomes the collocation method. The collocation method will force the residual $R_N(x, c_i)$ to be zero at points x_k in Ω. This greatly speeds up the calculations, due to the simplification of the integrals.

In the following sections, the Galerkin method will be applied to equations (2.21) and (2.22) in a domain $a_k \in [0, a_0]$ and $\phi_k \in [0, 2\pi]$, and also to equations (2.7) and (2.8) in a domain $u_k \in [-U_b, U_b]$ and $v_k \in [-V_b, V_b]$. The collocation method will be applied to equations (2.21) and (2.22) in a local domain defined later, and also to equations (2.7) and

(2.8) in another local domain defined later.

2.3.2.1 Galerkin Method with Global-Basis Functions in Modal Amplitude and Phase Angle

Pesheck *et al.* ([33]) applied the Galerkin method to solve equations (2.21) and (2.22) for P_i and Q_i in the domain $a_k \in [0, a_0]$ and $\phi_k \in [0, 2\pi]$ using an expansion of basis functions. A brief summary of the approach in [33] is reviewed here.

The unknown position and velocity constraints (P_i, Q_i) are expanded as a double series in the master modal amplitude a_k and phase ϕ_k as

$$P_i(a_k, \phi_k) = \sum_{l=1}^{N_a} \sum_{m=1}^{N_\phi} C_i^{l,m} T_{l,m}(a_k, \phi_k) \tag{2.36}$$

$$Q_i(a_k, \phi_k) = \sum_{l=1}^{N_a} \sum_{m=1}^{N_\phi} D_i^{l,m} U_{l,m}(a_k, \phi_k) \tag{2.37}$$

$$\text{for} \quad i = 1, 2, 3, ..., Q, \ i \neq k,$$

where $C_i^{l,m}$ and $D_i^{l,m}$ are coefficients to be determined, $T_{l,m}(a_k, \phi_k)$ and $U_{l,m}(a_k, \phi_k)$ are known basis functions. The basis functions $T_{l,m}(a_k, \phi_k)$ and $U_{l,m}(a_k, \phi_k)$ are products of selected basis functions in the a_k and ϕ_k directions, and they are defined over the domain $a_k \in [0, a_0]$ and $\phi_k \in [0, 2\pi]$. N_a and N_ϕ are the number of shape functions used in a_k and ϕ_k respectively. Since ϕ_k has period 2π, the basis functions in the ϕ_k direction are chosen to be the Fourier basis, $\{1, \cos(n\phi), \sin(n\phi)\}$. The basis functions in the a_k direction are chosen to be polynomial functions, $L_l(a_k)$. Therefore the form of $T_{l,m}(a_k, \phi_k)$ and $U_{l,m}(a_k, \phi_k)$ are given by

$$T_{l,m}(a_k, \phi_k) = L_l(a_k) \cos((m-1)\phi_k) \qquad (2.38)$$

$$U_{l,m}(a_k, \phi_k) = L_l(a_k) \sin(m\phi_k). \qquad (2.39)$$

It can be shown that for a conservative non-gyroscopic system to posses synchronous motions only the cosine functions are needed for basis functions in ϕ_k for $T_{l,m}$, and only sine functions are needed in ϕ_k for $U_{l,m}$. The polynomial functions $L_l(a_k)$ are chosen to be a set of polynomials defined over the domain $a_k \in [0, a_0]$ with zero value and zero slope at $a_k = 0$, which will satisfy the conditions that the invariant manifold pass through the origin $(a_k, \phi_k) = (0, 0)$ (the stable-equilibrium point) and be tangent to the two-dimensional eigenspace at that point . Also, for convenience, they are chosen to satisfy the orthogonality condition

$$\int_0^{a_0} \frac{a_k}{a_0^2} L_i(a_k) L_j(a_k) \, da_k = \begin{cases} 1 & \text{for } i = j \\ 0 & \text{for } i \neq j, \end{cases} \qquad (2.40)$$

which can be achieved by starting with a set of polynomial functions $\{(\frac{a_k}{a_0})^2, (\frac{a_k}{a_0})^3, (\frac{a_k}{a_0})^4, \dots\}$, and then applying the Gram-Schmidt process ([80]). The form of the $L_l(a_k)$ can be found in [33]. Equations (2.36) and (2.37) are substituted into the invariant-manifold governing equations, equations (2.21) and (2.22), and each of these is projected onto each basis function using the L_2-inner product over the entire domain. This leads to

$$0 = \int_{a_k,\phi_k} (\frac{1}{a_0^2}) U_{p,q} \left[-a_k \sum_{l,m} D_i^{l,m} U_{l,m} + \sum_{l,m} C_i^{l,m} \frac{\partial T_{l,m}}{\partial a_k} (\frac{-f_k \ a_k \ \sin(\phi_k)}{\omega_k}) \right.$$

$$\left. + \sum_{l,m} C_i^{l,m} \frac{\partial T_{l,m}}{\partial \phi_k} (a_k \ \omega_k - \frac{f_k \ \cos(\phi_k)}{\omega_k}) \right] da_k \ d\phi_k \tag{2.41}$$

$$0 = \int_{a_k,\phi_k} (\frac{1}{a_0^2}) T_{p,q} \left[\omega_i^2 \ a_k \sum_{l,m} C_i^{l,m} T_{l,m} - a_k \ f_i + \sum_{l,m} D_i^{l,m} \frac{\partial U_{l,m}}{\partial a_k} (\frac{-f_k \ a_k \ \sin(\phi_k)}{\omega_k}) \right.$$

$$\left. + \sum_{l,m} D_i^{l,m} \frac{\partial U_{l,m}}{\partial \phi_k} (a_k \ \omega_k - \frac{f_k \ \cos(\phi_k)}{\omega_k}) \right] da_k \ d\phi_k \tag{2.42}$$

for $\quad i = 1, 2, 3, ..., Q, \ i \neq k$;

$\quad p = 1, ..., N_a$;

$\quad q = 1, ..., N_\phi$.

The integrations in equations (2.41) and (2.42) are computed numerically. Therefore, equations (2.41) and (2.42) result in a set of $2(Q-1)N_aN_\phi$ nonlinear algebraic equations in the C's and D's. For simplicity in referring to the method subsequently, this method is named "the global $a - \phi$ approach".

Note that for the special case of a conservative non-gyroscopic system with only cubic nonlinearities in the modal positions, all harmonic terms in the expansion of basis functions for each state are needed. Therefore, the number of nontrivial coefficients remains $2(Q - 1)N_aN_\phi$. This fact is observed by performing numerical experiments. In contrast, for the global $u - v$ approach, this special case results in a reduction in the number of coefficients, as described in section 2.3.2.2.

Once all of the expansion coefficients are obtained, the P's and Q's, which describe the slaved modes, are known functions of the master states (a_k, ϕ_k). These known functions are used to express f_k in equations (2.17) and (2.18) in terms of only a_k and ϕ_k, rendering

a single-DOF oscillator as the reduced-order-model for the kth NNM.

2.3.2.2 Galerkin Method with Global-Basis Functions in Modal Position and Velocity

In this section, we apply the Galerkin method to solve equations (2.7) and (2.8) for X_i and Y_i in the domain $u_k \in [-U_b, U_b]$ and $v_k \in [-V_b, V_b]$ using an expansion of polynomial basis functions. For nonlinear structures, the form of nonlinear terms is often a polynomial function, and solving the invariant manifold equations in modal position and velocity would have advantages over those in modal amplitude and phase angle. This is so since the terms that are necessarily zero from symmetry , i.e., the trivial terms, are easily identified and can be removed from the expansion of basis functions. Moreover, the integration of polynomial functions can be computed exactly using Gaussian integration, while the integration of sine and cosine functions in equations (2.41) and (2.42) cannot be computed explicitly. Therefore, the integrands in equations (2.41) and (2.42) have to be evaluated at many points, which in turn increases the computational effort of the procedure.

The unknown position and velocity constraints (X_i, Y_i) are expanded as a double series in the master modal position u_k and velocity v_k as

$$X_i(u_k, v_k) = \sum_{l=1}^{Np,u} \sum_{m=1}^{Np,v} C_i^{l,m} LM_{l,m}(u_k, v_k) \tag{2.43}$$

$$Y_i(u_k, v_k) = \sum_{l=1}^{Np,u} \sum_{m=1}^{Np,v} D_i^{l,m} LM_{l,m}(u_k, v_k) \tag{2.44}$$

$$\text{for} \quad i = 1, 2, 3, ..., Q, \, i \neq k,$$

where $C_i^{l,m}$ and $D_i^{l,m}$ are to-be-determined coefficients, and the $L_{l,m}(u_k, v_k)$ are known

basis functions. The basis functions $L_{l,m}(u_k, v_k)$ are chosen to be two-dimensional polynomial-basis functions in u_k and v_k such that $L_{l,m}(0,0) = 0$, $\dfrac{\partial L_{l,m}}{\partial u_k}(0,0) = 0$, and $\dfrac{\partial L_{l,m}}{\partial v_k}(0,0) = 0$, which insure that the invariant manifold passes through the origin $(u_k, v_k) = (0,0)$ (the stable equilibrium point) and is tangent to the two-dimensional eigenspace at that point. The construction of $LM_{l,m}(u_k, v_k)$ is obtained by performing the tensor product of two sets of polynomial functions given by

$$L = \left\{ 1, \left(\frac{u_k}{U_b}\right), \left(\frac{u_k}{U_b}\right)^2, \left(\frac{u_k}{U_b}\right)^3, ..., \left(\frac{u_k}{U_b}\right)^{l-1}, ... \right\} \tag{2.45}$$

$$M = \left\{ 1, \left(\frac{v_k}{V_b}\right), \left(\frac{v_k}{V_b}\right)^2, \left(\frac{v_k}{V_b}\right)^3, ..., \left(\frac{v_k}{V_b}\right)^{m-1}, ... \right\}. \tag{2.46}$$

The terms 1, $\left(\frac{v_k}{V_b}\right)$, and $\left(\frac{u_k}{U_b}\right)$ are eliminated from the set $\{LM_{l,m}(u_k, v_k)\}$, since they do not satisfy the boundary conditions at the origin. The Gram-Schmidt process is applied to the reduced set $\{LM_{l,m}(u_k, v_k)\}$, such that the following orthogonality conditions are satisfied:

$$\int_{-V_b}^{V_b} \int_{-U_b}^{U_b} \left(\frac{1}{U_b}\right)\left(\frac{1}{V_b}\right) LM_{l,m}(u_k, v_k) \, LM_{p,q}(u_k, v_k) \, du_k \, dv_k = \begin{cases} 1 & \text{for } lm = pq \\ 0 & \text{for } lm \neq pq. \end{cases} \tag{2.47}$$

Samples of the $\{LM_{l,m}(u_k, v_k)\}$ can be found in Appendix 2A. Equations (2.43) and (2.44) are substituted into the invariant-manifold governing equations, equations (2.7) and (2.8), and each of these is projected onto each basis function using the L_2-inner product over the entire domain. This leads to:

$$0 = \int_{u_k,v_k} (\frac{1}{U_b}) (\frac{1}{V_b}) LM_{p,q} \left[- \sum_{(l+m)\neq 2,3} D_i^{l,m} LM_{l,m} \right.$$

$$\left. + \sum_{(l+m)\neq 2,3} C_i^{l,m} v_k \frac{\partial LM_{l,m}}{\partial u_k} + \sum_{(l+m)\neq 2,3} C_i^{l,m} \frac{\partial LM_{l,m}}{\partial v_k} (-\omega_k^2 u_k + f_k) \right] du_k \, dv_k$$

$$\equiv F_i^{Y,pq} \tag{2.48}$$

$$0 = \int_{u_k,v_k} (\frac{1}{U_b}) (\frac{1}{V_b}) LM_{p,q} \left[\omega_i^2 \sum_{(l+m)\neq 2,3} C_i^{l,m} LM_{l,m} - f_i \right.$$

$$\left. + \sum_{(l+m)\neq 2,3} D_i^{l,m} v_k \frac{\partial LM_{l,m}}{\partial u_k} + \sum_{(l+m)\neq 2,3} D_i^{l,m} \frac{\partial LM_{l,m}}{\partial v_k} (-\omega_k^2 u_k + f_k) \right] du_k \, dv_k$$

$$\equiv F_i^{X,pq} \tag{2.49}$$

for $\quad i = 1, 2, 3, ..., Q, \; i \neq k;$

$\quad\quad p = 1, ..., N_{p,u};$

$\quad\quad q = 1, ..., N_{p,v};$

and $\quad (p+q) \neq 2, 3$.

The integration in equations (2.48) and (2.49) is computed numerically. Therefore, equations (2.48) and (2.49) represent a set of $2(Q-1)(N_{p,u}N_{p,v} - 3)$ nonlinear-algebraic equations in the C's and D's. For simplicity in referring to the method subsequently, this method is named "the global $u - v$ approach".

For a conservative non-gyroscopic system to posses a synchronous modal response, some of the C's and D's must be zero. The basis functions corresponding to such C's are the ones that are generated from

$$\{(\frac{u_k}{U_b})(\frac{v_k}{V_b})\,,\,(\frac{u_k}{U_b})^2(\frac{v_k}{V_b})\,,\,(\frac{u_k}{U_b})^3(\frac{v_k}{V_b})\,,\,(\frac{u_k}{U_b})^4(\frac{v_k}{V_b})\,,\,(\frac{u_k}{U_b})^5(\frac{v_k}{V_b})\,,\,...\,,$$
$$(\frac{v_k}{V_b})^3\,,\,(\frac{u_k}{U_b})(\frac{v_k}{V_b})^3\,,\,(\frac{u_k}{U_b})^2(\frac{v_k}{V_b})^3\,,\,(\frac{u_k}{U_b})^3(\frac{v_k}{V_b})^3\,,\,(\frac{u_k}{U_b})^4(\frac{v_k}{V_b})^3\,,\,(\frac{u_k}{U_b})^5(\frac{v_k}{V_b})^3\,,\,...\,,$$
$$(\frac{v_k}{V_b})^5\,,\,(\frac{u_k}{U_b})(\frac{v_k}{V_b})^5\,,\,(\frac{u_k}{U_b})^2(\frac{v_k}{V_b})^5\,,\,(\frac{u_k}{U_b})^3(\frac{v_k}{V_b})^5\,,\,(\frac{u_k}{U_b})^4(\frac{v_k}{V_b})^5\,,\,(\frac{u_k}{U_b})^5(\frac{v_k}{V_b})^5\,,\,...\,\},\quad (2.50)$$

where the elements in the set are linear in $(\frac{v_k}{V_b})^1$, $(\frac{v_k}{V_b})^3$, $(\frac{v_k}{V_b})^5$, ... The basis functions corresponding to such D's are the ones that are generated from

$$\{(\frac{u_k}{U_b})^2\,,\,(\frac{u_k}{U_b})^3\,,\,(\frac{u_k}{U_b})^4\,,\,(\frac{u_k}{U_b})^5\,,\,...\,,$$
$$(\frac{v_k}{V_b})^2\,,\,(\frac{u_k}{U_b})(\frac{v_k}{V_b})^2\,,\,(\frac{u_k}{U_b})^2(\frac{v_k}{V_b})^2\,,\,(\frac{u_k}{U_b})^3(\frac{v_k}{V_b})^2\,,\,(\frac{u_k}{U_b})^4(\frac{v_k}{V_b})^2\,,\,(\frac{u_k}{U_b})^5(\frac{v_k}{V_b})^2\,,\,...\,,$$
$$(\frac{v_k}{V_b})^4\,,\,(\frac{u_k}{U_b})(\frac{v_k}{V_b})^4\,,\,(\frac{u_k}{U_b})^2(\frac{v_k}{V_b})^4\,,\,(\frac{u_k}{U_b})^3(\frac{v_k}{V_b})^4\,,\,(\frac{u_k}{U_b})^4(\frac{v_k}{V_b})^4\,,\,(\frac{u_k}{U_b})^5(\frac{v_k}{V_b})^4\,,\,...\,\},\quad (2.51)$$

where the elements in the set are linear in $(\frac{v_k}{V_b})^0$, $(\frac{v_k}{V_b})^2$, $(\frac{v_k}{V_b})^4$, ... Therefore, in this case the number of nonlinear algebraic equations to be solved for the remaining C's and D's is $(Q-1)(N_{p,u}N_{p,v}-3)$.

For a conservative non-gyroscopic system with cubic nonlinearities, the additional C's and D's that correspond to $l+m=$ an even number, would all be zero. Therefore, the number of nonlinear-algebraic equations in the C's and D's to be solved is about $\frac{1}{2}(Q-1)(N_{p,u}N_{p,v}-3)$.

Once all of the expansion coefficients are obtained, the X's and Y's, which describe the slaved modes, are known functions of the master states (u_k, v_k). For $i=k$, these known functions are used to express f_k in equation (2.2) in terms of only u_k and v_k, rendering a single-DOF oscillator as the reduced-order-model for the kth NNM.

2.3.2.3 Collocation Method with Local-Basis Functions in Modal Amplitude and Phase Angle (Annular Strip Representation)

In [33], Pesheck *et al.* mentioned that as the number of retained linear modes Q increases, the computational time associated with solving equations (2.41) and (2.42) increases drastically. Therefore, they developed a new approach to solve the invariant manifold equations. In this approach, the desired domain in the a_k direction is divided into K small sections, producing annular subdomains given by $\phi_k \in [0, 2\pi]$ and $a_k \in [a_{k,j}, a_{k,j} + \triangle a_k]$. For each subdomain, as before the shape functions in the ϕ_k direction are chosen to be the Fourier basis. However, the shape functions in the a_k direction are chosen to be piecewise linear segments, which are accurate, providing the subdomains are sufficiently small. Therefore $P_i(a_k, \phi_k)$ and $Q_i(a_k, \phi_k)$ can be expressed over the jth interval as:

$$
\begin{aligned}
P_i(a_k, \phi_k) &= \sum_{l,m} C_i^{l,m} T_{l,m}(a_k, \phi_k) \\
&= \sum_{m=1}^{N_\phi} \left[C_i^{1,m}(\frac{a_k - a_{k,j}}{\triangle a_k}) \right. \\
&\qquad \left. + C_i^{2,m}(1 - \frac{a_k - a_{k,j}}{\triangle a_k}) \right] \cos((m-1)\phi_k)
\end{aligned}
\tag{2.52}
$$

$$
\begin{aligned}
Q_i(a_k, \phi_k) &= \sum_{l,m} D_i^{l,m} U_{l,m}(a_k, \phi_k) \\
&= \sum_{m=1}^{N_\phi} \left[D_i^{1,m}(\frac{a_k - a_{k,j}}{\triangle a_k}) + D_i^{2,m}(1 - \frac{a_k - a_{k,j}}{\triangle a_k}) \right] \sin(m\phi) \quad (2.53)
\end{aligned}
$$

$$
\text{for} \quad i = 1, 2, 3, ..., Q, \ i \neq k \ .
$$

The Galerkin method is then applied over each subdomain. Therefore, equations (2.41) and (2.42) without the scaling factor ($\frac{1}{a_0^2}$) are valid for each subdomain as well. Note that

there are K sets of C's and D's, one for each $\triangle a_k$ interval. These individual solutions are assembled to construct the invariant manifold. Note that this approach was applied to construct the accurate ROM of a nonlinear rotating beam in [34].

The computational effort associated with evaluating and solving equations (2.41) and (2.42) can be quite high. To reduce it, Apiwattanalunggarn *et al.* ([35]) implemented the collocation method to construct an accurate ROM for a nonlinear finite element model of the rotating beam. For this implementation of the collocation method, the nonlinear-algebraic equations (similar to equations (2.41) and (2.42)) are given by

$$
\begin{aligned}
0 \; = \; & \int_{a_k,\phi_k} \delta(a_k - a_{k,p}, \phi_k - \phi_{k,q_1}) \left[-a_k \sum_{l,m} D_i^{l,m} U_{l,m} \right. \\
& + \sum_{l,m} C_i^{l,m} \frac{\partial T_{l,m}}{\partial a_k} (\frac{-f_k \; a_k \; \sin(\phi_k)}{\omega_k}) \\
& \left. + \sum_{l,m} C_i^{l,m} \frac{\partial T_{l,m}}{\partial \phi_k} (a_k \; \omega_k - \frac{f_k \; \cos(\phi_k)}{\omega_k}) \right] da_k \; d\phi_k \qquad (2.54)
\end{aligned}
$$

$$
\begin{aligned}
0 \; = \; & \int_{a_k,\phi_k} \delta(a_k - a_{k,p}, \phi_k - \phi_{k,q_2}) \left[\omega_i^2 \; a_k \sum_{l,m} C_i^{l,m} T_{l,m} - a_k \; f_i \right. \\
& + \sum_{l,m} D_i^{l,m} \frac{\partial U_{l,m}}{\partial a_k} (\frac{-f_k \; a_k \; \sin(\phi_k)}{\omega_k}) \\
& \left. + \sum_{l,m} D_i^{l,m} \frac{\partial U_{l,m}}{\partial \phi_k} (a_k \; \omega_k - \frac{f_k \; \cos(\phi_k)}{\omega_k}) \right] da_k \; d\phi_k \qquad (2.55)
\end{aligned}
$$

for $\quad i = 1, 2, 3, ..., Q, \; i \neq k;$

$\qquad p = 1, 2;$

$\qquad q_1 = 1, ..., N_\phi;$

$\qquad q_2 = 1, ..., N_\phi,$

where $(a_{k,p}, \phi_{k,q_1}) \in [a_{k,j}, a_{k,j} + \triangle a_k] \times [0, 2\pi]$ are collocation points associated with

42

$Q_i(a_k, \phi_k)$ and $(a_{k,p}, \phi_{k,q_2}) \in [a_{k,j}, a_{k,j} + \triangle a_k] \times [0, 2\pi]$ are collocation points associated with $P_i(a_k, \phi_k)$. The collocation method greatly simplifies the integrals. Equations (2.54) and (2.55) are a set of $4(Q-1)N_\phi$ nonlinear-algebraic equations in the C's and D's. Recall, that one must solve K such sets of equations to obtain the manifold over the entire domain. For simplicity in referring to the method subsequently, this method is named "the local $a - \phi$ approach".

For a conservative non-gyroscopic system, only half of the harmonic terms in the expansion of the basis functions for each state are needed. Therefore the number of nontrivial coefficients is $2(Q-1)N_\phi$. This fact is known from the symmetry of such solutions, and is also confirmed by numerical calculations.

Once all of the expansion coefficients are obtained, the P's and Q's, which describe the slaved modes, are known functions of the master states (a_k, ϕ_k). These known functions are used to express f_k in equations (2.17) and (2.18) in terms of only a_k and ϕ_k, rendering a single-DOF oscillator as the reduced-order-model for the kth NNM.

2.3.2.4 Collocation Method with Local-Basis Functions in Modal Position and Velocity (Patch Representation)

The approach developed in section 2.3.2.2 has the same disadvantage as that described in section 2.3.2.1 when the number of retained linear modes Q increases. Hence, in this section we develop an approach similar to the approach given in section 2.3.2.3. However, we take the slightly different approach from that of section 2.3.2.3, wherein we use rectangular subdomains defined in the modal displacement and velocity. The solution is expanded over each such subdomain using two-dimensional polynomial basis functions. Since these subdomains are small, we can use low degree polynomial functions to describe the invariant manifold over the subdomain, which significantly reduces the computational time of solving for the invariant manifold.

43

Here we describe the development of the method for a local domain described by $u_k^e \in [-u_b, u_b]$ and $v_k^e \in [-v_b, v_b]$. Once this procedure has been developed, it can be applied to each patch, and the final result is obtained by collecting the results for all patches such that the entire domain is covered. The relations between the coordinates in the global domain (u_k, v_k) and those in the local domain (u_k^e, v_k^e) are given by

$$u_k = d_u + u_k^e, \tag{2.56}$$

$$v_k = d_v + v_k^e, \tag{2.57}$$

$$\text{where} \quad d_u = -U_b + (\frac{2U_b}{N_u^e})(e_u - 1) + u_b, \tag{2.58}$$

$$\text{and} \quad d_v = -V_b + (\frac{2V_b}{N_v^e})(e_v - 1) + v_b, \tag{2.59}$$

where e_u and e_v are the patch indices in the u_k and v_k directions respectively, and N_u^e and N_v^e are the number of patches used in the u_k and v_k directions, respectively, and d_u and d_v represent the shift from the origin of (u_k, v_k) to (u_k^e, v_k^e). Here e_u runs from 1 to N_u^e and e_v runs from 1 to N_v^e.

Substituting equations (2.56) and (2.57) into equations (2.7) and (2.8), the partial differential equations governing the geometry of the kth manifold in the local coordinates (u_k^e, v_k^e) are given by:

$$Y_i = \frac{\partial X_i}{\partial u_k^e}(d_v + v_k^e) + \frac{\partial X_i}{\partial v_k^e}(-\omega_k^2 (d_u + u_k^e)$$

$$+ f_k(X_j, Y_j, d_u + u_k^e, d_v + v_k^e)) \quad (2.60)$$

$$-\omega_i^2 X_i + f_i(X_j, Y_j, d_u + u_k^e, d_v + v_k^e) = \frac{\partial Y_i}{\partial u_k^e}(d_v + v_k^e) + \frac{\partial Y_i}{\partial v_k^e}(-\omega_k^2 (d_u + u_k^e)$$

$$+ f_k(X_j, Y_j, d_u + u_k^e, d_v + v_k^e)) \quad (2.61)$$

$$\text{for} \quad i, j = 1, 2, 3, ..., Q, \ i, j \neq k.$$

The solution of equations (2.60) and (2.61) on the local domain is obtained by expanding (X_i, Y_i) in terms of basis functions as:

$$X_i(u_k^e, v_k^e) = \sum_{l=1}^{N_{p,u}} \sum_{m=1}^{N_{p,v}} C_i^{l,m} LM_{l,m}(u_k^e, v_k^e) \quad (2.62)$$

$$Y_i(u_k^e, v_k^e) = \sum_{l=1}^{N_{p,u}} \sum_{m=1}^{N_{p,v}} D_i^{l,m} LM_{l,m}(u_k^e, v_k^e), \quad (2.63)$$

$$\text{where} \quad LM_{l,m}(u_k^e, v_k^e) = T_{l-1}(u_k^e/u_b) \times T_{m-1}(v_k^e/v_b), \quad (2.64)$$

where $T_{l-1}(x)$ and $T_{m-1}(x)$ are standard Chebyshev polynomials defined over $x \in [-1, +1]$, and the C's and D's are the to-be-determined expansion coefficients. Equations (2.62) and (2.63) are substituted into the local manifold-governing equations, equations (2.60) and (2.61). Normally, each of the resulting equations is projected onto the basis functions, but here we employ a collocation method, which is computationally more efficient, yet retains very good accuracy. This is carried out by projection of the equations onto *Dirac delta functions* in the local master coordinates over the local domain, as follows:

$$0 = \int_{u_k^e, v_k^e} \delta(u_k^e - u_{k,p}^e, v_k^e - v_{k,q}^e) \left[-\sum_{l,m} D_i^{l,m} LM_{l,m} \right.$$

$$\left. + \sum_{l,m} C_i^{l,m} (d_v + v_k^e) \frac{\partial LM_{l,m}}{\partial u_k^e} + \sum_{l,m} C_i^{l,m} \frac{\partial LM_{l,m}}{\partial v_k^e} (-\omega_k^2 (d_u + u_k^e) + f_k) \right] du_k^e \, dv_k^e$$

$$\equiv F_i^{Y,pq} \tag{2.65}$$

$$0 = \int_{u_k^e, v_k^e} \delta(u_k^e - u_{k,p}^e, v_k^e - v_{k,q}^e) \left[\omega_i^2 \sum_{l,m} C_i^{l,m} LM_{l,m} - f_i \right.$$

$$\left. + \sum_{l,m} D_i^{l,m} (d_v + v_k^e) \frac{\partial LM_{l,m}}{\partial u_k^e} + \sum_{l,m} D_i^{l,m} \frac{\partial LM_{l,m}}{\partial v_k^e} (-\omega_k^2 (d_u + u_k^e) + f_k) \right] du_k^e \, dv_k^e$$

$$\equiv F_i^{X,pq} \tag{2.66}$$

for $i = 1, 2, 3, ..., Q, \ i \neq k$;

$p = 1, ..., N_{p,u}$;

$q = 1, ..., N_{p,v}$.

where $(u_{k,p}^e, v_{k,q}^e) \in [-u_b, u_b] \times [-v_b, v_b]$ are the collocation points, which are zeroes of $T_{N_{p,u}}(u_k^e/u_b)$ and $T_{N_{p,v}}(v_k^e/v_b)$, respectively ([78], [81]). Equations (2.65) and (2.66) constitute a set of $2(Q - 1)N_{p,u}N_{p,v}$ nonlinear equations in the C's and D's. Note that there are $N_u^e \times N_v^e$ sets of C's and D's. However, if the system is conservative, non-gyroscopic, and the nonlinear terms are functions of solely the modal positions, then only $\frac{1}{4} \times N_u^e \times N_v^e$ sets of C's and D's need to be obtained, and the remaining coefficients can be generated using symmetries in the solution. For simplicity in referring to the method subsequently, this method is named "the local $u - v$ approach".

Once all of the expansion coefficients are obtained, the X's and Y's, which describe the slaved modes, are known functions of the master states (u_k^e, v_k^e). For $i = k$, these known

functions are used to express f_k in equation (2.2) in terms of only u_k^e and v_k^e, rendering a single-DOF oscillator as the reduced-order-model for the kth NNM.

2.3.3 Comparison of Computational Efforts

To compare the computational efforts of the approaches described above, there are three main aspects that we must consider: the total number of unknown coefficients, the number of evaluation points needed for the integrands in order to compute the integrals, and the methods used to solve the nonlinear-algebraic equations. First, the reduction in the number of unknown coefficients C's and D's for a specific class of systems of all four approaches (the global $a - \phi$, the global $u - v$, the local $a - \phi$, and the local $u - v$ approaches) is described. Next, a comparison of the number of unknown coefficients C's and D's and a comparison of the number of evaluation points needed for the integrands of the global approaches (the global $a - \phi$ and the global $u - v$ approaches) are described. Then, a comparison of the number of unknown coefficients C's and D's of the local approaches (the local $a - \phi$ and the local $u - v$ approaches) are described. This section is closed with a comparison of the methods used to solve the nonlinear-algebraic equations in this study. Summaries for the total number of unknown coefficients and the number of evaluation points for the global-domain and local-domain approaches are shown in Tables 2.1 and 2.2, respectively.

2.3.3.1 Coefficient Reduction for a Specific Class of Systems

For the most general class of systems, that is, those with general (i.e., non-Caughey) damping, gyroscopic effects, etc., one must obtain the entire set of C and D coefficients. However, in some commonly encountered cases the number of coefficients can be reduced simply due to symmetries in the equations of motion and the resulting responses. These symmetries may be in terms of temporal or spatial dependence. Specifically, consider the

forms of equations (2.41), (2.48), (2.54), and (2.65). If the nonlinear terms are functions of the modal positions only, it can be seen that the D's can be expressed as functions of the C's. By using this result in equations (2.42), (2.49), (2.55), and (2.66), the number of equations and the number of unknowns in all four approaches can be reduced by half, thereby reducing the computational time accordingly. We now turn to the details of the four approaches.

2.3.3.2 Comparison of Coefficients and Evaluation Points for the Global-Domain Approaches

Here a comparison of the number of unknown coefficients C's and D's of the global $a - \phi$ and the global $u - v$ approaches is described first. This comparison is based on the systems having nonlinear forces of polynomial types. The numbers of unknown coefficients C's and D's of the global $a - \phi$ and the global $u - v$ approaches for this class of systems have been described in sections 2.3.2.1 and 2.3.2.2. Second, a comparison on the reuse of previously-computed integrals, which is based on how the slave states are represented by the expansion of basis functions, is described. Then comparisons of the number of evaluation points needed for the integrands in order to compute the integrals of the global $a - \phi$ and the global $u - v$ approaches are described.

For the global-domain approaches, solving the invariant-manifold equations in terms of modal position and velocity has three advantages over solving them in modal amplitude and phase angle.

First, for systems having specific polynomial nonlinear terms, either quadratic or cubic, the trivial basis functions of the global $u - v$ approach (mentioned in section 2.3.2.2) can be easily determined, and therefore the number of coefficients can be significantly reduced. However for the global $a - \phi$ approach (mentioned in section 2.3.2.1), we can not take such an advantage from this specific class of systems.

Second, the basis functions of the slave positions and slave velocities, expressed in terms of the master position and velocity, are the same, therefore equations (2.48) and (2.49) share the same integrals. However, this is not true for equations (2.41) and (2.42) for the global $a - \phi$ approach, since the basis functions of the slave positions and slave velocities expressed in terms of the master amplitude and phase angle are different.

Third, as mentioned in [82], the number of evaluation points in the ϕ_k direction of the global $a - \phi$ approach is taken to be at least $10N_\phi$ to provide good results, and typically $N_\phi \geq 12$. The number of evaluation points in the v_k direction of the global $u - v$ approach, for which gaussian integration ([80]) is used, is $(\frac{5}{2}N_{p,v} - 2)$. Assuming that the number of terms used for the modal displacement is comparable to that used for the modal amplitude, i.e. $N_{p,u} \approx N_a$, therefore the number of evaluation points in the u_k and the a_k directions, for which gaussian integration are used, are comparable, i.e., $(\frac{5}{2}N_{p,u} - 2) \approx (\frac{5}{2}N_a + 3)$. Hence, one can make a comparison by considering the number of terms needed for the modal velocity versus those needed for the modal phase. If $N_{p,v}$ is assumed to be 12, which is the minimum number required for N_ϕ, it can be seen that the number of evaluation points in the ϕ_k direction is much higher than in v_k direction, i.e., $(10N_\phi = 10 \times 12) \gg (\frac{5}{2}N_{p,u} - 2 = \frac{5}{2} \times 12 - 2)$.

2.3.3.3 Comparison of Coefficients for the Local-Domain Approaches

Here, a comparison on the reuse of already-computed integrals, which is based on how the slave states are represented by the expansion of basis functions, is described first. Second, a comparison of computational times, which is based on how many terms in the expansion of basis functions are needed to sufficiently describe the slave states, is described. Note that the number of terms in the expansion of basis functions is determined from experience gained from numerical experiments. Note that a comparison of the number of evaluation points needed for the integrands in order to compute the integrals for the local $a - \phi$ and the local $u - v$ approaches is not considered since both approaches use the collocation method.

First, the basis functions for the slave positions and slave velocities, expressed in terms of master position and velocity, are the same, in the local $u - v$ approach, therefore equations (2.65) and (2.66) share the same integrals. However, this is not true for equations (2.54) and (2.55) for the local $a - \phi$ approach.

Second, the numbers of basis functions in the a_k and u_k directions for the local $a - \phi$ and the local $u - v$ approaches, respectively, are comparable to each other since the manifold is described in the a_k and u_k directions using local basis functions and typically $N_a = 2$ and typically $N_{p,u} = 3$. Many harmonic terms, typically $N_\phi \geq 12$ (as previously mentioned), are needed to describe the manifold globally in the ϕ_k direction. In contrast, only a few Chebyshev-polynomial basis terms, typically $N_{p,v} = 2$, are needed to describe the manifold locally in the v_k direction. Therefore, the dimension of each subproblem of the local $u - v$ approach is much smaller than the local $a - \phi$ approach, which implies that the computational time for each subproblem of the former method is much less than that for the latter method. Even though for each grid (piece) along the u_k direction many pieces along the v_k direction are needed, the total computational time for each grid (piece) along the u_k direction is just the sum of the computational times for the pieces along the v_k direction. However the computational time for each grid (piece) along the a_k direction does not grow proportionally with the number of harmonic terms N_ϕ, i.e., it grows nonlinearly with N_ϕ. Hence, there is a tendency that the local $u - v$ approach uses less computational time than the local $a - \phi$ approach. Note that this is only an educated estimate. In section 2.4.2.1, the computational times for the local $a - \phi$ and the local $u - v$ approaches will be measured and reported. Note that for both local-domain approaches applied to conservative non-gyroscopic systems, the conservative condition and the associated symmetry in the manifold solution are fully employed.

2.3.3.4 Comparison of Methods Used to Solve the Nonlinear-Algebraic Equations

In this study, three methods have been implemented to solve the system of nonlinear-algebraic equations for the unknown coefficients. They are Powell's Hybrid method ([83]), the Newton-Raphson method ([80]), and the Secant method ([80]). All three methods have been used in this study, and by previous researchers in this line of research. Note that this is a cooperative research program between the Department of Mechanical Engineering at Michigan State University and the Department of Mechanical Engineering at the University of Michigan. Powell's Hybrid method, as implemented via the NAG (Numerical Algorithms Group) routines, is available at the University of Michigan, and was used in the studies by Pesheck *et al.* ([33], [34], [71], and [82]), and in the study by Apiwattanalunggarn *et al.* ([35]). However the NAG routines are not available at Michigan State University, and therefore the Newton-Raphson method was implemented via the Numerical-Recipes routines([84]), and the Secant method was developed in-house and used in other parts of this study.

Powell's Hybrid method is a method used to find a minimum solution of an objective function, which in our case it is a summation of nonlinear-algebraic equations squared, whose global minimum point is the best available solution of the system of nonlinear-algebraic equations. The method requires no information on derivatives of the objective function. However it maintains a set of independent directions, where the number of directions is equal to the number of dimensions of the solution, and it performs successive line searches along the set in a cyclical manner. The set is also updated at each iteration. As mentioned in [84] and [83], for a problem with N unknowns, the quadratic-objective function would take N iterations of the basic procedure, which results in $N^2 + O(N)$ exact line searches, i.e., the minima is obtained along each line search. This estimate can be used as a guide for a general function since locally it behaves like a quadratic function at an arbitrary point. As mentioned in [82], it takes on average about $1.25N$ iterations to

reach a solution to equations (2.41) and (2.42) (with the D's expressed as functions of the C's), for either the global domain approach or the local domain approach (for one single strip) using this approach. Also, as mentioned in [82], the computational effort of the local $a - \phi$ approach using Powell's Hybrid method is only $\frac{360}{N_a^2}\%$ of the global $a - \phi$ approach using Powell's Hybrid method. This is because for large amplitude motions many terms of polynomial basis (N_a) are needed to describe the manifold globally along the a_k direction for the global $a - \phi$ approach. This causes the number of iterations to reach a solution to equations (2.41) and (2.42) to increase as N_a increases, and the number of evaluation points needed for the integrands increases as well. However this is not the case for the local $a - \phi$ approach since N_a is fixed at 2, the number of evaluation points needed for the integrands is fixed, and the total computational effort for the whole domain is just the sum of the computational efforts for each annular strip.

The Newton-Raphson method uses gradient information (the Jacobian matrix) of the system of nonlinear-algebraic equations, evaluated at a current step, to determine the direction of the subsequent step, which advances the process towards the solution. The gradient information of the Newton-Raphson method is determined in closed form from the system of nonlinear-algebraic equations. For a single nonlinear equation, the order of convergence ([80]) of the method is determined from $\lim\limits_{n\to\infty} \frac{|e_{n+1}|}{|e_n|^p} = \lim\limits_{n\to\infty} \frac{|r_{n+1} - r|}{|r_n - r|^p} = c$, where r is the exact solution, r_n is the approximate solution at the nth iteration, r_{n+1} is the approximate solution at the $(n+1)^{th}$ iteration, c is a constant called the asymptotic error $(c \neq 0$), and p is a constant called the order of convergence, where $p \geq 1$. For a system of nonlinear equations, similar definitions can be formed using norms instead of absolute values ([85]). For the Newton-Raphson method, the order of convergence is 2 (quadratic convergence) ([80], [85]). There is no such estimate for the number of iterations needed in order to reach the solution from an initial guess, since in practice the solution is not known beforehand, so the error at each iteration is not known. Also, the order of convergence and the asymptotic error constant hold only when the iterates are close to the solution.

The Secant method is similar to the Newton-Raphson method. However, the gradient

information is determined approximately using finite difference methods. The order of convergence of the Secant method is 1.6 (between linear and quadratic convergence) ([80], [85]). Just as for the Newton-Raphson method, there is no estimate for the number of iterations needed in order to reach the solution from an initial guess.

Among these three methods, Powell's Hybrid method has an advantage over the Newton-Raphson and the Secant methods. Since both Newton-Raphson and Secant methods require the Jacobian matrix, and the cost of computing the Jacobian grows rapidly as the dimension of the problem increases. The Newton-Raphson method would have an advantage over the Secant method since it generally requires fewer steps to reach the solution, due to the order of convergence ([80]). However, when the system of nonlinear-algebraic equations is complicated, the Secant method is efficient for computing the Jacobian matrix, since each entry of the Jacobian cannot be determined in closed form, or is complicated and therefore it takes significant time to compute.

In the next section, direct comparisons of the accuracy of the four approaches, both global-domain and local-domain, each using modal displacement/velocity and modal amplitude/phase, are made by comparing time simulations from two example systems.

2.4   Examples

A two-DOF nonlinear spring-mass system and a finite element (FE) model of a rotating beam are used as examples to demonstrate the accuracy of the four approaches used to solve the invariant manifold equations. The first example is used as a "proof of concept," while the second demonstrates the utility of the approach for systems with several DOF. For simplicity in identifying the various approaches, they are labeled as follows: global $a - \phi$, global $u - v$, local $a - \phi$, and local $u - v$, as described in sections 2.3.2.1, 2.3.2.2, 2.3.2.3, and 2.3.2.4, respectively. For the two-DOF nonlinear spring-mass system, all four

methods are considered. For the rotating beam, only the local $a - \phi$ and local $u - v$ approaches are considered.

2.4.1 A Two-DOF Nonlinear Spring-Mass System

The two-DOF nonlinear spring-mass system considered here is the same as the system studied in [33]. The system has nonlinear springs, described by linear spring stiffnesses k_1 and k_3 and nonlinear spring parameters k_2 and k_4; it is schematically depicted in Figure 2.1. The system parameters are $m_1 = m_2 = 1$, and $k_1 = 1, k_2 = 2, k_3 = 5$, and $k_4 = 1$. A comparison of $a - \phi$ and $u - v$ global methods is considered first, followed by a comparison of local methods in $a - \phi$ and $u - v$.

2.4.1.1 Comparison of Global Methods

The accuracy of the global methods is studied through a comparison of motions taking place on the NNM manifold of the first mode of the system. This manifold can be depicted as a pair of constraint surfaces which depend on either the first modal amplitude-phase or the first modal position-velocity. The two constraint surfaces restrict the second mode displacement and velocity, respectively, and describe motions that take place on the 2-dimensional NNM manifold in the 4-dimensional state space.

The C coefficients describing the manifold solution in equation (2.36), with the D's condensed out, were solved using Powell's Hybrid method implemented in the C language on a work-station computer (this was carried out by Mr. Dongying Jiang, a graduate student at the University of Michigan, and a collaborator on this project). A sample of such surfaces is shown in Figure 2.2, which corresponds to the contribution from the second linear mode displacement to the NNM manifold.

The boundary of all constraint surfaces in terms of modal amplitude is given by $a_0 = 2.6$.

These surfaces are obtained by using $N_a = 5$ polynomials and $N_\phi = 12$ harmonics, which are the same as used in [33]. Note that $N_a = 5$ and $N_\phi = 12$ result in 60 coefficients for each state when the conservative (symmetry) condition is used. Here the range of validity of the surfaces is based on comparing simulations of the original model and the NNM ROM. If the motion is initiated beyond a certain amplitude of the master mode, the time responses of the original model begin to have high frequency components. We define this amplitude to be the boundary of the valid domain. As mentioned in [33], the surfaces are valid up to $a = 1.5$ with $a_0 = 2.22$. Here with $a_0 = 2.6$, the surfaces are valid up to $a = 1.7$. Therefore, we suspect that an instability of the first NNM manifold may exist at near this amplitude limit. This suspicion is based on the fact that instabilities of NNMs were observed in 2-DOF systems with symmetry by Rosenberg *et al.* ([6], [15], and [19]).

The C coefficients describing the manifold solution in equation (2.43), with the D's condensed out, are solved using the secant method implemented with the symbolic processor Mathematica^{TM} on a personal computer. To yield a comparable number of C's for this case, the number of polynomials along u_k and v_k would need to be $N_{p,u} = 11$ and $N_{p,v} = 11$. Here the manifold-solver codes are written in Mathematica^{TM}, and are therefore computationally slower. Thus, for acceptable computational time we used $N_{p,u} = 8$ and $N_{p,v} = 8$. Note that $N_{p,u} = 8$ and $N_{p,v} = 8$ result in 15 coefficients for each state when the conservative and odd-polynomial conditions are imposed. The C coefficients are solved with three different sets of boundaries, given by: $(U_b, V_b) = (1.5, 1.5)$, $(U_b, V_b) = (1.7, 1.7 \times \omega_1)$, and $(U_b, V_b) = (2.6, 2.6 \times \omega_1)$, where $\omega_1 = 0.69$ rad/sec is the linear natural frequency of the first mode. The contributions from the second linear mode position to the first NNM manifold for the three different sets of boundaries are depicted in Figures 2.3, 2.5, and 2.7, respectively. Using the transformations given in equations (2.13) and (2.14), the previous contributions can be expressed as functions of modal amplitude and phase, as depicted in Figures 2.4, 2.6, and 2.8. It can be seen from Figure 2.5 that the surface bends sharply at around $u = 1.3$. Also, from Figure 2.8, which is solved for the larger amplitude, the solution surface shape looks completely different from the lower amplitude surfaces. These two observations are a sign of some type of instability, either dynamic or numerical, in the

first NNM manifold or its solution. Therefore, in order to compare the accuracy of the global $a - \phi$ and global $u - v$ approaches, the surface in Figure 2.4 is used to generate the time responses.

Figure 2.9 depicts the time responses of the first nonlinear mode displacement η_1 obtained from the ROM of the global $u - v$ approach, the ROM of the global $a - \phi$ approach, and the original model. The dotted line is the time response of the ROM defined at the end of section 2.3.2.2 with initial modal displacement $\eta_1(0) = 1.3$ and velocity $\dot{\eta}_1(0) = 0.0$. The dashed line is the time response of the ROM defined at the end of section 2.3.2.1 with initial modal amplitude $a_1(0) = 1.3$ and phase angle $\phi_1(0) = 0.0$. The solid line is the time response of the original model (2 DOFs) initiated quite precisely on the first-NNM manifold (as determined by a shooting algorithm that finds periodic responses). As these responses all appear to be quite close, an examination of the slaved modes is used to offer a more refined look at the methods.

Figure 2.10 depicts the time responses of the second linear mode displacement obtained from the ROM of the global $u - v$ approach, the ROM of the global $a - \phi$ method, and the original model. The dotted line is obtained by applying the master-slave constraint (depicted in Figure 2.3) to the numerical solution of the ROM of the global $u - v$ approach (the dotted line in Figure 2.9). The dashed line is obtained by applying the master-slave constraint (depicted in Figure 2.2) to the numerical solution of the ROM of the global $a - \phi$ approach (the dashed line in Figure 2.9). The solid line is obtained from the 2-DOF original model initiated on the NNM manifold.

Figure 2.11 depicts the time responses of the physical displacement x_1 from Figure 2.1 for the ROM of the global $u - v$ approach, the ROM of the global $a - \phi$ approach, and the original model. The line types definitions are the same as in the previous figure.

From Figures 2.9, 2.10, and 2.11, it can be seen that the time responses from the global $a - \phi$ approach are closer to the original model than the global $u - v$ approach. However,

this is not surprising, since the number of basis functions used for the global $a - \phi$ approach was twice the number of basis functions used for the global $u - v$ approach.

2.4.1.2   Comparison of Local Methods

Similarly, the accuracy of the two local methods is studied through a comparison of motions taking place on the first NNM manifold.

For the local $a - \phi$ method the C coefficients describing the manifold solution in equation (2.52), with the D's condensed out, were solved using Powell's Hybrid method implemented with the C language on a computer work-station (again, by Mr. D. Jiang). A sample of such a surface is shown in Figure 2.12, which depicts the contribution from the second linear mode displacement to the first NNM manifold. This NNM manifold is obtained over an amplitude range of $a \in [0, 2.6]$, which is generated using 52 piecewise linear manifold segments in a of width $\Delta a = 0.05$, and $N_\phi = 12$ harmonics in ϕ. Note that $N_a = 2$ and $N_\phi = 12$ result in 24 coefficients for each state within each strip when the conservative symmetry condition is used. The total number of coefficients for the local $a - \phi$ approach is $(Q - 1) \times 2N_\phi \times N_{strip} = 1248$. Here the surfaces are valid up to $a = 1.7$.

For the local $u - v$ method the C coefficients describing the manifold solution in equation (2.62), with the D's condensed out, are solved using the secant method implemented with the C language on a personal computer. The contribution from the second linear mode displacement to the first NNM manifold is depicted in Figure 2.13. The boundaries of all surfaces along the modal position and velocity are $U_b = 2.6$ and $V_b = 1.79$, respectively. All surfaces are obtained by using Chebyshev polynomials along u_k^e and v_k^e with $N_{p,u} = 3$ and $N_{p,v} = 2$, respectively, and the number of pieces along u_k and v_k to be $N_u^e = 100$ and $N_v^e = 100$, respectively. The total number of coefficients for the local $u - v$ approach is $(Q - 1) \times 2N_{p,u}N_{p,v} \times \dfrac{1}{4}N_u^e N_v^e = 30,000$.

Figure 2.14 depicts the time responses of the first nonlinear mode displacement η_1 obtained from the ROM of the local $u - v$ approach, the ROM of the local $a - \phi$ approach, and the original model. The dotted line is the time response of the ROM defined at the end of section 2.3.2.4 with initial modal displacement $\eta_1(0) = 1.5$ and velocity $\dot{\eta}_1(0) = 0.0$. The dashed line is the time response of the ROM defined at the end of section 2.3.2.3 with initial modal amplitude $a_1(0) = 1.5$ and phase angle $\phi_1(0) = 0.0$. The solid line is the time response of the original model (2 DOFs) initiated quite precisely on the first-NNM manifold (again, found using a shooting algorithm). Again, since these responses all appear to be quite close, an examination of the slaved modes is in order.

Figure 2.15 depicts the time responses of the second linear mode displacement obtained from the ROM of the local $u - v$ approach, the ROM of the local $a - \phi$ approach, and the original model, using the previously defined line types. Figure 2.16 depicts the time responses of the physical displacement x_1 from Figure 2.1 for the ROM of the local $u - v$ approach, the ROM of the local $a - \phi$ approach, and the original model.

From Figures 2.14, 2.15, and 2.16, it can be seen that the time responses from the local $a - \phi$ approach are generally closer to the original model than those from the local $u - v$ approach. Hence, for this example, and considering the number of coefficients used for each method, we conclude that the local $a - \phi$ approach provides more accurate manifold solutions than the local $u - v$ approach.

2.4.2 A Finite-Element-Based Model of a Rotating Beam

The finite element (FE) model of a rotating beam used here is the same as that described in [35], and analyzed in detail in the next chapter. The system consists of a uniform, unloaded Euler-Bernoulli beam attached to a hub that is rotating at a constant rate. The beam is restricted to vibrate in a plane that is parallel to the axis of rotation and rotating

with the hub, so that only transverse vibrations in one direction and axial vibrations are allowed. The corresponding transverse vibrations are commonly referred to as "flapping" motions, while transverse vibrations out of this plane are known as "lead-lag" motions. In this model, torsion, lead-lag, and other motions are neglected. The system is schematically depicted in Figure 2.17. The rotating beam parameters are $L = 9$ m, $m = 10$ kg/m, $EI = 3.99 \times 10^5$ N·m^2, $EA = 2.23 \times 10^8$ N, $\Omega = 30$ rad/s, and $h = 0.5$ m.

The objective here is to compare the accuracy of the methods for generating NNM manifolds (this model is discussed in more detail in the next chapter). The beam is modeled using 182 elements, which are used to construct linear modes and associated nonlinear coupling terms. This model is truncated to $Q = 21$ DOF, expressed in linear modal coordinates, and this is used as a starting point for developing the NNM ROM. This model has 9 transverse modes and 12 axial modes, selected according to the information described in the next chapter. For this system only the local methods in $a - \phi$ and $u - v$ are considered. As mentioned in section 2.3.3.4 the computational effort for the local $a - \phi$ approach with Powell's Hybrid method implemented is only $\dfrac{360}{N_a^2}\%$ of the global $a - \phi$ approach with Powell's Hybrid method implemented (as estimated by Pesheck in his dissertation [82]). Based on this estimate, it is reasonable to assume that the local approach is generally much faster than the global approach. Therefore the global approaches are not considered in this example.

2.4.2.1 Comparison of Local Methods

The accuracy of the local methods is studied by direct comparison of motions taking place on the computed first NNM manifold.

In collaboration with Mr. D. Jiang, the C coefficients describing the manifold solutions in equation (2.52) (with the D's condensed out) are obtained using Newton's method, implemented via the Numerical-Recipes routines ([84]) with the C language on a personal

computer. Note that for a single NNM there are 40 slave functions for this problem, that is, 40 constraint surfaces. Samples of these surfaces obtained by the local $a - \phi$ approach are shown in Figures 2.18, 2.19, 2.20, and 2.21. These correspond to the contributions from the second and fifth linear flapping mode displacements and the first and sixth linear axial mode displacements to the first NNM manifold, respectively. The first NNM manifold is obtained over an amplitude range of $a \in [0, 6.0]$, which is generated using 120 piecewise linear manifold segments in a with width $\Delta a = 0.05$, and $N_\phi = 16$ harmonics in ϕ. Note that $N_a = 2$ and $N_\phi = 16$ result in 16 coefficients for each state within one strip, when the conservative symmetry condition is used. Thus, there are a total of 120 problems, each with 16 unknowns, that must be solved, and it took about 12 hours to solve for the manifold solution using a 2.0 GHz personal computer. We will consider simulations of this model after describing the solution obtained using the local $u - v$ method.

The C coefficients describing the manifold solution in equation (2.62) (again, with the D's condensed out) were next solved using the secant method implemented with the C language on a 2.0 GHz personal computer. To yield a comparable number of the C's over the whole domain, the number of segments along u_k and v_k are taken to be approximately $N_u^e = 40$ and $N_v^e = 40$ with $N_{p.u} = 3$ and $N_{p.v} = 2$ to cover $u \in [-6.0, 6.0]$ and $v \in [-6.0 \times \omega_1, 6.0 \times \omega_1]$, where $\omega_1 = 34.03$ rad/sec is the linear natural frequency of the first flapping mode. It takes about 40 minutes for the manifold solution with $N_u^e = 40$ and $N_v^e = 40$ to converge. However, the residuals of the manifold-governing equations are large. To obtain the appropriate boundary U_b, we fix U_b to be 6.0 and then increase the number of patches, for instance, $N_u^e = 100$ and $N_v^e = 100$. Then we simply observe the residuals for pieces along the v_k direction for a few of the first pieces along the u_k direction. From these observations, we can determine the range in the v_k direction that gives acceptable residuals. This allows one to compute the appropriate V_b and the appropriate U_b. We then choose the same N_u^e and N_v^e for these reduced values of U_b and V_b, i.e., we choose $N_u^e = 100$ and $N_v^e = 100$. Therefore, we take $N_u^e = 100$ and $N_v^e = 100$ to cover the smaller domain, $u \in [-4.0, 4.0]$ and $v \in [-4.0 \times \omega_1, 4.0 \times \omega_1]$. This procedure yields small residuals over the entire domain. In this manner it takes about 4 hours to obtain the manifold solution.

Samples of constraint surfaces obtained by the local $u - v$ approach are shown in Figures 2.22, 2.23, 2.24, and 2.25, which correspond to the contributions from the second and fifth linear flapping mode displacements and the first and sixth linear axial mode displacements to the first NNM manifold, respectively.

Figure 2.26 depicts the time responses of the first nonlinear mode displacement η_1 obtained from the ROM of the local $u - v$ approach, the ROM of the local $a - \phi$ approach, and the original model with the full 21 DOF. The dotted line is the time response of the ROM of the local $u - v$ approach with initial modal displacement $\eta_1(0) = 2.375$ and velocity $\dot{\eta}_1(0) = 0.0$. The dashed line is the time response of the ROM of the local $a - \phi$ approach with initial modal amplitude $a_1(0) = 2.375$ and phase angle $\phi_1(0) = 0.0$. The solid line is the time response of the original model (21 DOF) initiated on first NNM manifold as obtained from a shooting algorithm. Figures 2.27, 2.28, 2.29, and 2.30 depict the time responses of the second and fifth linear flapping mode displacements and the first and sixth linear axial mode displacements obtained from the ROM of the local $u - v$ approach, the ROM of the local $a - \phi$ approach, and the original model, respectively. Figures 2.31 and 2.32 depict the time responses of the beam-tip flapping deflection and the time responses of the beam-tip axial deflection, respectively.

From the above figures, it is obvious that the time responses from the local $a - \phi$ approach are closer to the original model than the local $u - v$ approach. We conclude that the local $a - \phi$ approach yields more accurate manifold solutions than the local $u - v$ approach. However the local $u - v$ approach yields the manifold solutions with significantly less computational time. Therefore, the local $u - v$ approach can be used as a preliminary study or for a study in which very high accuracy is not required.

The drawbacks of using $u - v$ coordinates might be eliminated by first applying the invertible van der Pol transformation ([22]) to the master $u - v$ coordinates. This would results in a new rectangular coordinate system that rotates with the linear response, which would uncouple the governing equations of the master states up to linear order. In

other words, we would parameterize the invariant manifold using a dynamically motivated rotating-coordinate system. Once the invariant-manifold governing equations are reformulated, then the patch approach can be applied again with low-degree polynomials. Note that this idea has yet to be tested.

2.5   Conclusions

In this chapter, we have proposed two new methods for solving for individual NNM invariant manifolds. For both of these methods the manifold is parameterized by the master displacement and velocity and the manifold is obtained using Galerkin approaches. For the first method, the manifold is solved using global polynomial basis functions over the domain of interest. For the second method, the domain of interest is subdivided into small pieces and the manifold is solved using the collocation method over these sub domains, and then pieced together. These methods are compared, in terms of computational times and accuracy, to similar methods that employ amplitude and phase master coordinates, as developed by Pesheck et al. ([33]). In terms of computational time, the proposed methods have advantages over the methods of Pesheck et al.. In terms of accuracy, the methods of Pesheck et al. are superior to the methods proposed herein. In general, a combination of these approaches, which uses rotating rectangular coordinates, as described above, may offer good efficiency and accuracy.

2.6 Tables

Approaches	No. of Coefficients		No. of Eval. Points
	Consv. Syst.	Consv.-Cubic-NL Syst.	per integrand
Section 2.3.2.1 Global $a - \phi$	$(Q-1)$ $\times 2N_a N_\phi$	$(Q-1)$ $\times 2N_a N_\phi$	$(\frac{5}{2}N_a + 3)$ $\times 10N_\phi$
Section 2.3.2.2 Global $u - v$	$(Q-1)$ $\times (N_{p,u} N_{p,v} - 3)$	$(Q-1)$ $\times \frac{1}{2}(N_{p,u} N_{p,v} - 3)$	$(\frac{5}{2}N_{p,u} - 2)$ $\times (\frac{5}{2}N_{p,v} - 2)$

Table 2.1. Comparison of the total number of unknown coefficients and the number of evaluation points needed for the integrands in order to compute the integrals for the global domain approaches.

Approaches	No. of Coefficients for Consv. Syst.	No. of Eval. Points per Integrand
Section 2.3.2.3 Local $a - \phi$	$(Q-1)$ $\times 2N_\phi \times N_{strip}$	1
Section 2.3.2.4 Local $u - v$	$(Q-1)$ $\times 2N_{p,u} N_{p,v} \times \frac{1}{4}N_u^e N_v^e$	1

Table 2.2. Comparison of the total number of unknown coefficients and the number of evaluation points needed for the integrands in order to compute the integrals for the local domain approaches.

2.7 Figures
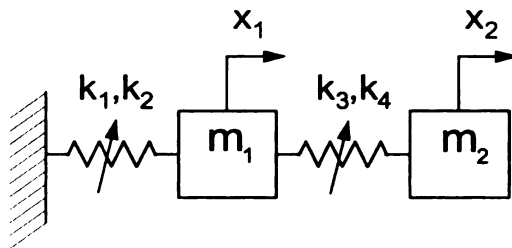
Figure 2.1. A two-DOF nonlinear spring-mass system.
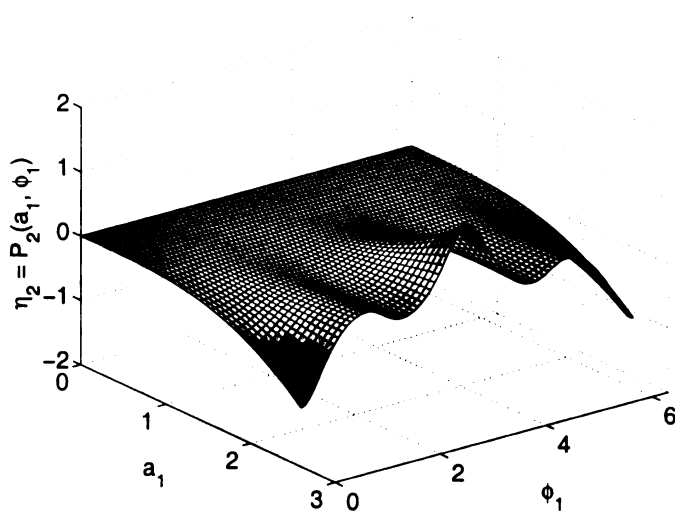
Figure 2.2. The contribution of the second linear mode position $\eta_2 = P_2(a_1, \phi_1)$ to the first nonlinear mode manifold obtained by the global $a - \phi$ approach.
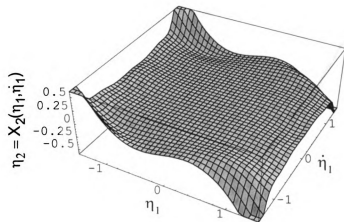
Figure 2.3. The contribution of the second linear mode position $\eta_2 = X_2(\eta_1, \dot{\eta}_1)$ to the first nonlinear mode manifold obtained by the global $u - v$ approach with $U_b = 1.5$ and $V_b = 1.5$.
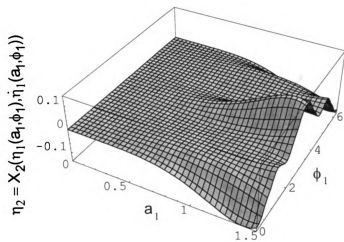
Figure 2.4. The contribution of the second linear mode position $\eta_2 = X_2(\eta_1(a_1, \phi_1), \dot{\eta}_1(a_1, \phi_1))$ to the first nonlinear mode manifold obtained by the global $u - v$ approach with $U_b = 1.5$ and $V_b = 1.5$.
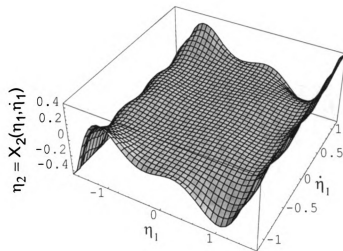
Figure 2.5. The contribution of the second linear mode position $\eta_2 = X_2(\eta_1, \dot{\eta}_1)$ to the first nonlinear mode manifold obtained by the global $u - v$ approach with $U_b = 1.7$ and $V_b = 1.17$.
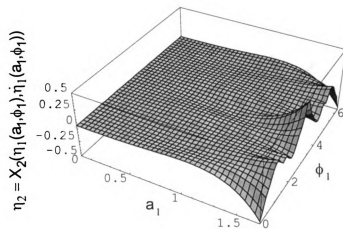
Figure 2.6. The contribution of the second linear mode position $\eta_2 = X_2(\eta_1(a_1, \phi_1), \dot{\eta}_1(a_1, \phi_1))$ to the first nonlinear mode manifold obtained by the global $u - v$ approach with $U_b = 1.7$ and $V_b = 1.17$.
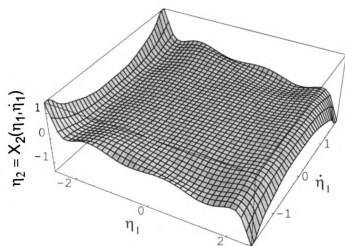
Figure 2.7. The contribution of the second linear mode position $\eta_2 = X_2(\eta_1, \dot{\eta}_1)$ to the first nonlinear mode manifold obtained by the global $u - v$ approach with $U_b = 2.6$ and $V_b = 1.79$.
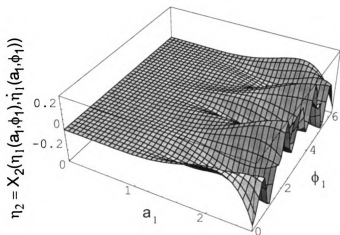
Figure 2.8. The contribution of the second linear mode position $\eta_2 = X_2(\eta_1(a_1, \phi_1), \dot{\eta}_1(a_1, \phi_1))$ to the first nonlinear mode manifold obtained by the global $u - v$ approach with $U_b = 2.6$ and $V_b = 1.79$.
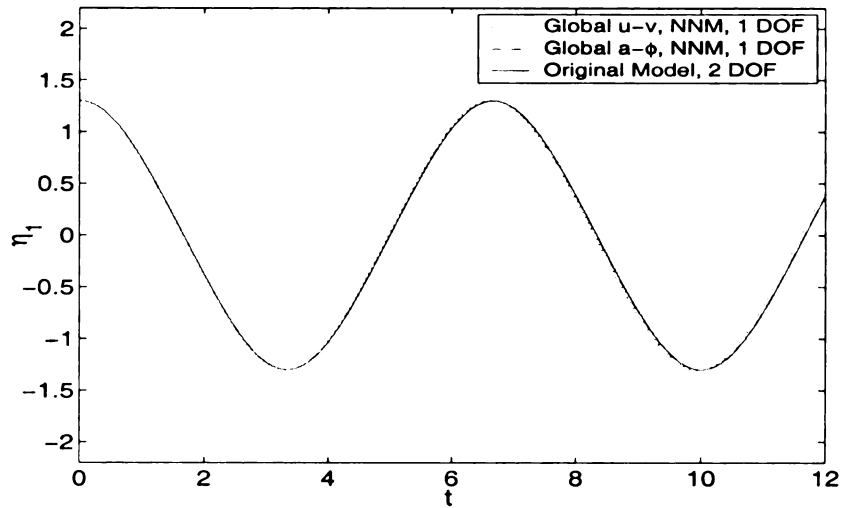
Figure 2.9. The time responses of the first nonlinear mode displacement for the ROM of the global $u - v$ approach with $\eta_1(0) = 1.3, \dot{\eta}_1(0) = 0.0$, the ROM of the global $a - \phi$ approach with $a_1(0) = 1.3, \phi_1(0) = 0.0$, and the original model with initial conditions from the shooting algorithm.
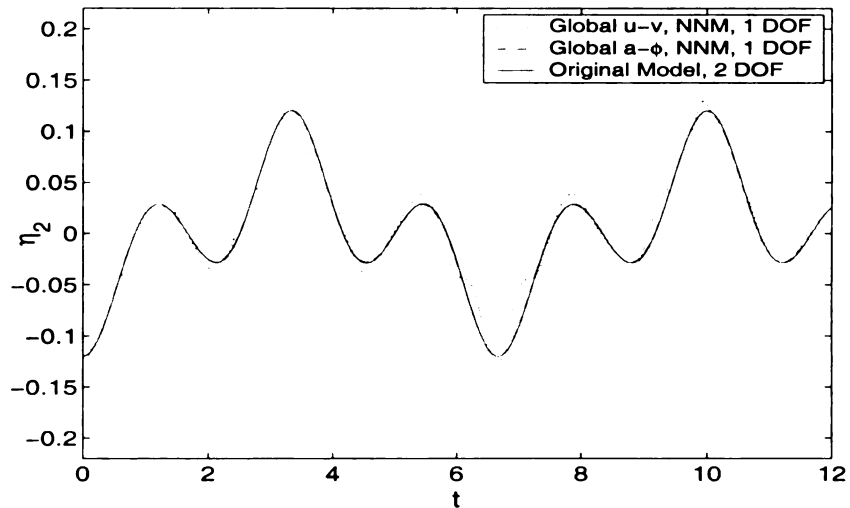
Figure 2.10. The time responses of the second linear mode displacement η_2 on the first nonlinear mode manifold for the ROM of the global $u - v$ approach, the ROM of the global $a - \phi$ approach, and the original model.
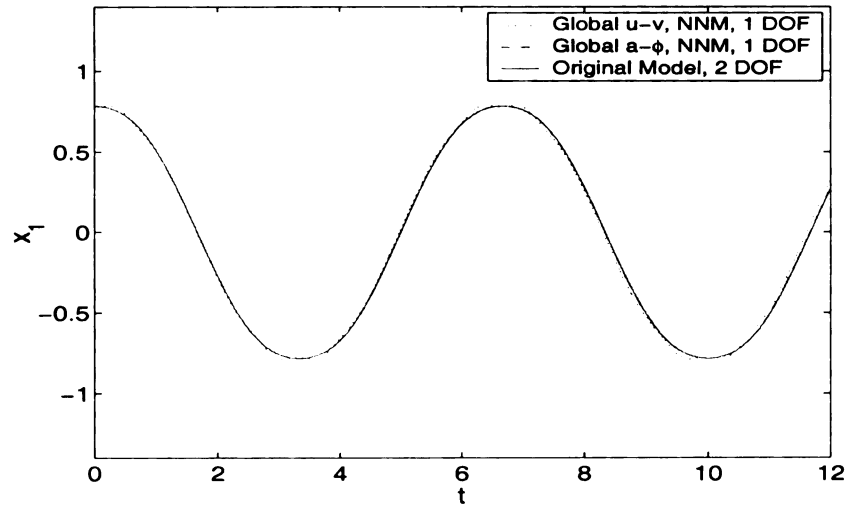
Figure 2.11. The time responses of the displacement x_1 from Figure 2.1 for the ROM of the global $u - v$ approach, the ROM of the global $a - \phi$ approach, and the original model.
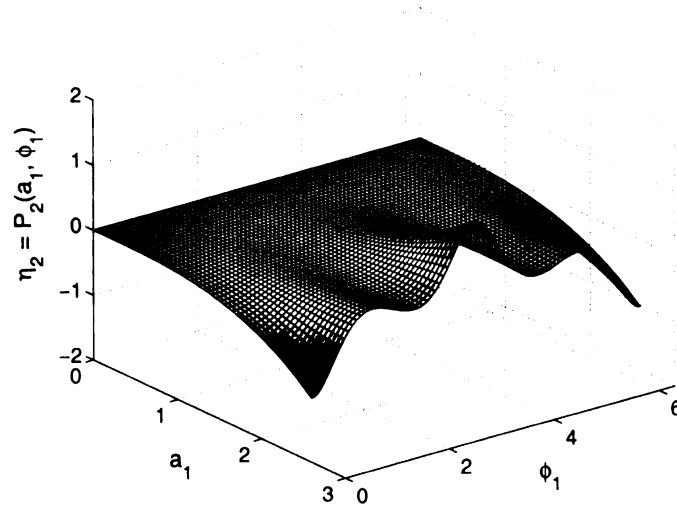
Figure 2.12. The contribution of the second linear mode position $\eta_2 = P_2(a_1, \phi_1)$ to the first nonlinear mode manifold obtained by the local $a - \phi$ approach.
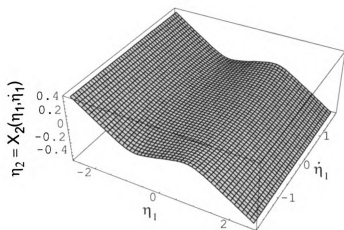
Figure 2.13. The contribution of the second linear mode position $\eta_2 = X_2(\eta_1, \dot{\eta}_1)$ to the first nonlinear mode manifold obtained by the local $u - v$ approach.
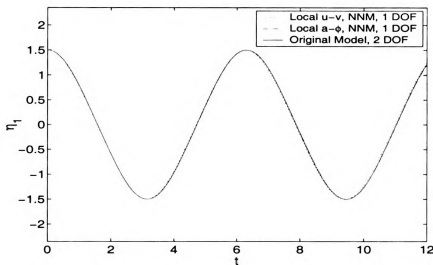
Figure 2.14. The time responses of the first nonlinear mode displacement for the ROM of the local $u - v$ approach with $\eta_1(0) = 1.5, \dot{\eta}_1(0) = 0.0$, the ROM of the local $a - \phi$ approach with $a_1(0) = 1.5, \phi_1(0) = 0.0$, and the original model with initial conditions from the shooting algorithm.
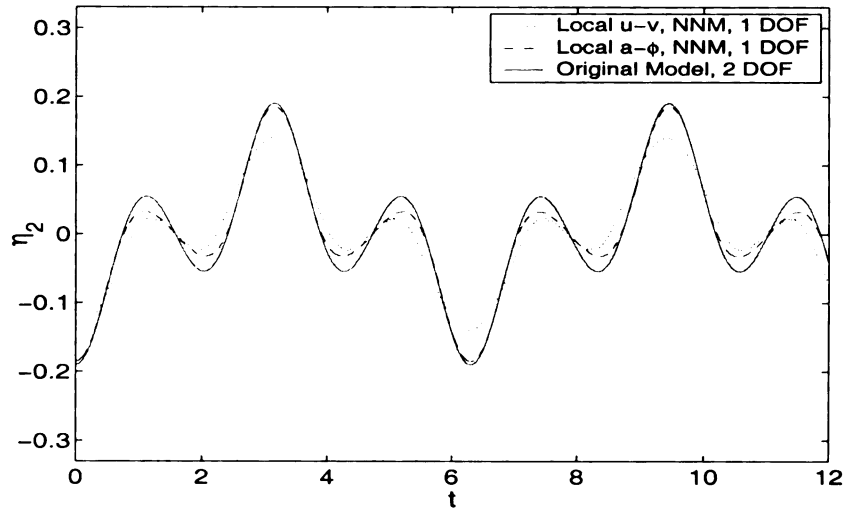
Figure 2.15. The time responses of the second linear mode displacement η_2 on the first nonlinear mode manifold for the ROM of the local $u - v$ approach, the ROM of the local $a - \phi$ approach, and the original model.
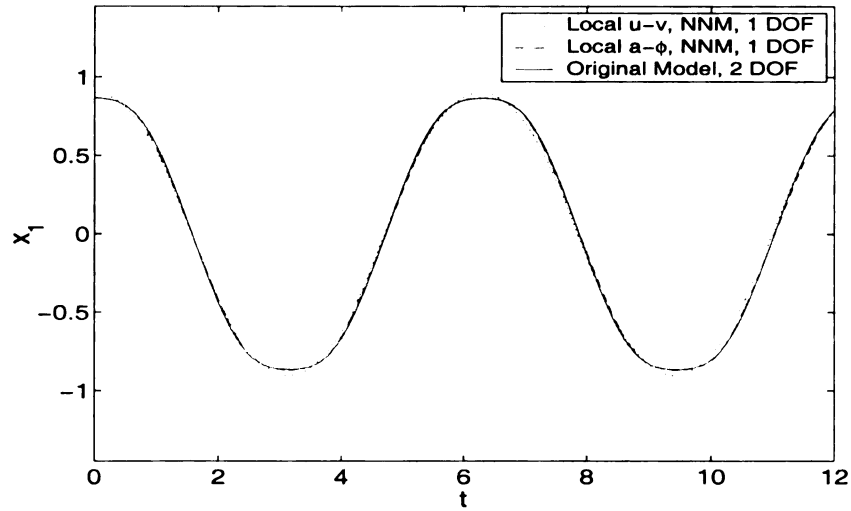
Figure 2.16. The time responses of the displacement x_1 from Figure 2.1 for the ROM of the local $u - v$ approach, the ROM of the local $a - \phi$ approach, and the original model.

71
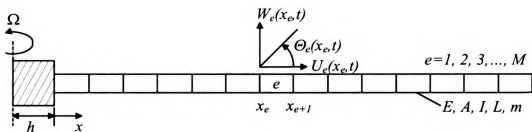
Figure 2.17. Finite element representation of a rotating beam with Ω = constant.
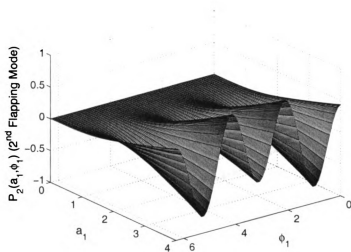
Figure 2.18. The contribution of the second linear flapping mode $\eta_2 = P_2(a_1, \phi_1)$ to the first nonlinear mode manifold obtained by the local $a - \phi$ approach.
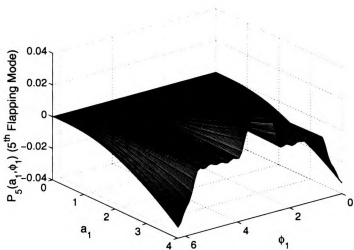
Figure 2.19. The contribution of the fifth linear flapping mode $\eta_2 = P_5(a_1, \phi_1)$ to the first nonlinear mode manifold obtained by the local $a - \phi$ approach.
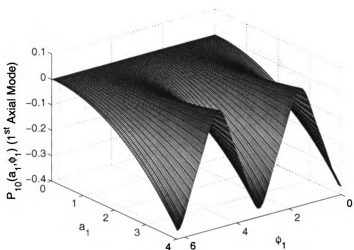
Figure 2.20. The contribution of the first linear axial mode $\eta_{10} = P_{10}(a_1, \phi_1)$ to the first nonlinear mode manifold obtained by the local $a - \phi$ approach.
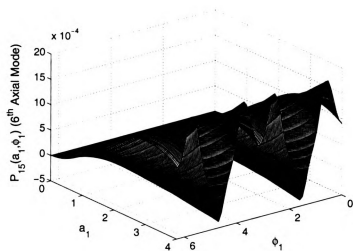
Figure 2.21. The contribution of the sixth linear axial mode $\eta_{15} = P_{15}(a_1, \phi_1)$ to the first nonlinear mode manifold obtained by the local $a - \phi$ approach.
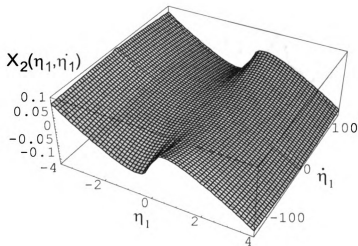
Figure 2.22. The contribution of the second linear flapping mode $\eta_2 = X_2(\eta_1, \dot{\eta}_1)$ to the first nonlinear mode manifold obtained by the local $u - v$ approach.
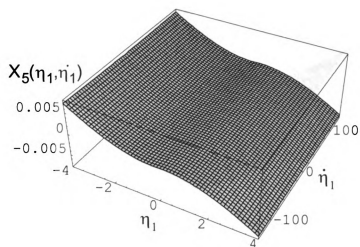
Figure 2.23. The contribution of the fifth linear flapping mode $\eta_2 = X_5(\eta_1, \dot{\eta}_1)$ to the first nonlinear mode manifold obtained by the local $u - v$ approach.
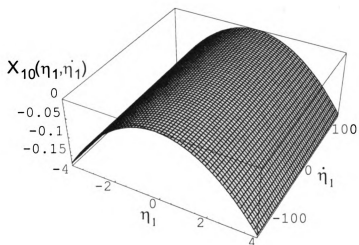
Figure 2.24. The contribution of the first linear axial mode $\eta_{10} = X_{10}(\eta_1, \dot{\eta}_1)$ to the first nonlinear mode manifold obtained by the local $u - v$ approach.
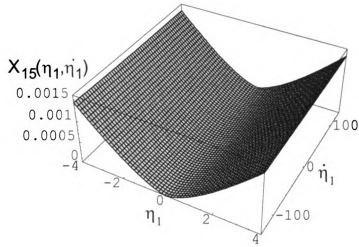
Figure 2.25. The contribution of the sixth linear axial mode $\eta_{15} = X_{15}(\eta_1, \dot{\eta}_1)$ to the first nonlinear mode manifold obtained by the local $u - v$ approach.
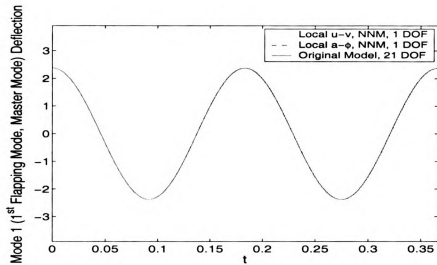
Figure 2.26. The time responses of the first nonlinear flapping mode displacement η_1 for the ROM of the local $u - v$ approach with $\eta_1(0) = 2.375$, $\dot{\eta}_1(0) = 0.0$, the ROM of the local $a - \phi$ approach with $a_1(0) = 2.375$, $\phi_1(0) = 0.0$, and the original model with initial conditions from the shooting algorithm.
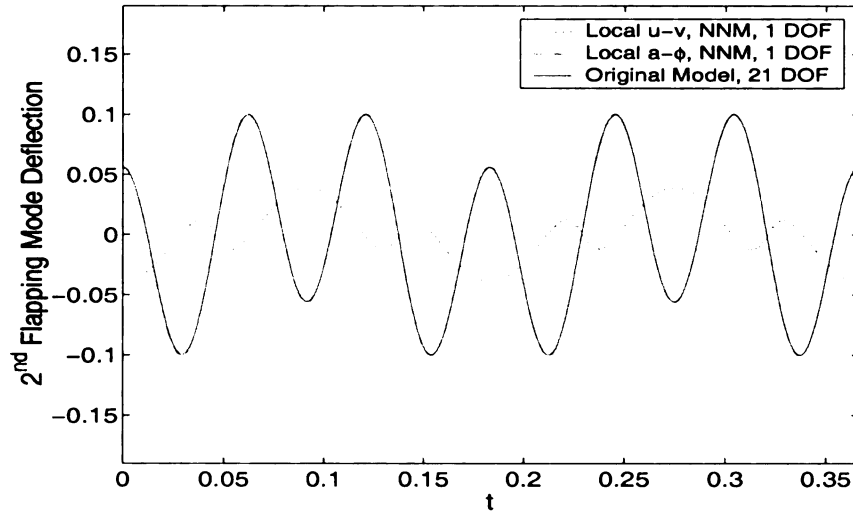
Figure 2.27. The time responses of the second linear flapping mode displacement η_2 on the first nonlinear mode manifold for the ROM of the local $u - v$ approach, the ROM of the local $a - \phi$ approach, and the original model.
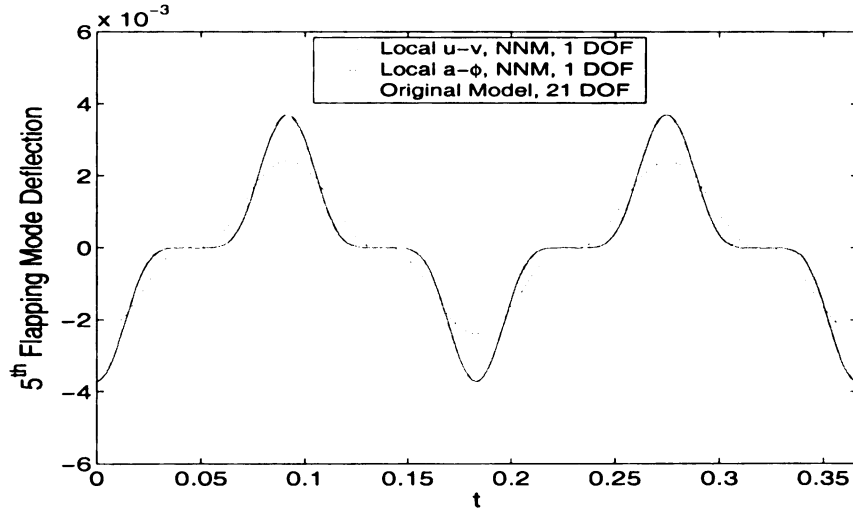
Figure 2.28. The time responses of the fifth linear flapping mode displacement η_5 on the first nonlinear mode manifold for the ROM of the local $u - v$ approach, the ROM of the local $a - \phi$ approach, and the original model.
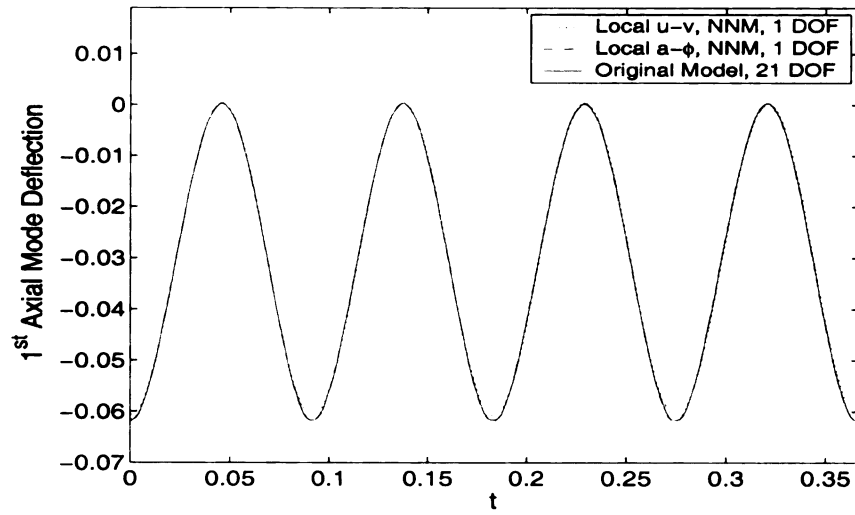
Figure 2.29. The time responses of the first linear axial mode displacement η_{10} on the first nonlinear mode manifold for the ROM of the local $u - v$ approach, the ROM of the local $a - \phi$ approach, and the original model.
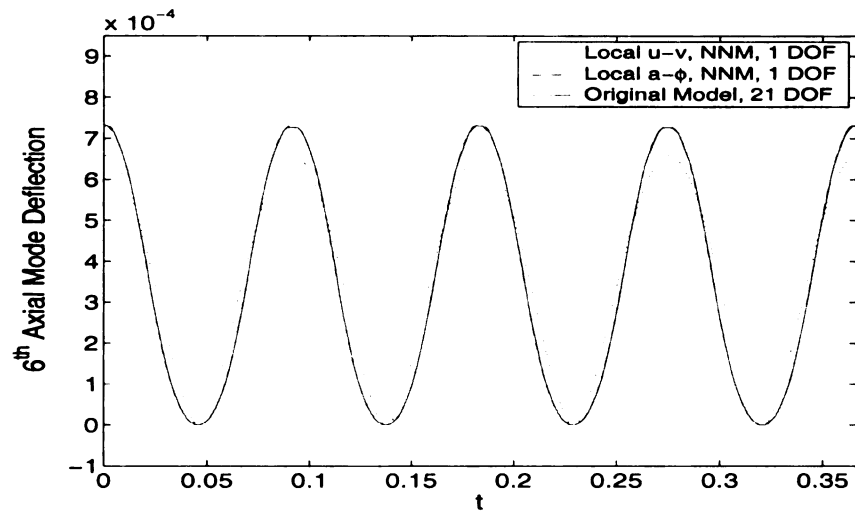
Figure 2.30. The time responses of the sixth linear axial mode displacement η_{15} on the first nonlinear mode manifold for the ROM of the local $u - v$ approach, the ROM of the local $a - \phi$ approach, and the original model.
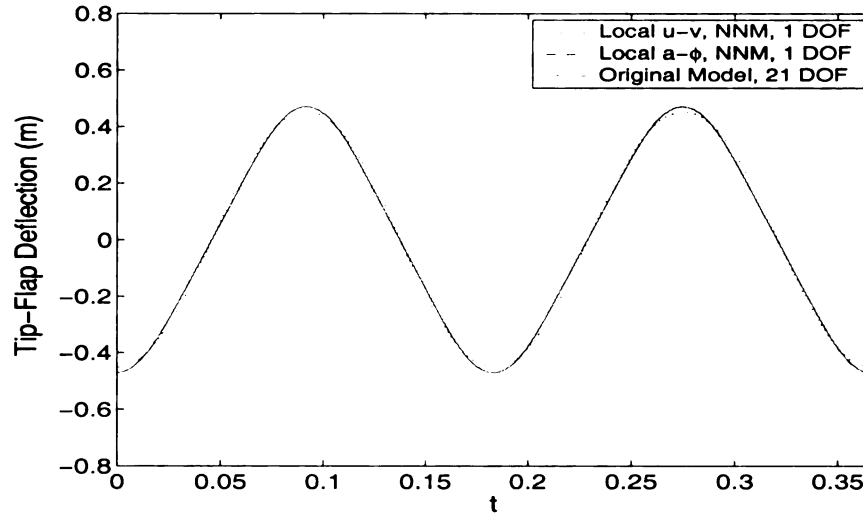
Figure 2.31. The time dependence of the beam-tip flap deflection, $w(L, t)$, for the ROM of the local $u - v$ approach, the ROM of the local $a - \phi$ approach, and the original model.
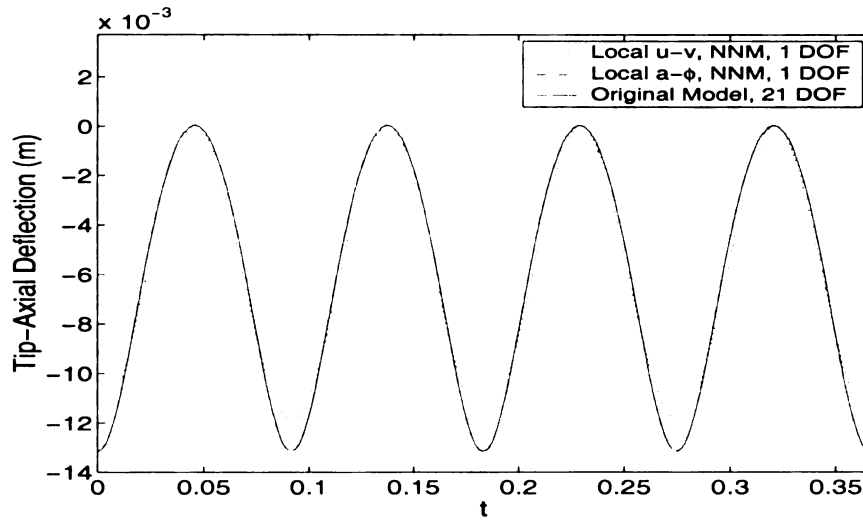
Figure 2.32. The time dependence of the beam-tip axial deflection, $u(L, t)$, for the ROM of the local $u - v$ approach, the ROM of the local $a - \phi$ approach, and the original model.

2.8　Appendix 2A

The samples of $\{LM_{l,m}(u_k, v_k)\}$ for $N_{p,u} = 3$ and $N_{p,v} = 3$ in section 2.3.2.2 are as follows:

$$LM_{1,1}(u_k, v_k) = 0$$

$$LM_{1,2}(u_k, v_k) = 0$$

$$LM_{1,3}(u_k, v_k) = 1.11803(\frac{v_k}{V_b})^2$$

$$LM_{2,1}(u_k, v_k) = 0$$

$$LM_{2,2}(u_k, v_k) = 1.5(\frac{u_k}{U_b})(\frac{v_k}{V_b})$$

$$LM_{2,3}(u_k, v_k) = 1.93649(\frac{u_k}{U_b})(\frac{v_k}{V_b})^2$$

$$LM_{3,1}(u_k, v_k) = 1.55005(\frac{u_k}{U_b})^2 - 65.7441(\frac{v_k}{V_b})^{10} + 172.187(\frac{v_k}{V_b})^8$$
$$- 163.124(\frac{v_k}{V_b})^6 + 67.1689(\frac{v_k}{V_b})^4 - 11.1948(\frac{v_k}{V_b})^2$$

$$LM_{3,2}(u_k, v_k) = 17.4667(\frac{v_k}{V_b})^9 - 40.4492(\frac{v_k}{V_b})^7 + 32.1214(\frac{v_k}{V_b})^5$$
$$- 9.99334(\frac{v_k}{V_b})^3 + 2.88269(\frac{u_k}{U_b})^2(\frac{v_k}{V_b})$$

$$LM_{3,3}(u_k, v_k) = -1.47321(\frac{u_k}{U_b})^2 + 62.4849(\frac{v_k}{V_b})^{10} - 163.651(\frac{v_k}{V_b})^8$$
$$+ 155.038(\frac{v_k}{V_b})^6 - 63.839(\frac{v_k}{V_b})^4 + 8.91533(\frac{v_k}{V_b})^2 + 5.17352(\frac{u_k}{U_b})^2(\frac{v_k}{V_b})^2.$$

2.9 Appendix 2B

Equations (2.48) and (2.49) in section 2.3.2.2 are solved using the Secant method. The method implemented is described here by assuming that the nonlinear term f_i in equation (2.2) is a function of the modal positions only. The orthogonality conditions from equation (2.47) are used in equations (2.48) and (2.49), the simplified equations are given respectively by

$$
\begin{aligned}
0 &= F_i^{Y,p,q} \\
&= -D_i^{p,q} + \sum_{(l+m)\neq 2,3} K_C^{p,q,l,m}(\boldsymbol{C})\, C_i^{l,m}
\end{aligned}
\tag{2.67}
$$

$$
\begin{aligned}
0 &= F_i^{X,p,q} \\
&= \omega_i^2\, C_i^{p,q} - f_i^{p,q}(\boldsymbol{C}) + \sum_{(l+m)\neq 2,3} K_D^{p,q,l,m}(\boldsymbol{C})\, D_i^{l,m},
\end{aligned}
\tag{2.68}
$$

, where $K_C^{p,q,l,m}$, $K_D^{p,q,l,m}$, and $f_i^{p,q}$ are given by

$$
\begin{aligned}
K_C^{p,q,l,m} &= K_D^{p,q,l,m} \\
&= \int_{u_k,v_k} \left(\frac{1}{U_b}\right)\left(\frac{1}{V_b}\right) LM_{p,q}\left[v_k\, \frac{\partial LM_{l,m}}{\partial u_k} \right. \\
&\quad \left. + (-\omega_k^2\, u_k + f_k)\, \frac{\partial LM_{l,m}}{\partial v_k} \right]\, du_k\, dv_k
\end{aligned}
\tag{2.69}
$$

$$
f_i^{p,q} = \int_{u_k,v_k} \left(\frac{1}{U_b}\right)\left(\frac{1}{V_b}\right) f_i\, LM_{p,q}\, du_k\, dv_k \, .
\tag{2.70}
$$

Note that if either the conservative conditions (equations (2.50) and (2.51)) or both the

conservative conditions (equations (2.50) and (2.51)) and the odd-polynomial conditions are used, then $K_C^{p,q,l,m} \neq K_D^{p,q,l,m}$.

From equation (2.67), it can be seen that we can express the D's as functions of the C's. Those expressions are used in equation (2.68). Hence $F_i^{X,p,q}$ will be functions of the C's only and they are given by

$$F_i^{X,p,q}(C) = 0 . \tag{2.71}$$

If C^* is a solution of equation (2.71) in vector form, then equation (2.71) in vector form $F^{X,p,q}(C)$ can be approximated using the Taylor series expansion about $C^{(0)}$, which is close to C^*, up to the first-order terms by

$$0 = F^{X,p,q}(C) \approx F^{X,p,q}(C^{(0)}) + \frac{\partial F^{X,p,q}}{\partial C}(C^{(0)})(C - C^{(0)}) . \tag{2.72}$$

Defining the Jacobian matrix $J \equiv \dfrac{\partial F^{X,p,q}}{\partial C}(C^{(0)})$, the approximate C^* is given by

$$C^* \approx -J^{-1} F^{X,p,q}(C^{(0)}) + C^{(0)} . \tag{2.73}$$

If J is determined in closed form, then the method is called the Newton-Raphson method. If J is determined approximately using the finite difference method and its components are given by

$$J_{i;j}^{l,m;p,q} = \frac{\partial F_i^{X,l,m}}{\partial C_j^{p,q}}(C^{(0)}) \approx \frac{F_i^{X,l,m}(C_j^{p,q,(0)} + \Delta C) - F_i^{X,l,m}(C_j^{p,q,(0)})}{\Delta C}, \qquad (2.74)$$

where ΔC is a chosen small number, then the method is called the Secant method. For each component $J_{i;j}^{l,m;p,q}$, it is required to recompute $K_C^{p,q,l,m}$ and $K_D^{p,q,l,m}$ at each step due to the perturbed C's. Therefore, the computation of each component can be very expensive. The following algorithm is implemented instead:

(i) Initialize $n = 0$, tol = small number, norm > tol, and $C^{(0)}$.

(ii) While norm > tol

    (a) Compute $K_C^{(n)} = \{K_C^{p,q,l,m}\}^{(n)}$ and $K_D^{(n)} = \{K_D^{p,q,l,m}\}^{(n)}$ using equation (2.69).

    (b) Compute $F^{X,p,q}(C^{(n)})$ using equation (2.71).

    (c) Compute $J^{(n)} = J^{(n)}(C^{(n)}, K_C^{(n)}, K_D^{(n)}, F^{X,p,q}(C^{(n)}))$ using equation (2.74). Note that here $K_C^{(n)}$ and $K_D^{(n)}$ from step (a) are used instead of recomputing them with the perturbed C's.

    (d) Compute $\delta C^{(n)} = -(J^{(n)})^{-1} F^{X,p,q}(C^{(n)})$.

    (e) Compute norm = $\| \delta C^{(n)} \|_2$

    (f) Compute $C^{(n+1)} = C^{(n)} + \delta C^{(n)}$.

    (g) Compute $n = n + 1$.

Similarly, equations (2.65) and (2.66) in section 2.3.2.4 are solved using the Secant method. Therefore, equations similar to equations (2.67) and (2.68) are given by

$$0 = F_i^{Y,p,q}$$

$$= \sum_{l,m} K_{D,1}^{p,q,l,m} \, D_i^{l,m} + \sum_{l,m} K_{C,2}^{p,q,l,m}(\boldsymbol{C}) \, C_i^{l,m} \tag{2.75}$$

$$0 = F_i^{X,p,q}$$

$$= \sum_{l,m} (-\omega_i^2) \, K_{C,1}^{p,q,l,m} \, C_i^{l,m} - f_i^{p,q}(\boldsymbol{C}) + \sum_{l,m} K_{D,2}^{p,q,l,m}(\boldsymbol{C}) \, D_i^{l,m}, \tag{2.76}$$

where $K_{C,1}^{p,q,l,m}$, $K_{D,1}^{p,q,l,m}$, $K_{C,2}^{p,q,l,m}$, $K_{D,2}^{p,q,l,m}$, and $f_i^{p,q}$ are given by

$$K_{C,1}^{p,q,l,m} = K_{D,1}^{p,q,l,m}$$

$$= -LM_{l,m}(u_{k,p}^e, v_{k,q}^e) \tag{2.77}$$

$$K_{C,2}^{p,q,l,m} = K_{D,2}^{p,q,l,m}$$

$$= \left[(d_v + v_k^e)\frac{\partial LM_{l,m}}{\partial u_k^e} + \frac{\partial LM_{l,m}}{\partial v_k^e}(-\omega_k^2(d_u + u_k^e) + f_k) \right]_{(u_k^e = u_{k,p}^e, v_k^e = v_{k,q}^e)} \tag{2.78}$$

$$f_i^{p,q} = f_i \big|_{(u_k^e = u_{k,p}^e, v_k^e = v_{k,q}^e)} . \tag{2.79}$$

Note that the algorithm used to solve equations (2.75) and (2.76) can be developed in the same manner as the one described above.

CHAPTER 3

Finite-Element-Based Nonlinear Modal Reduction of a Rotating Beam with Large-Amplitude Motion

3.1 Introduction

The dynamic analyses of helicopter blades, turbopropeller blades, wind-turbine blades and robotic arms has provided motivation for investigations of the vibration of rotating beams. To predict the dynamic characteristics of rotating flexible structures, the kinematics must be carefully modeled, which leads to nonlinear coupling effects between degrees of freedom (DOF) in different directions. These coupling effects can cause slow modal convergence, thereby often requiring large system models for accurate dynamic representation. Simulation of such large-scale models is a time consuming process, which slows parametric studies and design cycles.

Much work has been done using finite elements (FE) to model the nonlinear, large amplitude vibrations of rotating beams, including [44], [45], [46], [47], [48], and [49]. These models are typically quite complicated due to their geometry, degrees of freedom (flap, lead-lag, axial, and torsion), and nonlinear coupling effects. Furthermore, because of the nature of the finite element approach, many elements are required in order to obtain an accurate model.

A common approach is to use linearization of the finite element model about the nonlinear static equilibrium position and solve the eigenvalue problem of the resulting linearized model to obtain the linear natural frequencies of the system ([44] and [49]). Bauchau and Hong ([45]) also utilized finite elements in time to obtain nonlinear responses and stability results of the rotating beam undergoing large deflections. However, the computational time associated with obtaining the equilibrium solution was expensive, because all the spatial degrees of freedom at all time steps are coupled. Perturbation modes ([50] and [51]) were applied to the finite element model of a helicopter rotor blade in order to obtain a reduced order model ([46]). Bauchau and Bottasso ([52]) applied perturbation modes to the space-time finite element model of a beam subjected to a sinusoidal load in order to obtain a reduced order model. Crespo da Silva ([53]) utilized a truncated set of eigenfunctions or eigenvectors obtained from the linearized system of partial differential equations (PDEs) or the linearized finite element model about the nonlinear static equilibrium position in order to obtain a reduced order model of a beam in planar motion. Crespo da Silva ([54]) also extended his work to handle multi-beam structures in planar motion. In most nonlinear structures, there is no simple expansion of basis vectors which decouples the DOF (i.e., modes) in the frequency range of interest from those outside that range. Therefore, some (potentially important) nonlinear effects will be ignored in the truncation process. Generally, many linear modes must be retained in the nonlinear model in order to minimize these effects.

Over the past decade, systematic procedures have been developed to obtain reduced order models (ROM) via nonlinear normal modes (NNM) that are based on invariant manifolds in the state space of nonlinear systems ([20], [21], and [74]). These procedures initially used asymptotic series to approximate the geometry of the invariant manifold and have been used to study the nonlinear rotating Euler-Bernoulli Beam ([3]). More recent work has employed a numerically-based Galerkin approach to obtain the geometry of the NNM invariant manifolds out to large amplitudes ([33]). These procedures can be applied to more general nonlinearities over wider amplitude ranges, and have been recently applied to study the vibrations of a rotating Euler-Bernoulli beam ([34]). In that study, the system

of PDEs governing the axial and transverse motions of the nonlinear rotating beam are derived by Hamilton's principle and discretized by a Rayleigh-Ritz method. These PDEs are similar to those in [86], which were derived by Newtonian methods.

The study presented here uses the same PDE model considered in [34]. However, in this study we use Hamilton's principle as a basis for deriving a nonlinear finite element model of the rotating beam. The primary goal of this effort is to demonstrate that the invariant manifold NNM approach can interface with nonlinear FE models, thereby opening the door to the application of the approach to systems with more complex geometries and additional degrees of freedom (e.g., lead-lag and torsion).

This chapter is outlined as follows. The nonlinear FE model is first generated and converted into a truncated (but still large-scale) modal form that is convenient for the NNM analysis. The invariant manifold equations are formulated, and a numerical collocation method is used to obtain the solution of the NNM invariant manifold for the fundamental flapping mode of the beam. This invariant manifold is used to construct a nonlinear single DOF ROM, which is subsequently used for a simulation study. The linear natural frequencies of the transverse motion, obtained by solving the eigenvalue problem of the linearized FE model, are verified against analytical solutions from [1] and [2]. A study is also carried out to determine the size of an appropriate reference model for the full nonlinear system, which is used for comparisons with the ROM. Detailed results for the fundamental nonlinear flapping mode form the bulk of the numerical results, including the amplitude-frequency relationship, the nature of the NNM invariant manifold, the associated master-slave modal relations, and the actual beam dynamics. In all cases, the results obtained from the ROM are checked against the full reference model, and against the collocation-based ROM determined in [34]. Some conclusions are drawn at the end of the chapter.

3.2 Rotating Blade Formulation

A dynamic model for the vibrations of a uniform, cantilevered, Euler-Bernoulli beam, attached to a rigid rotating hub is considered. The system is schematically shown in Figure 3.1. In the formulation, the following assumptions are made: rotary inertia is neglected; the motion is restricted to axial and transverse vibrations in a rotating plane, i.e., twist and lead-lag motions are not considered; and, the nonlinear axial strain due to element extension is included *. A finite element approach is adopted, which is based on the element kinetic energy, T, and the element potential energy, U which are expressed as follows,

$$T = \frac{1}{2} \int_{x_e}^{x_e+1} m(\dot{u}^2 + \dot{w}^2) + m\Omega^2(h + x + u)^2 dx \tag{3.1}$$

$$U = \frac{1}{2} \int_{x_e}^{x_e+1} EI(w_{,xx})^2 + EA(u_{,x} + \frac{1}{2}(w_{,x})^2)^2 dx \tag{3.2}$$

where $u(x,t)$ and $w(x,t)$ are the axial and transverse displacements, respectively, $(\cdot)_{,x}$ is a derivative with respect to the spatial variable x, an overdot represents a time derivative, h is the hub radius, Ω is the constant angular velocity of the hub/beam, m is the beam mass per unit length, E, A, I are the usual beam material and geometric parameters, and x_e and x_{e+1} are the global coordinates at nodes e and $e+1$, respectively, of a typical element. By applying Hamilton's principle to these two expressions, the weak formulation for the equations of motion is obtained:

---

*Note that other sources of nonlinearity, such as finite curvature effects, while potentially significant in magnitude, are not considered here, since our primary interest is the axial/transverse coupling.

$$\int_{t_1}^{t_2} \int_{x_e}^{x_{e+1}} \quad [-m\ddot{u} + m\Omega^2(h + x + u)]\delta u + [-m\ddot{w}]\delta w +$$

$$[-EA(u_{,x} + \tfrac{1}{2}(w_{,x})^2)](\delta u_{,x} + w_{,x}\delta w_{,x}) +$$

$$[-EIw_{,xx}]\delta w_{,xx} \quad dxdt = 0. \tag{3.3}$$

A finite element model of the simplified rotorcraft blade is developed by introducing following expansions into the weak formulation

$$u^e(x,t) \approx \sum_{i=1}^{2} \phi_i(x)u_i(t) \qquad w^e(x,t) \approx \sum_{i=1}^{4} \psi_i(x)s_i(t) \tag{3.4}$$

where u^e and w^e are u and w restricted to the spatial domain of element e, $\phi_i(x)$ are standard linear shape functions, $u_i(t)$ are nodal variables for axial displacements, $\psi_i(x)$ are standard cubic shape functions, and $s_i(t)$ are nodal variables for transverse displacements and rotation angles. By substituting these approximations into the weak formulation, one obtains the linear element mass and stiffness matrices, the force vector due to rotational effects, and the quadratic and cubic nonlinear force vectors, for both axial and transverse deflections. These are given by the following expressions:

$$m_{ij}^u = \int_{x_e}^{x_{e+1}} m\phi_i(x)\phi_j(x) \ dx, \tag{3.5}$$

$$k_{ij}^u = \int_{x_e}^{x_{e+1}} (EA\frac{d\phi_i}{dx}\frac{d\phi_j}{dx} - m\Omega^2\phi_i(x)\phi_j(x)) \ dx, \tag{3.6}$$

$$f_i^u = \int_{x_e}^{x_{e+1}} m\Omega^2(h+x)\phi_i(x) \ dx, \tag{3.7}$$

$$g_i^u = \sum_{l=1}^{4}\sum_{n=1}^{4} a_{iln}^u s_l s_n, \tag{3.8}$$

$$\text{where} \quad a_{iln}^u = \int_{x_e}^{x_{e+1}} \frac{1}{2}EA\frac{d\phi_i}{dx}\frac{d\psi_l}{dx}\frac{d\psi_n}{dx} \ dx, \tag{3.9}$$

$$\text{and} \quad m_{kl}^s = \int_{x_e}^{x_{e+1}} m\psi_k(x)\psi_l(x) \ dx, \tag{3.10}$$

$$k_{kl}^s = \int_{x_e}^{x_{e+1}} EI\frac{d^2\psi_k}{dx^2}\frac{d^2\psi_l}{dx^2} \ dx, \tag{3.11}$$

$$g_k^s = \sum_{l=1}^{4}\sum_{m=1}^{2} a_{klm}^s s_l u_m, \tag{3.12}$$

$$\text{where} \quad a_{klm}^s = \int_{x_e}^{x_{e+1}} EA\frac{d\psi_k}{dx}\frac{d\psi_l}{dx}\frac{d\psi_m}{dx} \ dx, \tag{3.13}$$

$$\text{and} \quad h_k^s = \sum_{l=1}^{4}\sum_{n=1}^{4}\sum_{r=1}^{4} b_{klnr}^s s_l s_n s_r, \tag{3.14}$$

$$\text{where} \quad b_{klnr}^s = \int_{x_e}^{x_{e+1}} \frac{1}{2}EA\frac{d\psi_k}{dx}\frac{d\psi_l}{dx}\frac{d\psi_n}{dx}\frac{d\psi_r}{dx} \ dx, \tag{3.15}$$

where the indices take on values as follows $\{i = 1,2\}$, $\{j = 1,2\}$, $\{k = 1,2,3,4\}$, $\{l = 1,2,3,4\}$, $\{m = 1,2\}$, $\{n = 1,2,3,4\}$, and $\{r = 1,2,3,4\}$. $(\cdot)^u$ denotes quantities in the u direction. m_{ij}^u is the ij component of the linear axial mass matrix, k_{ij}^u is the ij component of the linear axial stiffness matrix, f_i^u is the i component of the axial force vector, g_i^u is the i component of the quadratic nonlinear axial force vector, and a_{iln}^u is the ln quadratic nonlinear coefficient of g_i^u. $(\cdot)^s$ denotes quantities in the s direction. m_{kl}^s is the kl component of the linear transverse mass matrix, k_{kl}^s is the kl component of the linear transverse stiffness matrix, g_k^s is the k component of the quadratic nonlinear transverse force vector, a_{klm}^s is the lm quadratic nonlinear coefficient of g_k^s, h_k^s is the k component of

90

the cubic nonlinear transverse force vector, and b^s_{klnr} is the lnr cubic nonlinear coefficient of h^s_k.

M one-dimensional beam elements are used and assembled using standard procedures ([87]). Since there are three degrees of freedom at each node, and accounting for the boundary conditions, one obtains $3M$ nonlinear equations of motion in the nodal coordinates, which can be expressed as follows:

$$M^U \ddot{U} + K^U U + G^U(S) \;=\; F_\Omega \tag{3.16}$$

$$M^S \ddot{S} + K^S S + G^S(U, S) + H^S(S) \;=\; 0 \tag{3.17}$$

where U is the global axial displacement vector and S contains the global transverse displacement W and rotation angle vectors Θ. Quantities in the U direction are denoted $(\cdot)^U$, as follows: M^U and K^U are the linear axial global mass and stiffness matrices, respectively, and $G^U(S)$ is the quadratic nonlinear axial global force vector. F_Ω is the axial global force vector due to rotational effects. Quantities in the S direction are denoted by $(\cdot)^S$, as follows: M^S and K^S are the linear transverse global mass and stiffness matrices, respectively, and $G^S(U, S)$ and $H^S(S)$ are the quadratic and cubic nonlinear transverse global force vectors, respectively.

To include rotational effects in the transverse stiffness K^S, thus accounting for centrifugal stiffening, the axial displacement U is separated into static and dynamic components, as follows:

$$U = U_s + U_d \tag{3.18}$$

where U_s is the "static" axial blade deflection due to F_Ω and U_d is the dynamic axial displacement relative to U_s. U_s is obtained by solving for the axial deformation in the case of no vibration in either the transverse or axial directions, i.e.,

$$K^U U_s = F_\Omega, \tag{3.19}$$

where $G^U(0) = 0$ has been used.

Figure 3.2 depicts the comparison between U_s obtained by a 182-element model and an analytical solution ([3]), indicating very close agreement. (In fact, good agreement can be achieved with as few as five elements for this simple shape.)

Substituting equation (3.18) into equations (3.16) and (3.17) offers a convenient form of the equations of motion. A linear transverse stiffness term in S, $K_q(U_s)$, which arises from rotational effects, can be separated out from $G^S(U, S)$. This represents the linear transverse centrifugal stiffening due to rotation, which is combined with K^S to provide the total transverse stiffness. Also, the rotational force vector is cancelled by using equation (3.19). The finite element model then takes the form:

$$M^U \ddot{U}_d + K^U U_d + G^U(S) = 0 \tag{3.20}$$

$$M^S \ddot{S} + (K^S + K_q)S + G^S(U_d, S) + H^S(S) = 0. \tag{3.21}$$

These equations have the form desired for the application of modal analysis. In particular, they have a zero solution, $(U_d, S) = (0, 0)$. Equations (3.20) and (3.21) are then rearranged such that the nodal variables at each node are grouped together, resulting in the following equations of motion in (finite element) physical coordinates:

$$M\ddot{X} + KX + G(X) + H(X) = 0 \tag{3.22}$$

where

$$X = [U_{d.2}\ W_2\ \Theta_2|...|U_{d.M+1}\ W_{M+1}\ \Theta_{M+1}]^T. \tag{3.23}$$

These equations of motion are next transformed into linear modal coordinates and truncated using the following coordinate transformation:

$$X = \Phi\,\eta \tag{3.24}$$

where the $3M \times Q$ matrix Φ is the collection of transverse and axial normal modes of interest of the linearized rotating beam. Here $Q = N_t + N_a$ is the number of kept modes, where N_t is the number of kept transverse (flapping) modes and N_a is the number of kept axial modes. This truncation is used to remove unreliable linear modes from the full finite element model. The model is still relatively large and is to be ultimately reduced to a single DOF. The component form of the equations of motion in these linear modal coordinates is given by

$$\ddot{\eta}_n + \omega_n^2\,\eta_n + \sum_{j=1}^{Q}\sum_{k=1}^{Q}\alpha_{njk}\,\eta_j\,\eta_k + \sum_{j=1}^{Q}\sum_{k=1}^{Q}\sum_{l=1}^{Q}\beta_{njkl}\,\eta_j\,\eta_k\,\eta_l = 0 \tag{3.25}$$

$$\text{for } n = 1,2,3,...,Q$$

93

where ω_n are the natural frequencies associated with the nth mode, α_{njk} are the coefficients of the jk quadratic nonlinear terms associated with the nth mode, and β_{njkl} are the coefficients of the jkl cubic nonlinear terms associated with the nth mode. The formulae for α_{njk} and β_{njkl} can be found in Appendix 3. The determination of these nonlinear coefficients has been computationally automated using the finite element formulation and the coordinate transformations outlined above.

3.3 Modal Reduction

3.3.1 Galerkin-based Invariant Manifold Approach

Typically, one is interested in the dynamics of modes that exhibit large amplitudes and/or lie in a certain frequency range, but not in the response of all system modes. To obtain an accurate ROM of a system of coupled nonlinear ODEs, one should not simply truncate the linear modes that lie outside the frequency range of interest. The contribution of the truncated modes can have important effects and should be accounted for in the ROM in order to accurately represent the dynamics of the system. The nonlinear model reduction approach based on NNM is a systematic procedure that accounts for the contributions of all linear modes to the NNM of interest, without the direct dynamic simulation of these linear modes. It does so by slaving the linear modes to the dynamics of the NNM of interest in a particular manner. The ROM obtained by this procedure can be made to be very accurate over a large amplitude range if one can accurately construct the invariant manifold corresponding to the NNM of interest. This has been accomplished by Pesheck et al. ([34]), by making use of a Galerkin-based numerical approach to solve the invariant manifold equations. This approach was applied to the rotating beam problem, where a Raleyigh-Ritz approach was used to create a discretized dynamic model of the blade ([34]). Some results from that paper are used for comparisons in the present work.

94

A brief summary of the invariant manifold procedure is reviewed here. It is followed by a description of a solution approach for the invariant manifold equations that is based on collocation methods, which offers some advantages in terms of computational efficiency.

From equation (3.25), the mode of interest, i.e., the master mode, is taken to be the mth mode. This linear mode is to be extended in order to generate the corresponding NNM. The generalized master modal position and velocity, η_m and $\dot{\eta}_m$, are expressed in terms of a master mode amplitude, a, and phase, ϕ, using the coordinate transformation

$$\eta_m = a \cos(\phi) \tag{3.26}$$

$$\dot{\eta}_m = -a \omega_m \sin(\phi). \tag{3.27}$$

Using these dynamic variables, the equation of motion for the master mode can be expressed as two coupled 1st order ODEs in a and ϕ, as follows,

$$\dot{a} = \frac{-f_m \sin(\phi)}{\omega_m}, \tag{3.28}$$

$$\dot{\phi} = \omega_m - \frac{f_m \cos(\phi)}{a \omega_m}, \tag{3.29}$$

$$\text{where} \quad f_m = -\left(\sum_{j=1}^{Q} \sum_{k=1}^{Q} \alpha_{mjk} \eta_j \eta_k + \sum_{j=1}^{Q} \sum_{k=1}^{Q} \sum_{l=1}^{Q} \beta_{mjkl} \eta_j \eta_k \eta_l \right) \tag{3.30}$$

corresponds to the nonlinear terms in the mth equation of motion, which contain coupling effects from all linear modes. The remaining $Q - 1$ linear modal positions and velocities are slaved to a and ϕ through functions that are to be determined. These are expressed as

95

$$\eta_i \quad = \quad P_i(a, \phi) \tag{3.31}$$

$$\dot{\eta}_i \quad = \quad Q_i(a, \phi) \tag{3.32}$$

for $\quad i = 1, 2, 3, ..., Q, \ i \neq m.$

Equations (3.31) and (3.32) are substituted back into the components of the equations of motion (equation (3.25)) associated with the slaved coordinates. The functions P_i and Q_i are then obtained using a standard invariant manifold approach. The time derivatives are removed from the equations of motion by the chain rule, resulting in the following nonlinear, time-independent, partial differential equations which govern the geometry of the manifold through the functions P_i and Q_i:

$$Q_i \quad = \quad \frac{\partial P_i}{\partial a}(\frac{-f_m \ \sin(\phi)}{\omega_m}) + \frac{\partial P_i}{\partial \phi}(\omega_m - \frac{f_m \ \cos(\phi)}{a \ \omega_m}) \tag{3.33}$$

$$-\omega_i^2 \ P_i + f_i \quad = \quad \frac{\partial Q_i}{\partial a}(\frac{-f_m \ \sin(\phi)}{\omega_m}) + \frac{\partial Q_i}{\partial \phi}(\omega_m - \frac{f_m \ \cos(\phi)}{a \ \omega_m}) \tag{3.34}$$

for $\quad i = 1, 2, 3, ..., Q, \ i \neq m.$

Equations (3.33) and (3.34) are PDEs in the P's and Q's and are solved using an expansion of basis functions. Via a Galerkin projection, each PDE, after the expansion is introduced, is projected onto each basis function. These basis functions are products of selected shape functions in the a and ϕ directions. Since ϕ has period 2π, the shape functions in the ϕ direction are chosen to be a Fourier basis, $\{1, \cos(n\phi), \sin(n\phi)\}$. The shape functions in the a direction are chosen to be piecewise linear segments. The desired domain in the a direction is divided into K small sections, producing annular subdomains given by ϕ

$\in [0, 2\pi]$ and $a \in [a_j, a_j + \triangle a]$. Therefore $P_i(a, \phi)$ and $Q_i(a, \phi)$ can be expressed over the jth interval as:

$$
\begin{aligned}
P_i(a, \phi) &= \sum_{l,n} C_i^{l,n} T_{l,n}(a, \phi) \\
&= \sum_{n=1}^{N_\phi} [C_i^{1,n}(\frac{a - a_j}{\triangle a}) + C_i^{2,n}(1 - \frac{a - a_j}{\triangle a})] \ \cos((n-1)\phi) \quad\quad (3.35) \\
Q_i(a, \phi) &= \sum_{l,n} D_i^{l,n} U_{l,n}(a, \phi) \\
&= \sum_{n=1}^{N_\phi} [D_i^{1,n}(\frac{a - a_j}{\triangle a}) + D_i^{2,n}(1 - \frac{a - a_j}{\triangle a})] \ \sin(n\phi) \quad\quad (3.36)
\end{aligned}
$$

for $\quad i = 1, 2, 3, ..., Q, \ i \neq m$

where the C's and D's are to-be-determined coefficients. (Note that only a particular subset of harmonic functions in ϕ are required for this conservative, gyroscopic system, since it possesses synchronous modes [34].) Equations (3.35) and (3.36) are substituted into the manifold-governing equations, equations (3.33) and (3.34), and each of these is projected onto each basis function using a Galerkin projection over the domain of interest. This leads to:

$$
0 \;=\; \int_{a,\phi} U_{p,q} \left[-a \sum_{l,n} D_i^{l,n} U_{l,n} + \sum_{l,n} C_i^{l,n} \frac{\partial T_{l,n}}{\partial a} \left(\frac{-f_m \; a \; \sin(\phi)}{\omega_m} \right) \right.
$$

$$
\left. + \sum_{l,n} C_i^{l,n} \frac{\partial T_{l,n}}{\partial \phi} \left(a \; \omega_m - \frac{f_m \; \cos(\phi)}{\omega_m} \right) \right] da \; d\phi \tag{3.37}
$$

$$
0 \;=\; \int_{a,\phi} T_{p,q} \left[\omega_i^2 a \sum_{l,n} C_i^{l,n} T_{l,n} - a \; f_i + \sum_{l,n} D_i^{l,n} \frac{\partial U_{l,n}}{\partial a} \left(\frac{-f_m \; a \; \sin(\phi)}{\omega_m} \right) \right.
$$

$$
\left. + \sum_{l,n} D_i^{l,n} \frac{\partial U_{l,n}}{\partial \phi} \left(a \; \omega_m - \frac{f_m \; \cos(\phi)}{\omega_m} \right) \right] da \; d\phi \tag{3.38}
$$

for $\quad i = 1, 2, 3, ..., Q, \; i \neq m$;

$\qquad p = 1, 2$;

$\qquad q = 1, ..., N_\phi$.

Equations (3.37) and (3.38) are a set of $2(Q-1) \times 2 \times N_\phi$ nonlinear equations in the C's and D's. Note that there are K sets of C's and D's, one for each Δa interval. These individual solutions are assembled to construct the invariant manifold over the domain of interest. Once all the expansion coefficients are obtained, the P's and Q's , which are the slaved linear modal positions and velocities, are known functions in terms of the master variables (a, ϕ). These functions dictate how the slaved linear modes must follow the master mode such that the equations of motion are satisfied and the overall motion is invariant. These known functions are used to express f_m in equation (3.28) and equation (3.29) in terms of only a and ϕ, rendering the ROM single degree of freedom oscillator. The key to the invariant manifold approach is that the solutions of this oscillator represent solutions of the full equations of motion for a particular NNM, and they systematically account for the dynamics of the slaved linear modes. The numerical solution of the invariant manifold equations allows one to obtain NNMs that are accurate over a large amplitude range.

3.3.2 Collocation-based Invariant Manifold Approach

The computational cost associated with evaluating and solving equations (3.37) and (3.38) can be quite expensive. To reduce these computational costs, the collocation method has been adopted here ([77]). Instead of projecting each manifold-governing equation onto each basis function, it is instead projected onto a set of *Dirac delta functions* in the master coordinates. This amounts to an approximation of the integrals over the domain, and it leads to:

$$
0 = \int_{a,\phi} \delta(a - a_p, \phi - \phi_{q_1}) \left[-a \sum_{l,n} D_i^{l,n} U_{l,n} + \sum_{l,n} C_i^{l,n} \frac{\partial T_{l,n}}{\partial a} \left(\frac{-f_m \ a \ \sin(\phi)}{\omega_m} \right) \right.
$$
$$
\left. + \sum_{l,n} C_i^{l,n} \frac{\partial T_{l,n}}{\partial \phi} \left(a \ \omega_m - \frac{f_m \ \cos(\phi)}{\omega_m} \right) \right] da \ d\phi \tag{3.39}
$$

$$
0 = \int_{a,\phi} \delta(a - a_p, \phi - \phi_{q_2}) \left[\omega_i^2 a \sum_{l,n} C_i^{l,n} T_{l,n} - a \ f_i + \sum_{l,n} D_i^{l,n} \frac{\partial U_{l,n}}{\partial a} \left(\frac{-f_m \ a \ \sin(\phi)}{\omega_m} \right) \right.
$$
$$
\left. + \sum_{l,n} D_i^{l,n} \frac{\partial U_{l,n}}{\partial \phi} \left(a \ \omega_m - \frac{f_m \ \cos(\phi)}{\omega_m} \right) \right] da \ d\phi \tag{3.40}
$$

for $\quad i = 1, 2, 3, ..., Q, \ i \neq m$;

$\qquad p = 1, 2$;

$\qquad q_1 = 1, ..., N_\phi$;

$\qquad q_2 = 1, ..., N_\phi$,

where $(a_p, \phi_{q_1}) \in [a_j, a_j + \Delta a] \times [0, 2\pi]$ are collocation points associated with $Q_i(a, \phi)$ and $(a_p, \phi_{q_2}) \in [a_j, a_j + \Delta a] \times [0, 2\pi]$ are collocation points associated with $P_i(a, \phi)$. This projection, while an approximation, greatly simplifies the integrals.

3.4 Results

The rotating beam parameters used here are the same as in [34]: $L = 9$ m, $m = 10$ kg/m, $EI = 3.99 \times 10^5$ N·m^2, $EA = 2.23 \times 10^8$ N, $\Omega = 30$ rad/s, and $h = 0.5$ m, which are feasible for a rotor blade with sub-sonic tip velocity. First, the convergence of the linear natural frequencies is considered as the number of elements is varied, and the results are verified with analytical solutions from [1] and [2]. Then the convergence of the nonlinear amplitude-dependent fundamental flapping natural frequency is studied and verified against the reference model and the collocation-based ROM of the model from [34]. Finally, the time response of the ROM of the fundamental flapping NNM is studied and compared with the reference model and the ROM based on results from [34].

3.4.1 Linear System Convergence

The finite-element model of the rotating beam is obtained by the procedures outlined in section 2. There are 8 cases considered: 5, 10, 15, 20, 45, 90, 136 and 182 elements. The linear natural frequencies of the rotating beam are calculated by solving the eigenvalue problem of the linear part of equation (3.22). The first four flapping linear natural frequencies are shown in Figure 3.3 as a function of the number of elements. These natural frequencies are compared with the natural frequencies from table 7 of [1] and from Table 3 of [2]. In [1], the following dimensionless parameters are defined:

$$\alpha = \frac{h}{L}, \quad \eta^2 = \frac{mL^4\Omega^2}{EI}, \quad \tau = \sqrt{\frac{EI}{mL^4}}\, t \tag{3.41}$$

where α is the dimensionless hub radius, η is the dimensionless rotating speed, and τ is the dimensionless time. Since the parameters used here do not fall in the parameter range used in [1] and [2], the frequencies must be extrapolated in η and interpolated in α. The

100

first four linear natural (flapping) frequencies in the τ time scale are presented in Table 3.1. These frequencies are then converted to frequencies in the t time scale and compared with the natural frequencies from the finite-element model in Table 3.2.

From Figure 3.3, it is clear that these four linear natural frequencies quickly converge as the number of elements is increased. In addition, from Table 3.2, the maximum difference between the reference natural frequencies and the natural frequencies from the finite-element model is 0.2%.

3.4.2 Nonlinear Model Development

The finite-element model of the rotating blade generated by M one-dimensional beam elements has $3M$ degrees of freedom (with boundary conditions included). Due to the fact that transverse displacement and element rotation degrees of freedom have the same natural frequencies and mode shapes, the natural frequencies that lie in the frequency range of modes $1.5M - 3M$ may be unreliable ([88]). To be conservative, we consider a frequency range that includes only the first M natural modes (that is, the M with the lowest natural frequencies), and we desire to keep $Q \leq M$ retained modes for our reference model. For this system it has been found that a reliable approach is to maintain an equal ratio of transverse modes to axial modes when reducing from M to Q. If $N_{t,M}$ and $N_{a,M}$ represent the number of transverse and axial modes among the first M modes, respectively, then we take $N_t = N_{t,M} \times (Q/M)$ and $N_a = N_{a,M} \times (Q/M)$ [†]. These Q modes are used in equation (3.24) to arrive at equation (3.25). The procedure outlined in section 3.3.2 is then applied to the model in linear modal coordinates to obtain the single DOF ROM.

In particular, the first linear modal coordinate (first flapping mode) is chosen to be the master mode of interest. The dynamics for this NNM, equations (3.28) and (3.29), are numerically integrated with initial conditions for mode 1 (flapping) amplitude and phase,

---

[†]Since $N_{t,M} + N_{a,M} = M$, then $N_t + N_a = Q$, as desired.

$a(0) = 4.0$ and $\phi(0) = 0$ [‡]. For this amplitude, the NNM frequency is studied as the number of linear modes and the number of elements are varied. For 90, 136, and 182 elements, the number of kept modes (Q) used to generate the frequency data are 15, 21, 27, 33, 39 and 45, respectively [§]. From the frequency data, it found that as the number of elements is increased, the frequency is nearly converged for 182 elements, over a wide range of values of Q. As the the number of kept modes, Q, increases, the frequency decreases. For 182 elements and 45 modes, the frequency differs from the 182 element, 39 mode case by only 0.0375 rad/s. However, it appears that more than 45 kept modes are needed to demonstrate convergence in a convincing manner. At this point, we employ the 45-mode model generated from 182 elements for use as the reference model.

The NNM manifold is obtained from this model over an amplitude range of $a \in [0, 6.0]$, which is generated using 120 piecewise linear manifold segments in a with width $\Delta a = 0.05$, and $N_\phi = 16$ harmonics in ϕ. This amplitude range, in physical terms, corresponds to the beam tip moving with a peak-to-peak amplitude of about 2.4 meters (recall that the beam is 9 meters in length). The single DOF ROM is obtained by restricting the dynamics of the 45 DOF reference model to this invariant manifold. This amounts to restricting the dynamics, which occur in a 90-dimensional state space, to a two-dimensional invariant manifold that is described by the master-slave relations given by the P_is and Q_i's. Note that there are 88 such relations in this case.

Figure 3.4 depicts the natural frequency of the first nonlinear flapping mode as a function of the initial mode amplitude, $a(0)$, with $\phi(0) = 0$. The + line is a result of the ROM (1 DOF) which is generated from the finite element reference model. The ∘ line is a result of the ROM (1 DOF) which is generated from the Rayleigh-Ritz model from [34], using the same N_t and N_a as used in the reference model. The solid line is a result of the full reference model (45 DOF), which is obtained by searching for periodic solutions using a shooting algorithm [¶]. The results from the three models are virtually identical over this

---

[‡]This amplitude corresponds to the beam having a peak-to-peak tip vibration amplitude of 1.59 meters.
[§]Due to computer memory limitations, the maximum number of kept modes we can achieve is 45.
[¶]Note that all modal solutions based on the reference model require use of this shooting algorithm.

102

amplitude range.

3.4.3 System Response

We now have a single DOF ROM (equations (3.28) and (3.29)), which is generated from 182 elements and 45 kept modes. This ROM is simulated with initial modal amplitude $a(0) = 5.9$ and phase $\phi(0) = 0$, and the result is shown as the dashed line in Figure 3.5. This Figure can be geometrically interpreted as the projection of the motion that occurs on the NNM manifold onto the linear eigenspace of the first linear flapping mode. This numerical solution is verified against the numerical solution of the ROM from [34] with the same initial conditions, which is shown as a dotted line. These two solutions are nearly identical.

Figure 3.6 depicts the corresponding time responses of the NNM displacement η_1 obtained from three different models. The dashed line is the time response of the ROM obtained by applying equation (3.26) to the numerical solution shown in Figure 3.5. Obtained by applying the same procedures, the dotted line is the time response of the ROM from [34], while the solid line is the time response of the reference model (45 DOF) initiated on the NNM manifold. These three responses are nearly identical.

Figure 3.7 depicts one of the attendant master-slave-constraint relations, specifically the second linear flapping mode displacement as a function of the NNM amplitude (a) and phase (ϕ). Note that solutions of the ROM are used to obtain (a, ϕ), after which the second linear flapping mode displacement is obtained by the corresponding trace on this surface. Of course, there are 87 other such surfaces, 43 more slaved displacements and 44 slaved velocities, for the linear modes. Note also that the contribution of this (and all) linear mode(s) start at zero at $a = 0$ and increase in amplitude as a increases.

Figure 3.8 depicts the time response for the second linear flapping mode displacement

obtained from the ROM, the ROM from [34], and the reference model. The dashed line is obtained by applying the master-slave constraint (depicted in Figure 3.7) to the numerical solution of the ROM (the dashed line in Figure 3.5). The dotted line is obtained by applying the master-slave constraint from [34] (which is similar to Figure 3.7 but is not shown here) to the numerical solution of the ROM from [34] (the dotted line in Figure 3.5). The solid line is obtained from the 45 DOF reference model. Again, the results are virtually identical, demonstrating that the invariant manifold accurately captures the effects of higher linear modes.

Further sample results are shown in Figure 3.9, Figure 3.11, and Figure 3.13, which depict the master-slave constraint relations for the tenth flapping mode, the first axial mode, and the twelfth axial mode, respectively. Associated with these are Figure 3.10, Figure 3.12, and Figure 3.14, which are similar in nature to Figure 3.8, and depict the slaved time responses for the tenth flapping mode, the first axial mode, and the twelfth axial mode, respectively. In all cases the NNM manifold accurately captures the contributions from these linear modes. It is interesting to note that the first linear axial mode makes a significant contribution to the fundamental flapping NNM, thus demonstrating the importance of the nonlinear axial/transverse coupling.

The 88 master-slave-constraint relations will generate the NNM manifold for the first non-linear flapping mode in the 90-dimensional state space. From Figure 3.7 through Figure 3.14, we see that the responses of the slaved linear flapping modes have the same fundamental frequency, as that of the NNM. However, the axial modes move at twice the frequency of the NNM. This arises from the physics of the beam motion, and is discussed below.

Figure 3.15 depicts time responses of the beam-tip transverse deflection obtained from the present ROM, the ROM from [34], and the reference model. The dashed line is obtained by applying equation (3.24) to the time responses of the linear flapping and axial modes of the ROM, and plotting the result for the transverse deflection of the end node of the beam. Obtained by applying the same procedures, the dotted line is the result from the ROM from

[34], and the solid line is the result from the reference model. Note that three responses are very close and correspond to a tip-to-tip deflection of 2.34 meters. The discrepancy in amplitude is, we believe, related to convergence difficulties with the Rayleigh-Ritz approach near the beam tip [3].

Figure 3.16, Figure 3.17, and Figure 3.18 depict the spatial nature of the transverse, angle, and axial motions of the beam in the NNM response for the same initial conditions as the previous Figures. They represent the motion starting from $t = 0$ up to a quarter of the period of the NNM. The time intervals between each deflection curve are equal. The bottom curves of Figure 3.16 and Figure 3.18 and the top curve of Figure 3.17 are at the initial time, corresponding to the peak NNM amplitude. The top curves of Figure 3.16 and Figure 3.18 and the bottom curve of Figure 3.17 are one quarter-period later. The dashed line in Figure 3.18 (close to the top curve in the Figure) is the static axial extension u_s due to rotation of the beam. At the initial time, the beam experiences axial foreshortening due to nonlinear effects through the transverse deflection, as can be seen by the negative axial displacements in Figure 3.18. At the quarter period, the transverse deflection is at zero, and the beam does not experience axial foreshortening, but deforms axially due to centrifugal loads. Note that during the first quarter-period, the transverse and angle responses go through a quarter-period of the periodic oscillation, but the axial response goes through one half of its full oscillation. This is due to the symmetry of the axial response about the zero transverse and angle deflections condition, that is, the axial foreshortening is the same for $-w$ and $-\theta$ as for $+w$ and $+\theta$. This is why the axial motion has twice the frequency of the transverse and angle motions.

By combining the transverse deflection from Figure 3.16 and the axial deflection from Figure 3.18, the deformed shape of the rotating beam on the first nonlinear mode manifold can be generated. Due to the small scale of the axial motions, the beam shape will be very close to the shapes shown for the transverse deflection (this is not true at all amplitudes, but is a very good approximation here). It is important to note that the shape of the beam changes in a periodic manner through the course of the NNM motion. This is due to the

contributions from the slaved linear modes, which are not fixed, but vary in time according to the NNM invariant manifold. This is in distinct contrast to more typical reduction methods in which the equations of motion are projected onto a single mode shape, resulting in a response during which the shape of the beam remains the same throughout the course of the motion.

3.4.4 Computational Considerations

An important issue related to this procedure is that of computational time. As a comparison, we consider here the relative times used to generate the invariant manifold solution and run simulations on it with those of generating the manifold using a shooting technique. It takes about 1,600 seconds to generate one strip of the manifold, yielding a total of about 192,000 seconds to generate the manifold. This is not trivial, but with the manifold in hand, a simulation for a set of initial conditions takes under 500 seconds for about two periods of response. In contrast, if one generates the manifold directly by using a shooting technique to find the correct initial conditions, each strip takes nearly 8,400 seconds to generate, a factor of five higher. And, note that this approach uses the master-slave relations as starting points for the shooting technique, which are not generally available, making this result quite conservative.

When parametric studies are required, it is possible that the ROM using invariant manifold techniques can be extended to handle the situation. A proposed approach is to augment the system by considering the parameters of interest as elements of the master mode coordinates. This is the so-called "suspension trick" ([89]). By this approach, the single nonlinear mode manifold of interest will also be a function of the parameters of interest. Hence, the computational cost of solving the invariant manifold does not become a recurring cost when the parameters of interest are changed, however the initial cost of generating the "suspended" manifold will be higher. This should be feasible and efficient for a single parameter.

3.5 Conclusions

In this chapter, the problem of obtaining nonlinear single-mode ROMs from a finite element formulation of a rotating beam was addressed using NNMs. Accurate simulations of this system typically require many DOF, due to the nonlinear coupling effects between axial and transverse deflections. The problem of obtaining accurate ROM was solved using invariant manifold-based NNMs. The ROMs obtained govern the dynamics of the NNM of interest (the master mode), and the approach allows one to accurately capture the dynamics of the slaved linear modes. Hence, only a single nonlinear oscillator is required for accurate simulation of the NNM out to large amplitudes. The numerical solution of the NNM invariant manifold equations was facilitated by employing a collocation method. Excellent agreement was found for the dynamics of the fundamental flapping mode of the beam, by comparing results from the single DOF ROM obtained here with the single DOF ROM based on a Rayleigh-Ritz discretization ([34]) and a full 45 DOF reference model. The method can be similarly applied to any mode of interest, and can be generalized to include dissipation effects, both linear and nonlinear.

The results presented demonstrate significant promise, since they combine procedures from the versatile finite element method with the accurate reduction procedures via numerically generated NNMs. This will allow the NNM method to be applied to the large amplitude vibrations of beams with more complex geometry and more nodal DOF, as required for more realistic models of rotor blades and other structural members. Also, current work on multi-mode manifolds shows promise for developing nonlinear ROM with two DOF in a similar manner.

3.6 Tables

η	$\alpha = 0.06$			
	$\omega1$	$\omega2$	$\omega3$	$\omega4$
12.17	13.8248	38.9163	81.37	142.606

Table 3.1. Dimensionless linear natural frequencies. ω_1 and ω_2 were computed using results from [1]. ω_3 and ω_4 were computed using results from [2].

Ω (rad/s)	$h = 0.5$ m							
	$\omega1$		$\omega2$		$\omega3$		$\omega4$	
	Analy.	FEM	Analy.	FEM	Analy.	FEM	Analy.	FEM
30	34.09	34.03	95.97	95.84	200.67	200.49	351.68	351.49

Table 3.2. Comparison of the linear natural frequencies obtained by power series and finite element methods. The analytical results for ω_1 and ω_2 were computed using results from [1]. The analytical results for ω_3 and ω_4 were computed using results from [2].

3.7 Figures
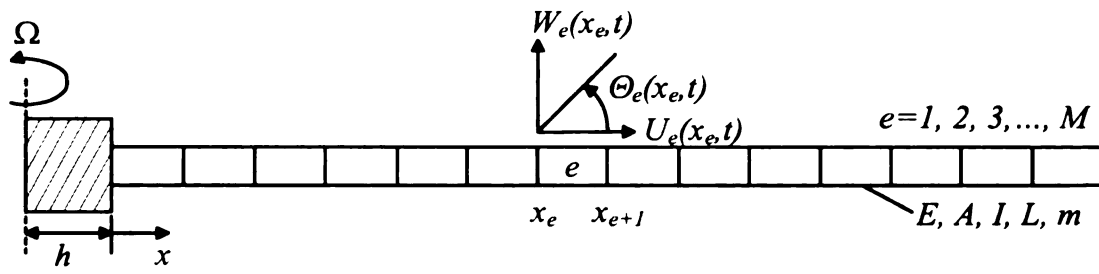
Figure 3.1. Finite element representation of a rotating beam with Ω = constant.
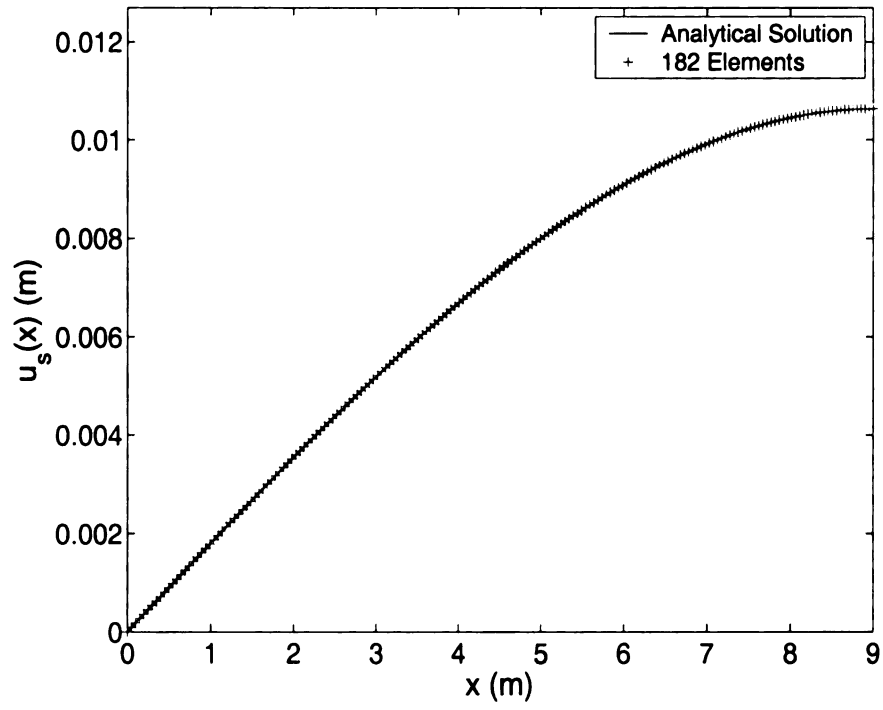
Figure 3.2. Comparison of the static axial blade deflection, u_s, obtained from an analytical solution [3] and by the finite element method.
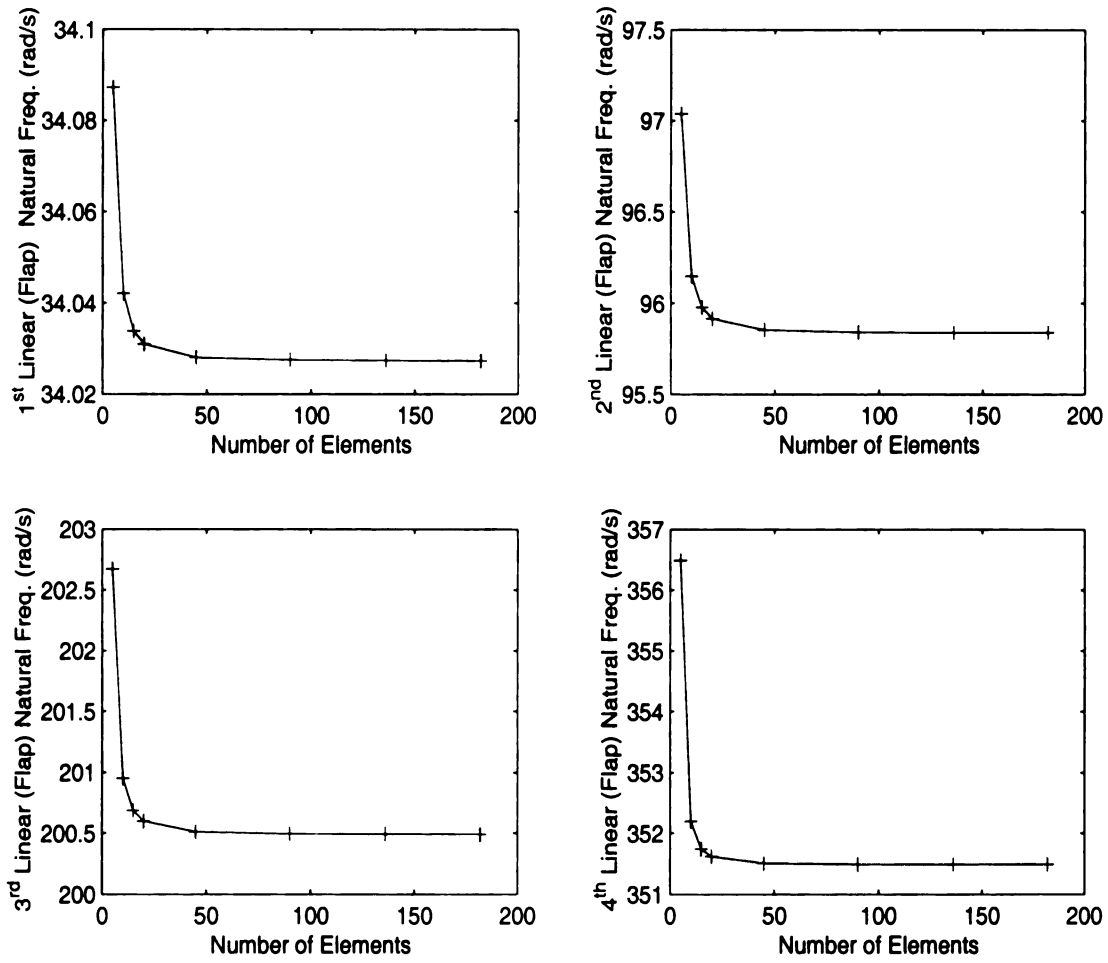
Figure 3.3. Convergence of the first four linear natural frequencies (flapping modes) of the finite element model.
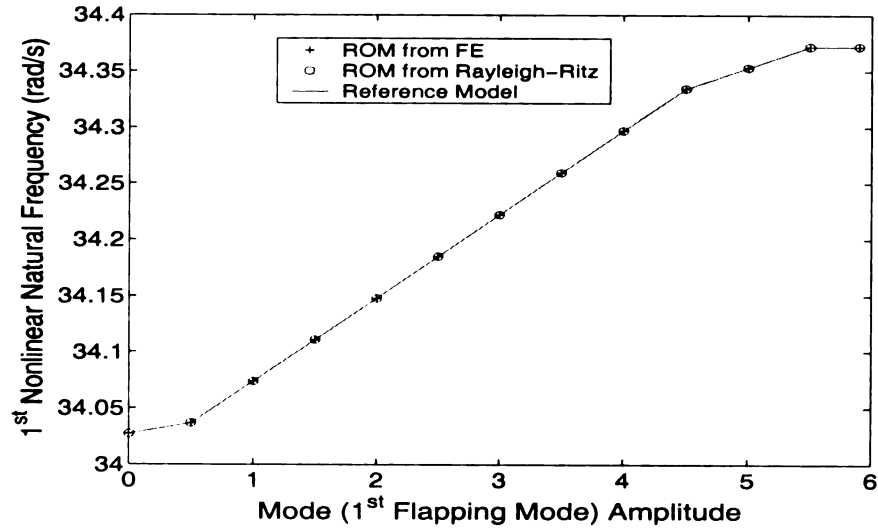
Figure 3.4. The first nonlinear flapping natural frequency as a function of initial mode amplitude $a(0)$ with $\phi = 0$ obtaining using three methods: the FE-based ROM, the Rayleigh-Ritz based ROM, and the reference model (182-element and 45-kept-modes).
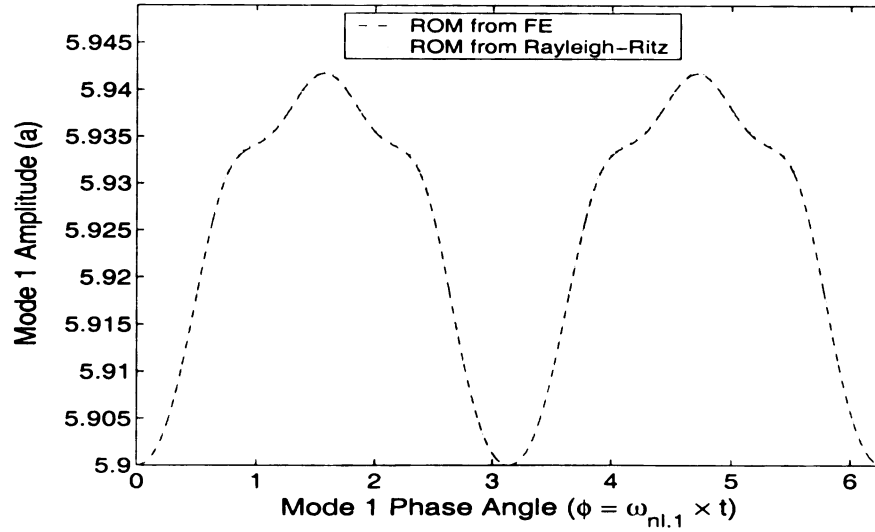
Figure 3.5. The projection of the motion occurring on the first nonlinear flapping mode manifold onto the linear eigenspace of the first linear flapping mode, in amplitude and phase coordinates.
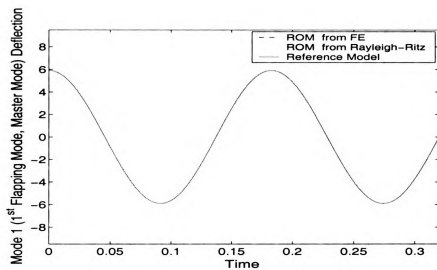
Figure 3.6. The time responses of the first nonlinear flapping mode displacement η_1 for the FE-based ROM, the Rayleigh-Ritz based ROM, and the reference model.
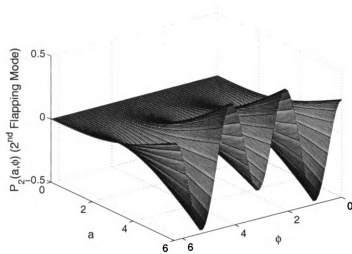
Figure 3.7. The contribution of the second linear flapping mode $\eta_2 = P_2(a, \phi)$ to the first nonlinear mode manifold, solved by the collocation method, as a function of the first nonlinear mode amplitude and phase.
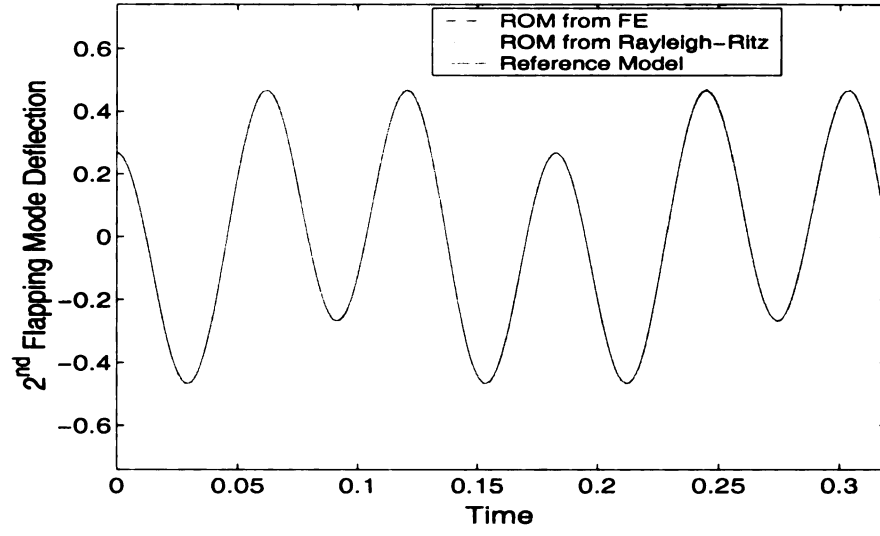
Figure 3.8. The time response of the second linear flapping mode deflection $\eta_2 = P_2(a(t), \phi(t))$ on the first nonlinear mode manifold for the FE-based ROM, the Rayleigh-Ritz based ROM, and the reference model.
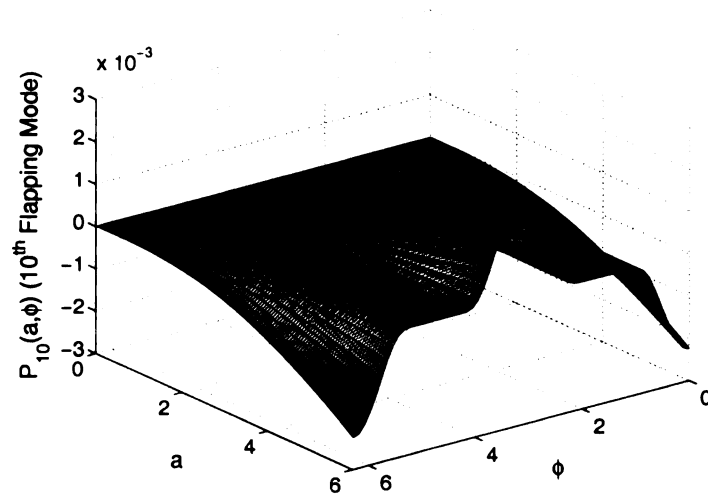
Figure 3.9. The contribution of the tenth linear flapping mode $\eta_{10} = P_{10}(a, \phi)$ to the first nonlinear mode manifold, solved by the collocation method, as a function of the first nonlinear mode amplitude and phase.

114
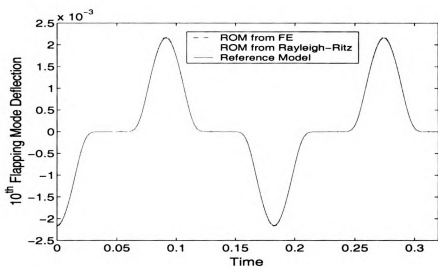
Figure 3.10. The time response of the tenth linear flapping mode deflection $\eta_{10} = P_{10}(a(t), \phi(t))$ on the first nonlinear mode manifold for the FE-based ROM, the Rayleigh-Ritz based ROM, and the reference model.
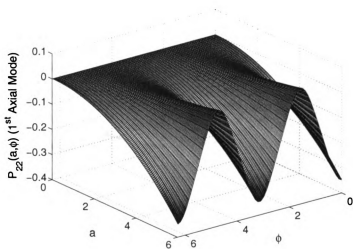
Figure 3.11. The contribution of the first linear axial mode $\eta_{22} = P_{22}(a, \phi)$ to the first nonlinear mode manifold, solved by the collocation method, as a function of the first nonlinear mode amplitude and phase.
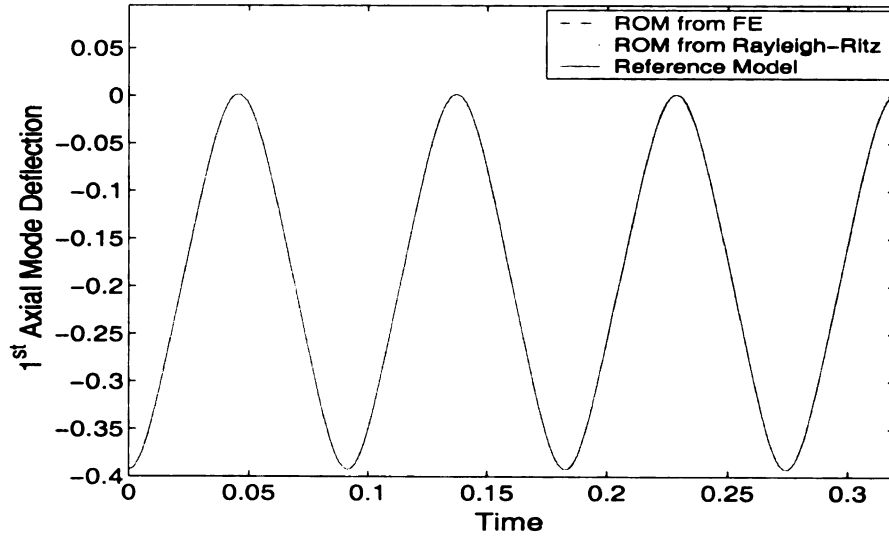
Figure 3.12. The time response of the first linear axial mode deflection $\eta_{22} = P_{22}(a(t), \phi(t))$ on the first nonlinear mode manifold for the FE-based ROM, the Rayleigh-Ritz based ROM, and the reference model.
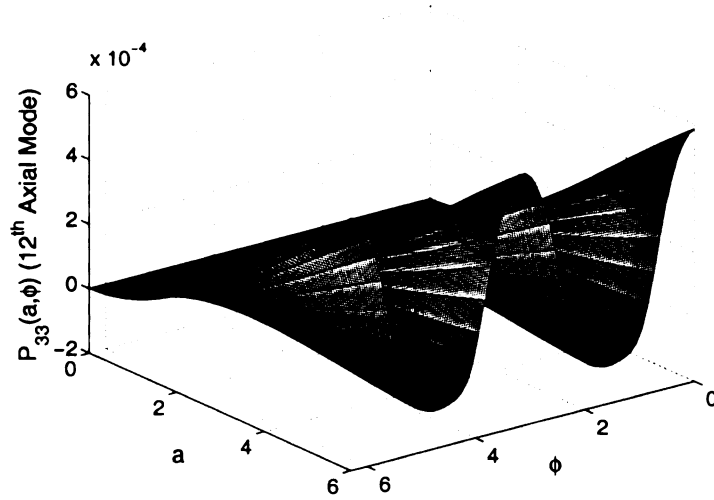
Figure 3.13. The contribution of the twelfth linear axial mode $\eta_{33} = P_{33}(a, \phi)$ to the first nonlinear mode manifold, solved by the collocation method, as a function of the first nonlinear mode amplitude and phase.

116
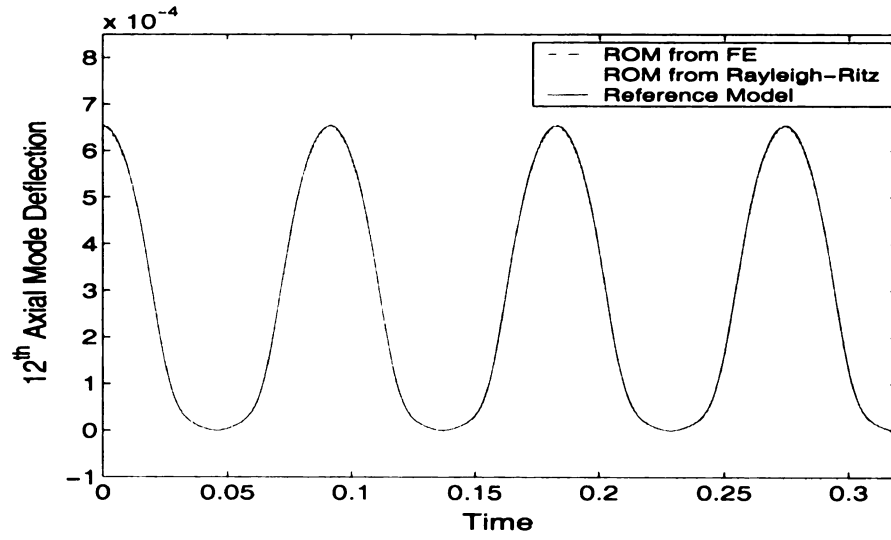
Figure 3.14. The time response of the twelfth linear axial mode deflection $\eta_{33} = P_{33}(a(t), \phi(t))$ on the first nonlinear mode manifold for the FE-based ROM, the Rayleigh-Ritz based ROM, and the reference model.
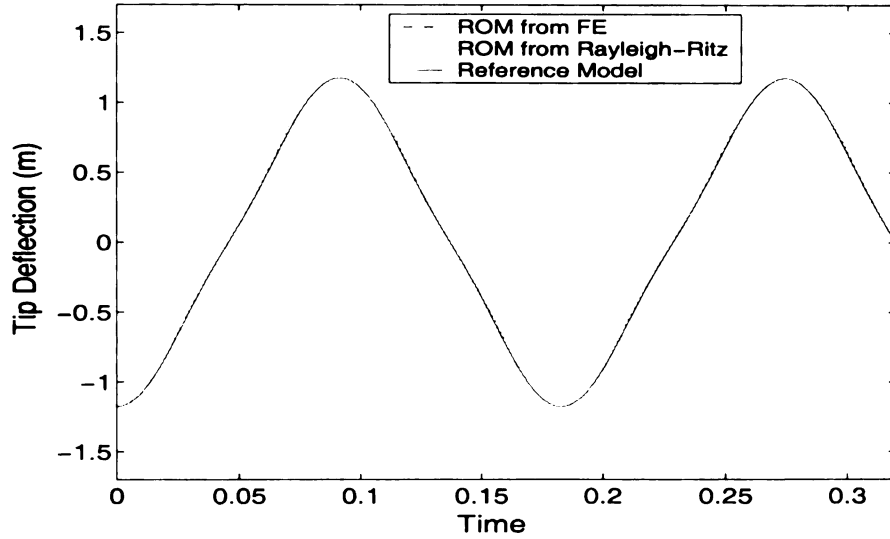
Figure 3.15. The time dependence of the beam-tip transverse deflection, $w(L, t)$, for the FE-based ROM, the Rayleigh-Ritz based ROM, and the reference model.
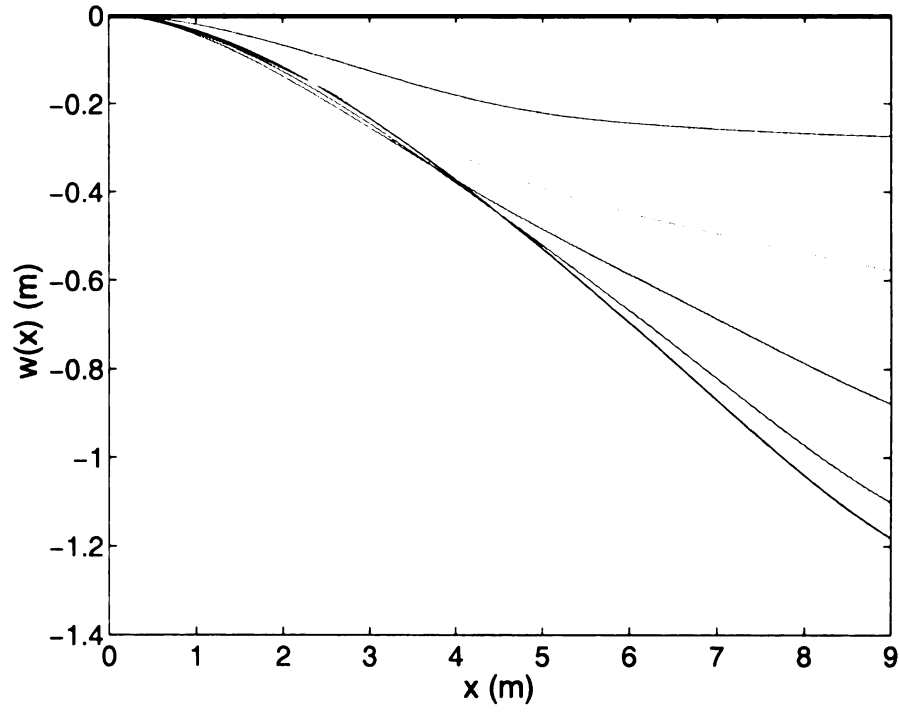
Figure 3.16. Transverse deflection $w(x, t)$ for a quarter-period of motion on the first non-linear mode manifold. The motion starts at the maximum deflection (the bottom curve) and moves as shown to the zero deflection at a quarter-period, after which it moves upward in a symmetric manner about $w = 0$ and then repeats.
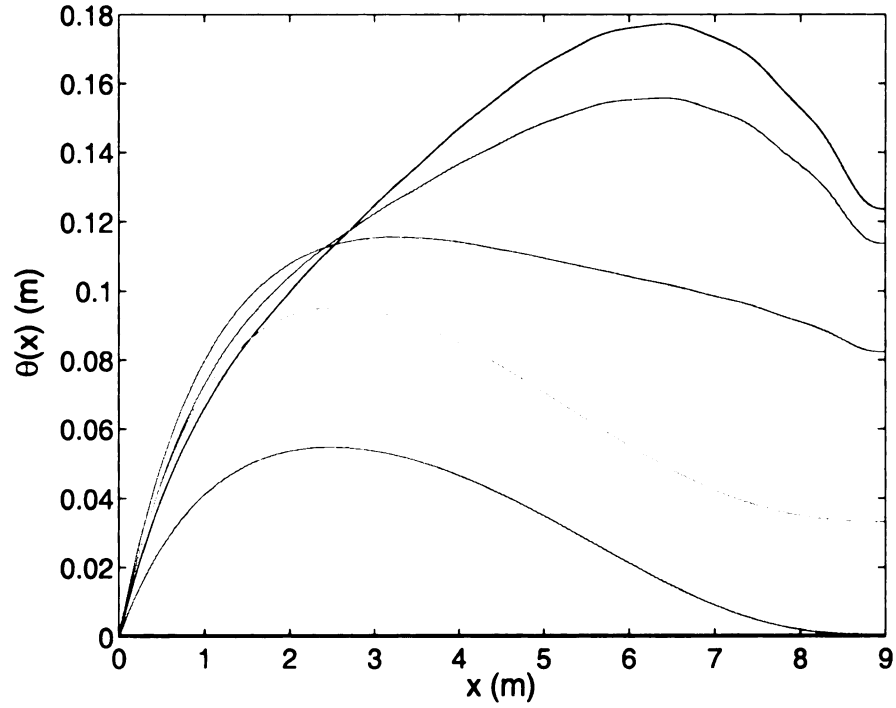
Figure 3.17. Angle deflection $\theta(x, t)$ for a quarter-period of motion on the first nonlinear mode manifold. The motion starts at the maximum deflection (the top curve) and moves as shown to the zero deflection at a quarter-period, after which it moves downward in a symmetric manner about $\theta = 0$ and then repeats.
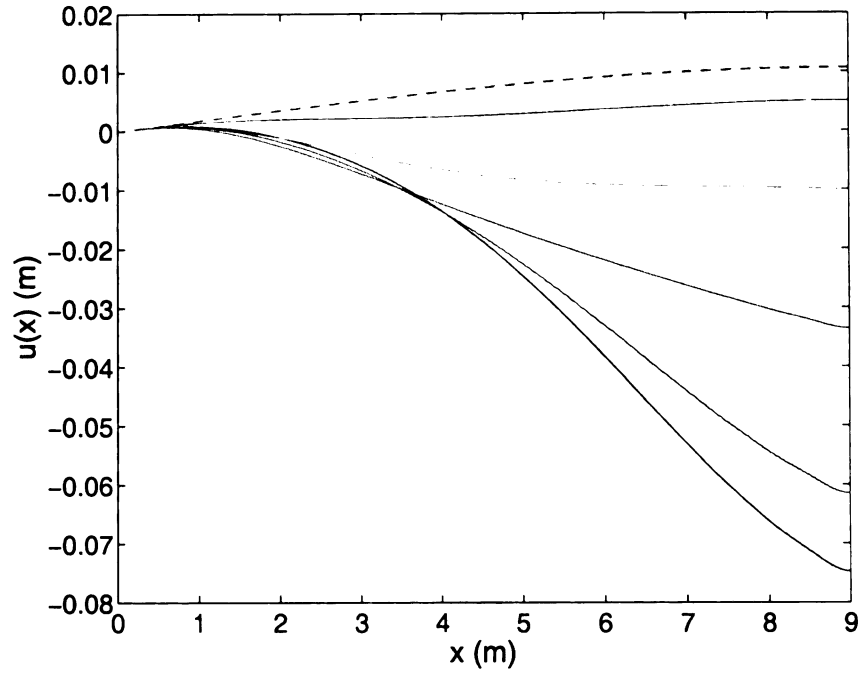
Figure 3.18. Axial deflection $u(x,t)$ for a quarter-period of motion on the first nonlinear mode manifold. The dashed line denotes the static deflection, $u_s(x)$. The bottom curve corresponds to the initial condition. The top curve from Figure 3.16 and the bottom curve from Figure 3.17 correspond to the top $u(x)$ curve here, all at one quarter-period. Note that the axial motion occurs at twice the frequency of the transverse and angle motions, due to symmetry. As time progresses beyond the quarter-period, the axial motion moves downward again, and oscillates between the top and bottom curves shown.

3.8 Appendix 3

The coefficients of the jk quadratic nonlinear terms associated with the nth mode are as follows:

$$\alpha_{njk} = \sum_{e=1}^{M+1} \left(\phi_{(3e-2)n}\, \alpha^U_{ejk} + \phi_{(3e-1)n}\, \alpha^W_{ejk} + \phi_{(3e)n}\, \alpha^\Theta_{ejk} \right) \tag{3.42}$$

$$\{n, j, k = 1, 2, 3, ..., Q\}$$

where ϕ_{ij} is the ij component of the modal matrix in equation (24), and α^U_{ejk}, α^W_{ejk} and α^Θ_{ejk} are:

$$\alpha^U_{ejk} = \sum_{l=1}^{4}\sum_{n=1}^{4} \alpha^U_{elnjk} \tag{3.43}$$

$$\alpha^W_{ejk} = \sum_{l=1}^{4}\sum_{m=1}^{2} \alpha^W_{elmjk} \tag{3.44}$$

$$\alpha^\Theta_{ejk} = \sum_{l=1}^{4}\sum_{m=1}^{2} \alpha^\Theta_{elmjk} \tag{3.45}$$

$$\{e = 1, 2, 3, ..., M+1\};\ \{j, k = 1, 2, 3, ..., Q\}$$

where α^U_{elnjk}, α^W_{elmjk} and α^Θ_{elmjk} are:

$$\alpha^U_{elnjk} = (a^u_{2ln})^{e-1} \phi_{(3e+l-5)j} \phi_{(3e+n-5)k} + (a^u_{1ln})^e \phi_{(3e+l-2)j} \phi_{(3e+n-2)k}$$

$$\{l = 1, 2\}; \{n = 1, 2\}; \{e = 1, 2, 3, ..., M+1\}; \{j, k = 1, 2, 3, ..., Q\}$$

$$= (a^u_{2ln})^{e-1} \phi_{(3e+l-5)j} \phi_{(3e+n-4)k} + (a^u_{1ln})^e \phi_{(3e+l-2)j} \phi_{(3e+n-1)k}$$

$$\{l = 1, 2\}; \{n = 3, 4\}; \{e = 1, 2, 3, ..., M+1\}; \{j, k = 1, 2, 3, ..., Q\}$$

$$= (a^u_{2ln})^{e-1} \phi_{(3e+l-4)j} \phi_{(3e+n-5)k} + (a^u_{1ln})^e \phi_{(3e+l-1)j} \phi_{(3e+n-2)k} \quad (3.46)$$

$$\{l = 3, 4\}; \{n = 1, 2\}; \{e = 1, 2, 3, ..., M+1\}; \{j, k = 1, 2, 3, ..., Q\}$$

$$= (a^u_{2ln})^{e-1} \phi_{(3e+l-4)j} \phi_{(3e+n-4)k} + (a^u_{1ln})^e \phi_{(3e+l-1)j} \phi_{(3e+n-1)k}$$

$$\{l = 3, 4\}; \{n = 3, 4\}; \{e = 1, 2, 3, ..., M+1\}; \{j, k = 1, 2, 3, ..., Q\}$$

$$\alpha^W_{elmjk} = (a^s_{3lm})^{e-1} \phi_{(3e+l-5)j} \phi_{(3e-5)k} + (a^s_{1lm})^e \phi_{(3e+l-2)j} \phi_{(3e-2)k}$$

$$\{l = 1, 2\}; \{m = 1\}; \{e = 1, 2, 3, ..., M+1\}; \{j, k = 1, 2, 3, ..., Q\}$$

$$= (a^s_{3lm})^{e-1} \phi_{(3e+l-5)j} \phi_{(3e-2)k} + (a^s_{1lm})^e \phi_{(3e+l-2)j} \phi_{(3e+1)k}$$

$$\{l = 1, 2\}; \{m = 2\}; \{e = 1, 2, 3, ..., M+1\}; \{j, k = 1, 2, 3, ..., Q\}$$

$$= (a^s_{3lm})^{e-1} \phi_{(3e+l-4)j} \phi_{(3e-5)k} + (a^s_{1lm})^e \phi_{(3e+l-1)j} \phi_{(3e-2)k} \quad (3.47)$$

$$\{l = 3, 4\}; \{m = 1\}; \{e = 1, 2, 3, ..., M+1\}; \{j, k = 1, 2, 3, ..., Q\}$$

$$= (a^s_{3lm})^{e-1} \phi_{(3e+l-4)j} \phi_{(3e-2)k} + (a^s_{1lm})^e \phi_{(3e+l-1)j} \phi_{(3e+1)k}$$

$$\{l = 3, 4\}; \{m = 2\}; \{e = 1, 2, 3, ..., M+1\}; \{j, k = 1, 2, 3, ..., Q\}$$

$$\alpha^{\Theta}_{elmjk} = (a^s_{4lm})^{e-1} \phi_{(3e+l-5)j} \phi_{(3e-5)k} + (a^s_{2lm})^e \phi_{(3e+l-2)j} \phi_{(3e-2)k}$$

$$\{l = 1, 2\}; \{m = 1\}; \{e = 1, 2, 3, ..., M+1\}; \{j, k = 1, 2, 3, ..., Q\}$$

$$= (a^s_{4lm})^{e-1} \phi_{(3e+l-5)j} \phi_{(3e-2)k} + (a^s_{2lm})^e \phi_{(3e+l-2)j} \phi_{(3e+1)k}$$

$$\{l = 1, 2\}; \{m = 2\}; \{e = 1, 2, 3, ..., M+1\}; \{j, k = 1, 2, 3, ..., Q\}$$

$$= (a^s_{4lm})^{e-1} \phi_{(3e+l-4)j} \phi_{(3e-5)k} + (a^s_{2lm})^e \phi_{(3e+l-1)j} \phi_{(3e-2)k} \qquad (3.48)$$

$$\{l = 3, 4\}; \{m = 1\}; \{e = 1, 2, 3, ..., M+1\}; \{j, k = 1, 2, 3, ..., Q\}$$

$$= (a^s_{4lm})^{e-1} \phi_{(3e+l-4)j} \phi_{(3e-2)k} + (a^s_{2lm})^e \phi_{(3e+l-1)j} \phi_{(3e+1)k}$$

$$\{l = 3, 4\}; \{m = 2\}; \{e = 1, 2, 3, ..., M+1\}; \{j, k = 1, 2, 3, ..., Q\}$$

where $(\cdot)^{e-1}$ denotes quantities associated with element $e - 1$, $(\cdot)^e$ denotes quantities associated with element e, and a^u_{iln} and a^s_{klm} are quantities defined by equations (9) and (13), respectively.

The coefficients of the jkl cubic nonlinear terms associated with the nth mode are as follows:

$$\beta_{njkl} = \sum_{e=1}^{M+1} (\phi_{(3e-1)n} \beta^W_{ejkl} + \phi_{(3e)n} \beta^{\Theta}_{ejkl}) \qquad (3.49)$$

$$\{n, j, k, l = 1, 2, 3, ..., Q\}$$

where ϕ_{ij} is the ij component of the modal matrix in equation (24), and β^W_{ejkl} and β^{Θ}_{ejkl} are:

123

$$\beta_{ejkl}^{W} = \sum_{l^*=1}^{4} \sum_{n=1}^{4} \sum_{r=1}^{4} \beta_{el^*nrjkl}^{W} \tag{3.50}$$

$$\beta_{ejkl}^{\Theta} = \sum_{l^*=1}^{4} \sum_{n=1}^{4} \sum_{r=1}^{4} \beta_{el^*nrjkl}^{\Theta} \tag{3.51}$$

$$\{e = 1, 2, 3, ..., M+1\}; \{j, k, l = 1, 2, 3, ..., Q\}$$

where $\beta_{el^*nrjkl}^{W}$ and $\beta_{el^*nrjkl}^{\Theta}$ are:

$$\beta^W_{el^*nrjkl} \tag{3.52}$$

$$= \left[(b^s_{3l^*nr})^{e-1}\,\phi_{(3e+l^*-5)j}\,\phi_{(3e+n-5)k}\,\phi_{(3e+r-5)l}\right.$$
$$\left. +(b^s_{1l^*nr})^e\,\phi_{(3e+l^*-2)j}\,\phi_{(3e+n-2)k}\phi_{(3e+r-2)l}\right]$$

$$\{l^*=1,2\};\ \{n=1,2\};\ \{r=1,2\};\ \{e=1,2,3,...,M+1\};\ \{j,k,l=1,2,3,...,Q\}$$

$$= \left[(b^s_{3l^*nr})^{e-1}\,\phi_{(3e+l^*-5)j}\,\phi_{(3e+n-5)k}\,\phi_{(3e+r-4)l}\right.$$
$$\left. +(b^s_{1l^*nr})^e\,\phi_{(3e+l^*-2)j}\,\phi_{(3e+n-2)k}\phi_{(3e+r-1)l}\right]$$

$$\{l^*=1,2\};\ \{n=1,2\};\ \{r=3,4\};\ \{e=1,2,3,...,M+1\};\ \{j,k,l=1,2,3,...,Q\}$$

$$= \left[(b^s_{3l^*nr})^{e-1}\,\phi_{(3e+l^*-5)j}\,\phi_{(3e+n-4)k}\,\phi_{(3e+r-5)l}\right.$$
$$\left. +(b^s_{1l^*nr})^e\,\phi_{(3e+l^*-2)j}\,\phi_{(3e+n-1)k}\phi_{(3e+r-2)l}\right]$$

$$\{l^*=1,2\};\ \{n=3,4\};\ \{r=1,2\};\ \{e=1,2,3,...,M+1\};\ \{j,k,l=1,2,3,...,Q\}$$

$$= \left[(b^s_{3l^*nr})^{e-1}\,\phi_{(3e+l^*-5)j}\,\phi_{(3e+n-4)k}\,\phi_{(3e+r-4)l}\right.$$
$$\left. +(b^s_{1l^*nr})^e\,\phi_{(3e+l^*-2)j}\,\phi_{(3e+n-1)k}\phi_{(3e+r-1)l}\right]$$

$$\{l^*=1,2\};\ \{n=3,4\};\ \{r=3,4\};\ \{e=1,2,3,...,M+1\};\ \{j,k,l=1,2,3,...,Q\}$$

$$= \left[(b^s_{3l^*nr})^{e-1}\,\phi_{(3e+l^*-4)j}\,\phi_{(3e+n-5)k}\,\phi_{(3e+r-5)l}\right.$$
$$\left. +(b^s_{1l^*nr})^e\,\phi_{(3e+l^*-1)j}\,\phi_{(3e+n-2)k}\phi_{(3e+r-2)l}\right]$$

$$\{l^*=3,4\};\ \{n=1,2\};\ \{r=1,2\};\ \{e=1,2,3,...,M+1\};\ \{j,k,l=1,2,3,...,Q\}$$

$$= \left[(b^s_{3l^*nr})^{e-1}\,\phi_{(3e+l^*-4)j}\,\phi_{(3e+n-5)k}\,\phi_{(3e+r-4)l}\right.$$
$$\left. +(b^s_{1l^*nr})^e\,\phi_{(3e+l^*-1)j}\,\phi_{(3e+n-2)k}\phi_{(3e+r-1)l}\right]$$

$$\{l^*=3,4\};\ \{n=1,2\};\ \{r=3,4\};\ \{e=1,2,3,...,M+1\};\ \{j,k,l=1,2,3,...,Q\}$$

$$= \left[(b^s_{3l^*nr})^{e-1}\,\phi_{(3e+l^*-4)j}\,\phi_{(3e+n-4)k}\,\phi_{(3e+r-5)l}\right.$$
$$\left. +(b^s_{1l^*nr})^e\,\phi_{(3e+l^*-1)j}\,\phi_{(3e+n-1)k}\phi_{(3e+r-2)l}\right]$$

$$\{l^*=3,4\};\ \{n=3,4\};\ \{r=1,2\};\ \{e=1,2,3,...,M+1\};\ \{j,k,l=1,2,3,...,Q\}$$

$$= \left[(b^s_{3l^*nr})^{e-1}\,\phi_{(3e+l^*-4)j}\,\phi_{(3e+n-4)k}\,\phi_{(3e+r-4)l}\right.$$
$$\left. +(b^s_{1l^*nr})^e\,\phi_{(3e+l^*-1)j}\,\phi_{(3e+n-1)k}\phi_{(3e+r-1)l}\right]$$

$$\{l^*=3,4\};\ \{n=3,4\};\ \{r=3,4\};\ \{e=1,2,3,...,M+1\};\ \{j,k,l=1,2,3,...,Q\}$$

$$\beta^{\Theta}_{el^*nrjkl} \tag{3.53}$$

$$= \left[(b^s_{4l^*nr})^{e-1} \ \phi_{(3e+l^*-5)j} \ \phi_{(3e+n-5)k} \ \phi_{(3e+r-5)l} \right.$$

$$\left. + (b^s_{2l^*nr})^e \ \phi_{(3e+l^*-2)j} \ \phi_{(3e+n-2)k} \phi_{(3e+r-2)l} \right]$$

$$\{l^* = 1, 2\}; \ \{n = 1, 2\}; \ \{r = 1, 2\}; \ \{e = 1, 2, 3, ..., M+1\}; \ \{j, k, l = 1, 2, 3, ..., Q\}$$

$$= \left[(b^s_{4l^*nr})^{e-1} \ \phi_{(3e+l^*-5)j} \ \phi_{(3e+n-5)k} \ \phi_{(3e+r-4)l} \right.$$

$$\left. + (b^s_{2l^*nr})^e \ \phi_{(3e+l^*-2)j} \ \phi_{(3e+n-2)k} \phi_{(3e+r-1)l} \right]$$

$$\{l^* = 1, 2\}; \ \{n = 1, 2\}; \ \{r = 3, 4\}; \ \{e = 1, 2, 3, ..., M+1\}; \ \{j, k, l = 1, 2, 3, ..., Q\}$$

$$= \left[(b^s_{4l^*nr})^{e-1} \ \phi_{(3e+l^*-5)j} \ \phi_{(3e+n-4)k} \ \phi_{(3e+r-5)l} \right.$$

$$\left. + (b^s_{2l^*nr})^e \ \phi_{(3e+l^*-2)j} \ \phi_{(3e+n-1)k} \phi_{(3e+r-2)l} \right]$$

$$\{l^* = 1, 2\}; \ \{n = 3, 4\}; \ \{r = 1, 2\}; \ \{e = 1, 2, 3, ..., M+1\}; \ \{j, k, l = 1, 2, 3, ..., Q\}$$

$$= \left[(b^s_{4l^*nr})^{e-1} \ \phi_{(3e+l^*-5)j} \ \phi_{(3e+n-4)k} \ \phi_{(3e+r-4)l} \right.$$

$$\left. + (b^s_{2l^*nr})^e \ \phi_{(3e+l^*-2)j} \ \phi_{(3e+n-1)k} \phi_{(3e+r-1)l} \right]$$

$$\{l^* = 1, 2\}; \ \{n = 3, 4\}; \ \{r = 3, 4\}; \ \{e = 1, 2, 3, ..., M+1\}; \ \{j, k, l = 1, 2, 3, ..., Q\}$$

$$= \left[(b^s_{4l^*nr})^{e-1} \ \phi_{(3e+l^*-4)j} \ \phi_{(3e+n-5)k} \ \phi_{(3e+r-5)l} \right.$$

$$\left. + (b^s_{2l^*nr})^e \ \phi_{(3e+l^*-1)j} \ \phi_{(3e+n-2)k} \phi_{(3e+r-2)l} \right]$$

$$\{l^* = 3, 4\}; \ \{n = 1, 2\}; \ \{r = 1, 2\}; \ \{e = 1, 2, 3, ..., M+1\}; \ \{j, k, l = 1, 2, 3, ..., Q\}$$

$$= \left[(b^s_{4l^*nr})^{e-1} \ \phi_{(3e+l^*-4)j} \ \phi_{(3e+n-5)k} \ \phi_{(3e+r-4)l} \right.$$

$$\left. + (b^s_{2l^*nr})^e \ \phi_{(3e+l^*-1)j} \ \phi_{(3e+n-2)k} \phi_{(3e+r-1)l} \right]$$

$$\{l^* = 3, 4\}; \ \{n = 1, 2\}; \ \{r = 3, 4\}; \ \{e = 1, 2, 3, ..., M+1\}; \ \{j, k, l = 1, 2, 3, ..., Q\}$$

$$= \left[(b^s_{4l^*nr})^{e-1} \ \phi_{(3e+l^*-4)j} \ \phi_{(3e+n-4)k} \ \phi_{(3e+r-5)l} \right.$$

$$\left. + (b^s_{2l^*nr})^e \ \phi_{(3e+l^*-1)j} \ \phi_{(3e+n-1)k} \phi_{(3e+r-2)l} \right]$$

$$\{l^* = 3, 4\}; \ \{n = 3, 4\}; \ \{r = 1, 2\}; \ \{e = 1, 2, 3, ..., M+1\}; \ \{j, k, l = 1, 2, 3, ..., Q\}$$

$$= \left[(b^s_{4l^*nr})^{e-1} \ \phi_{(3e+l^*-4)j} \ \phi_{(3e+n-4)k} \ \phi_{(3e+r-4)l} \right.$$

$$\left. + (b^s_{2l^*nr})^e \ \phi_{(3e+l^*-1)j} \ \phi_{(3e+n-1)k} \phi_{(3e+r-1)l} \right]$$

$$\{l^* = 3, 4\}; \ \{n = 3, 4\}; \ \{r = 3, 4\}; \ \{e = 1, 2, 3, ..., M+1\}; \ \{j, k, l = 1, 2, 3, ..., Q\}$$

where $(\cdot)^{e-1}$ denotes for quantities associated with element $e-1$, $(\cdot)^e$ denotes quantities associated with element e, and b^s_{kl*nr} are quantities defined by equation (15).

CHAPTER 4

Component Mode Synthesis Using Nonlinear Normal Modes

4.1   Introduction

Many complex structures are composed of several relatively simple substructures that are assembled together. This occurs in trusses, bladed-disk assemblies in turbine rotors, aerospace and ground vehicles, and many other applications. In such cases it is convenient to develop a dynamic model for the overall structure by taking advantage of the dynamic properties of the substructures. Component Mode Synthesis (CMS) was developed using these ideas, in order to synthesize models that are described in terms of the component structures and to take advantage of model size reduction carried out at the substructure level. There are two general types of CMS methods; they are known as the fixed-interface and the free-interface approaches. The fixed-interface CMS technique, developed by Hurty ([60],[61]) and simplified by Craig and Bampton ([62]), is widely used, since the reduction procedure is straightforward and typically produces highly accurate models with relatively few component modes ([64]). Free-interface CMS methods are more attractive than fixed-interface CMS methods when the component modes are obtained from modal testing or when an experimental verification of the component modes is required ([65]). The free-interface CMS technique developed by Craig and Chang ([66], [67] and [63]) is the most accurate among the free-interface CMS techniques. It is a modified version of Rubin's

128

method [68] and MacNeal's method [69]. It is superior to the CMS of Craig-Bampton in terms of accuracy, but is more difficult to implement ([64]). An extensive review on CMS can be found in [59]. CMS-type methods are well developed for linear structural models and they have been used extensively, especially in the aerospace industry, see ([55], [56], [57], and [58], for example).

The finite element (FE) method is used in CMS to model and characterize the behavior of the individual substructures. Often, accurate models of the component structures require a large number of FE degrees of freedom (DOF). For linear systems, model reduction can be achieved using linear modal analysis, wherein one simply truncates the higher modes of vibration. In fact, this is how one carries out model size reduction at the substructure level in linear CMS. However, the dynamic analysis (e.g., the determination of natural frequencies, mode shapes, time responses) of such structures can require considerable computational effort, and this is especially true for nonlinear structures ([5]).

The difficult issue of model size reduction for nonlinear structures continues to be a major challenge for computational vibration analysis. For relatively simple systems one can use nonlinear normal modes (NNMs) for this task. For example, Shaw and Pierre have developed systematic procedures to obtain reduced-order models (ROM) via NNMs using invariant manifolds ([20], [21], and [74]). Asymptotic series were initially used to approximate the geometry of the invariant manifold, and this approach was applied to the study of a variety of systems, such as a nonlinear rotating Euler-Bernoulli Beam ([3]). Pesheck et al. developed a numerically-based Galerkin approach to calculate the geometry of the NNM invariant manifolds out to large amplitudes of vibration ([33]). These procedures can be used for quite general nonlinearities over a wide range of amplitudes, and they have been applied to many systems, including the rotating beam ([34]). Recently, these methods have been shown to be applicable in conjunction with nonlinear FE models ([35]), which opens a new frontier for their application to more complex nonlinear structural systems. Jiang et al. have recently extended the work of Pesheck et al. to calculate the geometry of multi-mode invariant manifolds that are able to capture the dynamics for situations

where more than one mode is active, for example, in the case of internal resonance ([42]). However the computational cost involved in generating the multi-mode invariant manifold is still quite high.

The present chapter describes recent research that is aimed at extending the fixed-interface linear CMS method to nonlinear structures by making use of the fixed-interface NNMs of the component structures. By synthesizing the reduced-order representations of the substructures, one can obtain accurate low-order models of structures that are composed of assemblies of nonlinear substructures, with significantly less computational cost than by computing the ROM directly from the fully coupled system. It is found that such an approach is valid, so long as the coupling between substructures is relatively weak. It is also shown how this method relates to the usual linear CMS, and reduces to it under linearization of the model.

The chapter is outlined as follows. We first review the development of NNMs, as needed for the individual substructures. The associated invariant manifold equations, parameterized by modal position and velocity, are formulated, and a numerical collocation method is presented that allows one to obtain the solution of the NNM invariant manifold out to moderate amplitudes. Then, the procedures for fixed-interface nonlinear component mode synthesis are described. A five-DOF system and a forty-one-DOF system are used as examples to demonstrate the method, and some conclusions are drawn to close the chapter.

4.2 Formulation of the NNM Invariant Manifolds

4.2.1 Invariant-Manifold Governing Equations

We begin with a general discrete representation of the vibrations of a nonlinear structural system (in our case, a subsystem component), obtained either by a finite element model

followed by linear modal expansion, or by a Rayleigh-Ritz approach using the linear mode shapes. We assume that the system at linear order is undamped. (This assumption greatly simplifies the problem, but can be relaxed, in principle.) In this case, the equations of motion for a Q-DOF system are uncoupled at linear order and can be expressed in the form:

$$I \ddot{\eta} + \Lambda \eta = f(\eta, \dot{\eta}) \tag{4.1}$$

where I is the identity matrix, Λ is the diagonal matrix of squared linear natural frequencies, $f(\eta, \dot{\eta})$ a vector of nonlinear forces, η the modal position vector, and $\dot{\eta}$ the modal velocity vector. The component form of equation (4.1) is given by

$$\ddot{\eta}_i + \omega_i^2 \eta_i = f_i(\eta_j, \dot{\eta}_j) \tag{4.2}$$

$$\text{for} \quad i, j = 1, 2, 3, ..., Q$$

where ω_i is the linear free vibration natural frequency of mode i and Q is the number of retained linear modes.

In order to search for a particular individual NNM, it is assumed that the NNM manifold is parameterized by a single modal position-velocity pair corresponding to the mode of interest, referred to as the master mode. This is accomplished by using the fact that for a NNM response all of the remaining modal positions and velocities are slaved (constrained) to this master mode. For the kth nonlinear mode, we take $u_k = \eta_k$, and $v_k = \dot{\eta}_k$ as the master states. The remaining slave states are expressed as

131

$$\eta_i \quad = \quad X_i(u_k, v_k) \quad = \quad X_i(\eta_k, \dot{\eta}_k) \tag{4.3}$$

$$\dot{\eta}_i \quad = \quad Y_i(u_k, v_k) \quad = \quad Y_i(\eta_k, \dot{\eta}_k) \tag{4.4}$$

$$\text{for} \quad i = 1, 2, 3, ..., Q; \quad i \neq k.$$

Equations (4.3) and (4.4) constitute a set of constraint equations that are to be determined. The constraint functions in equations (4.3) and (4.4) are obtained by an invariant manifold procedure that generates equations that can be solved for the unknown constraint relations. The process begins by taking a time derivative of the constraint equations, yielding

$$\dot{\eta}_i \quad = \quad \frac{\partial X_i}{\partial u_k} \dot{u}_k + \frac{\partial X_i}{\partial v_k} \dot{v}_k \tag{4.5}$$

$$\ddot{\eta}_i \quad = \quad \frac{\partial Y_i}{\partial u_k} \dot{u}_k + \frac{\partial Y_i}{\partial v_k} \dot{v}_k \tag{4.6}$$

$$\text{for} \quad i = 1, 2, 3, ..., Q; \quad i \neq k.$$

The time dependence in these equations is eliminated by substitutions that make use of the the equations of motion, as follows: $\dot{u}_k = v_k$, $\dot{v}_k = \ddot{\eta}_k = -\omega_k^2 \eta_k + f_k(\eta_j, \dot{\eta}_j)$, $\ddot{\eta}_i = -\omega_i^2 \eta_i + f_i(\eta_j, \dot{\eta}_j)$. Then, the constraints (equations (4.3) and (4.4)) are substituted in the resulting expression everywhere in place of the slave state variables, resulting in a set of partial differential equations for the functions $(X_i(u_k, v_k), Y_i(u_k, v_k))$. This set of 2Q - 2, time-independent, partial differential equations govern the geometry of the kth manifold, and are given by

$$Y_i = \frac{\partial X_i}{\partial u_k} v_k + \frac{\partial X_i}{\partial v_k}(-\omega_k^2 \, u_k$$
$$+ f_k(X_j, Y_j, u_k, v_k)) \tag{4.7}$$

$$-\omega_i^2 \, X_i + f_i(X_j, Y_j, u_k, v_k) = \frac{\partial Y_i}{\partial u_k} v_k + \frac{\partial Y_i}{\partial v_k}(-\omega_k^2 \, u_k$$
$$+ f_k(X_j, Y_j, u_k, v_k)) \tag{4.8}$$

$$\text{for} \quad i, j = 1, 2, 3, ..., Q; \quad i, j \neq k.$$

These equations are not solvable in closed form (except in very special cases). Methods for obtaining approximate solutions for X_i and Y_i are described in the next section.

4.2.2 Invariant Manifold Solution

Asymptotic expansions can be used to obtain approximate solutions of the invariant manifold equations, equations (4.7) and (4.8), for smooth nonlinearities, but such solutions are only locally valid ([20], [21]). Numerical Galerkin-based solutions have also been developed, wherein one can utilize either local or global basis functions to describe the invariant manifold ([33]). In this work we employ a Galerkin-based procedure that relies on a patchwork of local solutions to obtain a solution that is valid over a given domain: $u_k \in [-U_b, U_b]$ and $v_k \in [-V_b, V_b]$.

We describe the development of the method for a local domain described by $u_k^e \in [-u_b, u_b]$ and $v_k^e \in [-v_b, v_b]$. Once this procedure has been developed, it can be applied to each patch, and the final result is obtained by collecting the results for all patches such that the entire domain is covered. The relations between the coordinates in the global domain (u_k, v_k) and those in the local domain (u_k^e, v_k^e) are given by

$$u_k = d_u + u_k^e, \tag{4.9}$$

$$v_k = d_v + v_k^e, \tag{4.10}$$

$$\text{where} \quad d_u = -U_b + (\frac{2U_b}{N_u^e})(e_u - 1) + u_b, \tag{4.11}$$

$$\text{and} \quad d_v = -V_b + (\frac{2V_b}{N_v^e})(e_v - 1) + v_b, \tag{4.12}$$

where e_u and e_v are the patch indices in the u_k and v_k directions, respectively, and N_u^e and N_v^e are the number of patches used in the u_k and v_k directions, and d_u and d_v represent the shift from the origin of (u_k, v_k) to (u_k^e, v_k^e), respectively. Here e_u runs from 1 to N_u^e and e_v runs from 1 to N_v^e.

Substituting equations (4.9) and (4.10) into equations (4.7) and (4.8), the partial differential equations governing the geometry of the kth manifold in the local coordinates (u_k^e, v_k^e) are given by:

$$Y_i = \frac{\partial X_i}{\partial u_k^e}(d_v + v_k^e) + \frac{\partial X_i}{\partial v_k^e}(-\omega_k^2 (d_u + u_k^e)$$
$$+ f_k(X_j, Y_j, d_u + u_k^e, d_v + v_k^e)) \tag{4.13}$$

$$-\omega_i^2 X_i + f_i(X_j, Y_j, d_u + u_k^e, d_v + v_k^e) = \frac{\partial Y_i}{\partial u_k^e}(d_v + v_k^e) + \frac{\partial Y_i}{\partial v_k^e}(-\omega_k^2 (d_u + u_k^e)$$
$$+ f_k(X_j, Y_j, d_u + u_k^e, d_v + v_k^e)) \tag{4.14}$$

$$\text{for} \quad i, j = 1, 2, 3, ..., Q; \quad i, j \neq k.$$

The solution of equations (4.13) and (4.14) on the local domain is obtained by expanding (X_i, Y_i) in terms of basis functions as:

$$X_i(u_k^e, v_k^e) = \sum_{l=1}^{N_{p,u}} \sum_{m=1}^{N_{p,v}} C_i^{l,m} LM_{l,m}(u_k^e, v_k^e) \tag{4.15}$$

$$Y_i(u_k^e, v_k^e) = \sum_{l=1}^{N_{p,u}} \sum_{m=1}^{N_{p,v}} D_i^{l,m} LM_{l,m}(u_k^e, v_k^e), \tag{4.16}$$

$$\text{where} \quad LM_{l,m}(u_k^e, v_k^e) = T_{l-1}(u_k^e/u_b) \times T_{m-1}(v_k^e/v_b), \tag{4.17}$$

where $T_{l-1}(x)$ and $T_{m-1}(x)$ are standard Chebyshev polynomials defined over $x \in [-1, +1]$, and the C's and D's are the to-be-determined expansion coefficients. Equations (4.15) and (4.16) are substituted into the local manifold-governing equations, equations (4.13) and (4.14). Normally, each of the resulting equations is projected onto the basis functions, but here we employ a collocation method, which is computationally more efficient, yet retains very good accuracy. This is carried out by projection of the equations onto *Dirac delta functions* in the local master coordinates over the local domain, as follows:

$$0 = \int_{u_k^e, v_k^e} \delta(u_k^e - u_{k,p}^e, v_k^e - v_{k,q}^e) \left[-\sum_{l,m} D_i^{l,m} LM_{l,m} + \sum_{l,m} C_i^{l,m} (d_v + v_k^e) \frac{\partial LM_{l,m}}{\partial u_k^e} \right.$$

$$\left. + \sum_{l,m} C_i^{l,m} \frac{\partial LM_{l,m}}{\partial v_k^e} (-\omega_k^2 (d_u + u_k^e) + f_k) \right] du_k^e \, dv_k^e \tag{4.18}$$

$$0 = \int_{u_k^e, v_k^e} \delta(u_k^e - u_{k,p}^e, v_k^e - v_{k,q}^e) \left[\omega_i^2 \sum_{l,m} C_i^{l,m} LM_{l,m} - f_i + \sum_{l,m} D_i^{l,m} (d_v + v_k^e) \frac{\partial LM_{l,m}}{\partial u_k^e} \right.$$

$$\left. + \sum_{l,m} D_i^{l,m} \frac{\partial LM_{l,m}}{\partial v_k^e} (-\omega_k^2 (d_u + u_k^e) + f_k) \right] du_k^e \, dv_k^e \tag{4.19}$$

for $\quad i = 1, 2, 3, ..., Q; \ i \neq k$;

$\quad p = 1, ..., N_{p,u}$;

$\quad q = 1, ..., N_{p,v}$,

135

where $(u_{k,p}^e, v_{k,q}^e) \in [-u_b, u_b] \times [-v_b, v_b]$ are the collocation points, which are zeroes of $T_{N_{p,u}}(u_k^e/u_b)$ and $T_{N_{p,v}}(v_k^e/v_b)$, respectively (see [78], [81]). Equations (4.18) and (4.19) constitute a set of $2(Q-1) \times N_{p,u} \times N_{p,v}$ nonlinear equations in the C's and D's. Note that there are $N_u^e \times N_v^e$ sets of C's and D's, that is, a set for each patch. However, if the system is conservative and the nonlinear terms are functions of solely the modal positions, then only $0.25 \times N_u^e \times N_v^e$ sets of C's and D's need to be solved for, and the remaining coefficients can be generated using symmetries in the NNM manifold. Once all of the expansion coefficients are obtained, the X's and Y's, which describe the slaved modes, are known functions of the master states (u_k^e, v_k^e). For $i = k$, these known functions are used to express f_k in equation (4.2) in terms of only u_k^e and v_k^e, rendering a single-DOF oscillator as the reduced-order-model for the kth NNM.

Once all of the coefficients have been determined for each subdomain, the entire manifold is known, in a patchwork form. It should be noted that a motion started on this manifold, that is, one that satisfies the master-slave relations captured by the X's and Y's, remains on that manifold for all time, by dynamic invariance. However, a given response will visit many subdomains, and thus the solution moves across this two dimensional surface like a curve tracing across a tiled floor. It should also be noted that these "tiles" are obtained in a patchwork manner, without any continuity or smoothness constraints, so that the slave constraints may exhibit jumps as the response moves across the tile boundaries. If the subdomains are taken to be sufficiently small, these jumps will likewise be small. Examples of nonlinear modes constructed from a similar approach can be found in [33] and [34].

4.3   Fixed-Interface Nonlinear Component Mode Synthesis

In this section, we extend the concept of the fixed-interface CMS of Craig and Bampton ([62]) by making use of the fixed-interface NNMs instead of the fixed-interface linear

normal modes (LNMs). The aim here is to account for nonlinearities at the substructure level without having to resort to the retention of several linear modes. First, the nonlinear structural system is partitioned into component substructures. Then, fixed-interface dynamic representations of the substructures are constructed, where the nonlinear models are expressed in terms of fixed-interface LNMs, which are coupled through nonlinear terms. These substructure models are then reduced, each to a single nonlinear mode, using the NNM constraint relations, and subsequently synthesized with linear constraint modes to produce a ROM that describes the dynamics of the combined structure.

4.3.1 System Representation in Physical Coordinates

Consider a structure that is partitioned into two substructures, denoted by α and β. The equations of motion of the substructures in physical coordinates can be written separately, along with appropriate conditions on the common junction coordinates, as follows:

$$\begin{bmatrix} M_{II} & M_{IJ} \\ M_{JI} & M_{JJ} \end{bmatrix}^{\alpha} \begin{bmatrix} \ddot{X}_I \\ \ddot{X}_J \end{bmatrix}^{\alpha} + \begin{bmatrix} K_{II} & K_{IJ} \\ K_{JI} & K_{JJ} \end{bmatrix}^{\alpha} \begin{bmatrix} X_I \\ X_J \end{bmatrix}^{\alpha}$$

$$+ \begin{bmatrix} G_I(X) \\ G_J(X) \end{bmatrix}^{\alpha} = \begin{bmatrix} 0 \\ F_J \end{bmatrix}^{\alpha}$$

(4.20)

$$\begin{bmatrix} M_{II} & M_{IJ} \\ M_{JI} & M_{JJ} \end{bmatrix}^{\beta} \begin{bmatrix} \ddot{X}_I \\ \ddot{X}_J \end{bmatrix}^{\beta} + \begin{bmatrix} K_{II} & K_{IJ} \\ K_{JI} & K_{JJ} \end{bmatrix}^{\beta} \begin{bmatrix} X_I \\ X_J \end{bmatrix}^{\beta}$$

$$+ \begin{bmatrix} G_I(X) \\ G_J(X) \end{bmatrix}^{\beta} = \begin{bmatrix} 0 \\ F_J \end{bmatrix}^{\beta},$$

(4.21)

with junction boundary conditions on displacements and forces, as follows,

$$X_J^\alpha = X_J^\beta, \tag{4.22}$$

$$F_J^\alpha + F_J^\beta = 0, \tag{4.23}$$

where $(\cdot)^\alpha$ denotes quantities associated with substructure α, and all terms defined below have $(\cdot)^\beta$ counterparts. The vector X^α contains all coordinates for the α substructure and has dimension N^α, X_I^α is the vector of interior (non-interface) physical coordinates of dimension n_I^α, and X_J^α is the vector of junction (interface) physical coordinates of dimension n_C. G_I^α is a vector of the nonlinear forces associated with the X_I^α equations, G_J^α is the vector of nonlinear forces associated with the X_J^α equations, and F_J^α is the vector of reaction forces from substructure β acting on substructure α. M_{II}^α, K_{II}^α, etc., are mass and stiffness matrices, respectively, defined in an obvious manner.

4.3.2 System Representation in Linear Modal Coordinates

In this section, the (typically) large number of physical coordinates for each substructure is first reduced to a smaller (yet still possibly large) number of coordinates by truncating using the substructures' fixed-interface linear modes. The physical coordinates of substructures α and β are transformed into a truncated set of fixed-interface linear modal coordinates using the following coordinate transformations:

$$X^\alpha = \Psi^\alpha\, \eta^\alpha = \begin{bmatrix} \Phi_N^\alpha & \Psi_C^\alpha \end{bmatrix} \begin{bmatrix} \eta_N^\alpha \\ \eta_C^\alpha \end{bmatrix} \tag{4.24}$$

138

$$X^\beta = \Psi^\beta \, \eta^\beta = \begin{bmatrix} \Phi_N^\beta & \Psi_C^\beta \end{bmatrix} \begin{bmatrix} \eta_N^\beta \\ \eta_C^\beta \end{bmatrix} , \qquad\qquad (4.25)$$

where Φ_N^α is the $N^\alpha \times n^\alpha$ matrix of retained fixed-interface linear normal modes, η_N^α is the vector of retained fixed-interface linear modal coordinates (of dimension n^α), Ψ_C^α is the $N^\alpha \times n_C$ matrix of linear constraint modes, η_C^α is the vector (of dimension n_C) of linear constraint modal coordinates, and similar terms are defined for substructure β. The procedures for calculating the retained fixed-interface linear normal modes and the linear constraint modes are described below. Note that at this step, the dimension of the system of equations for substructure α has been reduced from $(N^\alpha = n_I^\alpha + n_C)$ to $(n^\alpha + n_C)$ with $n^\alpha < n_I^\alpha$, and similarly for substructure β.

4.3.2.1 Fixed-Interface Linear and Nonlinear Normal Modes

The concept of fixed-interface linear CMS of Craig and Bampton ([62]) is extended by making use of the fixed-interface NNMs in place of the fixed-interface LNMs. Since the procedures for substructures α and β are the same, these superscripts will be omitted from the development here.

Consider equations (4.20) and (4.21) with $X_J = 0$, that is, with the interface fixed. This yields

$$M_{II}\ddot{X}_I + K_{II}X_I + G_I(X_I, X_J = 0) = 0. \qquad\qquad (4.26)$$

Using standard linear modal analysis (with the modes obtained for $G_I = 0$), we obtain the

normalized fixed-interface linear modal matrix Φ_{IN} associated with the interior physical coordinates (of dimension $n_I \times n$, where $n \ll n_I$). Then, the retained fixed-interface linear modal matrix Φ_N is defined as

$$\Phi_N = \begin{bmatrix} \Phi_{IN} \\ 0 \end{bmatrix}.$$

(4.27)

The nonlinear equations of motion (4.26) are then transformed into fixed-interface linear modal coordinates using the following coordinate transformation:

$$X_I = \Phi_{IN}\, \eta_N,$$

(4.28)

This yields the fixed interface nonlinear equations of motion expressed in fixed-interface linear modal coordinates, as follows:

$$I_{NN}\, \ddot{\eta}_N + \Lambda_{NN}\, \eta_N + \tilde{G}_N(\eta_N) = 0$$

(4.29)

$$\text{where}\quad I_{NN} = \Phi_{IN}^T M_{II} \Phi_{IN}$$

(4.30)

$$\Lambda_{NN} = \Phi_{IN}^T K_{II} \Phi_{IN}$$

(4.31)

$$\tilde{G}_N(\eta_N) = \Phi_{IN}^T G_I(\Phi_{IN}\eta_N, X_J = 0).$$

(4.32)

This fixed-interface model is still relatively large and is to be ultimately reduced to a single DOF using the nonlinear modal reduction procedure described in sections 4.2 and 4.2.2. Note that in terms of matching notation from those sections, the function $\tilde{G}_N$ and

dimension n are $-f$ and Q, respectively. The NNM reduction provides the constraint relations between the slaved states and the master states of the kth fixed-interface NNM for a substructure, and can be expressed as follows:

$$\eta_i^N = X_i(\eta_k^N, \dot{\eta}_k^N) \tag{4.33}$$

$$\dot{\eta}_i^N = Y_i(\eta_k^N, \dot{\eta}_k^N) \tag{4.34}$$

$$\text{for} \quad i = 1, 2, 3, ..., n; \quad i \neq k.$$

After obtaining the constraints X_i and Y_i, and doing so for each substructure, we have single mode nonlinear models for the substructures, based on fixed interface models. We now turn to the procedure for coupling these component structure models to one another through the interface.

4.3.2.2 Linear Constraint Modes

The definition of a linear constraint mode from Craig and Bampton [62] is adopted here. It is defined by statically imposing a unit displacement on one physical coordinate of the set of junction coordinates and zero displacements on the remaining coordinates of the set. This procedure is applied consecutively to all junction coordinates. Again, this process is the same for the α and β substructures, and therefore these superscripts are omitted. The collection of linear constraint modes is obtained from

$$\Psi_C = \begin{bmatrix} \Psi_{IC} \\ I_{JC} \end{bmatrix} = \begin{bmatrix} -K_{II}^{-1} K_{IJ} \\ I_{JC} \end{bmatrix}, \tag{4.35}$$

where $\mathbf{\Psi}_{IC}$ has dimension $n_I \times n_C$ and $\mathbf{I}_{JC}$ has dimension $n_C \times n_C$.

Note that nonlinear constraint modes are not considered in the present study, for a few reasons. First, to do so would require additional steps involving the derivation of another set of master-slave relations to describe nonlinear constraint modes (even if they are static). Also, if one were to use nonlinear constraint modes in the synthesis procedure, the coefficients of the nonlinear terms would be functions of the constraint mode amplitudes, which would make the synthesis process cumbersome to the point of being impractical. Furthermore, and perhaps most importantly, since fixed-interface methods work best for assemblies of weakly coupled subsystems, for which fixed-interface (linear or nonlinear, as the case may be) modes are well-suited to describe component motions accurately, it is appropriate to use linear constraint modes to represent the small interface-induced motions in the components. This restriction must be kept in mind, however, since it limits the method to a class of systems with weak coupling.

Equations (4.20) and (4.21) are transformed into linear modal coordinates using equations (4.24) and (4.25). The equations of motion for both substructures expressed in terms of these coordinates have the form

$$
\begin{bmatrix} I_{NN} & M_{NC} \\ M_{CN} & M_{CC} \end{bmatrix}^{\alpha} \begin{bmatrix} \ddot{\eta}_N \\ \ddot{\eta}_C \end{bmatrix}^{\alpha} + \begin{bmatrix} \Lambda_{NN} & 0 \\ 0 & K_{CC} \end{bmatrix}^{\alpha} \begin{bmatrix} \eta_N \\ \eta_C \end{bmatrix}^{\alpha}
$$

$$
+ \begin{bmatrix} \tilde{G}_N(\eta_N, \eta_C) \\ \tilde{G}_C(\eta_N, \eta_C) \end{bmatrix}^{\alpha} = \begin{bmatrix} 0 \\ F_C \end{bmatrix}^{\alpha}
\tag{4.36}
$$

$$
\left[\begin{array}{cc} I_{NN} & M_{NC} \\ M_{CN} & M_{CC} \end{array}\right]^{\beta} \left[\begin{array}{c} \ddot{\eta}_{N} \\ \ddot{\eta}_{C} \end{array}\right]^{\beta} + \left[\begin{array}{cc} \Lambda_{NN} & 0 \\ 0 & K_{CC} \end{array}\right]^{\beta} \left[\begin{array}{c} \eta_{N} \\ \eta_{C} \end{array}\right]^{\beta}
$$

$$
+ \left[\begin{array}{c} \tilde{G}_{N}(\eta_{N},\eta_{C}) \\ \tilde{G}_{C}(\eta_{N},\eta_{C}) \end{array}\right]^{\beta} = \left[\begin{array}{c} 0 \\ F_{C} \end{array}\right]^{\beta} ,
$$

(4.37)

with the following junction boundary conditions on the displacements and forces:

$$
X_{J}^{\alpha} = \eta_{C}^{\alpha} \quad = \quad \eta_{C}^{\beta} = X_{J}^{\beta}, \tag{4.38}
$$

$$
F_{C}^{\alpha} = F_{J}^{\alpha} \quad \text{and} \quad F_{C}^{\beta} = F_{J}^{\beta} \tag{4.39}
$$

$$
F_{C}^{\alpha} + F_{C}^{\beta} \quad = \quad 0. \tag{4.40}
$$

Note that the stiffness matrices are block diagonal due to the orthogonality between $\mathbf{\Phi}_{N}$ and $\mathbf{\Psi}_{C}$ with respect to K, which results from how $\mathbf{\Phi}_{N}$ and $\mathbf{\Psi}_{C}$ are defined in equations (4.27) and (4.35), respectively. We now turn to the synthesis procedure.

4.3.3 Synthesis with Nonlinear Modal Reduction

In this section, the model size of the substructures is reduced using the NNM constraint relations. The substructure ROMs are then synthesized to obtain the final ROM that describes the dynamics of the combined structure.

In summary, this nonlinear CMS process involves two steps of model reduction, one of which is standard and uses linear modes, while the other involves the NNMs. First, we

use the linear modal reduction described in section 4.3.2 to reduce the system DOF from

$(n_I^\alpha + n_I^\beta + n_C)$ to $(n^\alpha + n^\beta + n_C)$. Note that this reduction is not central to the technique,

and may not be used in some systems (in fact, it is not done in the examples considered

in the next section). Then, the key step makes use of the nonlinear modal reduction based

on the approach described in sections 4.2 and 4.2.2, which reduces the system size from

$(n^\alpha + n^\beta + n_C)$ to $(2 + n_C)$ DOFs.

Again, the superscripts α and β are omitted in the derivation. The component forms of

equations (4.36) and (4.37) are given by

$$\ddot{\eta}_i^N + \sum_{s=1}^{n_C} m_{is}^{NC} \ddot{\eta}_s^C + \omega_i^2 \eta_i^N + \tilde{g}_i^N(\eta_l^N, \eta_k^N, \eta_r^C) = 0 \tag{4.41}$$

$$\ddot{\eta}_k^N + \sum_{s=1}^{n_C} m_{ks}^{NC} \ddot{\eta}_s^C + \omega_k^2 \eta_k^N + \tilde{g}_k^N(\eta_l^N, \eta_k^N, \eta_r^C) = 0 \tag{4.42}$$

$$\sum_{j=1}^{n} m_{rj}^{CN} \ddot{\eta}_j^N + \sum_{s=1}^{n_C} m_{rs}^{CC} \ddot{\eta}_s^C + \sum_{s=1}^{n_C} k_{rs}^{CC} \eta_s^C + \tilde{g}_r^C(\eta_l^N, \eta_k^N, \eta_r^C) = F_r^J, \tag{4.43}$$

$$\text{for } i, l = 1, 2, 3, ..., n; \ i, l \neq k;$$

$$r = 1, 2, 3, ..., n_C,$$

where k is the kth fixed-interface master mode defined in section 4.3.2.1 (typically taken to

be the fundamental mode). From equation (4.41), the expression for $\ddot{\eta}_i^N$ is obtained , and

it is used in equation (4.43). Rearranging and grouping terms in equation (4.43) yields

$$m_{rk}^{CN} \, \ddot{\eta}_k^N + \sum_{s=1}^{n_C} m_{rs}^{CC,update} \, \ddot{\eta}_s^C \; + \; \sum_{s=1}^{n_C} k_{rs}^{CC} \, \eta_s^C + \tilde{g}_r^{C,update}(\eta_l^N, \eta_k^N, \eta_r^C) = F_r^J \quad (4.44)$$

$$\text{where} \quad m_{rs}^{CC,update} \;=\; m_{rs}^{CC} + m_{rs}^{CC,*}, \quad\quad\quad\quad (4.45)$$

$$m_{rs}^{CC,*} \;=\; \sum_{j=1,j\neq k}^{n} -m_{rj}^{CN} \, m_{js}^{NC}, \quad\quad\quad (4.46)$$

$$\tilde{g}_r^{C,update} \;=\; \tilde{g}_r^C + \tilde{g}_r^{C,*}, \quad\quad\quad\quad (4.47)$$

$$\text{and} \quad \tilde{g}_r^{C,*} \;=\; \sum_{j=1,j\neq k}^{n} m_{rj}^{CN} \, (-\omega_j^2 \, \eta_j^N - \tilde{g}_j^N), \quad (4.48)$$

$$\text{for} \quad r \;=\; 1,2,3,...,n_C.$$

The modal constraints given in equation (4.33) are used in equations (4.42) and (4.44) to reduce the equations of motion associated with the synthesized fixed-interface linear modal coordinates (which are coupled to the constraint modes) onto the kth fixed-interface NNM invariant manifold (which is uncoupled from the constraint modes). This approximation will yield an accurate ROM if substructures α and β are weakly coupled, that is, the actual NNM invariant manifold of dimension $2 \times (2+n_C)$ of the combined structure has invariant 2-dimensional submanifolds that are close to the kth fixed-interface NNM invariant manifolds of the substructures, which are each of dimension 2.

With the NNM reduction of substructures α and β, equations (4.42) and (4.44) can be expressed in matrix form as

$$\begin{bmatrix} 1 & M_{KC} \\ M_{CK} & M_{CC}^{update} \end{bmatrix}^\alpha \begin{bmatrix} \ddot{\eta}_k^N \\ \ddot{\eta}_C \end{bmatrix}^\alpha + \begin{bmatrix} \omega_k^2 & 0 \\ 0 & K_{CC} \end{bmatrix}^\alpha \begin{bmatrix} \eta_k^N \\ \eta_C \end{bmatrix}^\alpha$$

$$+ \begin{bmatrix} \tilde{G}_k(\eta_k^N, \dot{\eta}_k^N, \eta_C) \\ \tilde{G}_C^{update}(\eta_k^N, \dot{\eta}_k^N, \eta_C) \end{bmatrix}^\alpha = \begin{bmatrix} 0 \\ F_J \end{bmatrix}^\alpha \quad (4.49)$$

$$\begin{bmatrix} 1 & M_{KC} \\ M_{CK} & M_{CC}^{update} \end{bmatrix}^{\beta} \begin{bmatrix} \ddot{\eta}_k^N \\ \ddot{\eta}_C \end{bmatrix}^{\beta} + \begin{bmatrix} \omega_k^2 & 0 \\ 0 & K_{CC} \end{bmatrix}^{\beta} \begin{bmatrix} \eta_k^N \\ \eta_C \end{bmatrix}^{\beta}$$

$$\tag{4.50}$$

$$+ \begin{bmatrix} \tilde{G}_k(\eta_k^N, \dot{\eta}_k^N, \eta_C) \\ \tilde{G}_C^{update}(\eta_k^N, \dot{\eta}_k^N, \eta_C) \end{bmatrix}^{\beta} = \begin{bmatrix} 0 \\ F_J \end{bmatrix}^{\beta},$$

along with the junction boundary conditions from equations (4.38) and (4.40). The final form of the synthesized ROM is obtained by imposing the junction conditions, equations (4.38) and (4.40), on equations (4.49) and (4.50), resulting in

$$\begin{bmatrix} 1 & 0 & M_{KC}^{\alpha} \\ 0 & 1 & M_{KC}^{\beta} \\ M_{CK}^{\alpha} & M_{CK}^{\beta} & M_{CC}^{update} \end{bmatrix} \begin{bmatrix} \ddot{\eta}_k^{N,\alpha} \\ \ddot{\eta}_k^{N,\beta} \\ \ddot{\eta}_C \end{bmatrix}$$

$$\tag{4.51}$$

$$+ \begin{bmatrix} (\omega_k^{\alpha})^2 & 0 & 0 \\ 0 & (\omega_k^{\beta})^2 & 0 \\ 0 & 0 & K_{CC} \end{bmatrix} \begin{bmatrix} \eta_k^{N,\alpha} \\ \eta_k^{N,\beta} \\ \eta_C \end{bmatrix} + \begin{bmatrix} \tilde{G}_k^{\alpha} \\ \tilde{G}_k^{\beta} \\ \tilde{G}_C^{update} \end{bmatrix} = \begin{bmatrix} 0 \\ 0 \\ 0 \end{bmatrix}$$

$$\text{where} \quad M_{CC}^{update} = (M_{CC}^{update,\alpha} + M_{CC}^{update,\beta}), \tag{4.52}$$

$$K_{CC} = (K_{CC}^{\alpha} + K_{CC}^{\beta}), \tag{4.53}$$

$$\text{and} \quad \tilde{G}_C^{update} = \tilde{G}_C^{update,\alpha}(\eta_k^{N,\alpha}, \dot{\eta}_k^{N,\alpha}, \eta_C)$$

$$+ \tilde{G}_C^{update,\beta}(\eta_k^{N,\beta}, \dot{\eta}_k^{N,\beta}, \eta_C). \tag{4.54}$$

This is the desired model, which has $(2 + n_C)$ DOF, one for each substructure and n_C for the constraint modes.

Note that these procedures have been computationally automated. Therefore, it is quite practical to interface this fixed-interface nonlinear CMS with nonlinear finite element models of the form in equations (4.20) and (4.21).

4.4 A Five-DOF Nonlinear Spring-Mass System

A five-DOF nonlinear spring-mass system is used as a "proof of concept" example that demonstrates the procedures and shows the effectiveness of the proposed method. The system is schematically depicted in Figure 4.1, and naturally partitions into the three substructures shown in Figure 4.2. The general features of this system are that the coupling mass m_1 is connected to ground with a very stiff spring k_1, such that its isolated natural frequency is significantly larger than the fixed-interface natural frequencies of the two attached subsystems (that is, when they are attached to ground instead of to m_1). In such a case, mass m_1 will have a relatively small amplitude for typical responses, and the fixed-interface linear modes of the two attached subsystems will be strongly reflected in the linear modes of the combined system. The subsystems are assumed to vibrate at amplitudes such that significant nonlinear effects are encountered, and in a frequency range such that their responses are dominated by their respective fundamental NNMs. Thus, the procedure consists in developing single-DOF fixed-interface NNMs for the attached subsystems, and combining these using the proposed method, resulting in a three-DOF nonlinear ROM that captures the dynamics (except for the high-frequency modes of the two attached subsystems). However, by using NNMs to describe the subsystems, the essential nonlinear interactions between the linear modes within each substructure will be contained in the resulting ROM.

The equations of motion of the five-DOF spring-mass system are given by

$$
\begin{bmatrix}
m_1 & 0 & 0 & 0 & 0 \\
0 & m_2 & 0 & 0 & 0 \\
0 & 0 & m_3 & 0 & 0 \\
0 & 0 & 0 & m_4 & 0 \\
0 & 0 & 0 & 0 & m_5
\end{bmatrix}
\begin{bmatrix}
\ddot{x}_1 \\
\ddot{x}_2 \\
\ddot{x}_3 \\
\ddot{x}_4 \\
\ddot{x}_5
\end{bmatrix}
$$

$$
+ \begin{bmatrix}
(k_1 + k_2 + k_6) & -k_2 & 0 & -k_6 & 0 \\
-k_2 & (k_2 + k_4) & -k_4 & 0 & 0 \\
0 & -k_4 & k_4 & 0 & 0 \\
-k_6 & 0 & 0 & (k_6 + k_8) & -k_8 \\
0 & 0 & 0 & -k_8 & k_8
\end{bmatrix}
\begin{bmatrix}
x_1 \\
x_2 \\
x_3 \\
x_4 \\
x_5
\end{bmatrix} \qquad (4.55)
$$

$$
+ \begin{bmatrix}
-k_3(x_2 - x_1)^3 - k_7(x_4 - x_1)^3 \\
k_3(x_2 - x_1)^3 - k_5(x_3 - x_2)^3 \\
k_5(x_3 - x_2)^3 \\
k_7(x_4 - x_1)^3 - k_9(x_5 - x_4)^3 \\
k_9(x_5 - x_4)^3
\end{bmatrix}
= \begin{bmatrix}
0 \\
0 \\
0 \\
0 \\
0
\end{bmatrix} .
$$

The equations of motion for the individual substructures and the junction boundary conditions are given by

$$
m_1 \ddot{x}_1^\alpha + k_1 x_1^\alpha = F_J^{\alpha\beta} + F_J^{\alpha\gamma} \qquad (4.56)
$$

$$
\begin{bmatrix} 0 & 0 & 0 \\ 0 & m_2 & 0 \\ 0 & 0 & m_3 \end{bmatrix} \begin{bmatrix} \ddot{x}_1^\beta \\ \ddot{x}_2^\beta \\ \ddot{x}_3^\beta \end{bmatrix} + \begin{bmatrix} k_2 & -k_2 & 0 \\ -k_2 & (k_2 + k_4) & -k_4 \\ 0 & -k_4 & k_4 \end{bmatrix} \begin{bmatrix} x_1^\beta \\ x_2^\beta \\ x_3^\beta \end{bmatrix}
$$

$$
+ \begin{bmatrix} -k_3(x_2^\beta - x_1^\beta)^3 \\ k_3(x_2^\beta - x_1^\beta)^3 - k_5(x_3^\beta - x_2^\beta)^3 \\ k_5(x_3^\beta - x_2^\beta)^3 \end{bmatrix} = \begin{bmatrix} F_J^{\beta\alpha} \\ 0 \\ 0 \end{bmatrix}
$$

(4.57)

$$
\begin{bmatrix} 0 & 0 & 0 \\ 0 & m_4 & 0 \\ 0 & 0 & m_5 \end{bmatrix} \begin{bmatrix} \ddot{x}_1^\gamma \\ \ddot{x}_2^\gamma \\ \ddot{x}_3^\gamma \end{bmatrix} + \begin{bmatrix} k_6 & -k_6 & 0 \\ -k_6 & (k_6 + k_8) & -k_8 \\ 0 & -k_8 & k_8 \end{bmatrix} \begin{bmatrix} x_1^\gamma \\ x_2^\gamma \\ x_3^\gamma \end{bmatrix}
$$

$$
+ \begin{bmatrix} -k_7(x_2^\gamma - x_1^\gamma)^3 \\ k_7(x_2^\gamma - x_1^\gamma)^3 - k_9(x_3^\gamma - x_2^\gamma)^3 \\ k_9(x_3^\gamma - x_2^\gamma)^3 \end{bmatrix} = \begin{bmatrix} F_J^{\gamma\alpha} \\ 0 \\ 0 \end{bmatrix}
$$

(4.58)

with junction boundary conditions on displacements and forces:

$$
x_1^\alpha = x_1^\beta = x_1^\gamma
$$
(4.59)

$$
F_J^{\alpha\beta} + F_J^{\beta\alpha} = 0
$$
(4.60)

$$
F_J^{\alpha\gamma} + F_J^{\gamma\alpha} = 0.
$$
(4.61)

The system parameters used for this study are $m_1 = 5, m_2 = 1, m_3 = 1, m_4 = 1, m_5 = 1, k_1 = 50, k_2 = 1, k_3 = 2, k_4 = 5, k_5 = 1, k_6 = 4, k_7 = 1, k_8 = 45$, and $k_9 = 1$.

149

The linear natural frequency of substructure α is $\omega^\alpha = 3.16$ rad/s, the first linear natural frequency of substructure β is $\omega_1^\beta = 0.69$ rad/s, and the first linear natural frequency of substructure γ is $\omega_1^\gamma = 1.40$ rad/s. Therefore the substructures β and γ are coupled through substructure α via weak coupling, since $\omega^\alpha \gg \omega_1^\beta, \omega_1^\gamma$.

Applying the procedures from section 4.3.2.1, the fixed-interface nonlinear mode manifolds for the fundamental modes of substructures β and γ are obtained. In this simple case the manifolds can be expressed as constraint functions in which the second linear modal position and velocity for a substructure depend on the first modal position and velocity of that substructure. The results obtained numerically for the modal position functions for the two multi-DOF substructures are shown in figures (4.3) and (4.4). For substructure β, the boundaries of the surface along modal position and velocity are $U_b = 2.6$ and $V_b = 1.79$, respectively, the number of Chebyshev polynomials along each u_k^e and v_k^e are $N_{p,u} = 3$ and $N_{p,v} = 2$ respectively, and the number of pieces along u_k and v_k are $N_u^e = 100$ and $N_v^e = 100$, respectively. For substructure γ, the boundaries of the surface along modal position and velocity are $U_b = 12.0$, $V_b = 16.78$, respectively, the number of Chebyshev polynomials along u_k and along v_k are $N_{p,u} = 3$ and $N_{p,v} = 2$, respectively, and the number of pieces along u_k and v_k are $N_u^e = 100$ and $N_v^e = 100$, respectively. Note that similar surfaces exist for the slaved modal velocities, although they are not shown here.

Applying the procedures from section 4.3.3, a nonlinear three-DOF ROM is obtained. In this case it describes the motions of the coupling mass and the first NNM for each of the attached substructures. This model is simulated with initial conditions initiated on the first fixed-interface nonlinear mode manifolds of substructures β and γ, as follows: $\eta_1^{N,\beta}(0) = 1.5, \eta_1^{N,\gamma}(0) = 0.4$, along with a constraint amplitude of $\eta^C(0) = 0.1$, with initial modal velocities taken to be zero.

For comparison purposes we use four models constructed in various manners. They are: the original five-DOF nonlinear model given in equation (4.55), a three-DOF nonlinear

model obtained using linear CMS (that is, by projecting the nonlinear subsystems onto their fixed-interface linear modes and the linear constraint mode), a three-DOF linear model obtained using linear CMS (this is the linearized version of the previous model), and the three-DOF nonlinear CMS model developed by the proposed approach. Figures (4.5) - (4.9) depict the comparison of the time responses of the various physical degrees of freedom obtained by simulations of these four models. In these figures the dashed line labeled NLCMS corresponds to the three-DOF nonlinear CMS model, the dash-dot line labeled LCMS corresponds to the three-DOF nonlinear model obtained using linear CMS, the dotted line labeled LCMSLPrb corresponds to the three-DOF linear model obtained using linear CMS, and the solid line labeled Original Model corresponds to the five-DOF original model. From the simulation results it is clear that the fixed-interface nonlinear CMS model outperforms the other low-order models, including the linear CMS model, which is the approach most commonly used in this type of problems. In particular, the NLCMS correctly captures the frequencies of the substructures, as well as the effects of their coupling.

It should be noted that there is a range of system parameters where this method gives satisfactory results. One particular trend worth noting is obtained by varying the stiffness to ground k_1. As k_1 is reduced and approaches the same order as the stiffnesses of the substructures, the fixed-interface approximation begins to break down and the accuracy of the NLCMS model deteriorates. On the other hand, as k_1 is increased, the NLCMS model becomes more accurate, but the amount of substructure interaction is reduced, leading to a system which consists of essentially decoupled motions for the two attached substructures.

4.5 A Class of Systems

In order to illustrate the general applicability of the proposed method, a class of nonlinear spring-mass systems is examined. This class of systems is schematically depicted in Figure 4.10, and naturally partitions into N_a appendage substructures, as shown in Figure 4.11.

151

This system has the same general features as the system in section 4.4 except that each substructure has $(N_{mass} + 1)$ DOFs. (Note that this is easily generalized to the case where the substructures have different number of DOF). In the following sections, the model of this class of systems is first developed and then a system having $N_a = 2$ and $N_{mass} = 20$ is used as an example.

4.5.1 Model Development

The component forms of the equations of motion of the $N = (N_a\ N_{mass} + 1)$-DOF system are given by

$$\sum_{j=1}^{N} m_{ij}\ \ddot{x}_j \quad + \quad \sum_{j=1}^{N} k_{ij}\ x_j \quad + \quad g_i(\boldsymbol{X}) = 0 \tag{4.62}$$

$$\text{for} \quad i = 1,\ 2,\ 3,\ ...,\ N.$$

The formulae for m_{ij}, k_{ij} and g_i can be found in the Appendix.

The component forms of the equations of motion for the individual substructures and the junction boundary conditions are given by

$$m_1\ \ddot{x}_1^\alpha + k_1\ x_1^\alpha = \sum_{S=\beta,\gamma,\delta,...} F_J^{\alpha S} \tag{4.63}$$

$$\sum_{j=1}^{(N_{mass}+1)} m_{ij}^S \ddot{x}_j^S \quad + \quad \sum_{j=1}^{(N_{mass}+1)} k_{ij}^S x_j^S \quad + \quad g_i^S(\boldsymbol{X^S}) = f_i^S \qquad (4.64)$$

for $\quad i = 1, 2, 3, \ldots, (N_{mass} + 1)$,

and $\quad S = \beta, \gamma, \delta, \ldots$

with junction boundary conditions on displacements and forces:

$$x_1^\alpha \;=\; x_1^\beta \;=\; x_1^\gamma \;=\; x_1^\delta \;=\; \ldots \qquad (4.65)$$

$$F_J^{\alpha\beta} + F_J^{\beta\alpha} \;=\; F_J^{\alpha\gamma} + F_J^{\gamma\alpha} \;=\; F_J^{\alpha\delta} + F_J^{\delta\alpha} \;=\; \ldots = 0. \qquad (4.66)$$

The formulae for m_{ij}^S, k_{ij}^S, g_i^S, and f_i^S can be found in the Appendix.

For bookkeeping of the indices, the procedures from section 4.3.2.1 are slightly modified. Instead of applying the coordinate transformation from equation (4.28) to equation (4.26), the coordinate transformation $\boldsymbol{X} = \boldsymbol{\Phi_N \eta_N}$ is applied to equations (4.20) and (4.21) with the interface fixed ($\boldsymbol{X_J} = \boldsymbol{0}$); this step also lead to equation (4.29).

Therefore the nonlinear vectors of the fixed-interface nonlinear equations of motion, expressed in fixed-interface linear modal coordinates of substructures S, are given in their component forms by

$$\tilde{g}_i^{N,S}(\boldsymbol{\eta}_N^S) \quad = \quad \sum_{p=1}^{n^S}\sum_{q=p}^{n^S}\sum_{r=q}^{n^S} b_{ipqr}^{N,S,*} \; \eta_p^{N,S} \; \eta_q^{N,S} \; \eta_r^{N,S} \tag{4.67}$$

$$\text{for} \quad i = 1,\, 2,\, 3,\, \ldots,\, n^S$$

$$\text{and} \quad S = \beta,\, \gamma,\, \delta,\, \ldots,$$

where the formulae for $b_{ipqr}^{N,S,*}$ can be found in the Appendix. Then the fixed-interface non-linear mode manifolds for the fundamental modes of substructures β, γ, ... are computed.

Next, the linear constraint modes of the substructures S are computed. Equation (4.64) is then transformed into linear modal coordinates using the coordinate transformation defined in section 4.3.2. The nonlinear vectors of the nonlinear equations of motion (expressed in linear modal coordinates of substructures S) are given in their component forms by

$$\tilde{g}_i^S(\boldsymbol{\eta}^S) \quad = \quad \sum_{p=1}^{(n^S+n_C)}\sum_{q=p}^{(n^S+n_C)}\sum_{r=q}^{(n^S+n_C)} b_{ipqr}^{S,*} \; \eta_p^S \; \eta_q^S \; \eta_r^S \tag{4.68}$$

$$\text{for} \quad i = 1,\, 2,\, 3,\, \ldots,\, (n^S + n_C)$$

$$\text{and} \quad S = \beta,\, \gamma,\, \delta,\, \ldots.$$

The formulae for $b_{ipqr}^{S,*}$ can be found in the Appendix.

4.5.2 Example

As an example we consider a system with $N_a = 2$ and $N_{mass} = 20$. In the following sections, the fundamental fixed-interface NNMs of substructures β and γ are first

developed. Then, by applying the procedures described in section 4.3.3, a three-DOF nonlinear CMS model is obtained which describes the motion of the coupling mass and the first NNM for each of the attached substructures. For comparison purposes, four other models are also developed. They are: the forty-one-DOF nonlinear original model given in equation (4.62), a forty-one-DOF nonlinear model obtained by using linear CMS that retains all the fixed-interface LNMs from individual appendage substructures β and γ ($n^\beta = 20$, $n^\gamma = 20$), a three-DOF nonlinear model obtained by using linear CMS that retains only the first fixed-interface LNM from individual appendage substructures β and γ ($n^\beta = 1$, $n^\gamma = 1$), and a three-DOF linear model obtained by using linear CMS (this is the linearized version of the previous model).

4.5.2.1 Substructure β

In this study, the system parameters used to construct the fixed-interface NNM of substructure β are first chosen such that the system is similar to the equal-length FE model of a rod under axial vibration, i.e., each block has the same mass and each spring has the same spring constant. For the discrete system with equal parameters and under axial vibration, the ratios of the higher linear natural frequencies to the fundamental linear natural frequency are closed to 3:1 (mode 2 to mode 1), 5:1 (mode 3 to mode 1), 7:1 (mode 7 to mode 1), etc., which are the ratios of the continuous system under axial vibration ([90]). Since the nonlinearities present in the system are cubic polynomials, the system will experience internal resonances. Moreover, the system parameters chosen in this way will result in weak nonlinear couplings between the fundamental linear mode and the higher modes, which causes the fundamental nonlinear mode shape to be close to the fundamental linear mode shape. To remove internal resonances from the system, and to generate stronger nonlinear coupling and modal distortion, the linear spring that connects the subsystem to ground is taken to be softer than the other springs. This causes the fundamental nonlinear mode shape to be very different from the fundamental linear mode shape at the large amplitudes. Some details of this result follow.

For the first trial, the system parameters used to construct the fixed-interface NNM of substructure β are $m_2 = m_3 = m_4 = ... = m_{21} = 1$, $k_2 = k_3 = k_4 = ... = k_{41} = 1000$.

The number of retained fixed-interface LNMs (n^β) is chosen to be 20. The first four fixed-interface (linear) natural frequencies are $\omega_1^\beta = 2.42$ rad/s, $\omega_2^\beta = 7.25$ rad/s, $\omega_3^\beta = 12.04$ rad/s, $\omega_4^\beta = 16.76$ rad/s. The first four fixed-interface LNMs are shown in Figure 4.12.

Figure 4.13 depicts coefficients of the pqr cubic nonlinear terms expressed in fixed-interface linear modal coordinates and associated with the first mode (master mode). Note that there are 1540 nonlinear terms ($(n^\beta \times (n^\beta + 1) \times (n^\beta + 2))/6$) for each retained fixed-interface LNM. The horizontal axis corresponds to the nth term (i.e. the first term is $(\eta_1^{N,\beta})^3$, the second term is $(\eta_1^{N,\beta})^2 \eta_2^{N,\beta}$,..., the last term is $(\eta_{20}^{N,\beta})^3$). Note that there are 20 envelopes in the figure, and each envelope corresponds to a value of the first index p. We can see that most of the coefficients are zero, which means that the first mode is not strongly coupled with higher retained fixed-interface LNMs, and therefore they will not be reflected in the NNM.

The first fixed-interface NNM manifold can be depicted as constraint surfaces depending on the first modal position and velocity. A total of thirty-eight such constraint surfaces are needed to describe motions on the first fixed-interface NNM manifold in the 40-dimensional state space. Samples of such surfaces are shown in Figures 4.14, 4.15, and 4.16, which correspond to the contribution from the second, third, and fourth fixed-interface linear mode amplitudes to the first fixed-interface NNM manifold. The boundaries of these surfaces along modal position and velocity are $U_b = 40.0$ and $V_b = 96.9$, respectively. The surfaces are obtained by using Chebyshev polynomials along u_k^e and v_k^e with $N_{p,u} = 3$ and $N_{p,v} = 2$, respectively, and the number of pieces along u_k and v_k to be $N_u^e = 50$ and $N_v^e = 50$, respectively.

Figure 4.17 depicts the time responses of the first fixed-interface mode displacement ob-

tained from two different models. The dashed line is the time response of the ROM defined at the end of section 4.2.2 with initial modal displacement $\eta_1^{N,\beta}(0) = 33.9$ and velocity $\dot{\eta}_1^{N,\beta}(0) = 0$. The solid line is the time response of the original model (20 DOFs) initiated on the fixed-interface NNM manifold. Figures 4.18, 4.19, and 4.20 depict the time responses of the second, third, and fourth, respectively, fixed-interface linear mode displacement obtained from the ROM and the original model. The dashed line is obtained by applying the master-slave constraints (depicted in Figures 4.14, 4.15, and 4.16) to the numerical solution of the ROM (the dashed line in Figure 4.17). The solid line is obtained from the 20-DOF original model. The time responses of the ROM and the original model are almost identical at the beginning, and as time progress they begin to diverge. From the linear natural frequencies, we can observe that $\omega_2^\beta \approx 3\omega_1^\beta$, $\omega_3^\beta \approx 2\omega_2^\beta - \omega_1^\beta$, and $\omega_4^\beta \approx \omega_3^\beta + \omega_2^\beta - \omega_1^\beta$, which indicates that there are internal resonances (to the first-order perturbation approximation ([79])) among these modes in the fixed-interface system of substructure β. Therefore, energy is being exchanged among the modes involved in the internal resonances, which cause the motion of the original model initiated on (in practice, very near) the first fixed-interface NNM to eventually leave the manifold. In order to obtain the ROM that embeds the internal resonances, a multi-mode invariant manifold formulation is needed, as described in [29], [71], and [42]. The multi-mode invariant manifold formulation is beyond the scope of the current study. From Figures 4.17, 4.18, 4.19, and 4.20, we can see that the contribution of the higher modes to the first fixed-interface NNM is less than 3% of the initial modal displacement $\eta_1^{N,\beta}(0) = 33.9$. Hence we expect that the one-mode nonlinear model, which is obtained by projecting the fixed-interface subsystem onto the first fixed-interface LNM, will yield a good time response, at least for a limited time interval.

Figure 4.21 depicts the time responses of the first fixed-interface modal displacement obtained from the linearized one-mode model, the one-mode nonlinear model, and the ROM. The dotted line is obtained from the linearized one-mode model, which is the linearized version of the one-mode nonlinear model. The dashed line is obtained from the one-mode nonlinear model, which is acquired by projecting the fixed-interface subsystem onto the first fixed-interface linear mode. The solid line is obtained from the NNM ROM. We can

see that the time response of the one mode nonlinear model is close to the time response of the ROM for many periods. This is due to the fact that the first fixed-interface linear mode is not strongly coupled with the higher retained fixed-interface LNMs, as mentioned above.

To eliminate the internal resonances from the fixed-interface subsystem and to yield strong coupling between the first fixed-interface linear mode and higher linear modes, a new set of system parameters are introduced. These will make enhance the nonlinear aspects of the problem to more fully demonstrate the accuracy of the proposed approach. By observing coefficients $b_{ipqr}^{N,S}$ and $b_{hpqr}^{N,S}$ from the Appendix and Figure 4.12, we can see that the displacements of DOFs near the fixed-interface of the low-frequency linear mode shapes are small, which cause many of $b_{1pqr}^{N,\beta,*}$ coefficients to be small, or zero. In order to yield stronger coupling between the first fixed-interface linear mode and higher modes, a new set of system parameters are considered: $m_2 = m_3 = m_4 = ... = m_{21} = 1$, $k_2 = 10, k_3 = k_4 = ... = k_{41} = 1000$, which allows DOF near the interface to have significant displacements, in particular for the fundamental mode.

Twenty fixed-interface linear natural frequencies are presented in Table 4.1, and it is seen that they do not possess low-order internal resonances among them. Figure 4.22 depicts the first four fixed-interface LNMs obtained from using the second set of parameters. Figure 4.23 depicts the coefficients of the pqr cubic nonlinear terms expressed in fixed-interface linear modal coordinates and associated with the first mode (master mode), obtained using these parameters. Comparing Figure 4.23 with Figure 4.13 indicates that the first fixed-interface linear mode strongly couples with higher modes for this set of parameters.

Note that for these parameters the first fixed-interface linear mode is similar to a rigid-body mode. Therefore one might argue that the spring next to the wall is soft and the other springs are very stiff, which would imply that the fixed-interface subsystem would behave like a one-DOF lumped-mass system. Therefore the one-mode nonlinear model obtained by projecting the fixed-interface subsystem onto the first fixed-interface linear mode would be

adequate to capture the dynamics of the subsystem. However, Figure 4.23 indicates that the first fixed-interface linear mode is strongly coupled with higher retained fixed-interface LNMs, which indicates that such an argument is not justified. Hence, the concept of NNM is needed in order to capture the correct dynamics in the large amplitude regime, which is illustrated in following results.

Figures 4.24, 4.25, and 4.26 depict the contributions from the second, third, and fourth fixed-interface linear mode amplitudes to the first fixed-interface NNM manifold. The surfaces are obtained by using $U_b = 3.0$, $V_b = 2.06$, $N_{p,u} = 3$, $N_{p,v} = 2$, $N_u^e = 40$ and $N_v^e = 40$. Note that the maximum contribution from the second linear mode amplitudes to the first NNM manifold is around 10%, which indicates significant coupling between the first and second modes.

Figure 4.27 depicts the time responses of the first fixed-interface mode displacement obtained from four different models. The dashed-dotted line, the dotted line, and the dashed line are the time responses of the linearized one-mode model, the one-mode nonlinear model, and the ROM (based on invariant manifolds), respectively, with initial modal displacement $\eta_1^{N,\beta}(0) = 1.20$ and velocity $\dot{\eta}_1^{N,\beta}(0) = 0$. The solid line is the time response of the original model with initial conditions initiated on the fixed-interface NNM manifold. The time responses from the ROM and the original model are nearly identical.

Figures 4.28, 4.29, and 4.30 depict the time responses of the second, third, and fourth, respectively, fixed-interface linear mode displacements obtained from the ROM and the original model. The dashed and solid lines are the time responses of the ROM and the original model, respectively. The time responses from the ROM are close to the original model, and the errors are very small when compared with the amplitude of the overall response (> 1). (From these figures, there exist discontinuities in the time responses since continuity between patches of the constraint surfaces is not enforced. However if the subdomains are taken to be sufficiently small, these jumps will be small.)

Figures 4.31 and 4.32 depict the time responses of the physical displacements x_2^β and x_{21}^β, respectively, (the leftmost masses of each substructure) with the interface fixed for the linearized one-mode model, the one-mode model, the ROM, and the original model. The time responses from the ROM and the original model are nearly identical. The time responses from the linearized one-mode model and the one-mode nonlinear model are significantly different from the original model, since the contribution from the higher fixed-interface linear modes is not accounted for in those two models. In other words, the motions of those two models occur on a flat approximation of the invariant manifold (i.e., the linear eigenspace), which is inadequate in the present case.

Figure 4.33 depicts the comparison of deflections of all physical coordinates $x_i^\beta(t)$ at three different times: $t = 0$, the initial time, where the system is at its peak configuration; $t = \dfrac{T_{nl}}{8}$, one eighth of a period of the nonlinear system; and $t = \dfrac{T_{nl}}{4}$, a quarter of the period, at which the system is at zero displacement (with nonzero velocity, of course). Two cases are shown: the first fixed-interface LNM and the first fixed-interface NNM. Note that the shape of deflection on the linear mode manifold (linear mode shape) does not change with time, however the deflection shape on the nonlinear mode manifold (that is, the nonlinear mode shape) does change with time, due to the time-dependent contributions from the other retained linear modes, which is significant for this case. The distortion of the NNM is evident.

Note that the computational time required to obtain the manifold for this case (with $N_u^e = 40$ and $N_v^e = 40$)is about 30 minutes. The computational time associated with the simulation of the twenty-one-DOF original model is about 13 seconds. The computational time associated with the simulation of the ROM is about 2 seconds. Thus, if one is to carry out many simulations, the generation of the ROM is worthwhile.

4.5.2.2 Substructure γ

The system parameters used for substructure γ are $m_{22} = m_{23} = m_{24} = \ldots = m_{41} = 1$,

$k_{42} = 42.5$, $k_{43} = k_{44} = ... = k_{81} = 4250$. This yields strong nonlinear coupling between the linear modes, just as was done for substructure β.

The results that are analogous to Table 4.1 and Figures 4.22 to 4.33 for substructure β are shown in Table 4.2 and Figures 4.34 to 4.45. To avoid redundancy, detailed descriptions are not repeated here. Note that since the ratio among the linear and nonlinear spring coefficients are the same as for substructure β, the surfaces shown in Figures 4.36 to 4.38, obtained by using $U_b = 3.0$, $V_b = 4.24$, $N_{p,u} = 3$, $N_{p,v} = 2$, $N_u^e = 40$, $N_v^e = 40$, are similar to those shown in Figures 4.24 to 4.26. However, the fixed-interface linear-mode natural frequencies of substructure γ are higher than those of substructure β.

4.5.2.3 Synthesized Structure

The system parameters for the base structure (substructure α) are $m_1 = 1,500$ and $k_1 = 24,000$, which yields $\omega_C = 4.0$, which is close to the fundamental frequencies of the substructures. However, since this coupling structure is very stiff, its response will remain small, consistent with the assumptions needed to employ linear constraint modes.

A comparison of the linear natural frequencies of the three-DOF linear-CMS nonlinear model and the three-DOF nonlinear-CMS model is shown in Table 4.3. Comparison of the first sixteen Linear natural frequencies of the forty-one-DOF linear-CMS nonlinear model and the forty-one-DOF original model are shown in Table 4.4. These two comparisons are used as the first check to verify that the synthesized models are correct. The linear natural frequencies from Table 4.3 are in agreement with those from Table 4.4, at least up to the third decimal digit. Note that the forty-one-DOF linear-CMS nonlinear model is equivalent to the forty-one-DOF original model since the modal matrices from substructures β and γ together represent a complete set of forty-one bases that are used to describe the original model in the synthesized linear-modal coordinates.

Figure 4.46 depicts the time responses of the first synthesized fixed-interface mode dis-

placement $\eta_1^{N,\beta}$ obtained from four different models. The dashed-dotted line, the dotted line, and the dashed line are the time responses of the three-DOF linear-CMS linear model, the three-DOF linear-CMS nonlinear model, and the three-DOF nonlinear-CMS model, respectively, with initial modal displacements $\eta_1^{N,\beta}(0) = 1.2$, $\eta_1^{N,\gamma}(0) = 1.2$, $\eta^C(0) = 0.03$ and modal velocities $\dot{\eta}_1^{N,\beta}(0) = 0$, $\dot{\eta}_1^{N,\gamma}(0) = 0$, $\dot{\eta}^C(0) = 0$. The solid line is the time response of the forty-one-DOF linear-CMS nonlinear model with initial conditions initiated on the fixed-interface NNM manifolds of substructures β and γ (this is the full model). We can see that the time responses of the three-DOF nonlinear-CMS model and the forty-one-DOF linear-CMS nonlinear model are nearly identical over the time interval shown, and the other two models show significant errors, especially the fully linear model.

Figures 4.47, 4.48, and 4.49 depict the time responses of the second, third, and fourth, respectively, synthesized fixed-interface linear mode displacements ($\eta_2^{N,\beta}$, $\eta_3^{N,\beta}$, and $\eta_4^{N,\beta}$), respectively, obtained from the three-DOF nonlinear-CMS model and the forty-one-DOF linear-CMS nonlinear model. The dashed and solid lines are the time responses of the three-DOF nonlinear-CMS model and the forty-one-DOF linear-CMS nonlinear model, respectively. They are nearly identical except that the forty-one-DOF linear-CMS nonlinear model has some high frequency "ringing". This is because the initial conditions for the forty-one-DOF linear-CMS nonlinear model are initiated on the fixed-interface NNM manifolds of substructures β and γ, which are only an approximation of the actual 6-dimensional NNM invariant manifold of the whole structure.

Figures 4.50, 4.51, 4.52, and 4.53 are analogous to Figures 4.46, 4.47, 4.48, and 4.49. Therefore, the descriptions similar to those given for substructure β are not repeated here. The comments related to those analogous figures are also applicable to substructure γ. Note that since the first fixed-interface nonlinear-mode natural frequency of substructure γ is higher than that of substructure β, the time windows in Figures 4.50, 4.51, 4.52, and 4.53 are adjusted in order to depict clear comparisons.

Figures 4.54, 4.55, 4.56, 4.57, and 4.58 depict the time responses of masses m_1, m_2, m_{21},

m_{22}, and m_{41}, respectively, obtained from four different models (these are the coupling mass and the end masses of each substructure). The dashed-dotted lines and the dotted lines are the time responses of the three-DOF linear-CMS linear model and the three-DOF linear-CMS nonlinear model, respectively, obtained by applying the coordinate transformations defined in section 4.3.2 to the time responses of the synthesized fixed-interface linear modal coordinates of both models with $n^\beta = 1$, $n^\gamma = 1$, and $n_C = 1$. The dashed lines are the time responses of the three-DOF nonlinear-CMS model obtained by applying the coordinate transformations defined in section 4.3.2 to the time responses of the synthesized fixed-interface linear modal coordinates having $n^\beta = 20$, $n^\gamma = 20$, and $n_C = 1$. The solid lines are the time responses of the forty-one-DOF original model with initial conditions initiated on the fixed-interface NNM manifolds of substructures β and γ. It is seen that the time responses of the three-DOF nonlinear-CMS model and the forty-one-DOF original model are nearly identical. However, the time responses of the three-DOF linear-CMS linear model and the three-DOF linear-CMS nonlinear model are quite different from the time responses of the forty-one-DOF original model. This is due to the fact that the contributions from the higher fixed-interface linear modes are not accounted for in those two models. In other words, the motions of those two models occur on the flat approximation of the invariant manifold of dimension 6, which is not a good approximation in this case. (Note that such an approximation would be quite good for the original set of parameters, for which the modal coupling was small.)

Figures 4.59 and 4.60 depict the time responses of the first synthesized fixed-interface mode displacements $\eta_1^{N,\beta}$ and $\eta_1^{N,\gamma}$, respectively, obtained from the three-DOF nonlinear-CMS model and the forty-one-DOF linear-CMS nonlinear model. The dashed lines are the time responses of the three-DOF nonlinear-CMS model with initial modal displacements $\eta_1^{N,\beta}(0) = 1.3$, $\eta_1^{N,\gamma}(0) = 1.3$, $\eta^C(0) = 0.04$ and modal velocities $\dot{\eta}_1^{N,\beta}(0) = 0$, $\dot{\eta}_1^{N,\gamma}(0) = 0$, $\dot{\eta}^C(0) = 0$. The solid lines are the time response of the forty-one-DOF linear-CMS nonlinear model with initial conditions initiated on the fixed-interface NNM manifolds of substructures β and γ. It is seen that the time responses of the forty-one-DOF linear-CMS nonlinear model starts to deviate from the three-DOF nonlinear-CMS model

163

after several oscillations. This indicates that at these initial conditions, with the base-structure parameters $m_1 = 1,500$ and $k_1 = 24,000$, the actual NNM invariant manifold of the whole structure deviates from the fixed-interface NNM manifolds of substructures β and γ. Note that we also performed a numerical experiment by fixing the ratio between m_1 and k_1 and reducing their values. It was found that the valid time domains of the fixed-interface NNM manifolds of substructures β and γ are reduced as well. This is expected to occur, since this parameter trend allows more interaction between substructures β and γ. This causes the actual NNM invariant manifold to deviate further from the fixed-interface NNM manifolds of the individual substructures, especially for large-amplitude motions.

Finally, the computational time associated with the simulation of the three-DOF nonlinear-CMS model is compared with that of the forty-one-DOF linear-CMS nonlinear model. It takes about 180 seconds to simulate the forty-one-DOF linear-CMS nonlinear model. However it takes only 60 seconds to simulate the three-DOF nonlinear-CMS model, which is a factor of three lower. The primary reason for this is that a smaller time step (a factor of 2.5 smaller) is needed for the ode-solver to integrate the stiff forty-one-DOF linear-CMS nonlinear model. Therefore, in terms of computational time associated with the simulation, the three-DOF nonlinear-CMS model does not have much advantage over the forty-one-DOF linear-CMS nonlinear model, as we might expect. This is mainly due to the fact that one is required to compute the nonlinear update terms $\tilde{g}_r^{C,update}$ in equation (4.44) of both substructures, which represent nonlinear terms that arise from the slave fixed-interface linear-modal-coordinate equations of motion. This is the same scenario as for the forty-one-DOF linear-CMS nonlinear model, since all nonlinear terms in this model need to be computed. This situation is in contrast to the individual fixed-interface substructures. From section 4.5.2.1, it can be seen that the simulation time of the ROM is a factor of 6.5 smaller than the simulation time of the twenty-DOF original model. This is because the nonlinear terms of the master mode EOM are only computed in order to simulate the ROM, but all nonlinear terms in the twenty-DOF original model must be computed in order to simulate the original model.

4.6 Conclusions

In this chapter we have shown how to extend the fixed-interface linear CMS technique of Craig and Bampton ([62]) to nonlinear structures by making use of fixed-interface NNMs in place of fixed-interface LNMs. This approach allows one to build nonlinear reduced-order models with improved accuracy for systems that are composed of assemblies of substructures. The first example system presented here is quite simple, and the model reduction is not very significant (from five to three DOFs). A second system with many more DOFs is also used, and it shows a significant reduction in model size (from forty-one to three DOFs). In fact, the NNM method has been developed to the point where it can be applied to systems with thousands of DOFs. The roadblock to pushing this method further is that it is very computationally demanding to generate substructure ROM with more than one DOF using a NNM approach ([42]). Current work is focusing on systems with many more DOFs at the unreduced substructure level, and it includes substructures that are modeled by nonlinear FE techniques.

4.7 Tables

i^{th} Mode	ω_i^β	i^{th} Mode	ω_i^β
1	0.68596232102650	11	44.72697600017000
2	5.06072722592600	12	48.09670186700000
3	9.94306090168100	13	51.17011958090000
4	14.79648130027000	14	53.92824229550000
5	19.56717359004000	15	56.35403805246000
6	24.22073003072000	16	58.43253131062000
7	28.72676467269000	17	60.15089310481000
8	33.05675986752000	18	61.49851874983000
9	37.18364689122000	19	62.46709231770000
10	41.08177243723000	20	63.05063732260000

Table 4.1. Fixed-interface linear natural frequencies of substructure β using the second-trial parameters.

i^{th} Mode	ω_i^γ	i^{th} Mode	ω_i^γ
1	1.41414755239200	11	92.20702318159000
2	10.43295644747000	12	99.15389102074001
3	20.49814516979000	13	105.4899039538000
4	30.50372764424000	14	111.1759195941000
5	40.33876175326000	15	116.1768256602000
6	49.93231412311000	16	120.4617492830000
7	59.22174251389000	17	124.0042428732000
8	68.14825628723000	18	126.7824443123000
9	76.65605183909000	19	128.7792098755000
10	84.69224352313999	20	129.9822187218000

Table 4.2. Fixed-interface linear natural frequencies of substructure γ.

i^{th} Mode	ω_i^{LCMS}	i^{th} Mode	ω_i^{NLCMS}
1	0.68582383924810	1	0.68582383933910
2	1.41280504607300	2	1.41280505021300
3	4.00456599773800	3	4.00460940350200

Table 4.3. Comparison of the linear natural frequencies of the three-DOF linear-CMS nonlinear model and the three-DOF nonlinear-CMS model.

i^{th} Mode	$\omega_i^{LCMS,41DOF}$	i^{th} Mode	ω_i^{OM}
1	0.685823839247	1	0.68582383924720
2	1.41280504587300	2	1.41280504587300
3	4.00452879688600	3	4.00452879688500
4	5.06079466571000	4	5.06079466571000
5	9.94306486412500	5	9.94306486412500
6	10.43301741537000	6	10.43301741538000
7	14.79648235748000	7	14.79648235748000
8	19.56717401354000	8	19.56717401354000
9	20.49815228625000	9	20.49815228625000
10	24.22073023840000	10	24.22073023840000
11	28.72676478757000	11	28.72676478757000
12	30.50372969952000	12	30.50372969952000
13	33.05675993624000	13	33.05675993624000
14	37.18364693456000	14	37.18364693456000
15	40.33876259811000	15	40.33876259810000
16	41.08177246556000	16	41.08177246556000

Table 4.4. Comparison of the first-sixteen linear-natural frequencies of the forty-one-DOF linear-CMS nonlinear model and the forty-one-DOF original model.

4.8 Figures
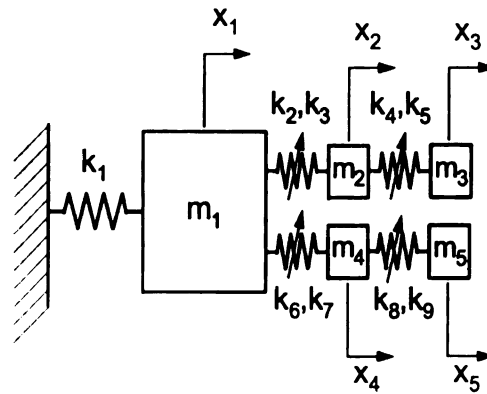
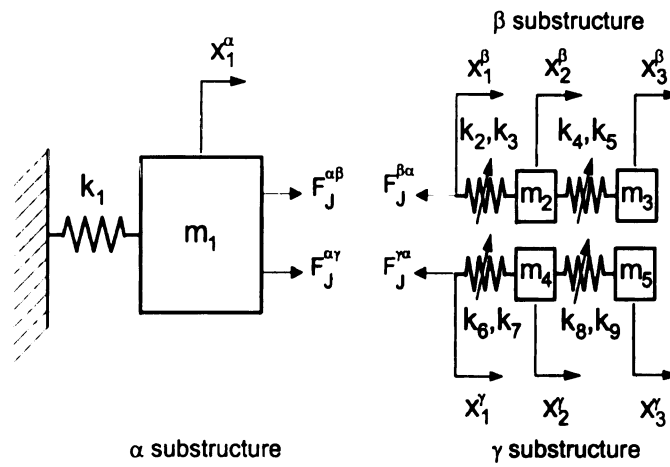Figure 4.1. A five-DOF nonlinear spring-mass system.
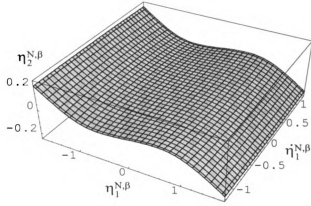

Figure 4.2. System substructures.

Figure 4.3. The contribution of the second fixed-interface linear mode amplitude $\eta_2^{N,\beta} = X_2^\beta(\eta_1^{N,\beta}, \dot{\eta}_1^{N,\beta})$ to the first fixed-interface nonlinear mode manifold of substructure β.
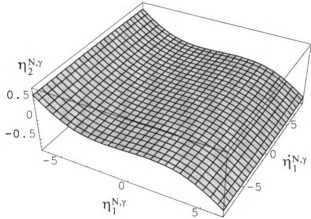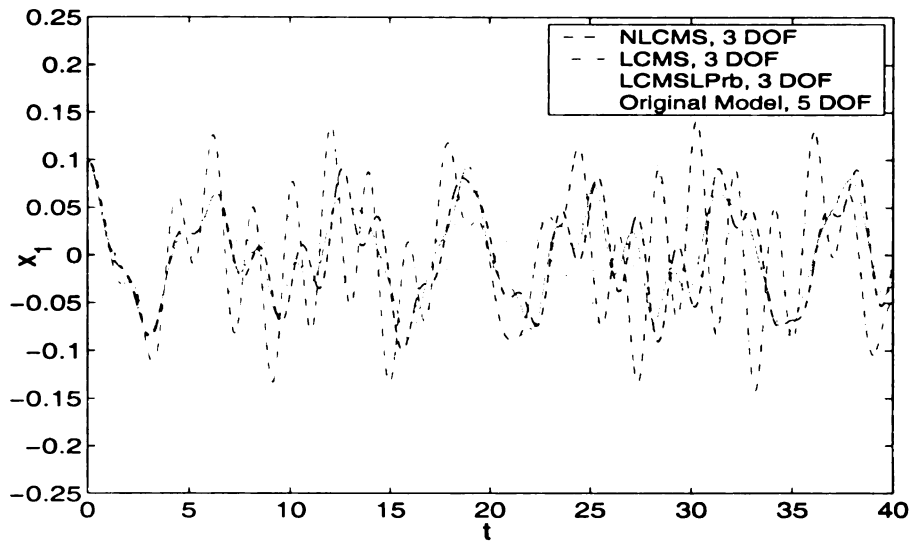

Figure 4.4. The contribution of the second fixed-interface linear mode amplitude $\eta_2^{N,\gamma} = X_2^\gamma(\eta_1^{N,\gamma}, \dot{\eta}_1^{N,\gamma})$ to the first fixed-interface nonlinear mode manifold of substructure γ.

Figure 4.5. The time response of the displacement x_1 of mass m_1 from Figure 4.1, which corresponds to x_1^α, x_1^β, and x_1^γ from Figure 4.2, for the nonlinear-CMS model, the linear-CMS nonlinear model, the linear-CMS linear model, and the original model.
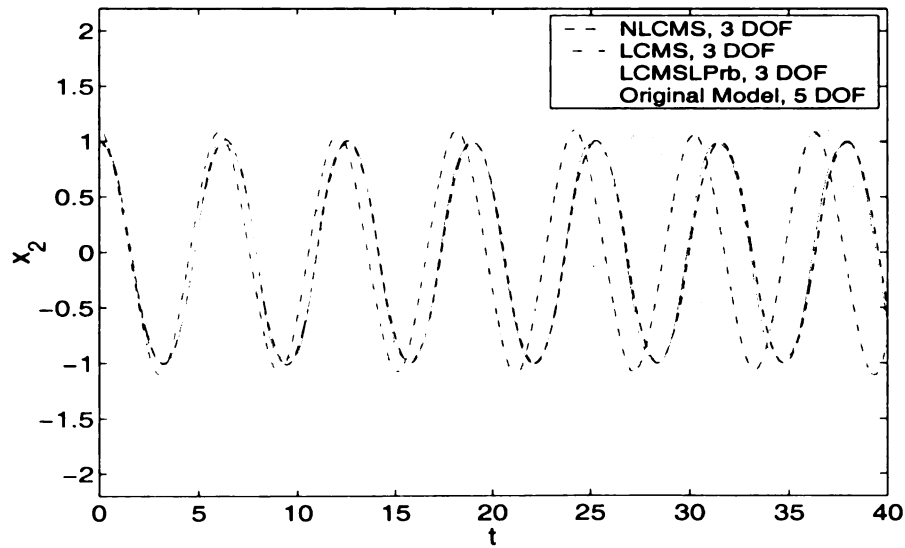
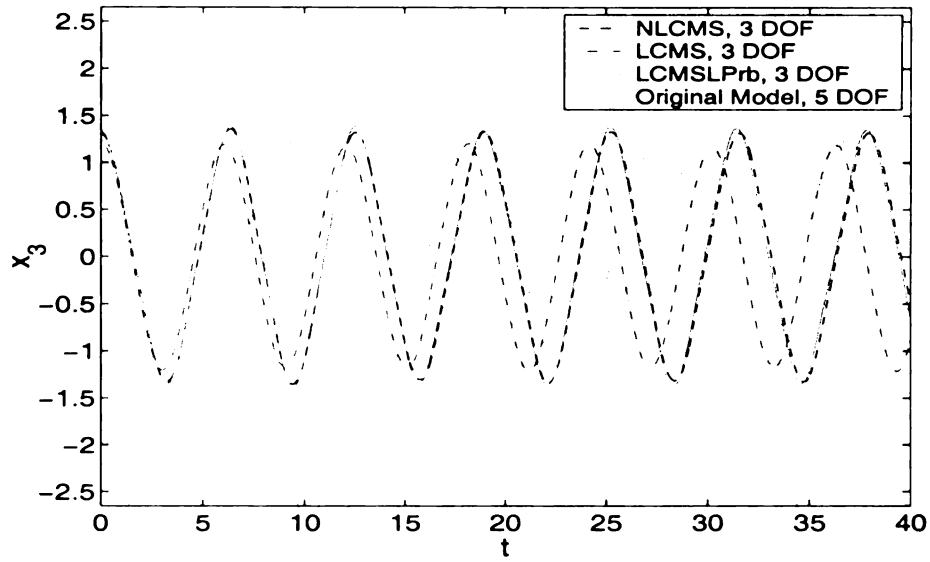Figure 4.6. The time responses of the displacement x_2 from Figure 4.1, which corresponds to x_2^β from Figure 4.2, for the nonlinear-CMS model, the linear-CMS nonlinear model, the linear-CMS linear model, and the original model.
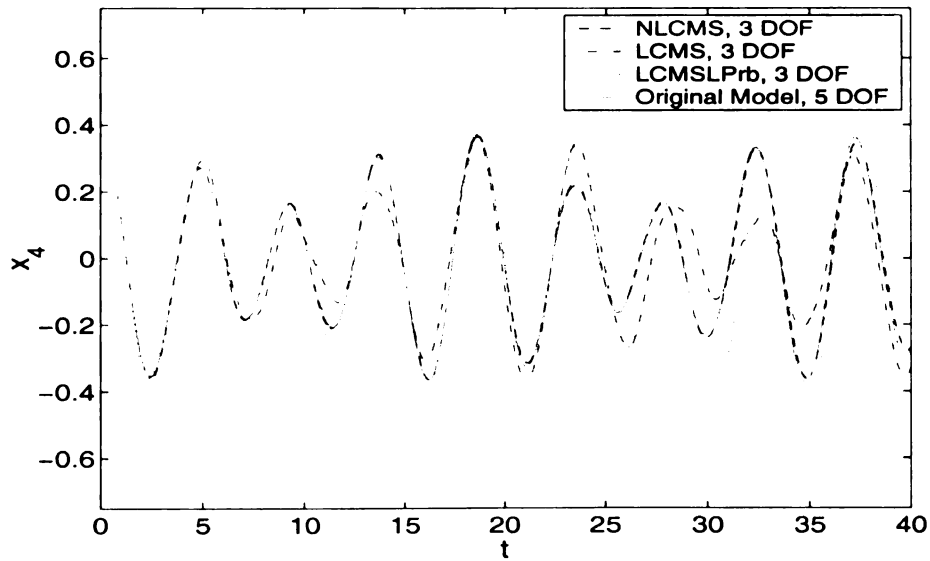
Figure 4.7. The time responses of the displacement x_3 from Figure 4.1, which corresponds to x_3^β from Figure 4.2, for the nonlinear-CMS model, the linear-CMS nonlinear model, the linear-CMS linear model, and the original model.
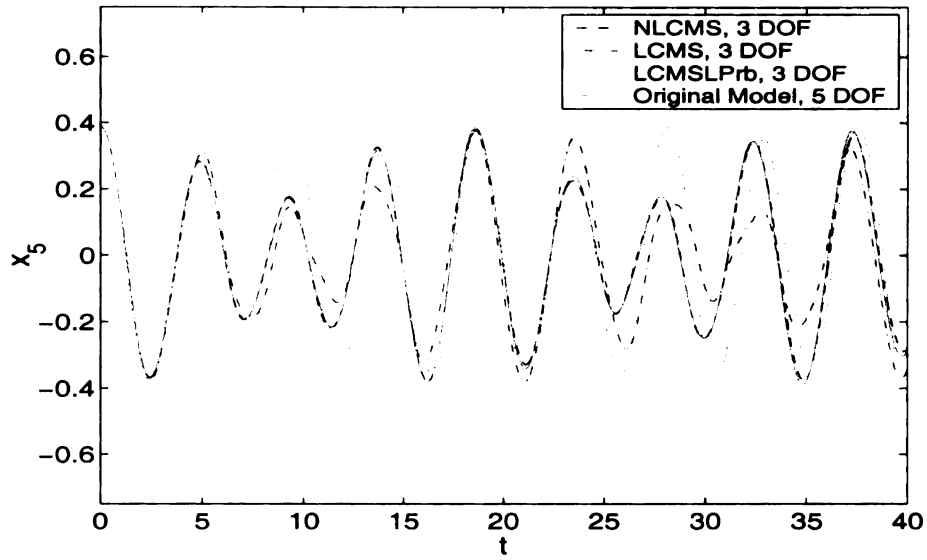

Figure 4.8. The time responses of the displacement x_4 from Figure 4.1, which corresponds to x_2^γ from Figure 4.2, for the nonlinear-CMS model, the linear-CMS nonlinear model, the linear-CMS linear model, and the original model.

Figure 4.9. The time responses of the displacement x_5 from Figure 4.1, which corresponds to x_3^γ from Figure 4.2, for the nonlinear-CMS model, the linear-CMS nonlinear model, the linear-CMS linear model, and the original model.
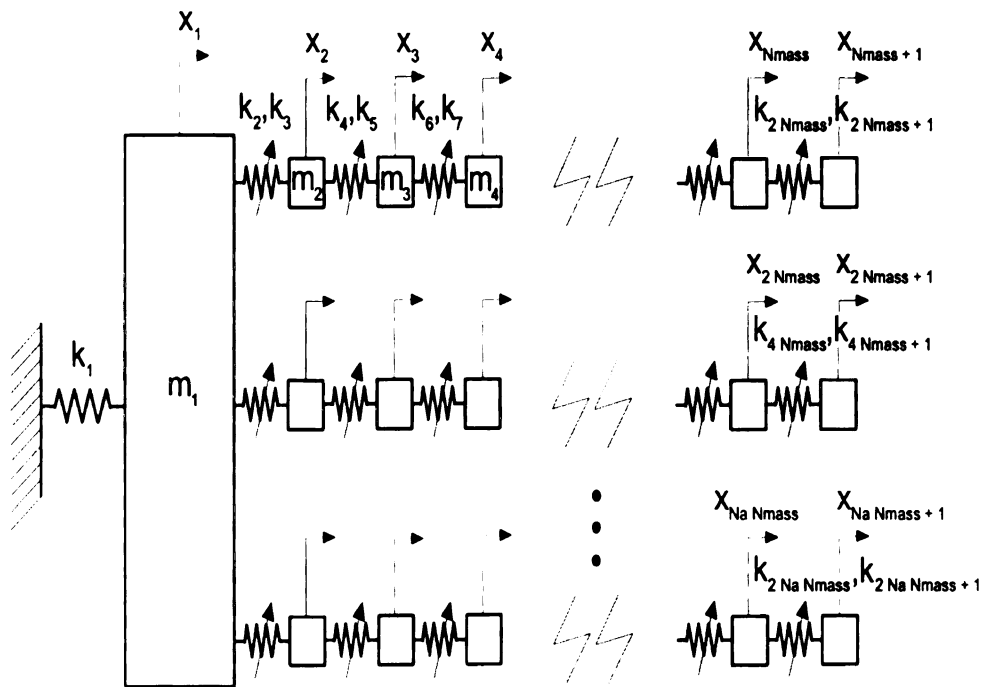

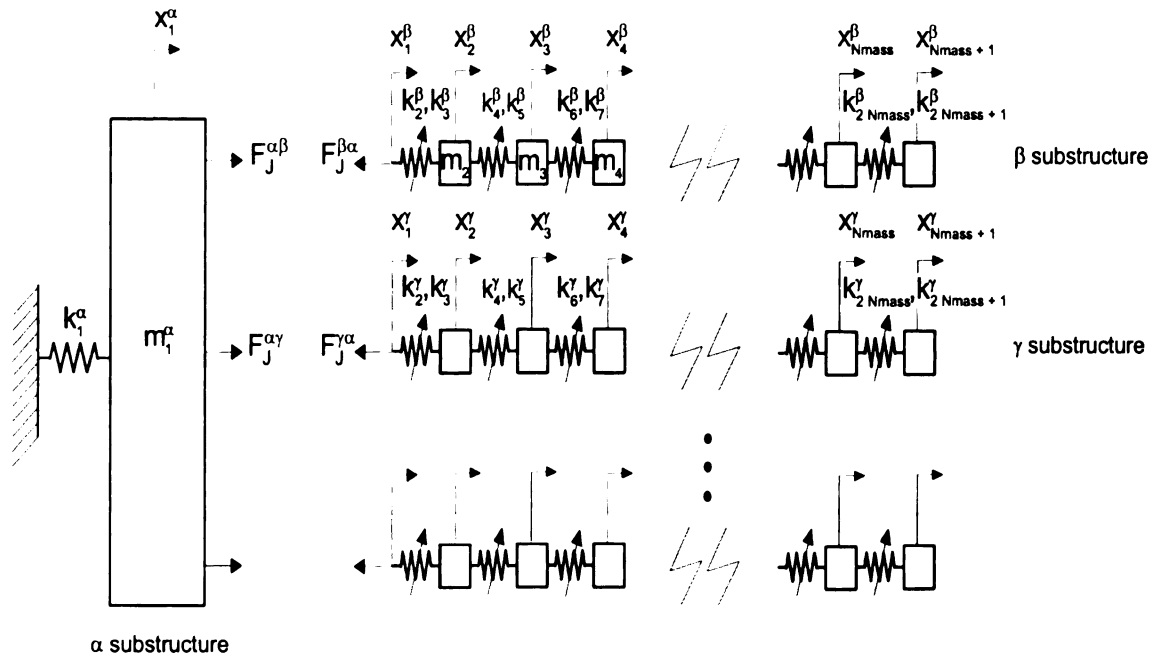Figure 4.10. A class of nonlinear spring-mass system.
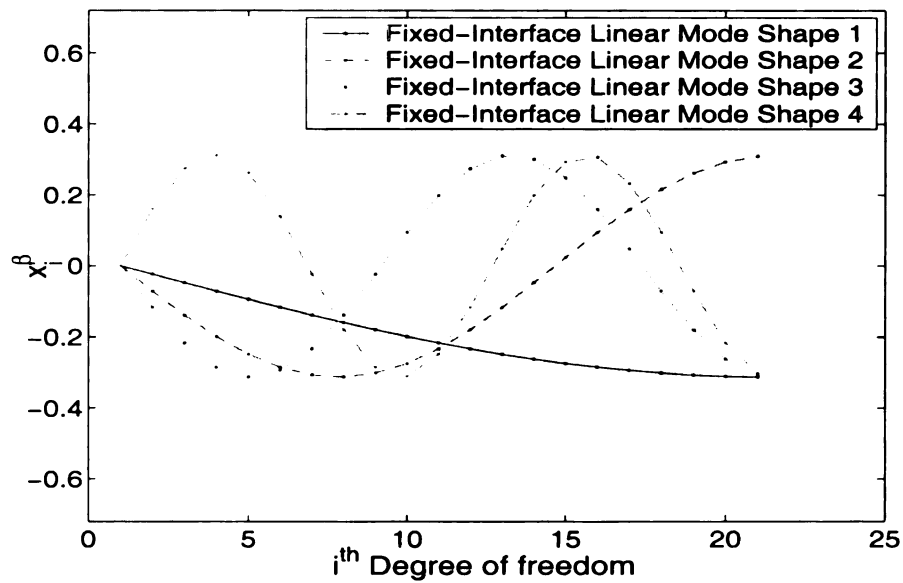
Figure 4.11. System substructures.

Figure 4.12. The first four fixed-interface LNMs of substructure β using the first-trial parameters.
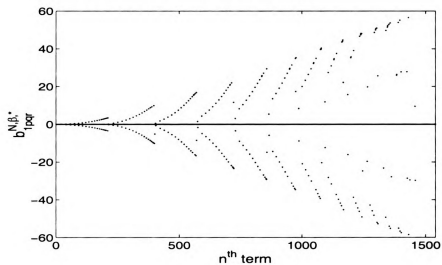
Figure 4.13. The coefficients of the *pqr* cubic nonlinear terms expressed in fixed-interface linear modal coordinates and associated with the first mode (master mode) of substructure β using the first-trial parameters.
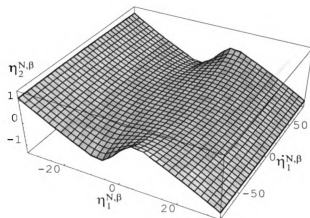

Figure 4.14. The contribution of the second fixed-interface linear mode amplitude $\eta_2^{N,\beta} = X_2^{\beta}(\eta_1^{N,\beta}, \dot{\eta}_1^{N,\beta})$ to the first fixed-interface nonlinear mode manifold of substructure β using the first-trial parameters.
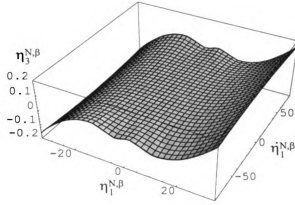
Figure 4.15. The contribution of the third fixed-interface linear mode amplitude $\eta_3^{N,\beta} = X_3^\beta(\eta_1^{N,\beta}, \dot{\eta}_1^{N,\beta})$ to the first fixed-interface nonlinear mode manifold of substructure β using the first-trial parameters.
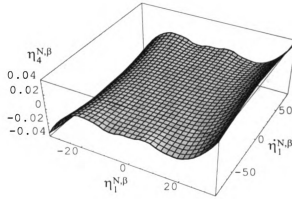

Figure 4.16. The contribution of the fourth fixed-interface linear mode amplitude $\eta_4^{N,\beta} = X_4^\beta(\eta_1^{N,\beta}, \dot{\eta}_1^{N,\beta})$ to the first fixed-interface nonlinear mode manifold of substructure β using the first-trial parameters.
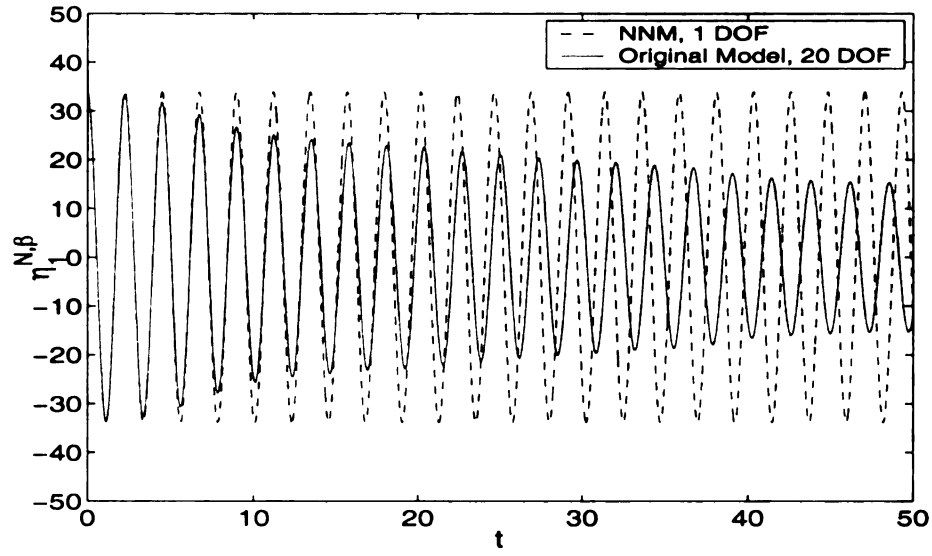
Figure 4.17. The time responses of the first fixed-interface mode displacement $\eta_1^{N,\beta}$ for the ROM and the original model of substructure β using the first-trial parameters.

Figure 4.18. The time responses of the second fixed-interface linear mode displacement $\eta_2^{N,\beta} = X_2^\beta(\eta_1^{N,\beta}, \dot\eta_1^{N,\beta})$ for the ROM and the original model of substructure β using the first-trial parameters.
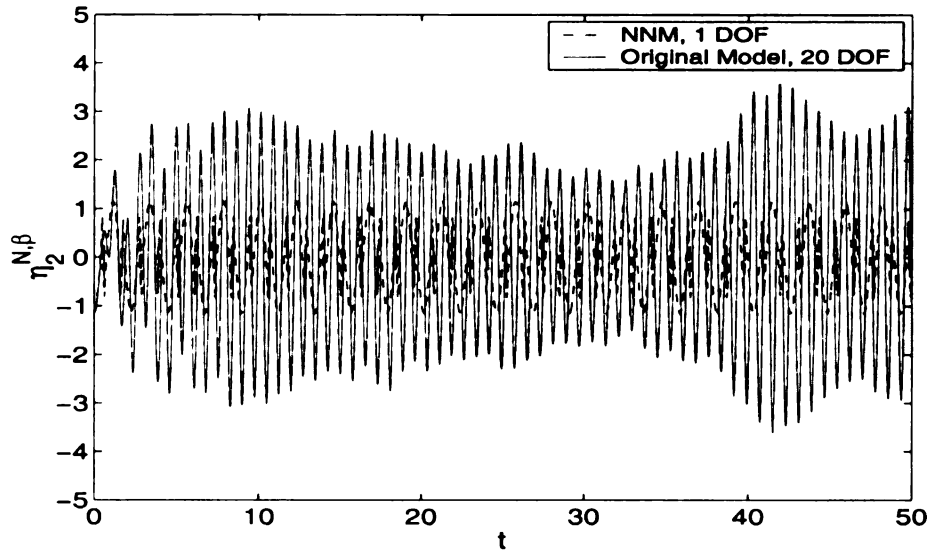
Figure 4.19. The time responses of the third fixed-interface linear mode displacement $\eta_3^{N,\beta} = X_3^\beta(\eta_1^{N,\beta}, \dot{\eta}_1^{N,\beta})$ for the ROM and the original model of substructure β using the first-trial parameters.
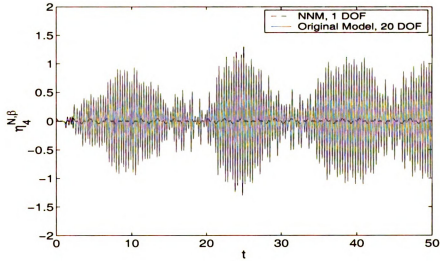
Figure 4.20. The time responses of the fourth fixed-interface linear mode displacement $\eta_4^{N,\beta} = X_4^\beta(\eta_1^{N,\beta}, \dot{\eta}_1^{N,\beta})$ for the ROM and the original model of substructure β using the first-trial parameters.
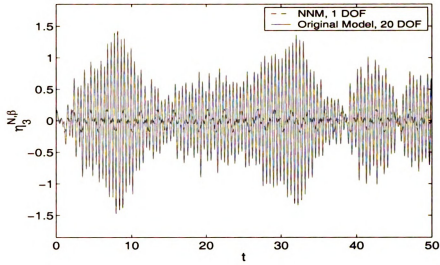
Figure 4.21. The time responses of the first fixed-interface mode displacement $\eta_1^{N,\beta}$ for the linearized one-mode model, the one-mode model, and the ROM of substructure β using the first-trial parameters.
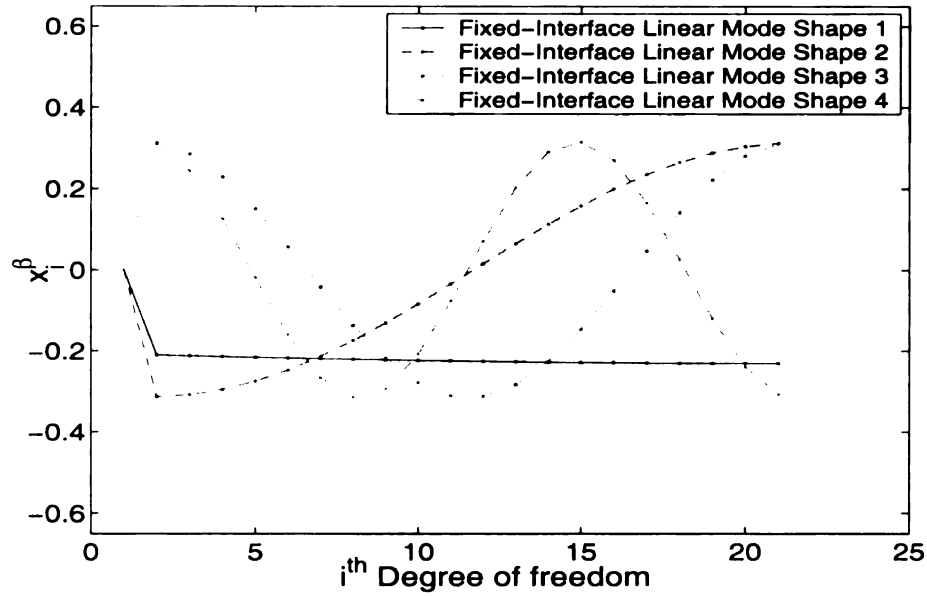
Figure 4.22. The first four fixed-interface LNMs of substructure β using the second-trial parameters.
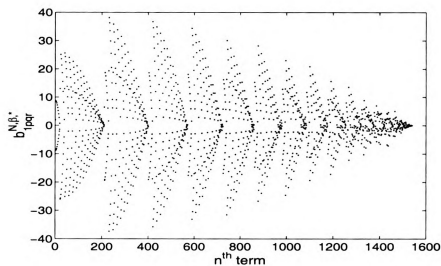
Figure 4.23. The coefficients of the *pqr* cubic nonlinear terms expressed in fixed-interface linear modal coordinates and associated with the first mode (master mode) of substructures β using the second-trial parameters.

Figure 4.24. The contribution of the second fixed-interface linear mode amplitude $\eta_2^{N,\beta} = X_2^{\beta}(\eta_1^{N,\beta}, \dot{\eta}_1^{N,\beta})$ to the first fixed-interface nonlinear mode manifold of substructure β using the second-trial parameters.
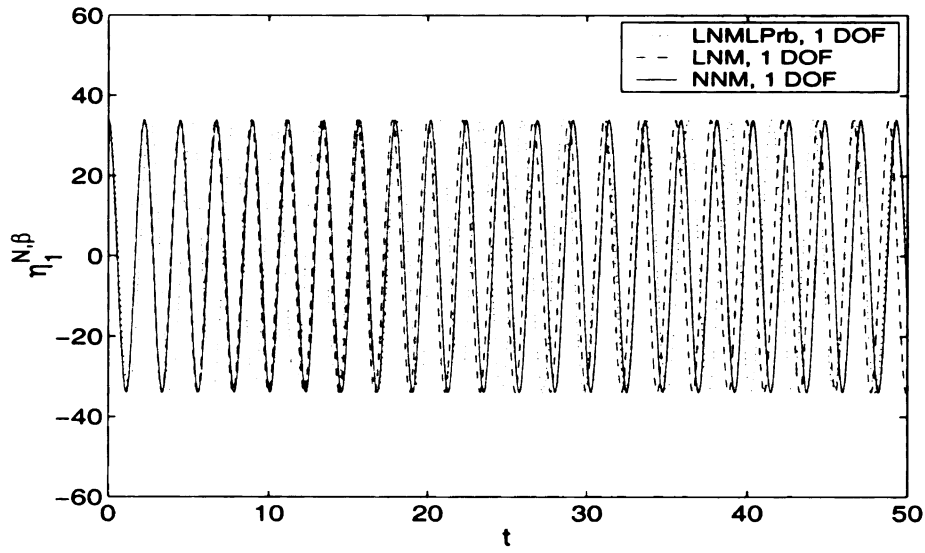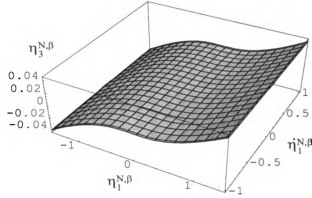
Figure 4.25. The contribution of the third fixed-interface linear mode amplitude $\eta_3^{N,\beta} = X_3^\beta(\eta_1^{N,\beta}, \dot{\eta}_1^{N,\beta})$ to the first fixed-interface nonlinear mode manifold of substructure β using the second-trial parameters.
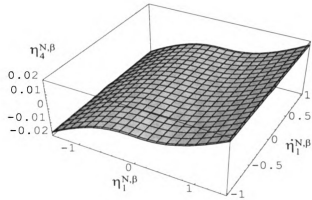
Figure 4.26. The contribution of the fourth fixed-interface linear mode amplitude $\eta_4^{N,\beta} = X_4^\beta(\eta_1^{N,\beta}, \dot{\eta}_1^{N,\beta})$ to the first fixed-interface nonlinear mode manifold of substructure β using the second-trial parameters.
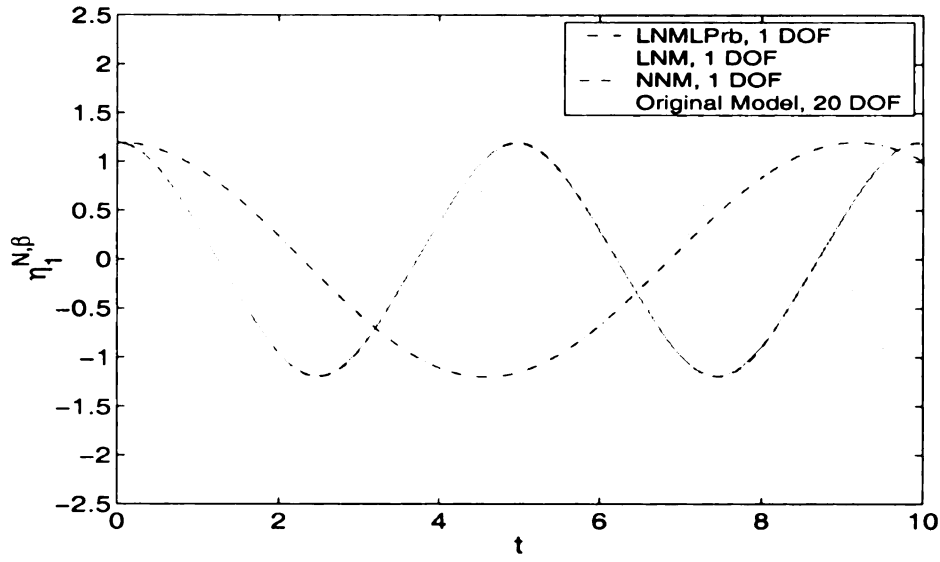
Figure 4.27. The time responses of the first fixed-interface mode displacement $\eta_1^{N,\beta}$ for the linearized one-mode model, the one-mode model, the ROM, and the original model of substructure β using the second-trial parameters.
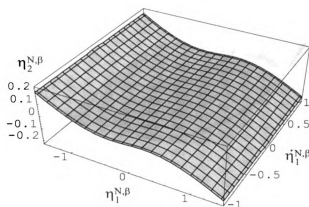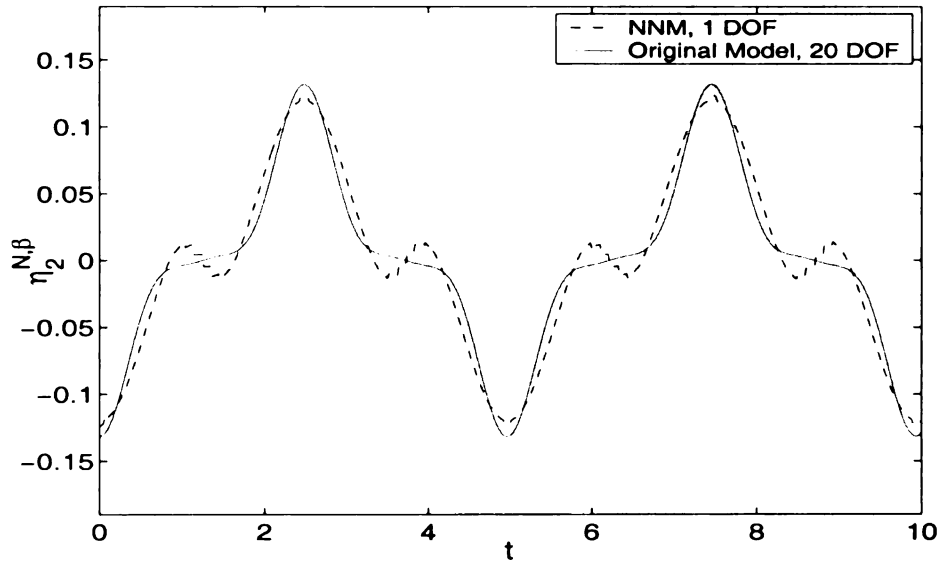

Figure 4.28. The time responses of the second fixed-interface linear mode displacement $\eta_2^{N,\beta} = X_2^{\beta}(\eta_1^{N,\beta}, \dot{\eta}_1^{N,\beta})$ on the first fixed-interface nonlinear mode manifold for the ROM and the original model of substructure β using the second-trial parameters.
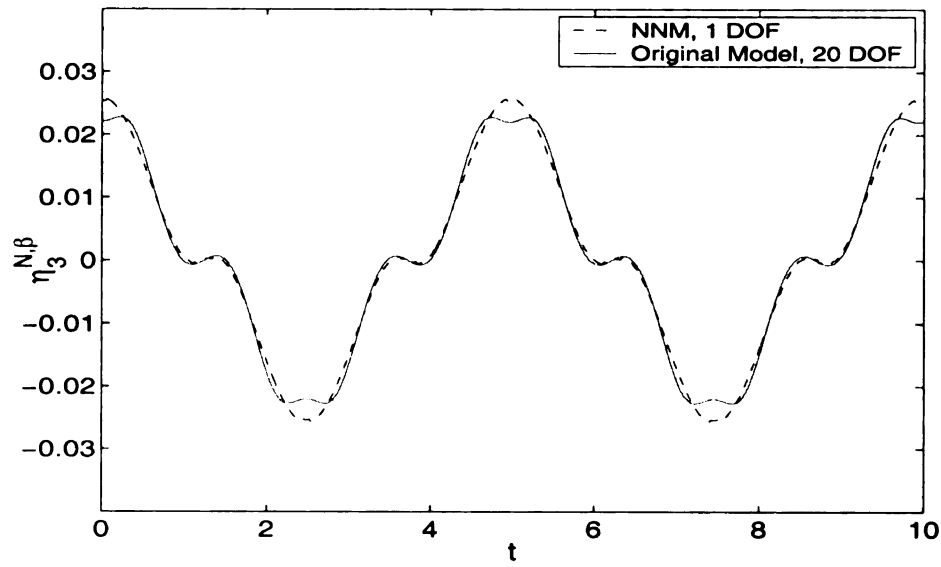
Figure 4.29. The time responses of the third fixed-interface linear mode displacement $\eta_3^{N,\beta} = X_3^{\beta}(\eta_1^{N,\beta}, \dot{\eta}_1^{N,\beta})$ on the first fixed-interface nonlinear mode manifold for the ROM and the original model of substructure β using the second-trial parameters.
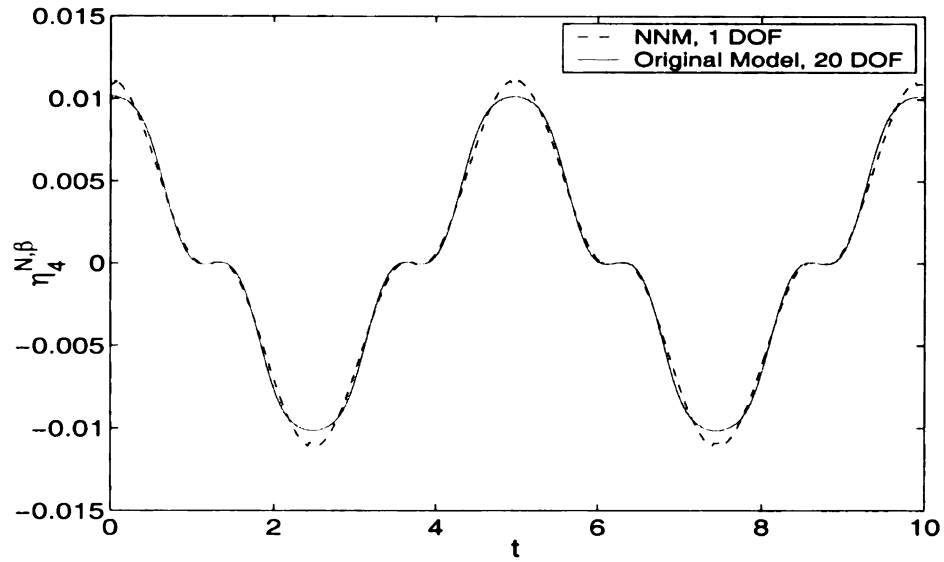
Figure 4.30. The time responses of the fourth fixed-interface linear mode displacement $\eta_4^{N,\beta} = X_4^{\beta}(\eta_1^{N,\beta}, \dot{\eta}_1^{N,\beta})$ on the first fixed-interface nonlinear mode manifold for the ROM and the original model of substructure β using the second-trial parameters.
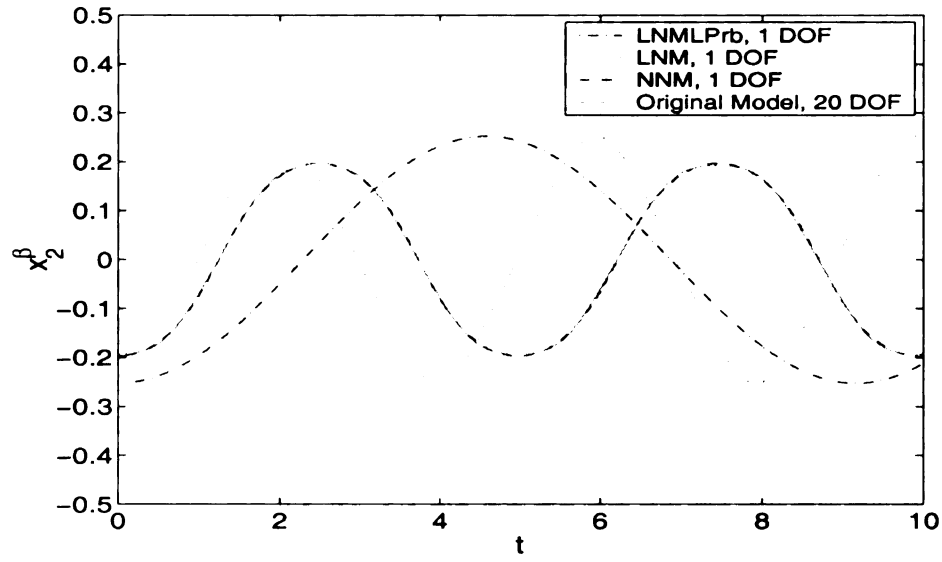
Figure 4.31. The time responses of the displacement x_2^β from Figure 4.11 with the interface fixed for the linearized one-mode model, the one-mode model, the ROM, and the original model of substructure β using the second-trial parameters.
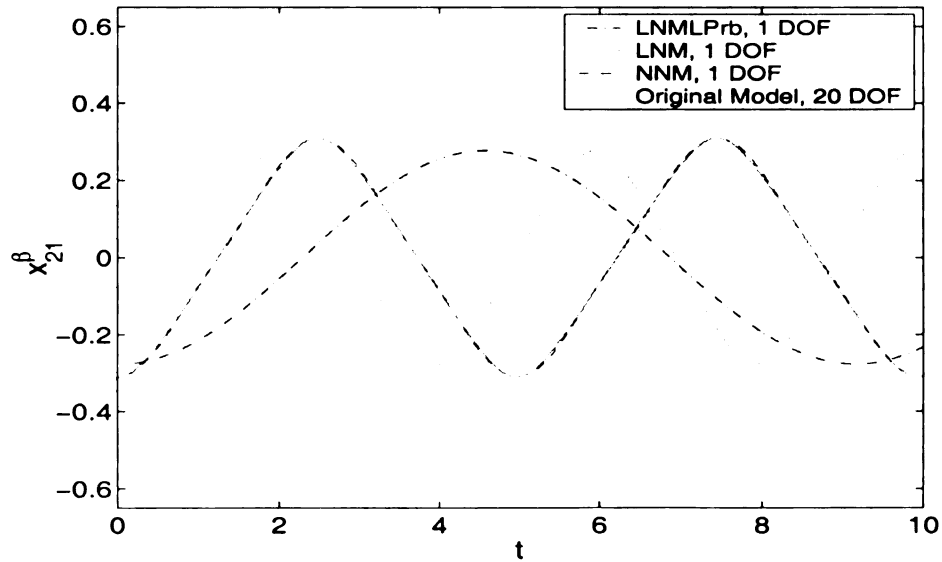
Figure 4.32. The time responses of the displacement x_{21}^β from Figure 4.11 with the interface fixed for the linearized one-mode model, the one-mode model, the ROM, and the original model of substructure β using the second-trial parameters.
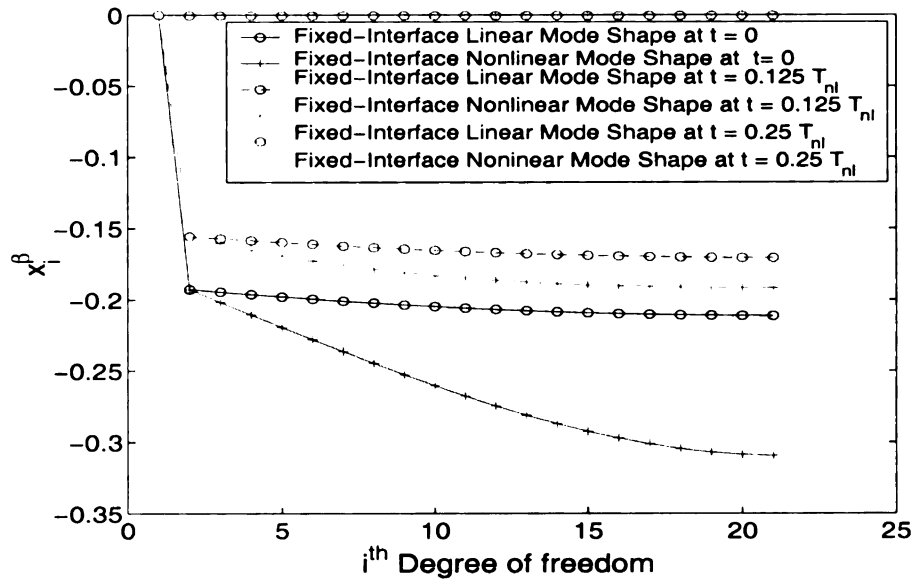
Figure 4.33. Comparison of deflections $x_i^\beta(t)$ for a quarter-period of motion on the first fixed-interface linear mode manifold (linear eigenspace) and on the first fixed-interface nonlinear mode manifold of substructure β using the second-trial parameters. The motion starts at the maximum deflection (the bottom curve) and moves as shown to the zero deflection at a quarter-period. Note that linear mode shape is normalized such that x_1^β is the same as x_1^β of the nonlinear mode shape at each time.
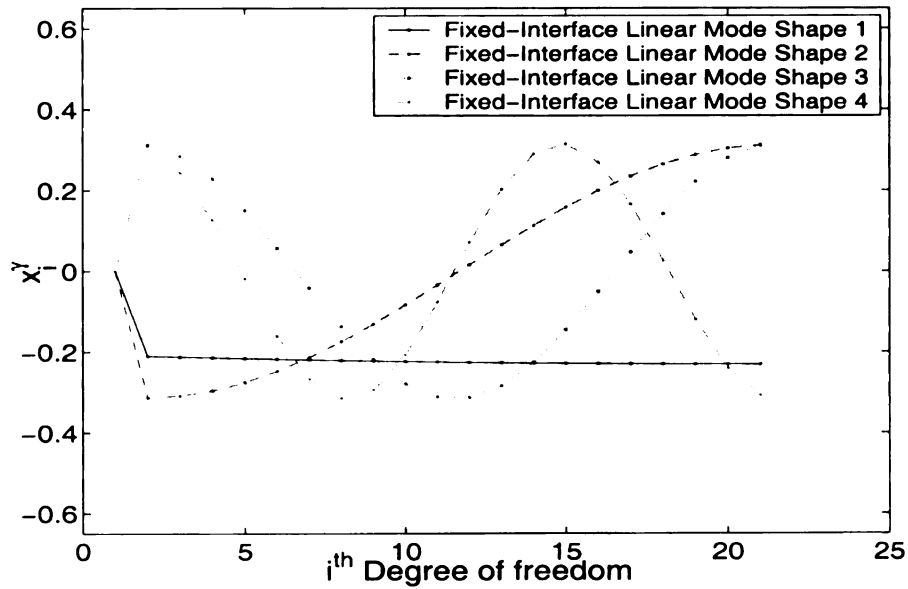
Figure 4.34. The first four fixed-interface LNMs of substructure γ.
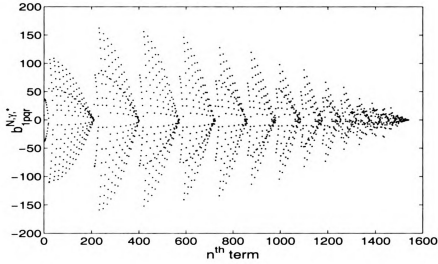
Figure 4.35. The coefficients of the pqr cubic nonlinear terms expressed in fixed-interface linear modal coordinates and associated with the first mode (master mode) of substructure γ.
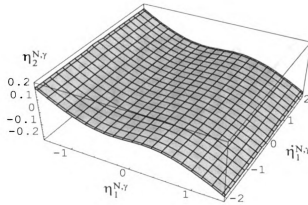
Figure 4.36. The contribution of the second fixed-interface linear mode amplitude $\eta_2^{N,\gamma} = X_2^{\gamma}(\eta_1^{N,\gamma}, \dot{\eta}_1^{N,\gamma})$ to the first fixed-interface nonlinear mode manifold of substructure γ.
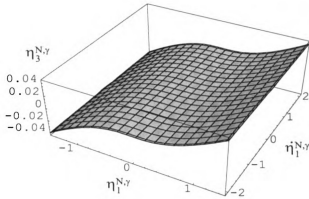
Figure 4.37. The contribution of the third fixed-interface linear mode amplitude $\eta_3^{N,\gamma} = X_3^{\gamma}(\eta_1^{N,\gamma}, \dot{\eta}_1^{N,\gamma})$ to the first fixed-interface nonlinear mode manifold of substructure γ.
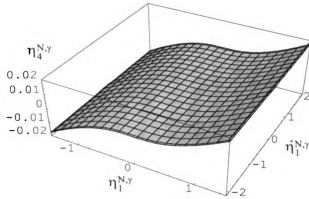
Figure 4.38. The contribution of the fourth fixed-interface linear mode amplitude $\eta_4^{N,\gamma} = X_4^{\gamma}(\eta_1^{N,\gamma}, \dot{\eta}_1^{N,\gamma})$ to the first fixed-interface nonlinear mode manifold of substructure γ.
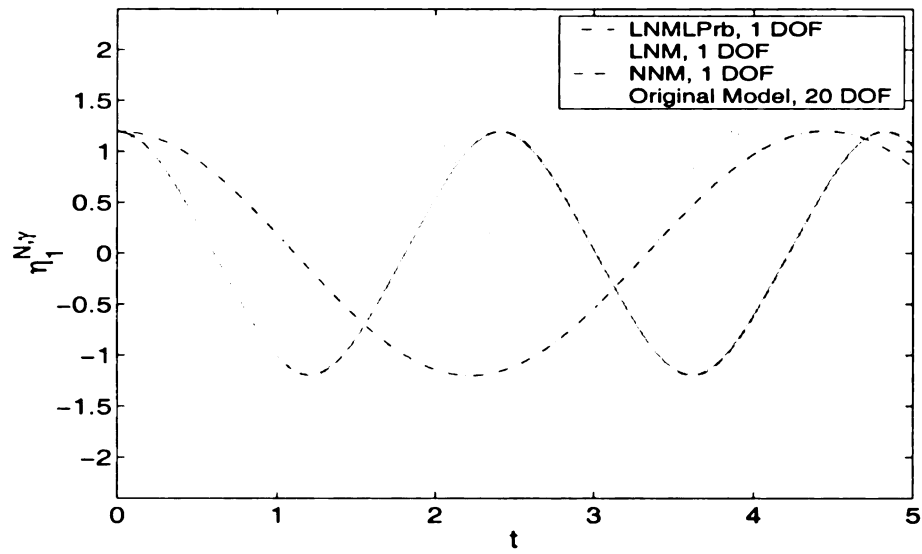
Figure 4.39. The time responses of the first fixed-interface mode displacement $\eta_1^{N,\gamma}$ for the linearized one-mode model, the one-mode model, the ROM, and the original model of substructure γ.
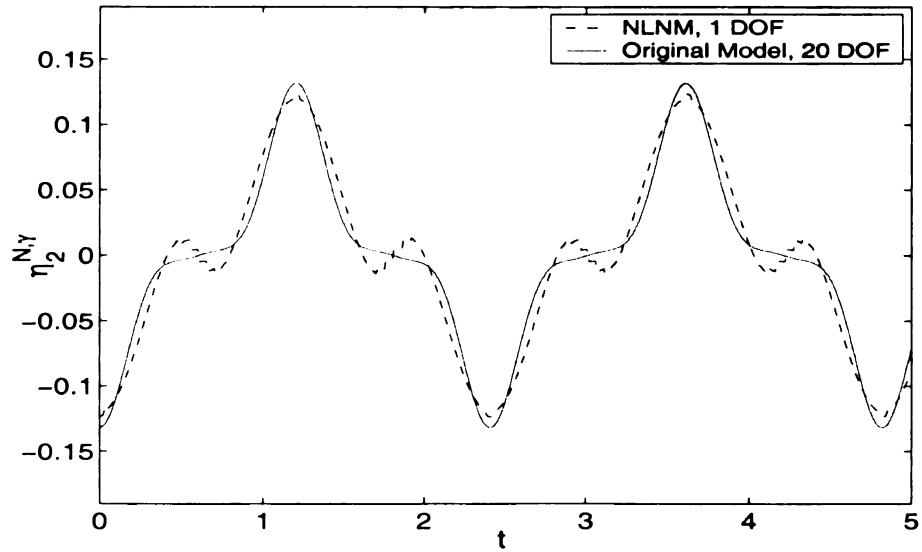
Figure 4.40. The time responses of the second fixed-interface linear mode displacement $\eta_2^{N,\gamma} = X_2^\gamma(\eta_1^{N,\gamma}, \dot{\eta}_1^{N,\gamma})$ on the first fixed-interface nonlinear mode manifold for the ROM and the original model of substructure γ.
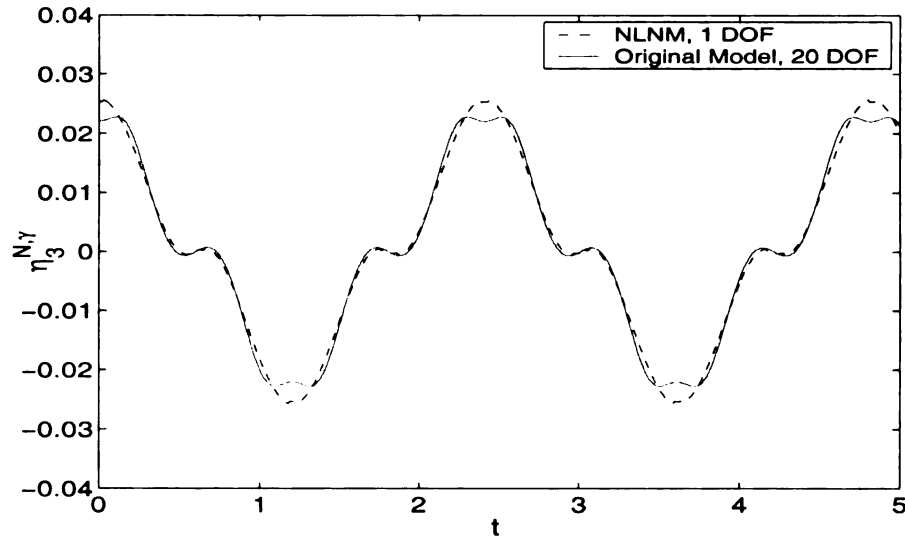
Figure 4.41. The time responses of the third fixed-interface linear mode displacement $\eta_3^{N,\gamma} = X_3^\gamma(\eta_1^{N,\gamma}, \dot{\eta}_1^{N,\gamma})$ on the first fixed-interface nonlinear mode manifold for the ROM and the original model of substructure γ.
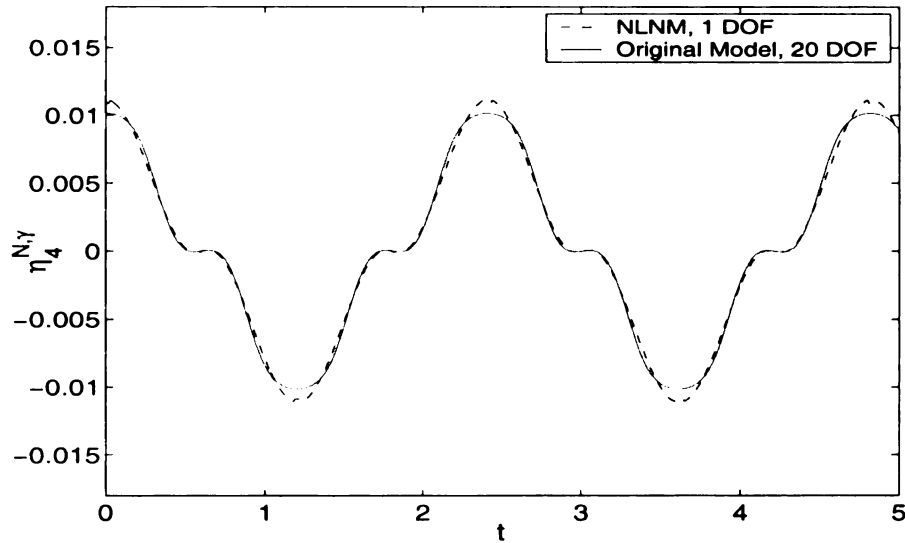
Figure 4.42. The time responses of the fourth fixed-interface linear mode displacement $\eta_4^{N,\gamma} = X_4^\gamma(\eta_1^{N,\gamma}, \dot{\eta}_1^{N,\gamma})$ on the first fixed-interface nonlinear mode manifold for the ROM and the original model of substructure γ.
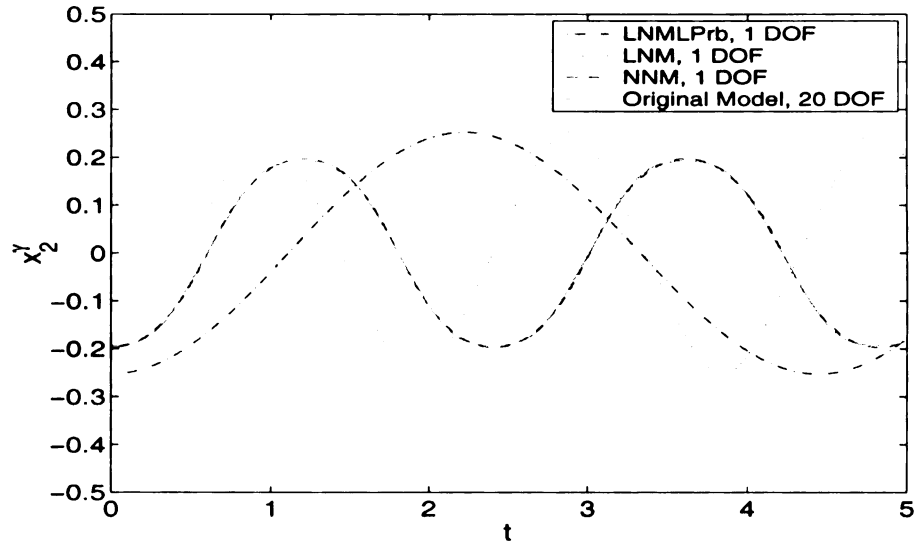
Figure 4.43. The time responses of the displacement x_2^γ from Figure 4.11 with the interface fixed ($x_1^\beta(t) = 0$) for the linearized one-mode model, the one-mode model, the ROM, and the original model of substructure γ.
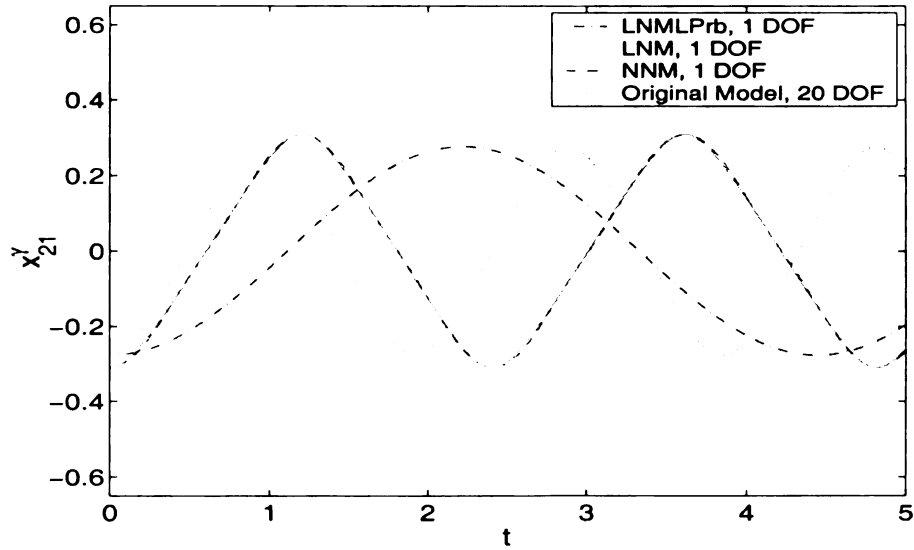
Figure 4.44. The time responses of the displacement x_{21}^γ from Figure 4.11 with the interface fixed for the linearized one-mode model, the one-mode model, the ROM, and the original model of substructure γ.

P
fi
u
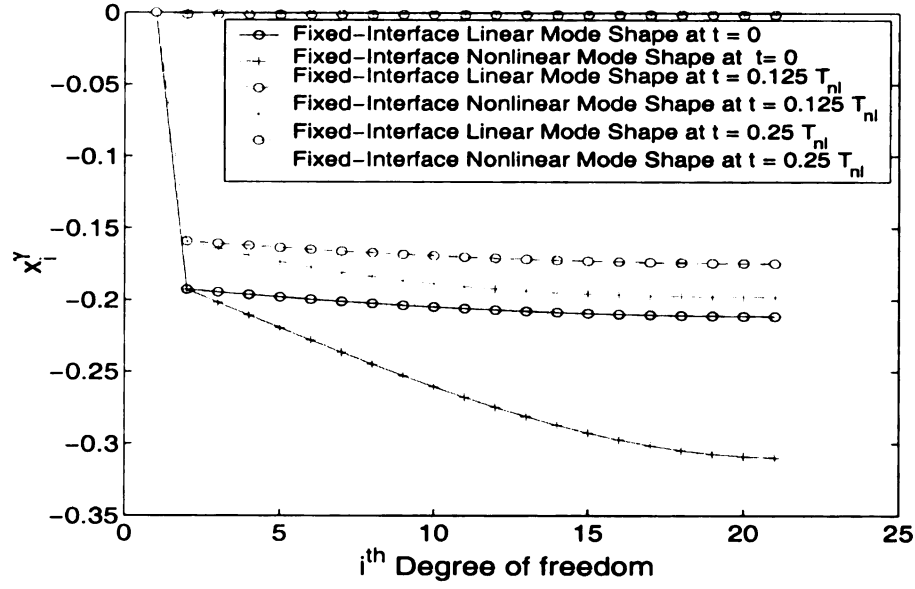
Figure 4.45. Comparison of deflections $x_i^\gamma(t)$ for a quarter-period of motion on the first fixed-interface linear mode manifold (linear eigenspace) and on the first fixed-interface nonlinear mode manifold of substructure γ. The motion starts at the maximum deflection (the bottom curve) and moves as shown to the zero deflection at a quarter-period.

Figure 4.46. The time responses of the first synthesized fixed-interface mode displacement $\eta_1^{N,\beta}$ for the three-DOF linear-CMS linear model, the three-DOF linear-CMS nonlinear model, the three-DOF nonlinear-CMS model, and the forty-one-DOF linear-CMS nonlinear model of substructure β.

Figure 4.47. The time responses of the second synthesized fixed-interface linear mode displacement $\eta_2^{N,\beta}$ for the three-DOF nonlinear-CMS model and the forty-one-DOF linear-CMS nonlinear model of substructure β.
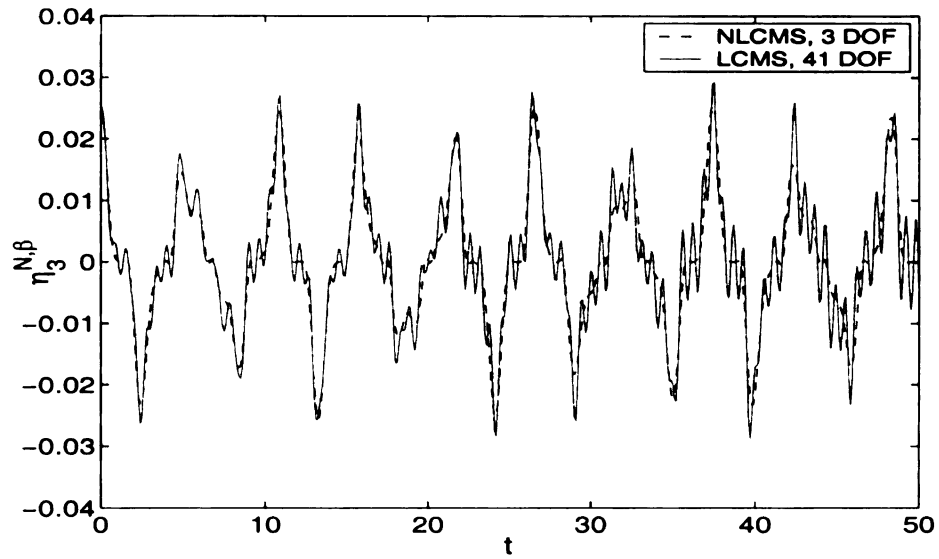
Figure 4.48. The time responses of the third synthesized fixed-interface linear mode displacement $\eta_3^{N,\beta}$ for the three-DOF nonlinear-CMS model and the forty-one-DOF linear-CMS nonlinear model of substructure β.
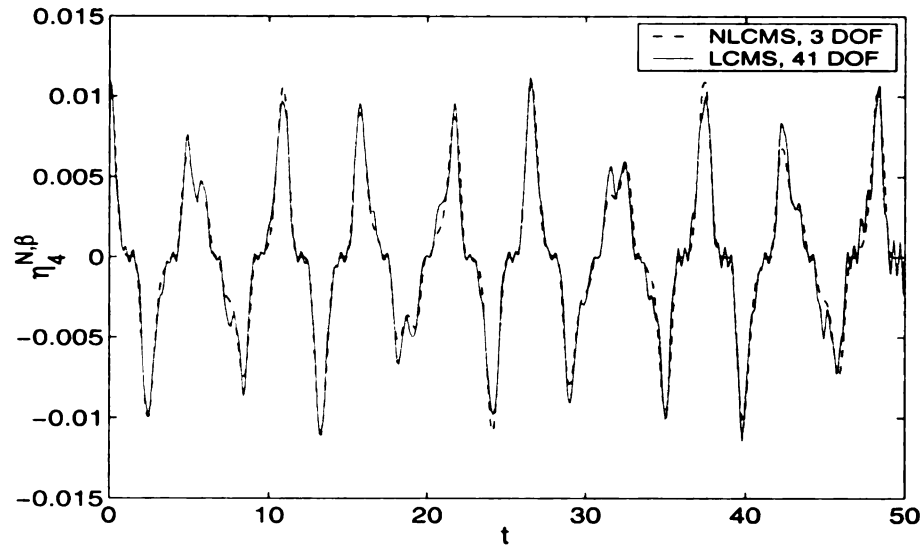
Figure 4.49. The time responses of the fourth synthesized fixed-interface linear mode displacement $\eta_4^{N,\beta}$ for the three-DOF nonlinear-CMS model and the forty-one-DOF linear-CMS nonlinear model of substructure β.
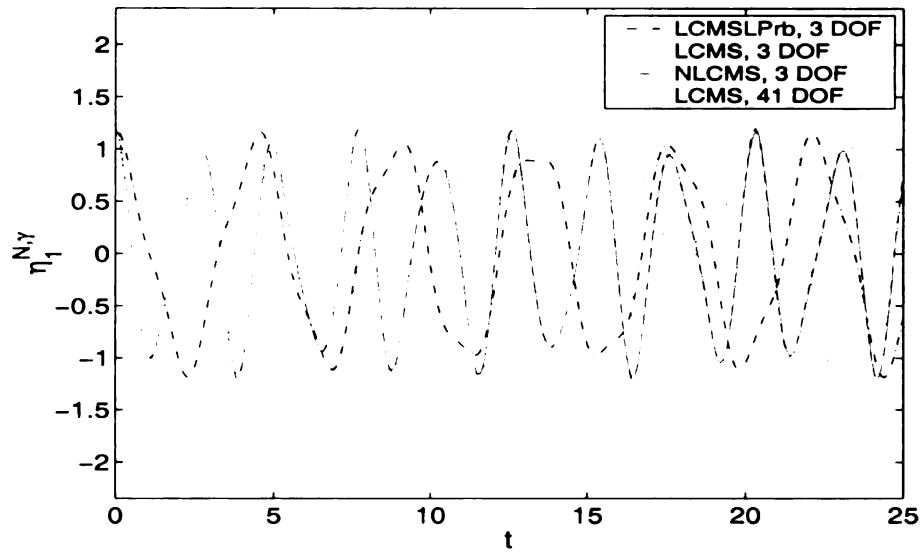
Figure 4.50. The time responses of the first synthesized fixed-interface mode displacement $\eta_1^{N,\gamma}$ for the three-DOF linear-CMS linear model, the three-DOF linear-CMS nonlinear model, the three-DOF nonlinear-CMS model, and the forty-one-DOF linear-CMS nonlinear model of substructure γ.
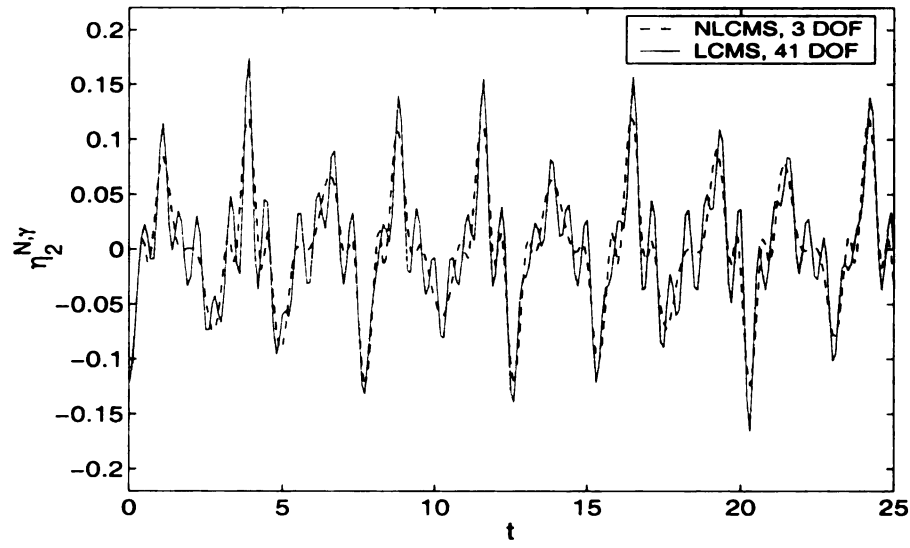
Figure 4.51. The time responses of the second synthesized fixed-interface linear mode displacement $\eta_2^{N,\gamma}$ for the three-DOF nonlinear-CMS model and the forty-one-DOF linear-CMS nonlinear model of substructure γ.
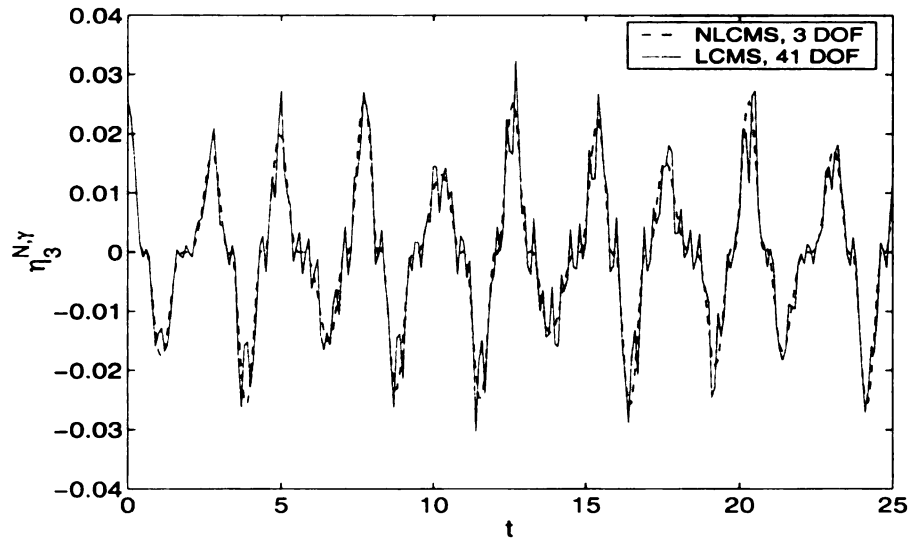
Figure 4.52. The time responses of the third synthesized fixed-interface linear mode displacement $\eta_3^{N,\gamma}$ for the three-DOF nonlinear-CMS model and the forty-one-DOF linear-CMS nonlinear model of substructure γ.
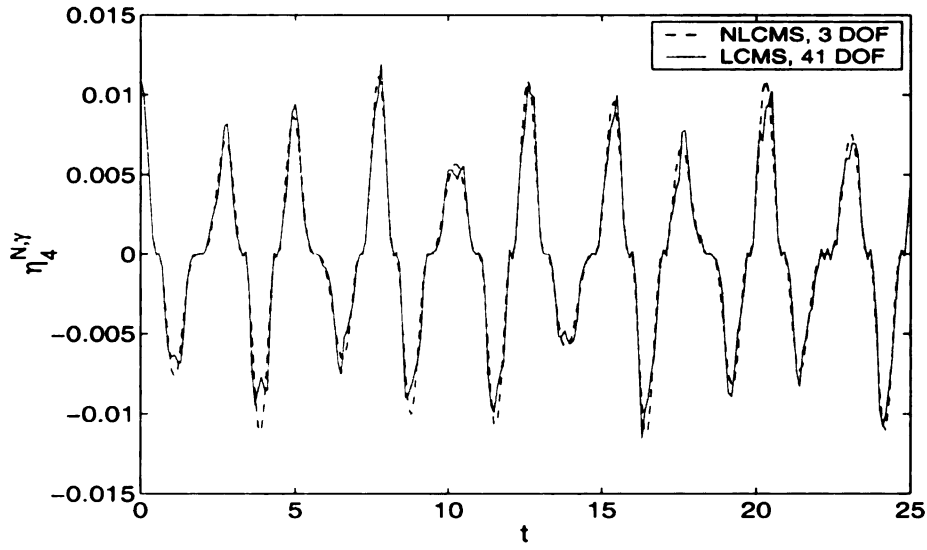
Figure 4.53. The time responses of the fourth synthesized fixed-interface linear mode displacement $\eta_4^{N,\gamma}$ for the three-DOF nonlinear-CMS model and the forty-one-DOF linear-CMS nonlinear model of substructure γ.
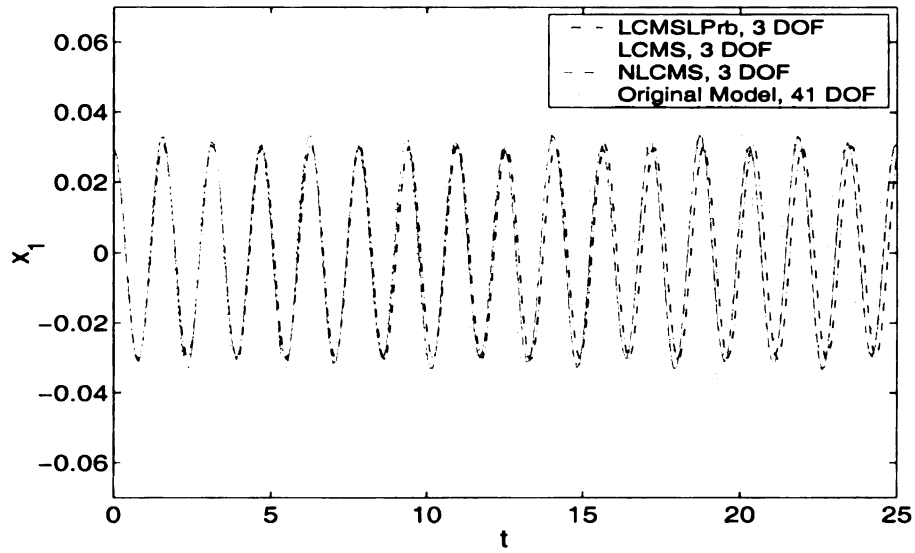
Figure 4.54. The time response of the displacement x_1 of mass m_1 from Figure 4.10, which corresponds to x_1^α, x_1^β, and x_1^γ from Figure 4.11, for the three-DOF linear-CMS linear model, the three-DOF linear-CMS nonlinear model, the three-DOF nonlinear-CMS model, and the forty-one-DOF original model.
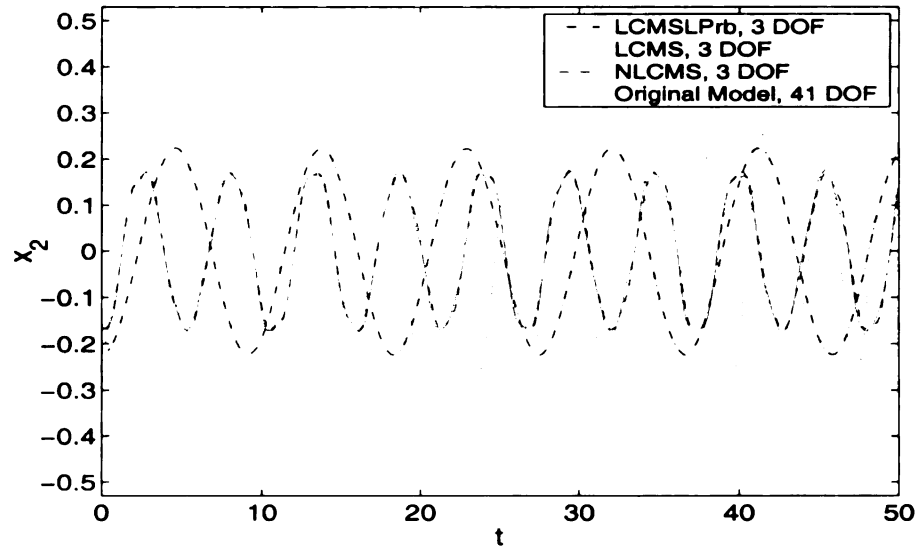
Figure 4.55. The time response of the displacement x_2 of mass m_2 from Figure 4.10, which corresponds to x_2^β from Figure 4.11, for the three-DOF linear-CMS linear model, the three-DOF linear-CMS nonlinear model, the three-DOF nonlinear-CMS model, and the forty-one-DOF original model.
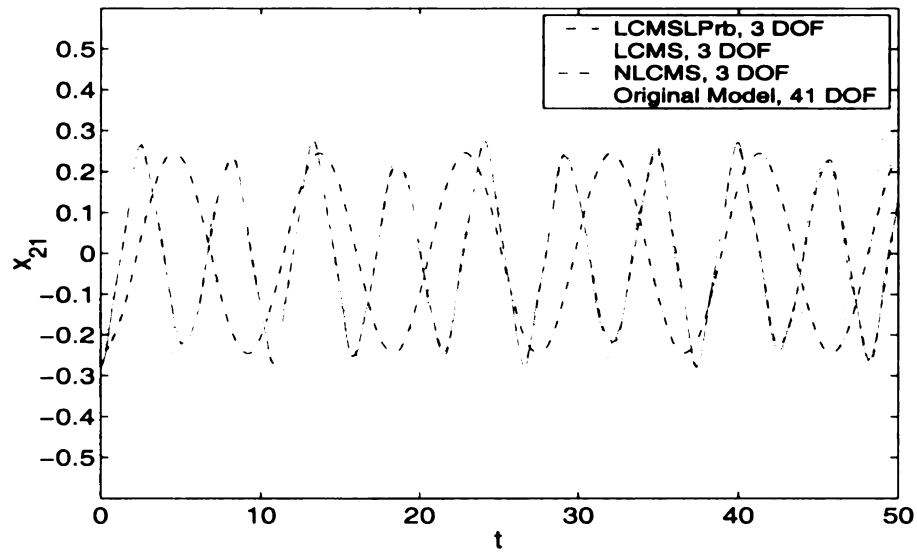
Figure 4.56. The time response of the displacement x_{21} of mass m_{21} from Figure 4.10, which corresponds to x_{21}^β from Figure 4.11, for the three-DOF linear-CMS linear model, the three-DOF linear-CMS nonlinear model, the three-DOF nonlinear-CMS model, and the forty-one-DOF original model.
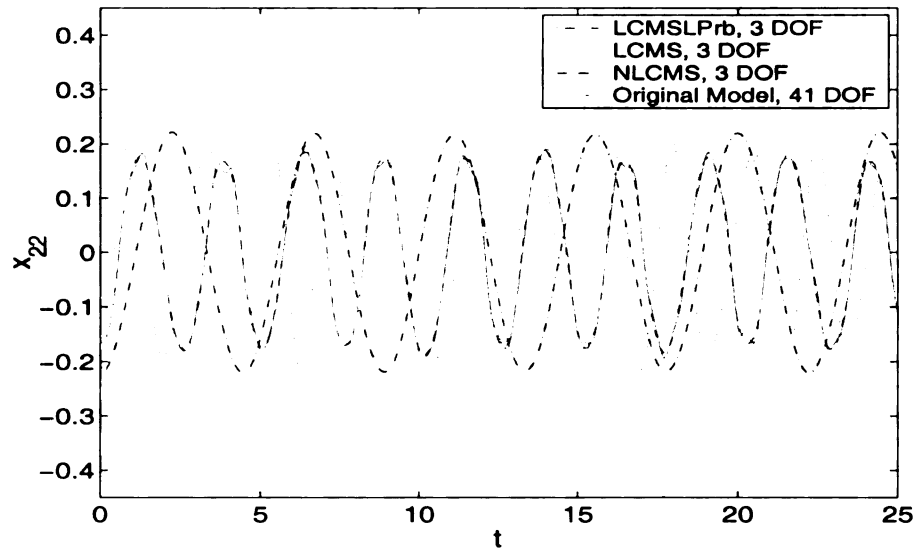
Figure 4.57. The time response of the displacement x_{22} of mass m_{22} from Figure 4.10, which corresponds to x_2^γ from Figure 4.11, for the three-DOF linear-CMS linear model, the three-DOF linear-CMS nonlinear model, the three-DOF nonlinear-CMS model, and the forty-one-DOF original model.
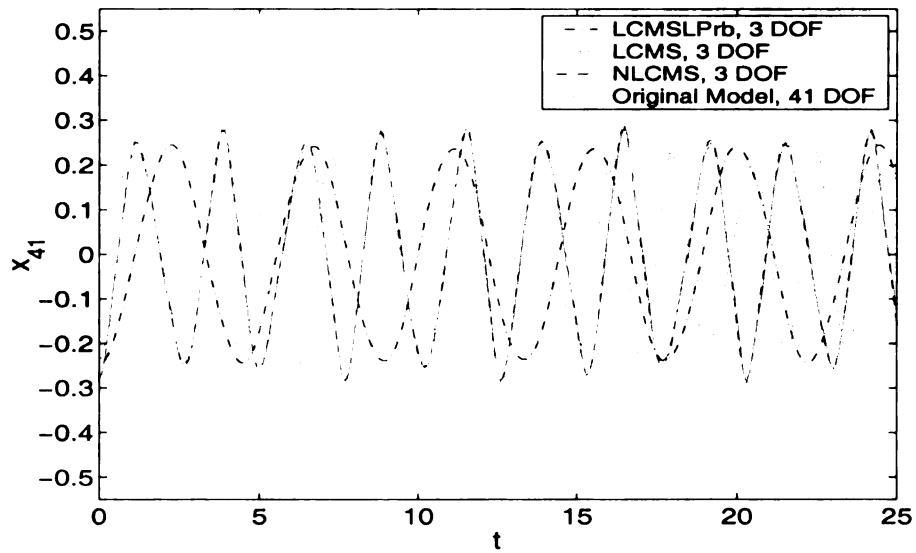
Figure 4.58. The time response of the displacement x_{41} of mass m_{41} from Figure 4.10, which corresponds to x_{21}^γ from Figure 4.11, for the three-DOF linear-CMS linear model, the three-DOF linear-CMS nonlinear model, the three-DOF nonlinear-CMS model, and the forty-one-DOF original model.
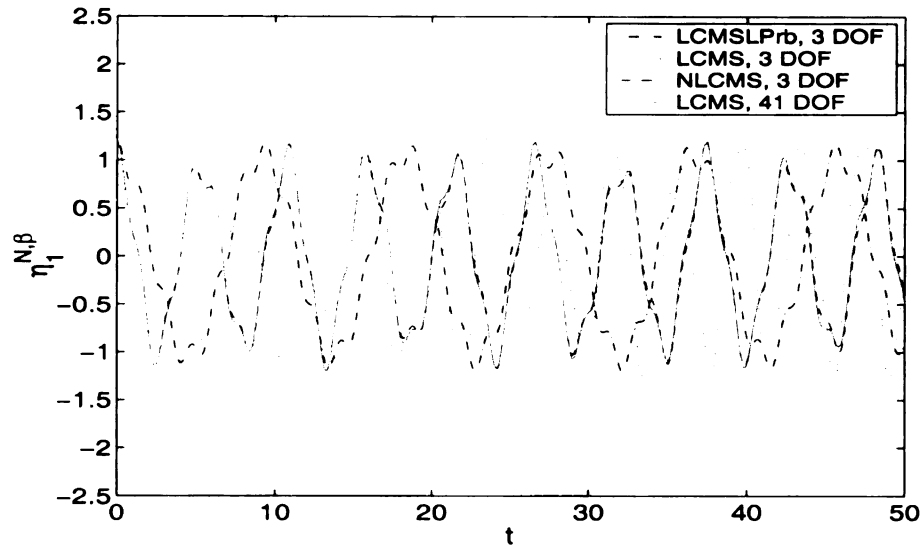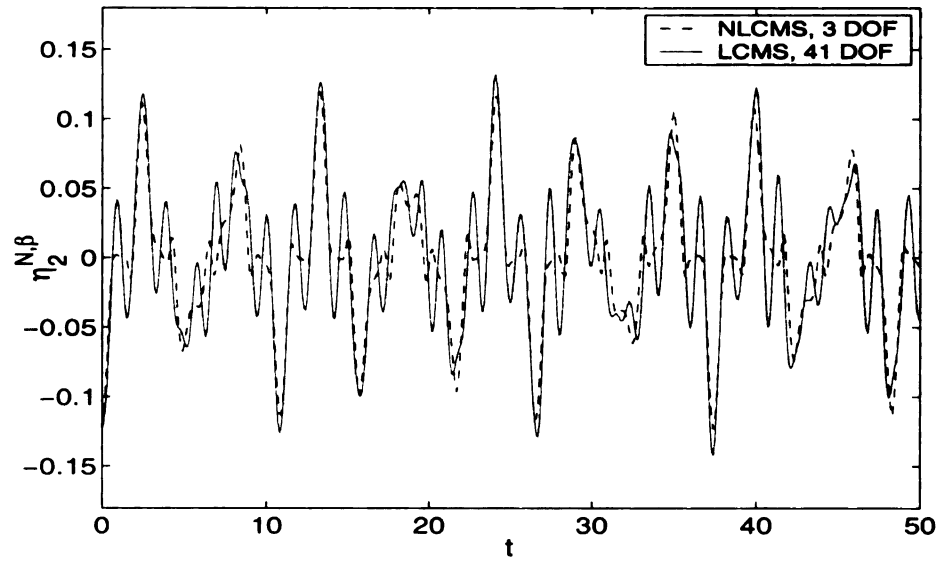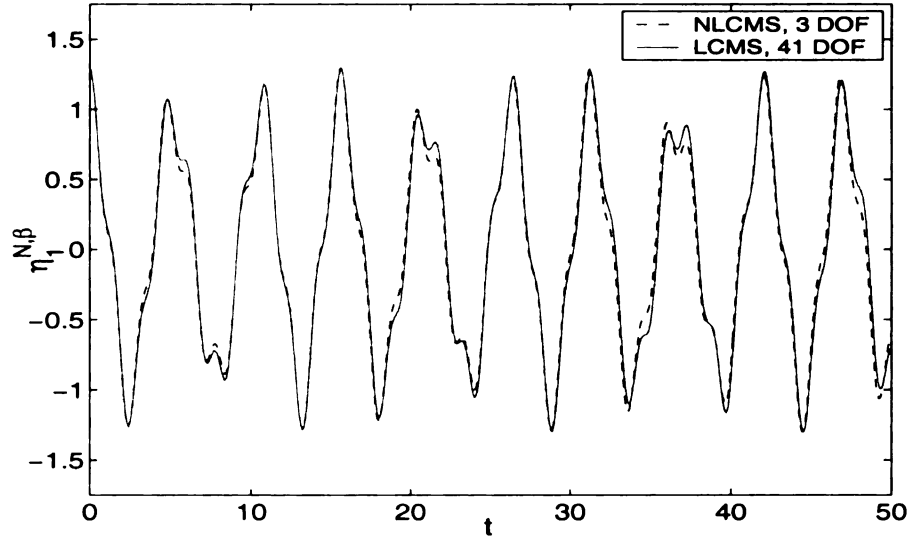
Figure 4.59. The time responses of the first synthesized fixed-interface mode displacement $\eta_1^{N,\beta}$ for the three-DOF nonlinear-CMS model and the forty-one-DOF linear-CMS nonlinear model of substructure β with $\eta_1^{N,\beta}(0) = 1.3$, $\eta_1^{N,\gamma}(0) = 1.3$, $\eta^C(0) = 0.04$, $\dot{\eta}_1^{N,\beta}(0) = 0$, $\dot{\eta}_1^{N,\gamma}(0) = 0$, $\dot{\eta}^C(0) = 0$.

Figure 4.60. The time responses of the first synthesized fixed-interface mode displacement $\eta_1^{N,\gamma}$ for the three-DOF nonlinear-CMS model and the forty-one-DOF linear-CMS nonlinear model of substructure $\gamma$ with $\eta_1^{N,\beta}(0) = 1.3$, $\eta_1^{N,\gamma}(0) = 1.3$, $\eta^C(0) = 0.04$, $\dot{\eta}_1^{N,\beta}(0) = 0$, $\dot{\eta}_1^{N,\gamma}(0) = 0$, $\dot{\eta}^C(0) = 0$.

4.9   Appendix 4

The component forms of the mass and stiffness matrices and the nonlinear force vector of the class of spring-mass systems from section 4.5 are given by

$$m_{ij} = \begin{cases} m_i & \text{if } j = i \\ 0 & \text{otherwise} \end{cases} \qquad (4.69)$$

$$k_{ij} = \begin{cases} k_1 + \displaystyle\sum_{s=0}^{(N_a-1)} k_{(2\,s\,N_{mass}+2)} & \text{if } i=1,\ j=1 \\[2ex] -k_{(2\,s\,N_{mass}+2)} & \text{if } i=1,\ j=s\,N_{mass}+2, \\[1ex] & \quad s=0,1,2,...,(N_a-1) \\[1ex] -k_{(2\,s\,N_{mass})} & \text{if } i=s\,N_{mass}+1,\ j=i-1, \\[1ex] & \quad s=1,2,...,N_a \\[1ex] k_{(2\,s\,N_{mass})} & \text{if } i=s\,N_{mass}+1,\ j=i, \\[1ex] & \quad s=1,2,...,N_a \\[1ex] -k_{(2\,s\,N_{mass}+2)} & \text{if } i=s\,N_{mass}+2,\ j=1, \\[1ex] & \quad s=1,2,...,(N_a-1) \\[1ex] k_{(2\,s\,N_{mass}+2)} + k_{(2\,s\,N_{mass}+4)} & \text{if } i=s\,N_{mass}+2,\ j=i, \\[1ex] & \quad s=1,2,...,(N_a-1) \\[1ex] -k_{(2\,s\,N_{mass}+4)} & \text{if } i=s\,N_{mass}+2,\ j=i+1, \\[1ex] & \quad s=1,2,...,(N_a-1) \\[1ex] -k_{(2i-2)} & \text{if } (2 \le i \le N_{mass}) \\[1ex] & \text{or } (s\,N_{mass}+3 \le i \le (s+1)\,N_{mass}), \\[1ex] & \quad j=i-1,\ s=1,2,...,(N_a-1) \\[1ex] k_{(2i-2)} + k_{(2i)} & \text{if } (2 \le i \le N_{mass}) \\[1ex] & \text{or } (s\,N_{mass}+3 \le i \le (s+1)\,N_{mass}), \\[1ex] & \quad j=i,\ s=1,2,...,(N_a-1) \\[1ex] -k_{(2i)} & \text{if } (2 \le i \le N_{mass}) \\[1ex] & \text{or } (s\,N_{mass}+3 \le i \le (s+1)\,N_{mass}), \\[1ex] & \quad j=i+1,\ s=1,2,...,(N_a-1) \\[1ex] 0 & \text{otherwise} \end{cases} \tag{4.70}$$

$$
g_i = \begin{cases}
-\sum_{s=0}^{(N_a-1)} k_{(2\,s\,N_{mass}+3)}\big(x_{(s\,N_{mass}+2)} - x_1\big)^3 \\
\quad \text{if } i = 1 \\[2em]
k_{(2\,s\,N_{mass}+1)}\big(x_i - x_{(i-1)}\big)^3 \\
\quad \text{if } i = s\,N_{mass} + 1,\ s = 1, 2, ..., N_a \\[2em]
k_{(2\,s\,N_{mass}+3)}\big(x_i - x_1\big)^3 - k_{(2\,s\,N_{mass}+5)}\big(x_{(i+1)} - x_i\big)^3 \\
\quad \text{if } i = s\,N_{mass} + 2,\ s = 1, 2, ..., (N_a - 1) \\[2em]
k_{(2i-1)}\big(x_i - x_{(i-1)}\big)^3 - k_{(2i+1)}\big(x_{(i+1)} - x_i\big)^3 \\
\quad \text{if } i = 2, ..., N_{mass},\ \text{or } i = s\,N_{mass} + 3, ..., (s+1)\,N_{mass}, \\
\quad s = 1, 2, ..., (N_a - 1)
\end{cases}
\tag{4.71}
$$

for $i, j = 1, 2, 3, ..., (N_a\,N_{mass} + 1)$.

The component forms of the mass and stiffness matrices, the nonlinear force vector, and the reaction force vector for substructures S are given by

$$
m_{ij}^S = \begin{cases}
0 & \text{if } i = 1, j = 1 \\
m_i^S & \text{if } j = i \\
0 & \text{otherwise}
\end{cases}
\tag{4.72}
$$

$$
k_{ij}^S = \begin{cases}
k_2^S & \text{if } i = 1, \; j = 1 \\[6pt]
-k_2^S & \text{if } i = 1, \; j = 2 \\[6pt]
-k_{(2N_{mass})}^S & \text{if } i = N_{mass} + 1, \; j = i - 1 \\[6pt]
k_{(2N_{mass})}^S & \text{if } i = N_{mass} + 1, \; j = i \\[6pt]
-k_{(2i-2)}^S & \text{if } (2 \le i \le N_{mass}), \; j = i - 1 \\[6pt]
k_{(2i-2)}^S + k_{(2i)}^S & \text{if } (2 \le i \le N_{mass}), \; j = i \\[6pt]
-k_{(2i)}^S & \text{if } (2 \le i \le N_{mass}), \; j = i + 1 \\[6pt]
0 & \text{otherwise}
\end{cases} \tag{4.73}
$$

$$
g_i^S = \begin{cases}
-k_3^S(x_2^S - x_1^S)^3 & \text{if } i = 1 \\[6pt]
k_{(2N_{mass}+1)}^S(x_i^S - x_{(i-1)}^S)^3 & \text{if } i = N_{mass} + 1 \\[6pt]
k_{(2i-1)}^S(x_i^S - x_{(i-1)}^S)^3 - k_{(2i+1)}^S(x_{(i+1)}^S - x_i^S)^3 & \text{if } i = 2, ..., N_{mass}
\end{cases} \tag{4.74}
$$

$$
f_i^S = \begin{cases}
F_J^{S\alpha} & \text{if } i = 1 \\[6pt]
0 & \text{otherwise}
\end{cases} \tag{4.75}
$$

for $i, j = 1, 2, 3, ..., (N_{mass} + 1)$, and $S = \beta, \gamma, \delta, ...$. Note that $m_2^\beta = m_2$, $m_3^\beta = m_3$, ..., $m_{(N_{mass}+1)}^\beta = m_{(N_{mass}+1)}$, $k_2^\beta = k_2$, $k_3^\beta = k_3$, ..., $k_{(2N_{mass}+1)}^\beta = k_{(2N_{mass}+1)}$, $m_2^\gamma = m_{(N_{mass}+2)}$, $m_3^\gamma = m_{(N_{mass}+3)}$, ..., $m_{(N_{mass}+1)}^\gamma = m_{(2N_{mass}+1)}$, $k_2^\gamma = k_{(2N_{mass}+2)}$, $k_3^\gamma = k_{(2N_{mass}+3)}$, ..., $k_{(2N_{mass}+1)}^\gamma = k_{(4N_{mass}+1)}$, and so on.

The coefficients of the *pqr* cubic nonlinear terms expressed in terms of fixed-interface linear modal coordinates and associated with the *i*th mode of substructures S are given by

$$
b_{ipqr}^{N,S,*} = \begin{cases} b_{ipqr}^{N,S} & \text{if} \quad p = q = r \\ b_{ipqr}^{N,S} + b_{iprq}^{N,S} + b_{irpq}^{N,S} & \text{if} \quad p = q \\ b_{ipqr}^{N,S} + b_{iqpr}^{N,S} + b_{iqrp}^{N,S} & \text{if} \quad q = r \\ b_{ipqr}^{N,S} + b_{iprq}^{N,S} + b_{iqpr}^{N,S} + b_{iqrp}^{N,S} + b_{irpq}^{N,S} + b_{irqp}^{N,S} & \text{otherwise,} \end{cases}
\tag{4.76}
$$

where $b_{ipqr}^{N,S}$ are

$$
b_{ipqr}^{N,S} = \sum_{h=2}^{(N_{mass}+1)} \phi_{hi}^{N,S} \, b_{hpqr}^{N,S}
\tag{4.77}
$$

for $\quad S = \beta, \gamma, \delta, \ldots,$

where $\phi_{hi}^{N,S}$ is the hi component of the modal matrix defined in section 4.3.2.1, and $b_{hpqr}^{N,S}$ are given by

$$b_{hpqr}^{N,S} = \begin{cases} \left[k_3^S \; \phi_{2p}^{N,S} \; \phi_{2q}^{N,S} \; \phi_{2r}^{N,S} - k_5^S \; \phi_{3p}^{N,S} \; \phi_{3q}^{N,S} \; \phi_{3r}^{N,S} + 3 \; k_5^S \; \phi_{3p}^{N,S} \; \phi_{3q}^{N,S} \; \phi_{2r}^{N,S} \right. \\ \left. -3 \; k_5^S \; \phi_{3p}^{N,S} \; \phi_{2q}^{N,S} \; \phi_{2r}^{N,S} + k_5^S \; \phi_{2p}^{N,S} \; \phi_{2q}^{N,S} \; \phi_{2r}^{N,S} \right] \\ \text{if} \quad h = 2 \\[2em] \left[k_{(2h-1)}^S \; \phi_{hp}^{N,S} \; \phi_{hq}^{N,S} \; \phi_{hr}^{N,S} - 3 \; k_{(2h-1)}^S \; \phi_{hp}^{N,S} \; \phi_{hq}^{N,S} \; \phi_{(h-1)r}^{N,S} \right. \\ +3 \; k_{(2h-1)}^S \; \phi_{hp}^{N,S} \; \phi_{(h-1)q}^{N,S} \; \phi_{(h-1)r}^{N,S} - k_{(2h-1)}^S \; \phi_{(h-1)p}^{N,S} \; \phi_{(h-1)q}^{N,S} \; \phi_{(h-1)r}^{N,S} \\ -k_{(2h+1)}^S \; \phi_{(h+1)p}^{N,S} \; \phi_{(h+1)q}^{N,S} \; \phi_{(h+1)r}^{N,S} + 3 \; k_{(2h+1)}^S \; \phi_{(h+1)p}^{N,S} \; \phi_{(h+1)q}^{N,S} \; \phi_{hr}^{N,S} \\ \left. -3 \; k_{(2h+1)}^S \; \phi_{(h+1)p}^{N,S} \; \phi_{hq}^{N,S} \; \phi_{hr}^{N,S} + k_{(2h+1)}^S \; \phi_{hp}^{N,S} \; \phi_{hq}^{N,S} \; \phi_{hr}^{N,S} \right] \\ \text{if} \quad h = 3, 4, 5, ..., N_{mass} \\[2em] \left[k_{(2N_{mass}+1)}^S \; \phi_{hp}^{N,S} \; \phi_{hq}^{N,S} \; \phi_{hr}^{N,S} - 3 \; k_{(2N_{mass}+1)}^S \; \phi_{hp}^{N,S} \; \phi_{hq}^{N,S} \; \phi_{(h-1)r}^{N,S} \right. \\ \left. +3 \; k_{(2N_{mass}+1)}^S \; \phi_{hp}^{N,S} \; \phi_{(h-1)q}^{N,S} \; \phi_{(h-1)r}^{N,S} - k_{(2N_{mass}+1)}^S \; \phi_{(h-1)p}^{N,S} \; \phi_{(h-1)q}^{N,S} \; \phi_{(h-1)r}^{N,S} \right] \\ \text{if} \quad h = N_{mass} + 1 \end{cases} \tag{4.78}$$

The coefficients of the pqr cubic nonlinear terms expressed in terms of the linear modal coordinates and associated with the ith mode of substructures S are given by

$$b_{ipqr}^{S,*} = \begin{cases} b_{ipqr}^S & \text{if} \quad p = q = r \\ b_{ipqr}^S + b_{iprq}^S + b_{irpq}^S & \text{if} \quad p = q \\ b_{ipqr}^S + b_{iqpr}^S + b_{iqrp}^S & \text{if} \quad q = r \\ b_{ipqr}^S + b_{iprq}^S + b_{iqpr}^S + b_{iqrp}^S + b_{irpq}^S + b_{irqp}^S & \text{otherwise,} \end{cases} \tag{4.79}$$

where b_{ipqr}^S are

$$b^S_{ipqr} \quad = \quad \sum_{h=1}^{(N_{mass}+1)} \psi^S_{hi} \, b^S_{hpqr} \qquad\qquad (4.80)$$

for $\quad S = \beta,\, \gamma,\, \delta,\, ... ,$

where ψ^S_{hi} is the hi component of the modal matrix defined in section 4.3.2, and b^S_{hpqr} are given by

$$
b^S_{hpqr} =
\begin{cases}
\begin{aligned}
&\left[-k^S_3 \, \psi^S_{2p} \, \psi^S_{2q} \, \psi^S_{2r} + 3\, k^S_3 \, \psi^S_{2p} \, \psi^S_{2q} \, \psi^S_{1r} \right. \\
&\left. -3\, k^S_3 \, \psi^S_{2p} \, \psi^S_{1q} \, \psi^S_{1r} + k^S_3 \, \psi^S_{1p} \, \psi^S_{1q} \, \psi^S_{1r} \right] \\
&\text{if } h = 1
\end{aligned} \\[3em]
\begin{aligned}
&\left[k^S_{(2h-1)} \, \psi^S_{hp} \, \psi^S_{hq} \, \psi^S_{hr} - 3\, k^S_{(2h-1)} \, \psi^S_{hp} \, \psi^S_{hq} \, \psi^S_{(h-1)r} \right. \\
&+3\, k^S_{(2h-1)} \, \psi^S_{hp} \, \psi^S_{(h-1)q} \, \psi^S_{(h-1)r} - k^S_{(2h-1)} \, \psi^S_{(h-1)p} \, \psi^S_{(h-1)q} \, \psi^S_{(h-1)r} \\
&-k^S_{(2h+1)} \, \psi^S_{(h+1)p} \, \psi^S_{(h+1)q} \, \psi^S_{(h+1)r} + 3\, k^S_{(2h+1)} \, \psi^S_{(h+1)p} \, \psi^S_{(h+1)q} \, \psi^S_{hr} \\
&\left. -3\, k^S_{(2h+1)} \, \psi^S_{(h+1)p} \, \psi^S_{hq} \, \psi^S_{hr} + k^S_{(2h+1)} \, \psi^S_{hp} \, \psi^S_{hq} \, \psi^S_{hr} \right] \\
&\text{if } h = 2,3,4,...,N_{mass}
\end{aligned} \\[3em]
\begin{aligned}
&\left[k^S_{(2N_{mass}+1)} \, \psi^S_{hp} \, \psi^S_{hq} \, \psi^S_{hr} - 3\, k^S_{(2N_{mass}+1)} \, \psi^S_{hp} \, \psi^S_{hq} \, \psi^S_{(h-1)r} \right. \\
&\left. +3\, k^S_{(2N_{mass}+1)} \, \psi^S_{hp} \, \psi^S_{(h-1)q} \, \psi^S_{(h-1)r} - k^S_{(2N_{mass}+1)} \, \psi^S_{(h-1)p} \, \psi^S_{(h-1)q} \, \psi^S_{(h-1)r} \right] \\
&\text{if } h = N_{mass} + 1
\end{aligned}
\end{cases}
\qquad (4.81)
$$

CHAPTER 5

Conclusions and Future Works

Within this work techniques are developed that can be used to construct reduced order models (ROMs) of nonlinear structural systems. The techniques are numerical in nature and are all based on invariant manifold-based nonlinear normal modes. The methods consist of NNM reduction from large-scale models, including those generated by nonlinear FE analysis, and a component mode synthesis (CMS) technique that incorporates these models for substructures. This latter method allows one to use NNM ROMs of substructures to build ROMs of the combined structure through a CMS technique. The contributions made in these subjects are summarized as follows:

- In Chapter 2, two new methods to numerically solve for single NNM invariant manifolds are developed. In both of these methods the manifold is parameterized by a modal master displacement and velocity pair and the resulting invariant manifold equations are solved using Galerkin approaches. The first method solves for the manifold using global polynomial basis functions over the entire domain of interest. For the second method, the domain of interest is subdivided into small pieces and the manifold is solved using low-degree polynomial basis functions over these sub domains, which are then pieced together. When compared with similar methods that utilize amplitude and phase variables (Pesheck *et al.*, [33]), the new methods are found to be superior in terms of computational time but inferior in terms of accuracy.

- In Chapter 3 a specific application is considered; a NNM ROM of a rotating beam is

developed from a nonlinear finite element formulation, wherein the invariant manifold equations are numerically solved using the collocation method. The NNM formulation allows one to systematically account for the nonlinear coupling effects between axial and transverse motions, which are the source of slow modal convergence for this type of problem when attacked by conventional approaches. The results demonstrate promise for the field of nonlinear structural dynamics, since they combine the versatility of the finite element method with the accurate NNM model reduction technique. However, there is a trade-off between acquiring the accurate ROM and the computational effort involved, since solving for a single-NNM invariant manifold with many retained linear modes requires significant computational time.

- In Chapter 4, a model reduction technique is developed that combines numerically generated NNMs and the CMS technique. This allows one to build ROMs at the substructure level and assemble these to formulate a ROM of the assembled structure. The fixed-interface linear CMS technique of Craig and Bampton ([62]) is extended to nonlinear structures by making use of fixed-interface NNMs in place of fixed-interface linear normal modes. This approach is suitable for systems composed of assemblies of substructures, and it allows one to build nonlinear models with significant model reduction and improved accuracy. By this approach, engineers can independently design each nonlinear substructure and then build an approximate multi-mode model of a complex structure that is the assembly of these substructures. This approach is much less computationally intensive than a brute force approach that directly uses the multi-mode models based on the multi-NNM invariant-manifold approach described in sections 2.1.2 and 2.2.2 ([42]). This is especially true when the number of retained linear modes of the assembled structure is large. However, the proposed nonlinear CMS approach generally provides an accurate model only when the couplings between substructures are weak.

The methods developed in this dissertation are numerical techniques geared toward simple structural elements and systems that are composed of assemblies of substructures. Much

work in this field remains to be done. Some ideas that require further investigation, using both analytical and numerical approaches, along this line of work include the following:

- An instability of single NNM manifolds in terms of vibration amplitude is suspected to exist in several of the systems considered. This suspicion is based on the fact that when the amplitude of the master mode of interest goes beyond a certain point, the family of trajectories on the exact single-NNM manifold is very difficult to numerically find using the shooting method. This causes the time response of the original model to have two components: a component having the nonlinear natural frequency of interest and a component having a high frequency. This indicates that the NNM of interest can not be uncoupled from the other NNMs. An analytical approach to this issue is possible only if the original model size in terms of modes is limited to 2 or 3 degrees of freedom. A numerical approach using a simulation based variational method and Floquet theory could address this problem for large-scale problems. Such investigations would provide an estimate of the amplitude range of validity of the NNMs. If known analytically, such information could be used as a guide to the computational generation of the NNMs, since one would know a priori the range over which the formulation is valid. The works of Rosenberg and Atkinson ([6]), Rand *et al.* ([15]), and Vakakis *et al.* ([19]) would be good starting points for guiding such an investigation.

- The continuation of a single NNM manifold in terms of a system parameter could be studied by using the "suspension trick" ([89]), wherein the parameter(s) of interest is (are) included as dynamics states (with trivial dynamics). Using such an approach, the NNM of interest will be of higher dimension ($2M + p$, where M is the number of NNMs and p is the number of parameters), and will depend on the parameters of interest. Galerkin-type methods can be used to solve for the parameterized family of NNM manifolds, and would provide useful information that can be used in the design process of structural systems. It is unclear, however, that such an approach would be computationally more efficient than simply generating the family of NNM manifolds by direct computation over the parameter range of interest.

- As mentioned in Chapter 2, the drawbacks of using $u - v$ coordinates might be eliminated by first applying the invertible van der Pol transformation ([22]) to the master $u - v$ coordinates. This would result in a new rectangular coordinate system which rotates at the linear natural frequency of the master mode. In this manner it would mimic more closely the amplitude and phase formulation, since the variables would be varying on a slower time scale. In addition, this method uncouples the u and v equations from one another up to linear order, which may simplify the formulation of the NNM manifold equations.

- It is well known that for systems composed of substructures, if the finite element mesh of the substructures is refined, the number of generalized constraint coordinates increases accordingly. This can result in a cumbersome CMS model in which there are many more constraint modes than substructure modes. For linear structural systems, Castenier *et al.* ([91]) have developed an effective technique to reduce the number of constraint coordinates using the concept of "linear constraint modes". It may be possible to develop a similar technique for nonlinear structural systems using invariant manifolds as the basis for the reduction of the constraint coordinates.

- An approximate multi-mode model of a system possessing an internal resonance can be developed through the NLCMS technique. This idea can be explored by subdividing the whole structural system of interest and then synthesizing the substructures using the NLCMS technique in such a way that the modes participating in the internal resonance are incorporated in the synthesized model. This idea is appealing due to the large computational efforts required for attacking such problems directly using the multi-NNM approach described in sections 2.1.2 and 2.2.2 ([42]).

- When the component modes are obtained from modal testing, or when an experimental verification of the component modes is required, the free-interface CMS methods are more attractive than the fixed-interface CMS methods. Therefore, it is worthwhile exploring the idea of extending the free-interface CMS technique developed by Craig and Chang ([66], [67] and [63]) to nonlinear structures by making use of free-interface NNMs in place of free-interface linear normal modes (LNMs). The extension of the

method of assembly to the nonlinear case appears to be challenging and remains for future work.

BIBLIOGRAPHY

BIBLIOGRAPHY

[1] A. D. Wright, C. E. Smith, R. W. Thresher, and J. L. C. Wang, "Vibration modes of centrifugally stiffened beams," *Journal of Applied Mechanics*, vol. 49, pp. 197–202, 1982.

[2] H. Du, M. K. Lim, and K. M. Liew, "A power series solution for vibration of a rotating timoshenko beam," *Journal of sound and vibration*, vol. 175, no. 4, pp. 505–523, 1994.

[3] E. Pesheck, C. Pierre, and S. W. Shaw, "Model reduction of a nonlinear rotaing beam through nonlinear normal modes," *Journal of Vibration and Acoustics*, vol. 124, pp. 229–236, 2002a.

[4] A. L. Hale and L. Meirovitch, "A general substructure synthesis method for the dynamic simulation of complex structures," *Journal of Sound and Vibration*, vol. 69, no. 2, pp. 309–326, 1980.

[5] A. K. Noor, "Recent advances and applications of reduction methods," *Applied Mechanics Reviews*, vol. 47, no. 5, pp. 125–146, 1994.

[6] R. M. Rosenberg and C. P. Atkinson, "On the natural modes and their stability in nonlinear two-degree-of-freedom systems," *Journal of Applied Mechanics*, vol. 26, pp. 377–385, 1959.

[7] C. P. Atkinson, "On the stability of the linearly related modes of certain nonlinear two-degree-of-freedom systems," *Journal of Applied Mechanics*, vol. 28, pp. 71–77, 1961.

[8] R. M. Rosenberg, "Normal modes of nonlinear dual-mode systems," *Journal of Applied Mechanics*, vol. 27, pp. 263–268, 1960.

[9] R. M. Rosenberg, "On normal vibrations of a general class of nonlinear dual-mode systems," *Journal of Applied Mechanics*, vol. 28, pp. 275–283, 1961.

[10] R. M. Rosenberg, "The normal modes of nonlinear n-degree-of-freedom systems," *Journal of Applied Mechanics*, vol. 29, pp. 7–14, 1962.

[11] R. M. Rosenberg, "Nonsimilar normal mode vibrations of nonlinear systems having two degrees of freedom," *Journal of Applied Mechanics*, vol. 31, pp. 7–14, 1964.

[12] R. M. Rosenberg, "On nonlinear vibrations of systems with many degrees of freedom," *Advances in Applied Mechanics*, vol. 9, pp. 155–242, 1966.

[13] L. Month and R. Rand, "The stability of bifurcating periodic solutions in a two-degree-of-freedom nonlinear system," *Journal of Applied Mechanics*, vol. 44, pp. 782–783, 1977.

[14] T. K. Caughey, A. Vakakis, and J. M. Sivo, "Analytical study of similar normal modes and their bifurcations in a class of strongly non-linear systems," *International Journal of Non-Linear Mechanics*, vol. 25, no. 5, pp. 521–533, 1990.

[15] R. Rand, C. Pak, and A. Vakakis, "Bifurcation of nonlinear normal modes in a class of two-degree-of-freedom-systems," *Acta Mechanica*, vol. 3, pp. 129–145, 1992.

[16] A. F. Vakakis, "Non-similar normal oscillations in a strongly non-linear discrete system," *Journal of Sound and Vibration*, vol. 158, no. 2, pp. 341–361, 1992.

[17] T. K. Caughey and A. F. Vakakis, "A method for examining steady state solutions of forced discrete systems with strong non-linearities.," *International Journal of Non-Linear Mechanics*, vol. 26, no. 1, pp. 89–103, 1991.

[18] A. F. Vakakis and T. K. Caughey, "A theorem on the exact nonsimilar steady-state motions of a nonlinear oscillator," *Journal of Applied Mechanics*, vol. 59, pp. 418–424, 1992.

[19] A. F. Vakakis, L. I. Manevitch, Y. V. Mikhlin, V. N. Pilipchuk, and A. A. Zevin, *Normal Modes and Localization in Nonlinear Systems*. John Wiley Sons, 1996.

[20] S. W. Shaw and C. Pierre, "Normal modes for non-linear vibratory systems," *Journal of Sound and Vibration*, vol. 164, no. 1, pp. 85–124, 1993.

[21] S. W. Shaw and C. Pierre, "Normal modes of vibration for non-linear continuous systems," *Journal of Sound and Vibration*, vol. 169, no. 3, pp. 319–347, 1994.

[22] J. Guckenheimer and P. Holmes, *Nonlinear Oscillations, Dynamical Systems, and Bifurcations of Vector Fields*. Springer-Verlag, New York, 1983.

[23] M. Marion and R. Temam, "Nonlinear galerkin methods," *SIAM Journal of Numerical Analysis*, vol. 26, no. 5, pp. 1139–1157, 1989.

[24] A. Steindl and H. Troger, "Nonlinear galerkin methods applied in the dimension reduction of vibrating fluid conveying tubes," in *Proceedings of the 4th Int. FSE, AE FIV + N Symposium*, (ASME Congress in Dallas), 1997.

[25] M. E. King and A. F. Vakakis, "An energy-based formulation for computing nonlinear normal modes in undamped continuous systems," *Journal of Vibration and Acoustics*, vol. 116, pp. 332–340, 1994.

[26] A. H. Nayfeh and S. A. Nayfeh, "On nonlinear modes of continuous systems," *Journal of Vibration and Acoustics*, vol. 116, pp. 129–136, 1994.

[27] A. H. Nayfeh, "On direct methods for constructing nonlinear normal modes of continuous systems," *Journal of Vibration and Control*, vol. 1, pp. 389–430, 1995.

[28] N. Boivin, C. Pierre, and S. W. Shaw, "Non-linear modal analysis of structural systems using multi-mode invariant manifolds," in *Proceedings of the AIAA Dynamics Specialists Conference*, no. 94-1672, (Hilton Head, South Carolina), April 1994.

[29] N. Boivin, C. Pierre, and S. W. Shaw, "Non-linear modal analysis of structural systems featuring internal resonances," *Journal of Sound and Vibration*, vol. 182, no. 2, pp. 336–341, 1995.

[30] A. H. Nayfeh, C. Chin, and S. A. Nayfeh, "On nonlinear normal modes of systems with internal resonance," *Journal of Vibration and Acoustics*, vol. 118, pp. 340–345, 1996.

[31] M. E. King and A. F. Vakakis, "An energy-based approach to computing resonant nonlinear normal modes," *Journal of Applied Mechanics*, vol. 63, pp. 810–819, 1996.

[32] J. C. Slater, "A numerical method for determining nonlinear normal modes," *Nonlinear Dynamics*, vol. 10, pp. 19–30, 1996.

[33] E. Pesheck, C. Pierre, and S. W. Shaw, "A new galerkin-based approach for accurate nonlinear normal modes through invariant manifolds," *Journal of Sound and Vibration*, vol. 249, no. 5, pp. 971–993, 2002b.

[34] E. Pesheck, C. Pierre, and S. W. Shaw, "Accurate reduced order models for a simple rotor blade model using nonlinear normal modes," *Mathematical and Computer Modelling*, vol. 33, pp. 1085–1097, 2001.

[35] P. Apiwattanalunggarn, S. W. Shaw, C. Pierre, and D. Jiang, "Finite-element-based nonlinear modal reduction of a rotating beam with large-amplitude motion," *Journal of Vibration and Control*, vol. 9, no. 3-4, pp. 235–263, 2003.

[36] D. Jiang, C. Pierre, and S. S. W., "Large-amplitude nonlinear normal modes of piecewise linear systems," *Journal of Sound and Vibration*, vol. In Preparation, 2003.

[37] X. Ma and A. F. Vakakis, "Karhunen-loeve decomposition of the transient dynamics of a multibay truss," *AIAA Journal*, vol. 37, no. 8, pp. 939–946, 1999.

[38] X. Ma, M. F. A. Azeez, and A. F. Vakakis, "Non-linear normal modes and non-parametric system identification of non-linear oscillators," *Mechanical Systems and Signal Processing*, vol. 14, no. 1, pp. 37–48, 2000.

213

[39] X. Ma and A. F. Vakakis, "Nonlinear transient localization and beat phenomena due to backlash in a coupled flexible system," *Journal of Vibration and Acoustics*, vol. 123, pp. 36–44, 2001.

[40] X. Ma, A. F. Vakakis, and L. A. Bergman, "Karhunen-loeve modes of a truss: Transient response reconstruction and experimental verification," *AIAA Journal*, vol. 39, no. 4, pp. 687–696, 2001.

[41] N. Boivin, C. Pierre, and S. W. Shaw, "Non-linear normal modes, invariance, and modal dynamics approximations of non-linear systems," *Nonlinear Dynamics*, vol. 8, pp. 315–346, 1995.

[42] D. Jiang, C. Pierre, and S. S. W., "The construction of nonlinear normal modes for systems with internal resonance: Application to rotating beams," *Nonlinear Dynamics, In Preparation*, 2003.

[43] D. Jiang, C. Pierre, and S. S. W., "Nonlinear normal modes for vibratory systems under periodic excitation," in *Proceeding of DETC'03, ASME 2003 Design Engineering Technical Conferences and Computers and Information in Engineering Conference*, (Chicago, Illinois, USA), September 2003.

[44] O. A. Bauchau and C. H. Hong, "Finite element approach to rotor blade modelling," *Journal of the American Helicopter Society*, vol. 32, no. 1, pp. 60–67, 1987.

[45] O. A. Bauchau and C. H. Hong, "Nonlinear response and stability analysis of beams using finite elements in time," *AIAA Journal*, vol. 26, no. 9, pp. 1135–1142, 1988.

[46] O. A. Bauchau and S. P. Liu, "Finite element based modal analysis of helicopter rotor blades," *Vertica*, vol. 13, no. 2, pp. 197–206, 1989.

[47] J. C. Simo and L. Vu-Quoc, "On the dynamics in space of rods undergoing large motions - a geometrically exact approach," *Computer Methods in Applied Mechanics and Engineering*, vol. 66, pp. 125–161, 1988.

[48] D. H. Hodges, A. S. Hopkins, and D. L. Kunz, "Analysis of structures with rotating, flexible substructures applied to rotorcraft aeroelasticity," *AIAA Journal*, vol. 27, no. 2, pp. 192–200, 1989.

[49] J. B. Kosmatka and P. P. Friedmann, "Vibration analysis of composite turbopropellers using a nonlinear beam-type finite-element approach," *AIAA Journal*, vol. 27, no. 11, pp. 1606–1614, 1989.

[50] A. K. Noor and J. M. Peters, "Reduced basis technique for nonlinear analysis of structures," *AIAA Journal*, vol. 18, no. 4, pp. 455–462, 1980.

[51] A. K. Noor, "Recent advances in reduction methods for nonlinear problems," *Computers Structures*, vol. 13, pp. 31–44, 1981.

[52] O. A. Bauchau and C. Bottasso, "Space-time perturbation modes for non-linear dynamic analysis of beams," *Nonlinear Dynamics*, vol. 6, no. 1, pp. 21–35, 1994.

[53] M. R. M. Crespo Da Silva, "General reduced order analytical model for nonlinear dynamic analyses of beams with or without lumped masses," *Applied Mechanics Reviews*, vol. 50, no. 11, pp. S28–S35, 1997.

[54] M. R. M. Crespo Da Silva, "A reduced-order analytical model for the nonlinear dynamics of a class of flexible multi-beam structures," *International Journal of Solids and Structures*, vol. 35, no. 25, pp. 3299–3315, 1998.

[55] R. Bamford, B. K. Wada, J. A. Garba, and J. Chisholm, "Dynamic analysis of large structural systems," 1971. Synthesis of Vibrating Systems, ASME Booklet.

[56] S. Goldenberg and M. Shapiro, "A study of modal coupling procedures for the space shuttle," tech. rep., Grumman Aerospace Corp., 1972. NASA Contractor Report 112252.

[57] J. T. Spanos and W. S. Tsuha, "Selection of component modes for flexible multibody simulation," *Journal of Guidance, Control, and Dynamics*, vol. 14, no. 2, pp. 278–286, 1991.

[58] C. Farhat and M. Geradin, "On a component mode synthesis method and its application to incompatible substructures," *Computers Structures*, vol. 51, no. 5, pp. 459–473, 1994.

[59] P. Seshu, "Review substructuring and component mode synthesis," *Shock and Vibration*, vol. 4, no. 3, pp. 199–210, 1997.

[60] W. C. Hurty, "Vibration of structural systems by component mode synthesis," *Proceedings of the American Society of Civil Engineers*, vol. 85, no. 4, pp. 51–69, 1960.

[61] W. Hurty, "Dynamic analysis of structural systems using component modes," *AIAA Journal*, vol. 3, no. 4, pp. 678–685, 1965.

[62] R. R. Craig and M. C. C. Bampton, "Coupling of substructures for dynamic analyses," *AIAA Journal*, vol. 6, no. 7, pp. 1313–1319, 1968.

[63] C. J. Chang, *A General Procedure for Substructure Coupling in Dynamic Analysis*. Phd. thesis, The University of Texas, Austin, Texas, 1977.

[64] R. R. Craig, "Substructure methods in vibration," *Journal of Mechanical Design*, vol. 117, pp. 207–213, 1995.

[65] W. Wang and J. Kirkhope, "Component mode synthesis for damped rotor systems with hybrid interfaces," *Journal of Sound and Vibration*, vol. 177, no. 3, pp. 393–410, 1994.

[66] R. R. Craig and C. J. Chang, "Free-interface methods of substructure coupling for dynamic analysis," *AIAA Journal*, vol. 14, no. 11, pp. 1633–1635, 1976.

[67] R. R. Craig and C. J. Chang, "On the use of attachment modes in substructure coupling for dynamic analysis," in *AIAA/ASME 18th Struct., Structural Dynamics, and Materials Conference*, no. 77-405, (San Diego, CA), pp. 89–99, 1977.

[68] S. Rubin, "Improved component-mode representation for structural dynamic analysis," *AIAA Journal*, vol. 13, no. 8, pp. 995–1006, 1975.

[69] R. H. MacNeal, "A hybrid method of component mode synthesis," *Journal of Computers and Structures*, vol. 1, no. 4, pp. 581–601.

[70] S. W. Shaw and C. Pierre, "Non-linear normal modes and invariant manifolds," *Journal of Sound and Vibration*, vol. 150, no. 1, pp. 170–173, 1991.

[71] E. Pesheck, N. Boivin, C. Pierre, and S. W. Shaw, "Nonlinear modal analysis of structural systems using multi-mode invariant manifolds," *Nonlinear Dynamics*, vol. 25, pp. 183–205, 2001.

[72] S. W. Shaw, "An invariant manifold approach to nonlinear normal modes of oscillation," *Journal of Nonlinear Science*, vol. 4, pp. 419–448, 1994.

[73] S. Hsieh, S. W. Shaw, and C. Pierre, "Normal modes for large amplitude vibration of a cantilever beam," *International Journal of Solids and Structures*, vol. 31, no. 14, pp. 1981–2014, 1994.

[74] S. W. Shaw, C. Pierre, and E. Pesheck, "Modal analysis-based reduced-order models for nonlinear structures-an invariant manifold approach," *The Shock and Vibration Digest*, vol. 31, no. 1, pp. 3–16, 1999.

[75] D. Jiang, C. Pierre, and S. S. W., "The construction of nonlinear normal modes for systems with internal resonance: Application to rotating beams," in *Proceedings of 2002 ASME International Mechanical Engineering Congress*, 2002.

[76] B. A. Finlayson, "The method of weighted residuals and variational principles with application in fluid mechanics, heat and mass transfer," 1972.

[77] J. N. Reddy, *Applied Functional Analysis and Variational Methods in Engineering*. McGraw-Hill, 1986.

[78] J. P. Boyd, *Chebyshev and Fourier Spectral Methods*. Dover Publications, New York, 2001.

[79] A. H. Nayfeh and D. T. Mook, *Nonlinear Oscillations*. Wiley-Interscience, New York, 1979.

[80] V. A. Patel, *Numerical Analysis*. Harcourt Brace College Publishers, Florida, 1994.

[81] J. V. Villadsen and W. E. Stewart, "Solution of boundary-value problems by orthogonal collocation," *Chemical Engineering Science*, pp. 1483–1501, 1967.

[82] E. Pesheck, *Reduced Order Modelling of Nonlinear Structural Systems Using Nonlinear Normal Modes and Invariant Manifolds*. Phd. thesis, The University of Michigan, Ann Arbor, MI., 2000.

[83] R. Fletcher, *Practical Methods of Optimization*. John Wiley Sons, 2001.

[84] W. H. Press, S. A. Teukolsky, W. T. Vetterling, and B. P. Flannery, *Numerical Recipes*. Cambridge University Press, 1999.

[85] J. Stoer and R. Bulirsch, *Introduction to Numerical Analysis*. Springer-Verlag, New York, 1993.

[86] G. L. Anderson, "On the extensional and flexural vibrations of rotating bars," *International Journal of Non-Linear Mechanics*, vol. 10, pp. 223–236, 1975.

[87] J. N. Reddy, *An Introduction to The Finite Element Method*. McGraw-Hill, 1993.

[88] L. Meirovitch, *Computational Methods in Structural Dynamics*. Sijthoff Noordhoff, 1980.

[89] J. Carr, *Applications of Centre Manifold Theory*. Springer-Verlag, 1981.

[90] L. Meirovitch, *Analytical Methods in Vibrations*. Macmillan Publishing, New York, 1967.

[91] M. P. Castanier, Y. C. Tan, and C. Pierre, "Characteristic constraint modes for component mode synthesis," in *Proceedings of Design Engineering Technical Conference 1999*, no. DETC99/VIB-8187, September 1999.